N° d’ordre : 3320

THÈSE

Présentée à

L’UNIVERSITÉ BORDEAUX I

ÉCOLE DOCTORALE DES SCIENCES CHIMIQUES

par **Chih-Hao HUANG**

POUR OBTENIR LE GRADE DE

DOCTEUR

SPÉCIALITÉ : CHIMIE ORGANIQUE

****

Towards supramolecular heterojunctions: Self-assembled hydrogen-bonded architectures for organic photovoltaic devices

****

Soutenue le : 11 Décembre 2006

Après avis de :

MM.	**J.-F. Nierengarten**	Directeur de recherche, LCC, CNRS	Rapporteur
	G. Dennler	Directeur de recherche, Konarka, Autriche	Rapporteur

Devant la commission d’examen formée de :

MM.	**A. Kuhn**	Professeur, Université de Bordeaux I	Président
	J.-F. Nierengarten	Directeur de recherche, LCC, CNRS	Rapporteur
	G. Dennler	Directeur de recherche, Konarka, Autriche	Rapporteur
	L. Hirsch	Chargé de Recherche, Université de Bordeaux I	Examinateur
	C. Dagron-Lartigau	Maître de conférences, Université de PAU	Examinateur
	D. M. Bassani	Directeur de recherche, Université de Bordeaux I	Examinateur

Membres invité :

MM.	**G. Wantz**	*Maître de conférences,* Université de Bordeaux I	Examinateur

-2006-

Acknowledgements

Before I started making a PhD, I already knew that this will be my most memorable journey in my life, because I can devote myself totally to the scientific research.

First of all, I would like to thank all my thesis juries for their conduct: Prof. **Alexander Kuhn**, Professeur, École Nationale Supérieure de Chimie et de Physique de Bordeaux, Université Bordeaux 1; Dr. **Jean-François Nierengarten**, Directeur de Recherche, Laboratoire de Chimie de Coordination du CNRS; Dr. **Gilles Dennler**, Director of research, Konarka (Austria); Dr. **Christine Dagron-Lartigau**, Maître de conférences, Laboratoire de Physico-Chimie des Polymères, Université de Pau et des pays de l'Adour; Dr. **Lionel Hirsch**, Chargé de Recherche, Laboratoire IXL, Université Bordeaux 1; Dr. **Guillaume Wantz**, Maître de conférence, Université de Bordeaux 1, and my advisor : Dr. **Dario Bassani**, Directeur de Recherche, Laboratoire de Chimie Organique et Organométallique, Université Bordeaux 1.

I am grateful to Dr. Dario Bassani, for the scientific and moral support that he gave to me. Dear Dario, I would like to thank you for giving me this great opportunity to do the research in your group, and for introducing me to such a wild and interesting field of science. Not so many students can have this kind of experience to do the research covering different areas at same time: the supramolecular chemistry, organic synthesis, electro- and photoelectrochemistry, materials science and solar cell devices fabrication. I really appreciate your guidance during this doctoral research period.

Also, I would like to thank Prof. Kuhn Under his instructions, I completed all the electro- and photoelectrochemical measurements. And it is my great honor to have him being the president of my thesis juries.

Prof. Niyazi Serdar Sariciftci and Dr. Gilles Dennler, thank you for giving me this great opportunity to have one month scientific visit in *LIOS*, Linz (Austria). During this month, I did learn a lot in the field of organic solar cells, and it's a very nice experience to stay in Linz. Dr. Lionel Hirsch and Dr. Guillaume Wantz, thank you very much to allow me working freely in *PIOM*. We have a very good collaboration for the pass two years.

Many people I would like to thank in the pass four years, my friends and colleagues, they help me a lots, not only in the chemistry but also in the daily life: Vincent, Fabien, David, Alya, Eric, Mounir, Alex, Cecile, Yoann and Pascale.

Vincent and Fabien: we have shared the office for four years; it is an unusual experience for me. Both of you are my closed friends.

David: we work together side-by-side in the laboratory, and we both agree what is the most difficult part while we worked in the laboratory. We shared all the good and difficult times together.

Many thanks to all the members and ex-members in NEO group: Jean-Pierre, Jean-Luc, Jean-Marc, Brigitte, Andre, Guillaume, Delphine, and special thanks to Nathan for his kindly help during my doctoral research.

I would like to thank my parent who supported me to go abroad for such a long time. And I really want to thank Vivian; it is not easy for both of us to keep this relationship through such a long time and a long distance between Bordeaux and Taipei, but we made it.

It is not easy for a foreign student who has to stay alone and is far away from home. I am grateful to have so many good friends during this period of time, all the best to you and I wish to see you soon in France.

Bordeaux, January, 2007 Chih-Hao Huang

CONTENT

ABBREVIATIONS

Chemical Reagents and Protective Groups

Ac	acetyl
Bn	benzyl
DABCO	1,4-diazabicyclo[2.2.2]octane
DBU	1,8-diazabicyclo[5.4.0]undec-7-ene
DMAP	4-N,N-dimethylaminopyridine
DMF	N,N-dimethylformaldehyde
DMSO	dimethylsulfoxide
NBS	N-bromosuccinimide
$Ni(acac)_2$	nickel acetylacetonate
P3HT	poly(3-hexylthiophene)
PCBM	[6,6]-phenyl C61-butyric acid methyl ester
PCC	pridium chlorochromate
PEDOT	poly(3,4-ethylenedioxythiophene)
PSS	polystyrene sulfonic acid
MDMO-PPV	poly[2-methoxy-5-(3',7'-dimethyloctyloxy)-1-4-phenylene vinylene]
TFA	trifluoroacetic acid
THF	tetrahydrofuran
TsOH	toluenesulfonyl acid

Physical/Chemical Characteristics

HOMO	highest occupied molecular orbital
LUMO	lowest occupied molecular orbital

M	mol/L (mole per liter)
L	liter
g	gramme
eq.	molar equivalent
δ	chemical shift
ppm	parts per million
A	ampere
J	current density
V	volt

Chapter 1

Introduction

The current issue of global energy supply and consumption deeply impacts daily life. Currently, the major part of energy resources used are stored energy, mainly from fuels in the form of coal, oil, natural gas, or nuclear power. However, a looming crises for the human population stems not only from using up all the fossil fuels, but also from the serious environmental pollution due to the consumption of these fossil fuels, such as global warming and depleting of the ozone shield. An important and urgent worldwide issue is to develop viable, renewable and environmentally friendly energy sources which will ensure continued and stable development.

Compared to other renewable and low pollution energy sources such as, for example, wind power, hydroelectric power, geothermal or biomass, sunlight provides by far the largest energy resource (4.3×10^{20} J per hour striking the Earth). Producing electricity through light-to-electrical (photovoltaic) energy conversion by solar cells is the most direct method to capture and to convert solar energy into a convenient form of usable energy. The current expansion trend of the photovoltaic industry over the last decade has revealed the progressive demand of the photovoltaic market, which is expected to grow extensively in near future (Figure 1.1).[1] In fact, since the beginning of 2006 the very strong demand of polycrystalline silicon, a basic raw material for silicon-based solar cells, already foreshadows this tendency.

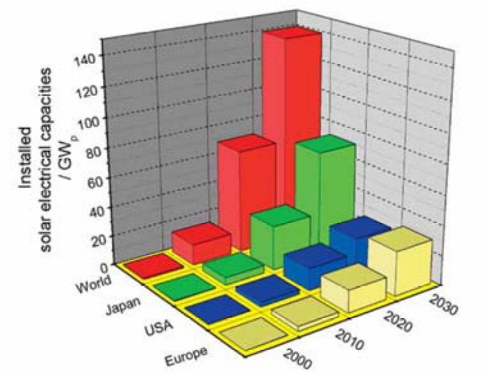

Figure 1.1 Estimation of present and future installed solar capacities expressed in GW (sources: Japanese, U.S. and EPIA roadmaps).[1]

Silicon-based photovoltaic devices have played a major role in the development of light-to-electrical energy conversion, with laboratory efficiencies now approaching 35%.[2] Durability and zero emission during operation are attractive features that are countered only by their high manufacturing costs and fragility. For these reasons, as well as concerns about the use of organic semiconductors, hybrid inorganic/organic and all-organic polymer alternatives have been actively pursued in recent years as alternatives amenable to large-scale deployment.[3] One of the most attractive developments in all-organic polymer-blended solar cells is their flexibility, enabling fabrication on plastic substrates. In addition to being flexible, this also dramatically reduces the weight of solar cell modules compared to those made from silicon-based devices.[1a,3b,3c,4] This capability allows more extensive applications in modern daily life such as the portable electronic devices, cars, and fabric. Current conjugated organic polymer technology originates from interest in the construction of o-LED (organic light emitting diode) and o-FET (organic field-effect transistor) devices. Over the last decade, conjugated polymers have benefited from increased interest since the report by Heeger *et al.*, [3a] and Sariciftci and co-workers [5] demonstrating that a substantial improvement in the photovoltaic properties of such materials could be obtained by blending [60]fullerene into the polymer mixture (Figure 1.2). In such composite devices, it has been proposed that the fullerene component acts as the electron transport material, increasing the efficiency of charge separation and transport, and high rectification ratios have been observed in PPV/C_{60} heterojunctions (PPV: poly(*p*-phenylenevinylene)). It has also been proposed that substantial improvements in performance could result from higher fullerene content. However, fullerenes are only marginally soluble and their incorporation into molecular or polymer devices poses significant challenges that have barred their use in numerous applications. The introduction of higher proportions of C_{60} results in phase separation, creating unwanted heterogeneous domains which adversely affect the photovoltaic response.[6] To overcome the poor solubility of fullerene, chemical modification is used to improve the physical behavior that is able to enhance compatibility between the organic polymer and fullerene components without altering the special electronic properties of fullerene. The soluble derivative of C_{60}, [6,6]-phenyl-C_{61} butyric acid methyl ester (PCBM)[7] is nowadays commercially available and is widely used in all-organic solar cells devices. The excellent solubility of PCBM in non-polar organic solvents, including toluene and chlorobenzenes, allows higher fullerene loading ratios of up to 80 % (w/w, PCBM *vs.* MDMO-PPV or P3HT) in the bulk heterojunction devices, thus resulting in improved performance (up to 5%).[8]

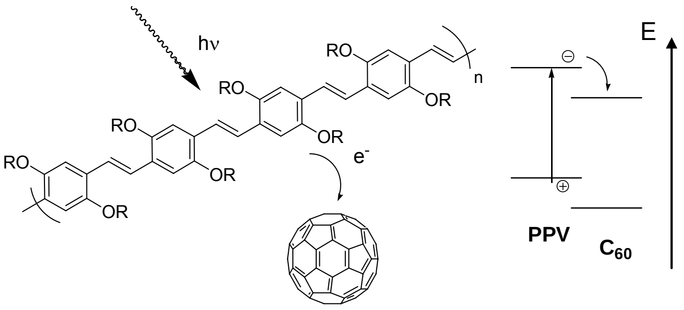

Figure 1.2. Schematic illustration of the photoinduced charge transfer (left) with a sketch of the energy level scheme (right). After excitation in the PPV polymer, the electron is transferred to the C_{60} due to its higher electron affinity.[3a]

Meanwhile, the synthesis and investigation of covalently-linked fullerene π-conjugated oligomer dyads, triads, and more complex dendritic assemblies has led to important breakthroughs in the comprehension of the fundamental energy and electron transfer processes leading to the generation of long-lived charge separated states. Thus, through covalent modification of C_{60}, introduction of a plethora of electron-rich oligomers, including oligo(*p*-phenylene vinylene)s (Figure 1.3),[9] oligo(thiophenes),[10] metalloporphyrin (Figure 1.4), arrays[11] and others[12] has been achieved and used to construct increasingly complex covalent architectures, including several doubly fullerene-appended oligomer "dumbells" (Figure 1.5).[13]

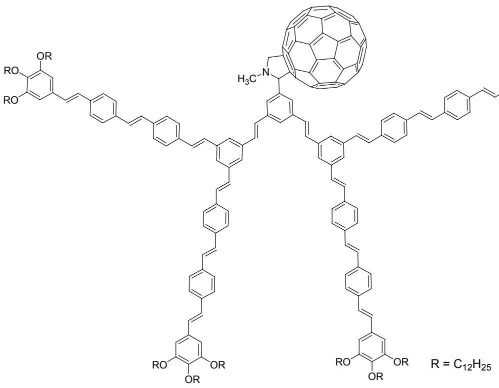

Figure 1.3. The covalent modification of [60]fullerene with oligo(*p*-phenylene vinylene)s -appended dendritic wedge.[9a]

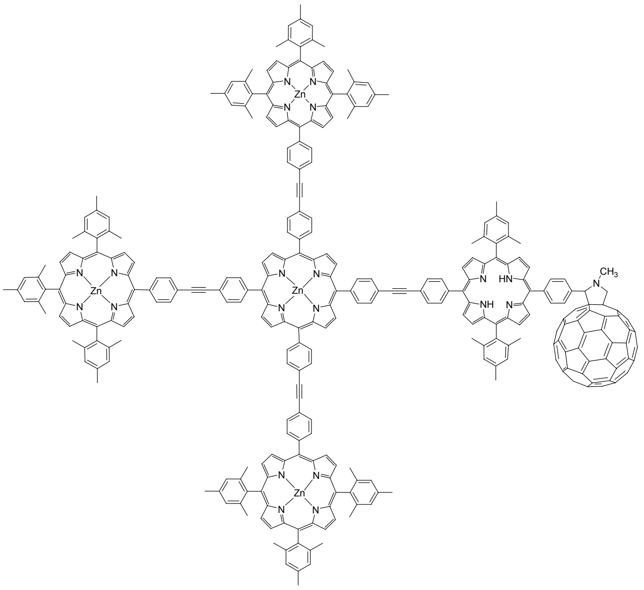

Figure 1.4. Metalloporphyrin-fullerene array.[11]

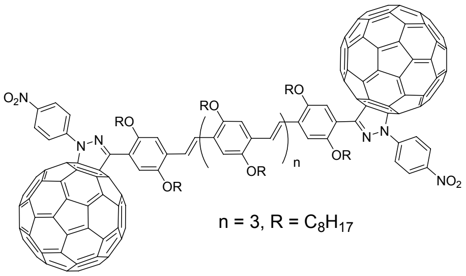

Figure 1.5. Dumbbell-shaped doubly fullerene-appendeded oligomer.[13b]

The construction of solid-state devices based on these covalent adducts has been investigated recently.[14] For example, coupled with oligothiophene as electron donors, C_{60}-containing systems such as dyads and triads onto solid substrates have recently been demonstrated as very promising candidates in artificial photosynthetic cells (see Figure 1.6).[15] Highly efficient photoinduced energy and electron transfer is common in donor-acceptor molecular systems, and photodynamic studies revealed that fullerene is essential in promoting photo-induced electron transfer and to slow down charge recombination.[16]

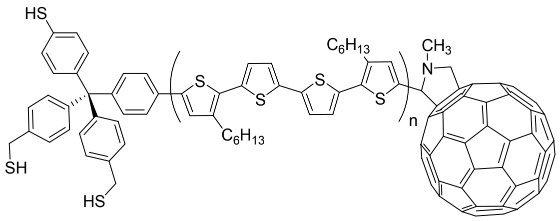

Figure 1.6 Oligothiophene-fullerene-linked photo- /and electroactive molecule applied towards to the self-assembled monolayer system bearing a tripod anchor on gold surface.[15]

Despite having excellent physical and electrical properties, the covalently-linked assemblies approach has severe limitations that impede further development towards large-scale applications. Most notably, the preparation of covalently-linked molecules requires lengthy and costly multi-step syntheses necessitating extensive purification techniques. Additionally, incorporation of these "small" molecules possibly introduces anisotropicity in the mobility of charge migration, which could attenuate the overall efficiency of charge transport. On the other hand, one of the advantages of studying monolayer-based devices is their straightforward photoelectrical mechanism due to the absence of intermolecular interactions. However, the incident light-to-electrical energy conversion efficiency in monolayer-based devices is limited by their low light absorbance, and although in some cases a very high efficiency of intramolecular photo-induced charge transfer is achieved, the only way to increase the photocurrent to meaningful value would be to tremendously enlarge the active surface area.

Considering the innate character of self-assembled multilayer systems, in which one anticipates strong light absorption to be a prerequisite for photonic devices, the spontaneous association of molecules under equilibrium conditions into stable aggregations with well-defined composition leads to a compromise between intra- and/or intermolecular charge separation and intermolecular charge transport in the organized material. Hydrogen-bonding interactions are successfully employed in

Nature to induce the self-assembly of molecular constituents into architectures possessing extensive complexity and functionality. To date, relatively few electroactive species capable of participating in hydrogen-bonding have been reported, although the rate of apparition of their reports has hastened very recently.[17] Effective hydrogen-bonding systems require that units contain matched complementary sites, which associate to give more sophisticated architectures (see Figure 1.7). In this approach, the ready and straightforward benefit gained from hydrogen-bonding is its capability to align the electron donor and electron acceptor components, thus potentially satisfying part of the fundamental requirements of photovoltaic devices: a close distance between the donor-acceptor pair, and shortest charge transport pathway to the electrodes.

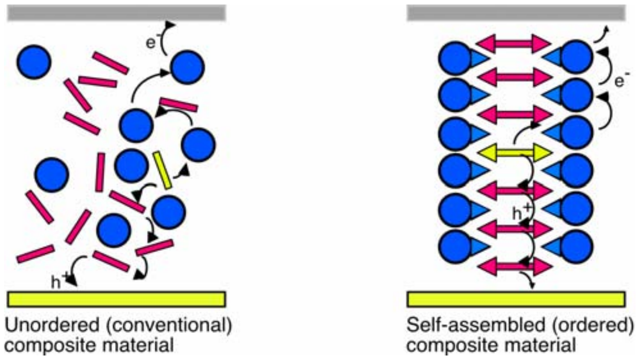

Figure 1.7. In a conventional composite material (left), charge separation from an excited donor (in yellow) results in an electron-hole pair that must then percolate through an ill-defined path to the corresponding electrodes. The same situation is much more efficient if the hole and electron transport materials are suitably ordered, for example thorough self-assembly (right).

Recent examples of self-assembled fullerene-containing architectures include the formation of asymmetric or symmetric dimeric structures, as shown in Figure 1.8 (left). The former species are exemplified by the systems introduced by Stoddart,[18] Guldi,[19] and Nierengarten,[20] where assembly is promoted by hydrogen-bonding interactions between an ammonium moiety and a crown ether unit. Examples of the latter type of system are presented by Janssen, Meijer and colleagues[17b] utilizing the self-complementary ureidopyrimidinone unit introduced by Meijer,[21] in which four donor/acceptor hydrogen-bonding sites promote the association of two similar units. (Figure 1.8, right).

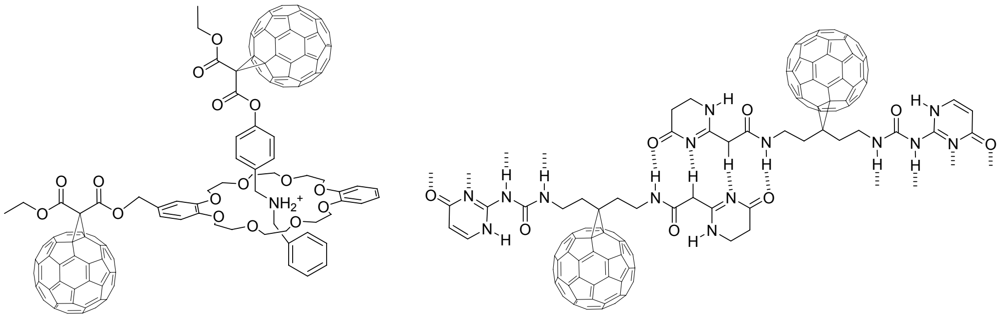

Figure 1.8 Hydrogen-bonded asymmetric dimer (left)[18] and multi-fullerene self-assembled polymers (right).[17b]

The objectives of this research are to test and verify the implementation of supramolecular self-assembly of photo-and electro-active components programmed to self-organize into molecular hetero-junctions to efficiently construct supramolecular architectures for photovoltaic applications. The aims of the project are to design and construct novel donor/acceptor-based (oligomer/fullerene) self-organized hybrid materials, and demonstrate the use of these new devices in the fabrication of light-to-energy conversion products.

References:

1. (a) G. Dennler, N.S. Sariciftci, *Proceedings of the IEEE*, **2005**, *93*, 1429-1439.; (b) A. Jäger-Waldau, "PV status report 2003," Institute for Environment and Sustainability, Eur. Commission, **2003**.
2. (a) S. J. Lade, A. Zahdi, *Microelectron. J.* **2005**, *35*, 401-410.; (b) W. Fuhs, "Silicon thin-film solar cells" In *Nanostructured and Advanced Materials*; A. Vaseashta, D. Dimova-Malinovska, J. M. Marshall, Ed.; Springer, the Netherlands, **2005**, pp:293-298.; (C) D. E. Caelson, *Sol. Energy Mater. Sol. Cells* **2003**, *78*, 627-645. (d) *PHOTON International,* Solar Verlag GmbH, **2003**, *9*, 17.
3. (a) N. S. Sariciftci, L. Smilowitz, A. J. Heeger, F. Wudl, *Science* **1992**, *258*, 1474-1476.; (b) C. J. Brabec, N. S. Sariciftci, J. C. Hummelen, *Adv. Funct. Mat.* **2001**, *11*, 15-26.; (c) C. J. Brabec, *Sol. Energy Mater. Sol. Cells,* **2004**, *83*, 273-292.
4. (a) G. Dennler, C. Lungenschmied, H. Neugebauer, N. S. Sariciftci, M. Latrèche, G. Czeremuszkin, M. R. Wertheimer, *Thin Solid Films*, **2006**, *511-512*, 349-353.; (b) G. Dennler, C. Lungenschmied, H. Neugebauer, N. S. Sariciftci, A. Labouret, *J. Mater. Res.* **2005**, *20*, 3224-3233.
5. S. E. Shaheen, C. J. Brabec, T. Fromherz, F. Padinger, N. S. Sariciftci, E. Gloetzl, (**Patent** no. WO0184645, published 2001-11-08)
6. (a) G. Yu, Y. Gao, J. C. Hummelen, F. Wudl, A. J. Heeger, *Science* **1995**, *270*, 1789-1791.; (b) K. Matsumoto, M. Fujitsuka, T. Sato, S. Onodera, O. Ito, *J. Phys. Chem. B*, **2000**, *104*, 11632-11638.
7. J. C. Hummelen, B. W. Knight, F. LePeq, F. Wudl, J. Yao, C. L. Wilkins, *J. Org. Chem.* **1995**, *60*, 532-538.
8. (a) P. Peumanns, S. R. Forrest, *Appl. Phys. Lett.* **2001**, *79*, 126-128.; (b) R. Koeppe, N.S. Sariciftci, P. Troshin, R. Lyubovskaya, *Applied Physics Letters*, **2005**, *87*, P244102.; (c) M. Al-Ibrahim, O. Ambacher, S. Sensfuss, G. Gobsch, *Appl. Phys. Lett.* **2005**, *86*, 201120/1-201120/3.
9. (a) G. Accorsi, N. Armaroli, J.-F. Eckertb, J.-F. Nierengarten, *Tetrahedron Lett.* **2002**, *43*, 65–68.; (b) J.-F. Nierengarten, J.-F. Eckert, J.-F. Nicoud, L. Ouali, V. Krasnikov, G. Hadziioannou, *Chem. Commun.* **1999**, 617-618., (c) E. Peeters, P. A. van Hal, J. Knol, C. J. Brabec, N. S. Sariciftci, J. C. Hummelen, R. A. J. Janssen, *J. Phys. Chem. B*, **2000**, *104*, 10174-10190.; (d) J.-F. Eckert, J.-F. Nicoud, J.-F. Nierengarten, S.-G. Liu, L. Echegoyen, N. Armaroli, F. Barigeletti, L. Ouali, V. Krasnikov, G. Hadziioannou, *J. Am. Chem. Soc.* **2000**, *122*, 7467-7479.
10. (a) T. Yamashiro, Y. Aso, T. Otsubo, H. Tang, Y. Harima, K. Yamashita, *Chem. Lett.* **1999**, *28*, 443-444.; (b) D. Hirayama, T. Yamashiro, K. Takimiya, Y. Aso, T.

Otsubo, H. Norieda, H. Imahori, Y. Sakata, *Chem. Lett.* **2000**, *29*, 570-571.; (c) L. Sànchez, M. T. Rispens, J. C. Hummelen, *Angew. Chem., Int. Ed. Eng*. **2002**, *41*, 838-840.

11. G. Kodis, P. A. Liddell, L. de la Garza, P. C. Clausen, J. S. Lindsey, A. L. Moore, T. A. Moore, D. Gust, *J. Phys. Chem. A*, **2002**, *106*, 2036-2048.
12. (a) T. Gu, J.-F. Nierengarten, *Tetrahedron. Lett.* **2001**, *42*, 3175-3178.; (b) C. Martineau, P. Blanchard, D. Rondeau, J. Delaunay, J. Roncali, *Adv. Mater.* **2002**, *14*, 283-287.; (c) J. J. Apperloo, C. Martineau, P. A. van Hal, J. Roncali, R. A. J. Janssen, *J. Phys. Chem. A*, **2002**, *106*, 21-31.; (d) Y. Obara, K. Takimiya, Y. Aso, T. Otsubo, *Tetrahedron Lett.* **2001**, *42*, 6877-6881.
13. (a) P. A. van Hal, J. Knol, B. H. W. Lamgeveld-Voss, S. C. J. Meskers, J. C. Hummelen, R. A. J. Janssen, *J. Phys. Chem. A,* **2000**, *104*, 5974-5988.; (b) M. J. Go´mez-Escalonilla, F. Langa, J.-M. Rueff, L. Oswaldb, J.-F. Nierengarten, *Tetrahedron Letters*, **2002**, *43*, 7507–7511.: (c) J. L. Segura, N. Martín, *Tetrahedron Lett.* **1999**, *40*, 3239-3242.; (d) D. M. Guldi, C. Luo, A. Swartz, R. Gomez, J. L. Segura, N. Martín, *J. Phys. Chem. A*, **2004**, *108*, 455-467.; (e) P. A. van Hal, E. H.A. Beckers, S. C. J. Meskers, R. A. J. Janssen, B. Jousselme, P. Blanchard, J. Roncali, *Chem. Eur. J.* **2002**, *8*, 5415-5429.; (f) A. Dhanabalen, J. Knol, J. C. Hummelen, R. A. J. Janssen, *Synth. Met.* **2001**, *119*, 519-522.
14. (a) D. M. Guldi, C. Luo, A. Swartz, R. Gómez, J. L. Segura, N. Martìn, C. J. Brabec, N. S. Sariciftci, *J. Org. Chem.* **2002**, *67*, 1141-1152.; (b) N. Negishi, K. Takimiya, T. Otsubo, Y. Harima, Y. Aso, *Chem. Lett*. **2004**, *33,* 654-655.
15. D. Hirayama, K. Takimiya, Y. Aso, T. Otsubo, T. Hasobe, H. Yamada, H. Imahori, S. Fukuzumi, Y. Sakata, *J. Am. Soc. Chem.* **2002**, *124*, 532-533.
16. H. Imahori, Y. Mori, Y. Matano, *J. Photochem. Photobiol. C,* **2003**, *4*, 51-83.
17. (a) P. Jonkheijm, J. K. J. van Duren, M, Kemerink, R, A. J. Janssen, A. P. H. J. Schenning, E. W. Meijer, *Macromolecules* **2006**, *39*, 784-788.; (b) E. H. A. Beckers, A. P. H. J. Schenning, P. A. van Hal, A. El-ghayoury, L. Sánchez, J. C. Hummelen, E. W. Meijer, R. A. J. Janssen, *Chem. Commun.* **2002,** 2888-2889.; (c) F. Wuerthner, Z. Chen, F. J. M. Hoeben, P. Osswald, C.-C. You, P. Jonkheijm, J. v. Herrikhuyzen, A. P. H. J. Schenning, P. P. A. M. van der Schoot, E. W. Meijer, E. H. A. Beckers, S. C. J. Meskers, R. A. J. Janssen, *J. Am. Chem. So*c. **2004**, *126*, 10611-10618.; (d) P. Jonkheijm, N. Stutzmann, Z. Chen, D. M. de Leeuw, E. W. Meijer, A. P. H. J. Schenning, F. Wurthner, *J. Am. Chem. Soc.* **2006**, *128*, 9535-9540.
18. F. Diederich, L. Echegoyen, M. Gómez-López, R. Kessinger, J.F. Stoddart, *J. Chem. Soc., Perkin Trans. 2,* **1999**, 1577-1586.
19. D. M. Guldi, J. Ramey, M. V. Martínez-Díaz, A. de la Escosura, T. Torres, T. Da

Ros, M. Prato, *Chem. Commun.* **2002,** 2774-2775.

20. M. Gutiérrez-Nava, H. Nierengarten, P. Masson, A. Van Dorsselar, J.-F. Nierengarten, *Tetrahedron Lett.* **2003,** *44,* 3043-3046.
21. R. P. Sijbesma, E. W. Meijer, *Chem. Commun.* **2003**, 5-16.

Chapter 2

Supramolecular Chemistry

Molecular self-assembly is the spontaneous association, under kinetic or equilibrium conditions, of molecules into stable, structurally-defined aggregates, held together by noncovalent interactions. The specific intermolecular interactions (comprising the recognition patterns) between the components can be considered as structural nodes of the architecture, and it is possible to describe the formation of molecular networks as resulting from translations of the nodes into one (1-D), two (2-D), or three directions (3-D) of space.[1] Weak forces and noncovalent interactions such as metal-ligand coordination interactions, hydrogen bonds, van der Waals, hydrophobic and Coulombic (electrostatic) forces are extensively used in enabling the self-assembly of supramolecular architectures of varying stability.

In Nature, self-assembly is a ubiquitous process, used to create complex functional biological structures with precision. Biologically self-assembled structures are built up by a modular approach from simpler subunits, thus minimizing the amount of information required for a specific ensemble. In artificial systems, the spontaneous but controlled generation of functional supramolecular architectures has emerged as a major development of supramolecular chemistry towards the design of increasing complexity,[2] and nowadays has spawned new and exciting perspectives on the way to multi-component architectures and molecular devices for specific functions.

For example, by using metal-ligand coordination interactions, square [4×4] grid-type assembly are formed, which could serve as components of information storage devices through the algorithm defined by their coordination geometry (Figure 2.1).[3] Similarly, self-assembled porphyrin boxes can serve as a three-dimensional light-harvesting model in the study of energy hopping process (Figure 2.2, left).[4] Other structurally well-defined coordination cages that self-assemble from six metal ions and four tridentate ligand selectively encapsulate large organic molecules at the fixed position of the nanosized cavity. These nanocages act as molecular flasks to promote intermolecular [2+2] photodimerization (Figure 2.2, right).[5]

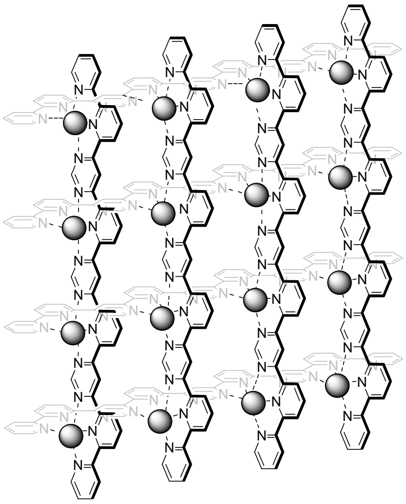

Figure 2.1. Schematic representation of square [4×4]Pb^{II}_{16} grid-type assembly.[3]

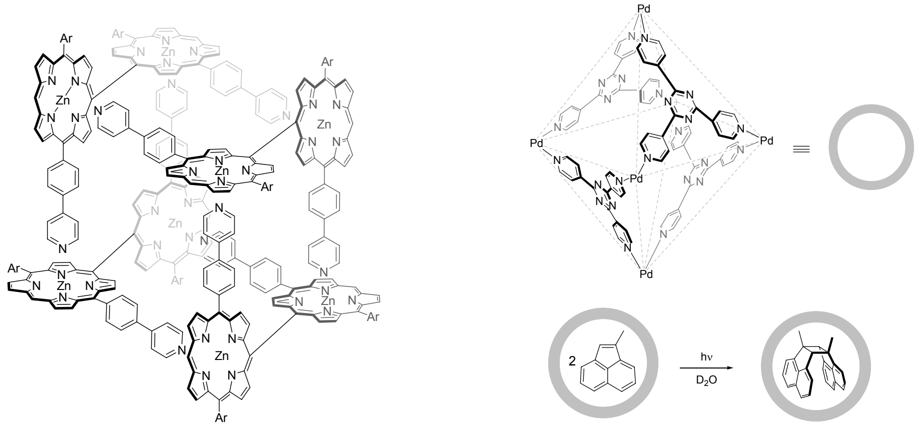

Figure 2.2. (Left) Porphyrin boxes constructed by homochiral self-sorting assembly.[4] (Right) Nanocages assembled from six metal ions and four tridentate ligands.[5]

In Figure 2.3, hydrogen-bonding interactions in the melamine-barbituric acid system triggers the supramolecular catalysis of [2+2] olefin photodimerization[6a] and [60]fullerene cyclodimerization.[6b] The supramolecular template (the barbiturate), operating through molecular recognition, can thus be used to promote and control excited-state reactions.

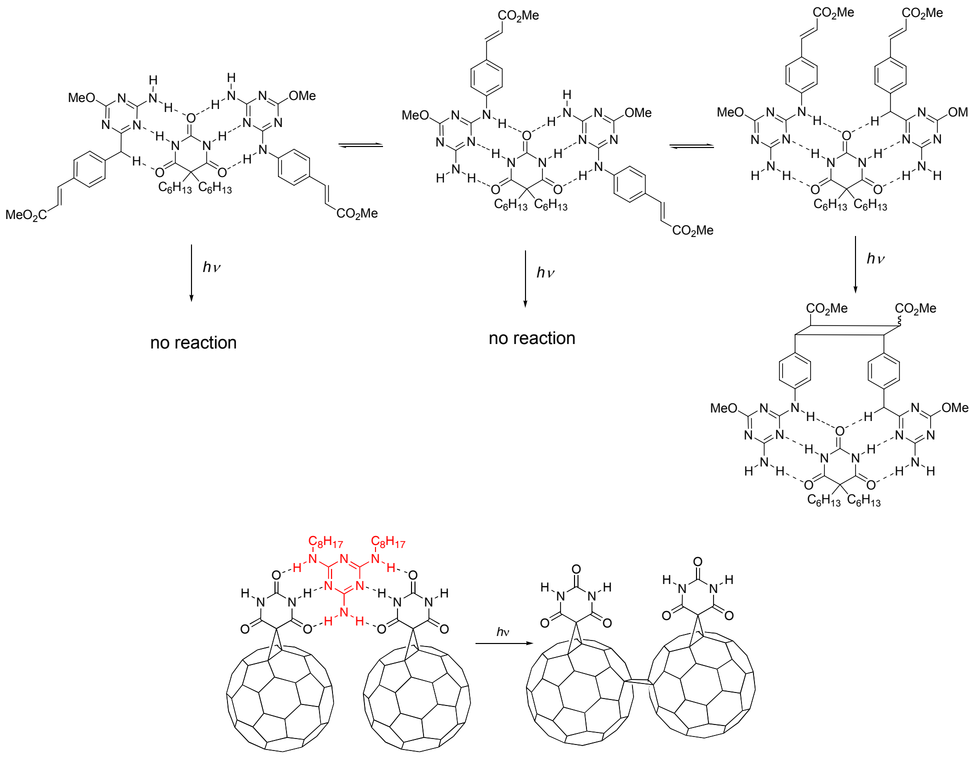

Figure 2.3. Supramolecular catalysis of [2+2] olefin photodimerization,[6a] and [60]fullerene cyclodimerization.[6b]

The examples shown in Figure 2.4 and 2.5 present the usefulness of artificial supramolecular architectures composing π-stacked nanofibers[7] and nanotubes[8] in the study of energy transfer process.

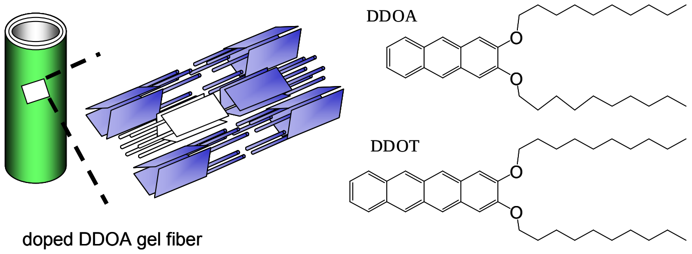

Figure 2.4. Schematic representation of a doped DDOA gel fiber, where the energy transfer process happened between one excited donor (DDOA, light gray color) and one emissive acceptor (DDOT, white color).[7]

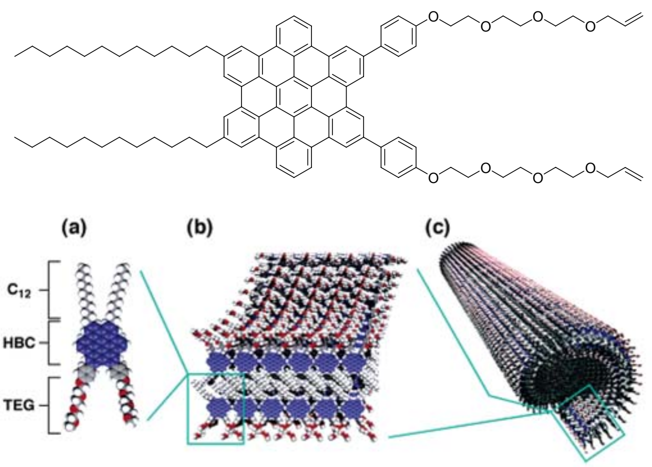

Figure 2.5. Schematic illustrations of the structures of (a) HBC amphiphile (C12; dodecyl group), (b) self-assembled bilayer tape, and (c) graphitic nanotube.[8]

Hydrogen-bonding (H-B) interactions have a strong directional component that simplifies the design of complementary subunits for recognition and binding.[9] The presence of complementary hydrogen-bonding donor acceptor sites in melamine and barbituric acid has been extensively used to drive the formation of various self-assembled supramolecular architectures. These have been widely investigated by numerous research groups,[6,10] and are amongst the best-understood self-assembled H-B structures. Figure 2.6 presents the melamine-cyanuric acid lattice, where two of the possible structural motifs, a cyclic rosette and a linear tape, are indicated. The crystal structure of this lattice was reported in 1990.[11] Early works by the groups of Lehn and Whitesides have shown that blocking one of the hydrogen-bonding faces of both the cyanuric acid and melamine components leads to the formation of either infinite tapes or cyclic rosette motifs,[12] and the crystal structures of those motifs in lattices also have been reported.[10e] While tape-like structures have been studied in the solid state[13] and in air-water interface monolayers,[14] the rosette motif has been the major topic of interest in solution-phase studies.[15]

In the field of molecular electronics, the cyanuric acid and melamine components assembled in a two-dimensional structure conceptually provides a perfect alignment-inducing motif that could be used to incorporate two or more electro- and/or photoactive moieties. The development of photoactive assemblies rests on the uncommon property of the linear, tape-like structure shown in Figure 2.7 to induce separation, at a molecular level, of like components during the self-assembly process. The formation of the hydrogen-bonded ribbons requires that all the barbiturate or melamine moieties occupy the same side of the ribbon.[16] This separation can be used to greater benefit than conventional covalent synthesis to induce ordering at the molecular level, particularly for the formation of molecular heterojunctions.

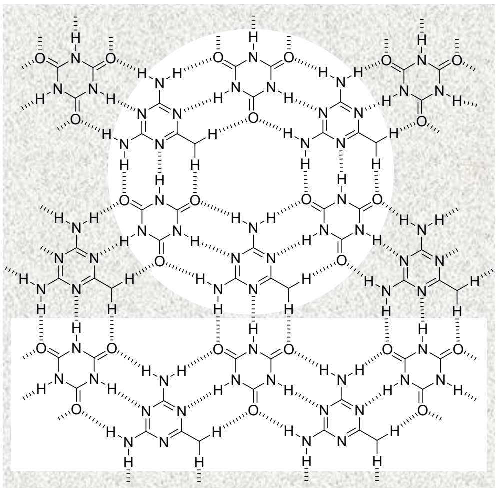

Figure 2.6. Schematic representation of melamine and cyanuric acid lattice, where two of the possible structural motifs- a cyclic rosette and a linear tape- are indicated.[10c]

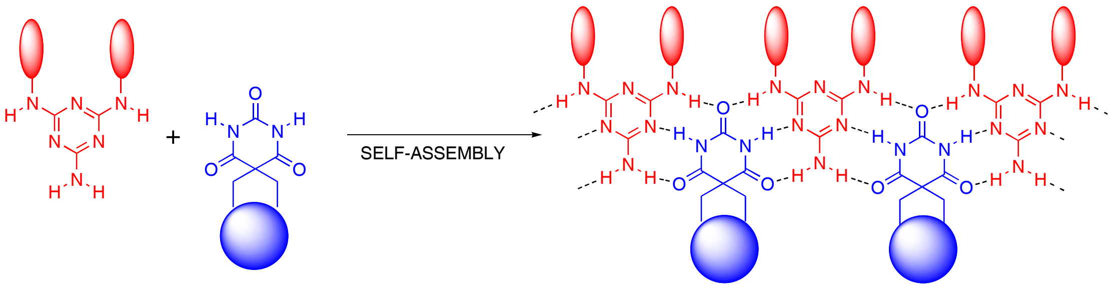

Figure 2.7. The formation of a hydrogen-bonded ribbon via the self-assembly of complementary molecular recognition motifs in melamine (red) and barbituric acid (blue) induces the formation of extended supramolecular architectures useful for the preparation of molecular level heterojunctions.

In a different approach, self-assembled monolayers (SAMs) of thiols on gold surface have attracted great interest over the past few decades mostly because of their possible application as sensors or as active substrates for molecular electronics.[17] Myles et al.[18] reported a system for probing molecular recognition events at organic interfaces using fluorescent receptors incorporated in mixed SAMs of alkanethiolates on gold (Figure 2.8). In this system, the interaction of barbituric acid derivatives with bis(2,6-diaminopyridine)amide of isophthalic acid-functionalized decanethiol on gold thin films and its complementary was investigated. This example demonstrates the capability of hydrogen-bonding architectures to form at the liquid-surface interface.

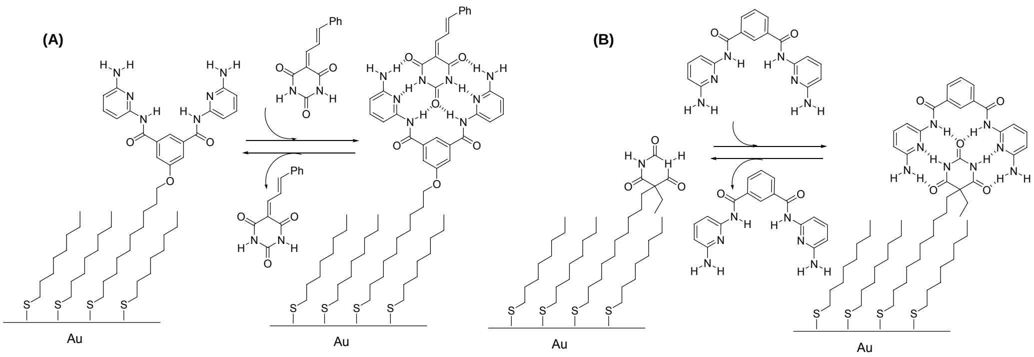

Figure 2.8. Schematic representation of functional self-assembled monolayer incorporating with hydrogen-bonding recognition motifs.[18]

Direct self-assembly of complementary H-B donor-acceptor sites in melamine and barbituric acid system onto recognition motif-modified SAMs has been demonstrated recently by Marks *et al.,*[19] who reported a vapor phase-deposition approach which used robust patterns of directed triple hydrogen bonds to assemble microstructurally acentric films in an expeditious growth process. The pyrimidine-2,4,6-trione and 4,6-diamino-1,3,5,-triazine-2-yl moieties formed longitudinally directed donor-acceptor triple hydrogen bonds between neighboring molecules to align the chromophores molecules in a head-to-tail orientation, preferentially perpendicular to the substrate (Figure 2.9). The synchrotron X-ray diffraction (XRD) measurements show long-range micro-structural order with a molecular tilt angle in good agreement with polarized transmission second harmonic generation (SHG) data, demonstrating out-of-plane ordering of the chromophores.

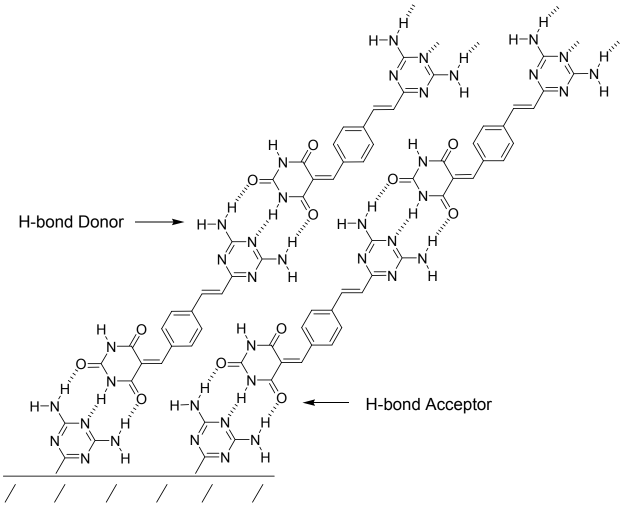

H-bond Donor

H-bond Acceptor

Figure 2.9. Schematic illustration for triple hydrogen bonds self-Assembly.[19]

2.1. Design and synthesis of photo/electro-active materials

The photoinduced charge separation in composite devices takes place at a heterojunction between the electron donor and electron acceptor materials. However, highly ordered materials are required for efficient charge transport, and the conciliation of these apparently contradictory requirements is a major challenge.[20] The effect of ordering on charge mobility was recently illustrated with sexithiophene (6T) whose charge carrier mobility increases on passing from an amorphous film (10^{-5} $cm^2V^{-1}s^{-1}$) to a partially organized film (2×10^{-3} $cm^2V^{-1}s^{-1}$) to the single crystal (10^{-1} $cm^2V^{-1}s^{-1}$).[21] Although covalent tethering surmounts the phase separation problem, a high degree of long-range ordering conducive to charge transport is more difficult to obtain. For these reasons, the induction of long-range ordering through self-assembly, using non-covalent supramolecular interactions, is particularly appealing. Hydrogen-bonded systems offer the possibility to generate preordained structures in which the binding strength can be modulated and the relative geometry between active units controlled. For a recent review on hydrogen-bonding fullerenes, see reference 22.

Additionally, in certain cases H-B has been shown to promote photoinduced electron transfer processes.[23] Several examples of hydrogen-bonding systems combining fullerenes and π-conjugated oligomers have recently appeared in the literature, for example interactions *via* hydrogen-bonding between ammonium groups and crown ethers (Figure 2.10, top),[24] and self-complementary ureidopyrimidinone units (Figure 2.10, bottom).[25]

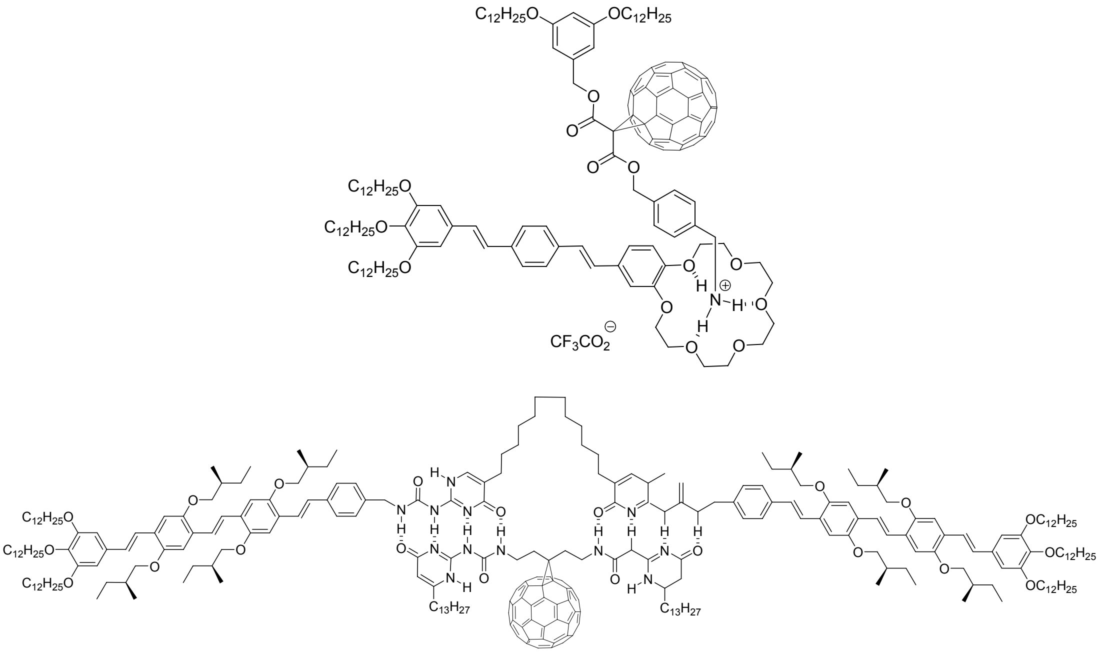

Figure 2.10. hydrogen-bonding systems combining fullerenes and π-conjugated oligomers: (top) interactions via between crown ethers and ammonium group;[24] (bottom) interactions via self-complementary ureidopyrimidinone units.[25]

The recently described fullerene-barbituric acid dyad **1** (see, Figure 2.11)[6b,26] presents a unique combination of features compatible with the construction of functional self-assembled devices: (i) the hydrogen-bonding motif, capable of forming up to 6 hydrogen bonds, is non-self-complementary and can be introduced in a single synthetic step; (ii) the symmetry of **1**, which presents two identical edges, is conducive with the formation of extended tape-like arrays, for example with conjugated oligomers bearing complementary hydrogen-bonding units; (iii) its compact nature is adapted to promote close inter-fullerene approach in a binary system where the other component is a melamine-like unit. The first two features are important to assure programmed extended photo-/electroactive molecular tapes and efficient photoinduced electron transfer, while the latter two points are prerequisites for charge movement following the primary electron transfer act. For recent development of fullerene chemistry, see reference 27a

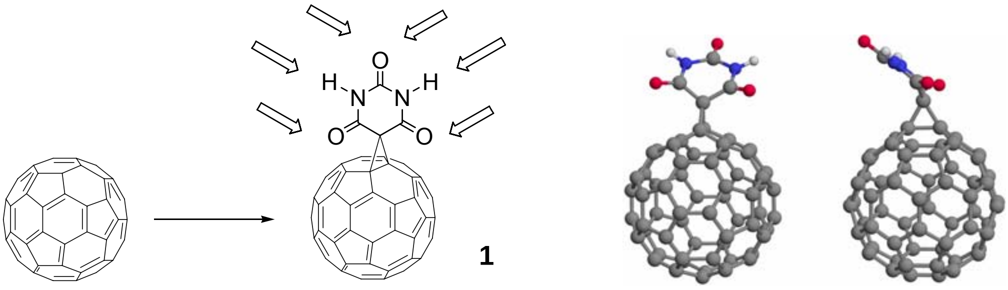

Figure 2.11. The direct fusion of barbituric acid onto [60]fullerene generates a methanofullerene derivative possessing six hydrogen-bonding sites (indicted by arrows) that are easily accessible, as shown by semi-empirical calculations (PM3, right).[6b]

Molecule **1** was recently reported to form supramolecular assemblies in solution with simple melamine units, in a manner related to unfunctionalized barbituric acid,[10c,27b] and to play the role of an electron acceptor in ultra-fast photoinduced electron transfer processes with oligo(thienylene vinylene)s electron donors in discrete 1:1 supramolecular complexes.[28] Clearly the presence of barbituric acid does not adversely affect the electronic properties of the fullerene cage, and the fullerene-grafted barbiturate is capable of forming hydrogen-bonded structures, even if a degree of distortion appears to be present on the barbiturate unit due to the close approach of the carbonyl groups to the fullerene.[29] Molecule **1** was therefore deemed a good candidate for the pursuit of functional supramolecular devices.

To be of interest for incorporation into optoelectronic devices, the electron donor (oligomer) and acceptor (fullerene) components should be easily accessible in high yields with direct synthetic approaches. The functionalized fullerene is obtained in one step,[6b,26] while the oligomer can be functionalized with hydrogen-bonding molecular recognition units, either melamine or barbituric acid. This can be achieved starting from the same dialdehyde intermediate also in one step, as described later.[30] These strategies in themselves constitute a widely applicable methodology to introduce complementary molecular recognition motifs, which is currently lacking. Thus the possibility to incorporate complementary, yet non-self-complementary hydrogen bonding motifs onto conjugated oligomers (potentially different oligomers) opens the door to the construction of molecular fabrics and libraries of mixed chromophor layers, where the judicious choice of suitably-decorated chromophores assures a better matching of absorption properties with the solar spectrum.

By adapting different C-N or C=N bond formation strategy during the synthesis of the triazine component, it is possible to vary the molar ratio of electron-donor and acceptor from 1:2, to 1:1, 2:1. The anticipated self-assembled oligothiophene-fullerene architectures with selected molecules anticipated to be readily available are shown in Figure 2.12. Mixing the molecular components under suitable conditions is expected to result in the spontaneous generation of architectures in which interchromophore distance and oligothiophene : fullerene content are constant. Diverse structures are anticipated, including the supramolecular n : p : n junction formed from components **1** and **7**. By carefully designing the bi-functional molecules **8** and **9**, which can form a self-assembled monolayer, it may be possible to bring the second layer consisting of the complementary molecule **1** on top of the previous layer as a metal : p :n junction.

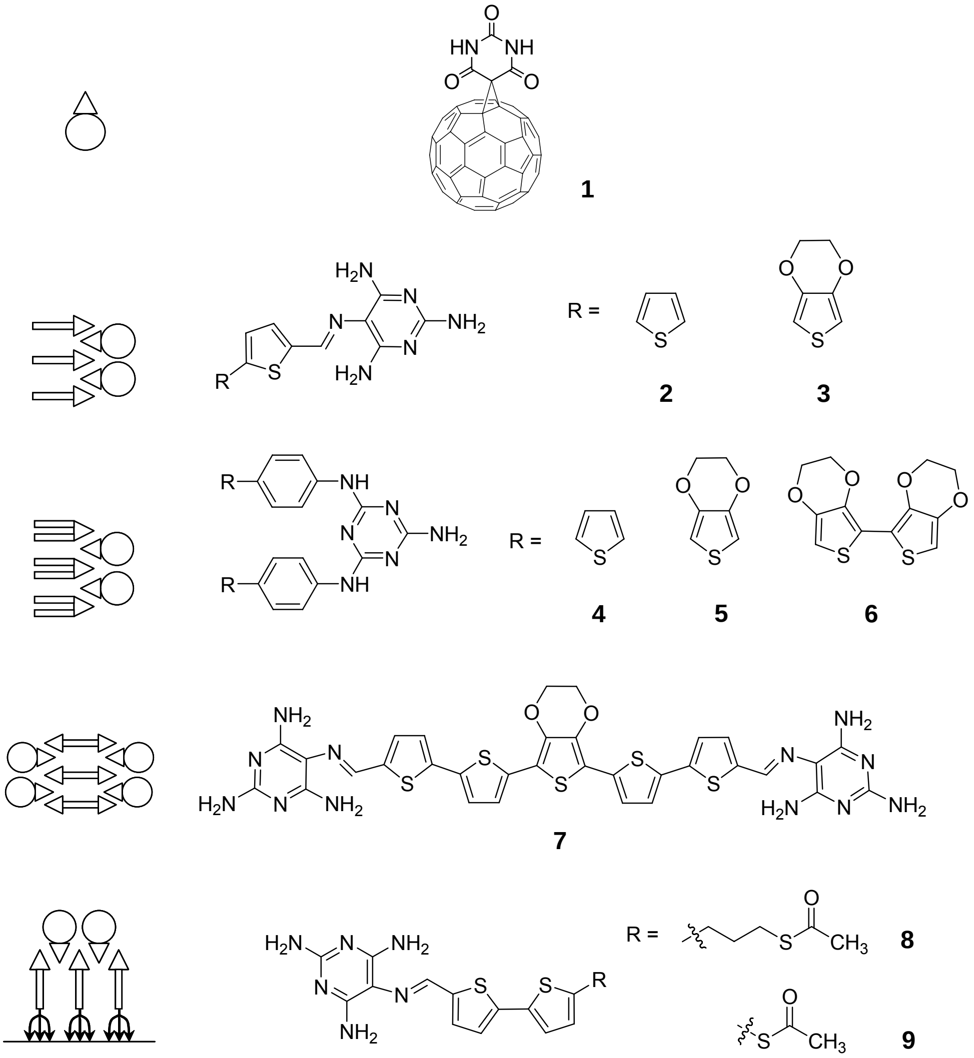

Figure 2.12. Anticipated molecular assemblies and corresponding molecular building blocks

Fullerene-barbituric acid dyad **1** has been prepared by a Bingel reaction between 5-bromobarbituric acid and C60 in a toluene : DMSO mixture,[6b,26,31] but the synthesis of the oligomers and introduction of molecular recognition motifs require more complicate retro-synthetic strategy. Typically, the construction of substituted melamine derivatives (triamino-triazines or pyrimidines) relies on the availability of suitably substituted amine starting materials, which are notoriously difficult to prepare and purify in the case of conjugated oligomers, combined with harsh reaction conditions, such as high temperatures. To overcome this synthetic hurdle, a methodology that is based on the formation of a stable Schiff base between tetraaminopyrimidine which is commercially available in bulk quantities, and the aldehyde derivative of the conjugated oligomer was investigated (Figure 2.13). The latter are easily obtained in good to excellent yields by Vilsmeier-Haack formylation of the corresponding oligomer. The enabling intuition in developing this approach is that the amino group at 5-position in tetraaminopyrimidine is more reactive than the other three. Because Schiff base formation is an equilibrium process, high yields of the more stable adduct are obtained directly.

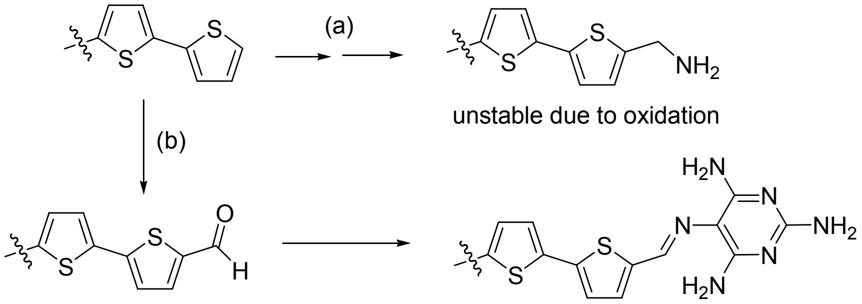

Figure 2.13. Introduction of a molecular recognition element onto an oligothiophene. (a) traditional route to functionalizing oligothiophenes; (b) rapid introduction using high-yielding steps.

2.1.1. Synthesis of oligothiophene

Current methodologies for oligothiophene preparation rely on the use of transition-metal catalyzed cross-coupling reactions involving highly reactive organomagnesium reagents (Kumada reaction),[32] or the more stable organostannane derivatives (Stille reaction).[33] The latter method is unfortunately complicated by the frequent occurrence of homo-coupled products, which limits its applicability. The novel pentathiophene **10** (Figure 2.14) was prepared in moderate yield using the aforementioned Grignard reaction. However, this approach was not amenable to scale-up, and proved unsuccessful on a multi-gram scale. This prompted us to investigate the use of milder conditions, using organoboron reagents as intermediates in the synthesis of conjugated oligomers *via* a Suzuki coupling reaction (Figure 2.15). Compared to previous methods, this approach offers considerable advantages, such as the stability of the organoboron reagent which can readily be prepared from commercially-available starting materials, high conversion yields, and mild reaction conditions that are tolerant to a wide variety of functional groups, even water.

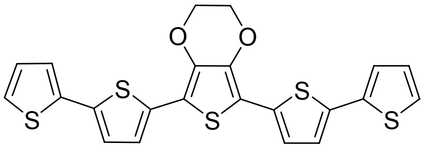

10

Figure 2.14. EDOT-mixed oligothiophene pentamer **10**.

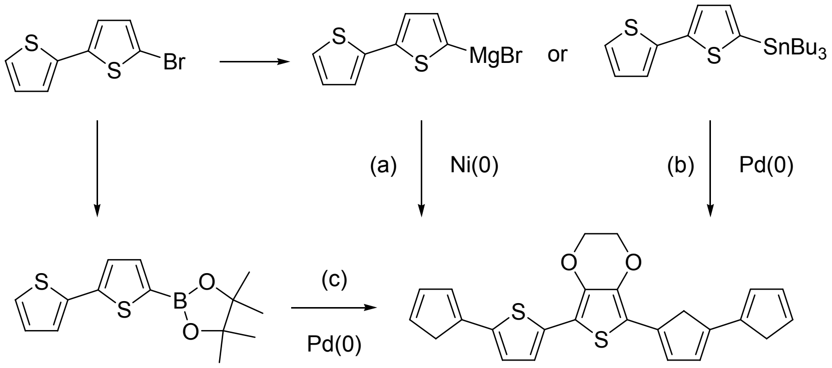

Figure 2.15. Conventional route using Kumada reactions (a) and Stille reaction (b) gives low and irreproducible yields of pentamer, whereas the use of palladium-catalyzed Suzuki coupling (c) affords the oligothiophene in excellent yields.

The wide scope of Suzuki coupling reactions allowed the preparation of numerous compounds of increasing complexity. These combine a conjugated oligomer and a hydrogen bonding molecular recognition element. These are briefly outlined in Figure 2.16.

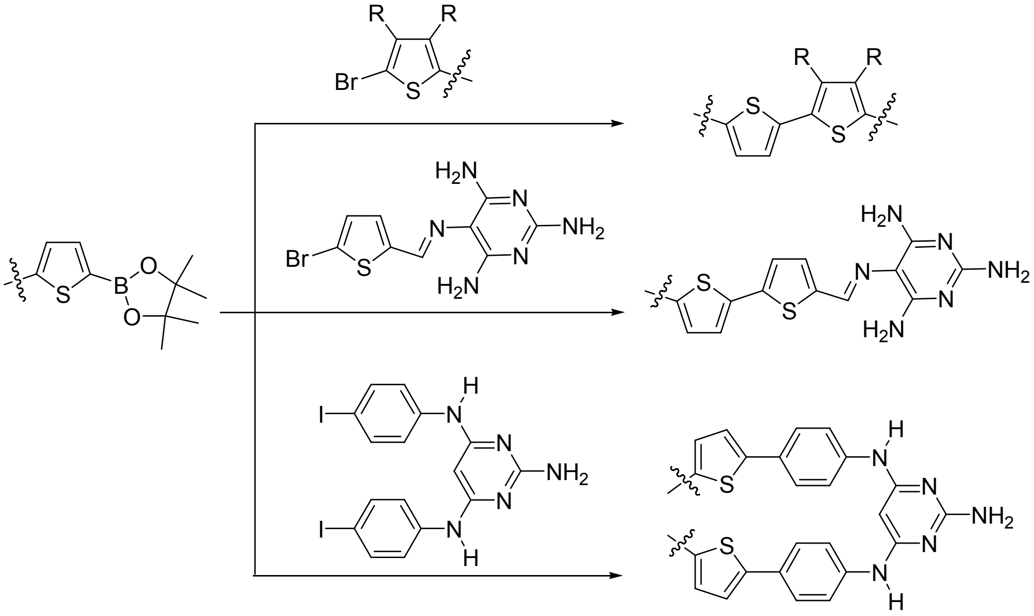

Figure 2.16. Application of Suzuki reaction to produce a variety of structures:- oligomer (top), oligomer with molecular recognition motif (middle), molecular recognition motif bearing two oligomers (bottom).

The π-conjugated oligomer used in this study is based on a pentameric oligothiophene containing a central EDOT unit (**10**). Like the well-studied sexithiophene,[34] the pentameric unit offers attractive electronic properties, notably the capacity to participate in photoinduced electron transfer reactions with C_{60}.

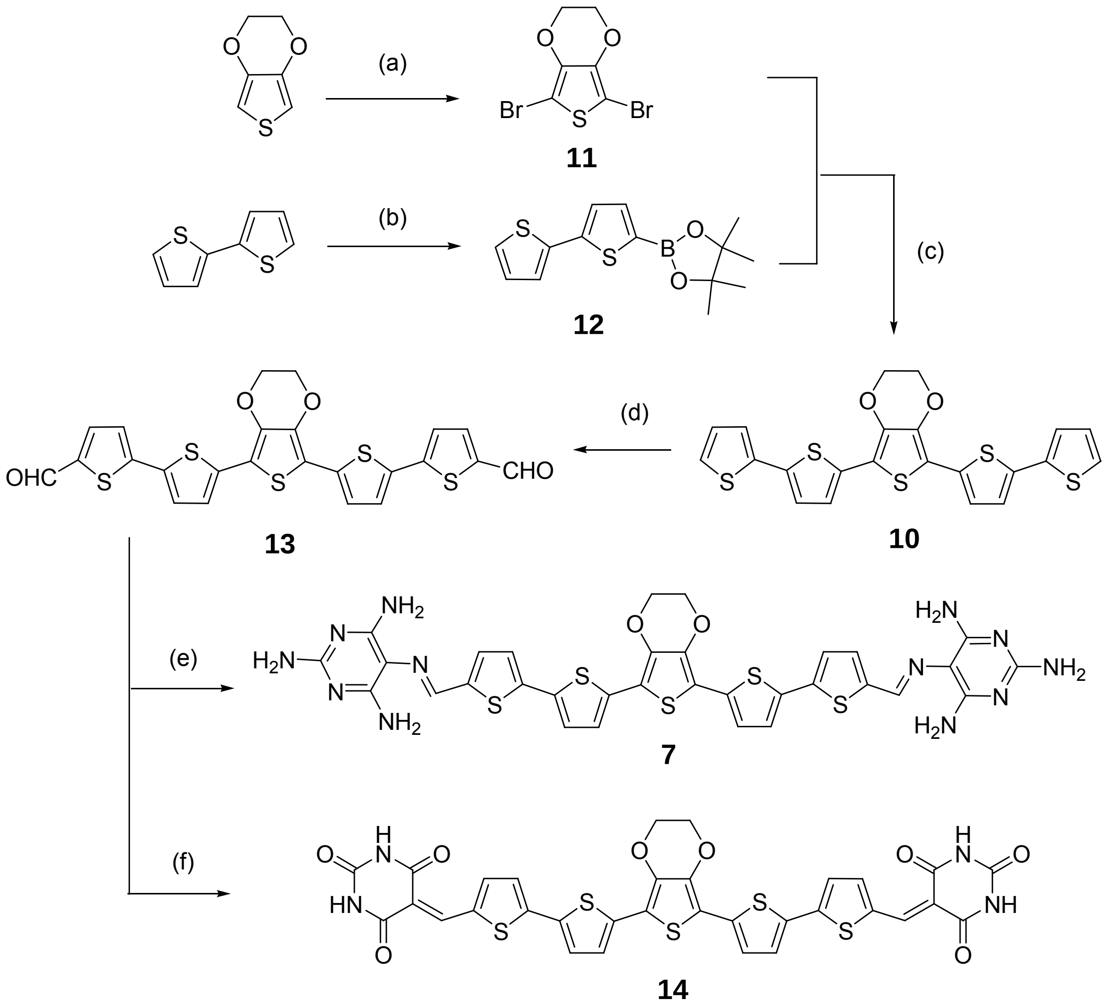

Scheme 2.1. Reagents and conditions: (a) *N*-bromosuccinimide, chloroform/AcOH, rt, 2h, 92%; (b) *n*-BuLi, THF, -80℃, then 2'-isopropoxy-4',4',5',5'-tetramethyl-1,3,2-dioxaboronate, 99% conversion; (c) $Pd(PPh_3)_4$, K_2CO_3, toluene/THF/H_2O, reflux, overnight, 90%; (d) POCl3, DMF, 1,2-dichloroethane, reflux, overnight, 82%; (e) 2,4,5,6-tetraaminopyrimidine sulfate, (*i*-Pr)$_2$NEt,DMSO/EtOH, reflux, 3 days, 61%; (f) barbituric acid, piperidine, pyridine/EtOH, 80℃, 3h, 99%.

The synthesis of oligothiophene **10** is carried out as shown in Scheme 2.1, *via* a Suzuki cross-coupling reaction between 2,5-dibromo-EDOT **11** and boronate ester **12**, followed by formylation. Compared to the use of other organometallic cross-coupling methods, such as the Kumada[32] or Stille reaction,[33] **10** is obtained in high yield (90%) and does not require purification by column chromatography. Here, the methodology developed is very useful in oligothiophene synthesis because of its high conversion yield in multi-gram scale combined with very simple purification requiring only washing with absolute ethanol. The parent chromophore **10** is subsequently functionalized by a double Vilsmeier-Haack formylation giving dialdehyde functionalized oligomer **13**, which can be considered to be a versatile starting point for the introduction of terminal molecular recognition motifs. Subsequent introduction of the melamine unit is achieved using the previously-mentioned Schiff base reaction to give **7**. As Schiff base formation is an equilibrium process, high yields of the most stable adduct can be obtained on reaction with an excess of 2,4,5,6-tetraaminopyrimidine. Likewise, quantitative preparation of the symmetric complementary barbituric acid-appended oligomer **14** is possible in one step by a Knoevenagel condensation with barbituric acid.

The diversity of Suzuki coupling reaction provides a wild range of molecular design possibilities combining conjugated oligomers and H-B molecular recognition moieties. By adapting the synthetic strategy outlined above, mixed π-conjugated oligomers of thiophene and EDOT[35] **17**, **20**, and **21** are synthesized efficiently (Scheme 2.2). However, the very poor solubility of **21** and its α,ω-bisformyl derivative in common organic solvent limit the further synthetic modification and application.[36]

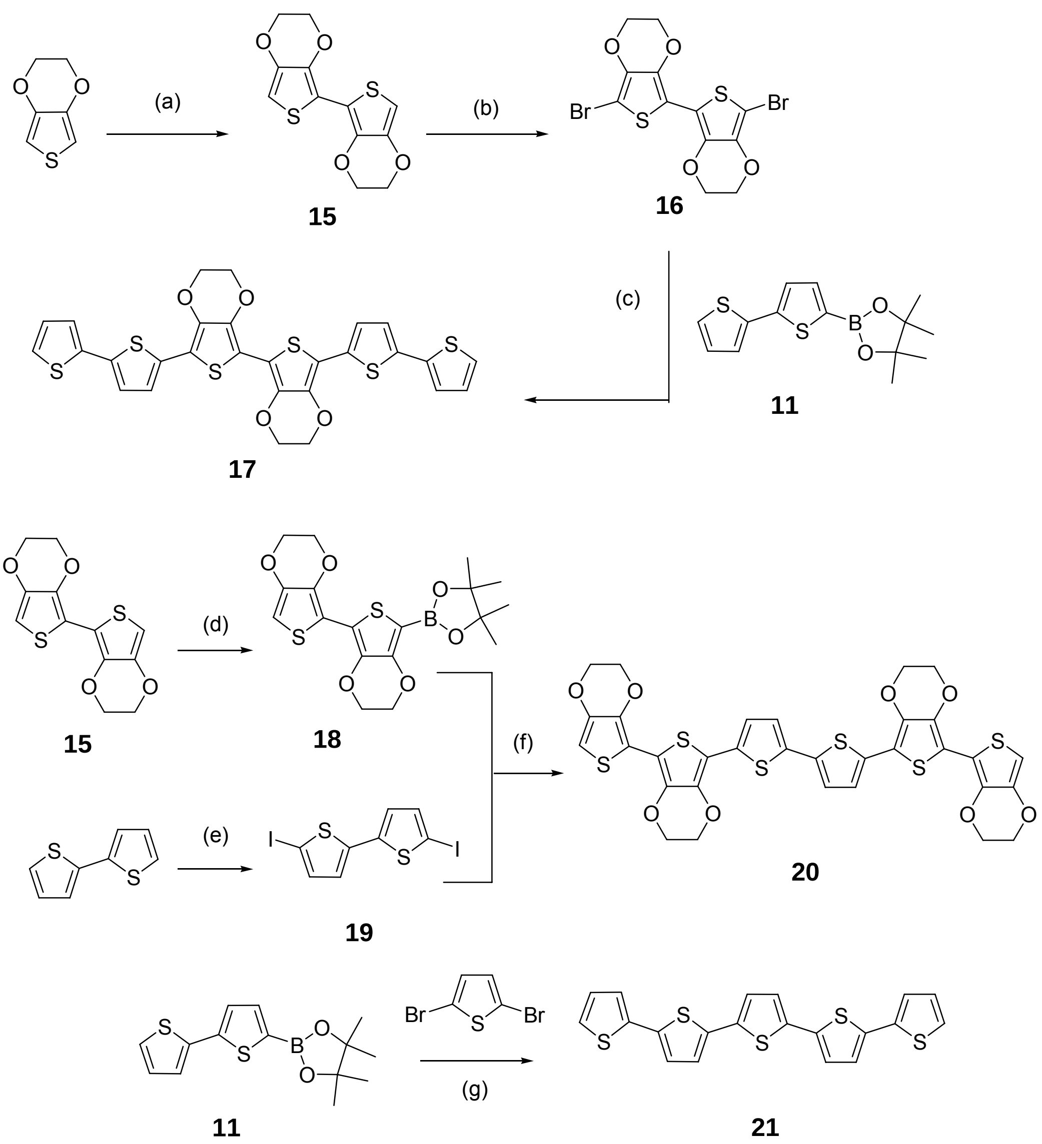

Scheme 2.2. Reagents and conditions: (a) *n*-BuLi, THF, -80℃, then $CuBr_2$, overnight, 62%; (b) N-bromosuccimide, dichloromethane, 0℃ 94%; (c) $Pd(PPh_3)_4$, K_2CO_3, toluene/THF/H_2O, reflux, overnight, 61%; (d) *n*-BuLi, THF, -80℃, 2'-isopropoxy-4',4',5',5'-tetramethyl-1,3,2-dioxaboronate; (e) Hg(II)O, iodine, benzene, rt, overnight, 77%; (f) $Pd(PPh_3)_4$, K_2CO_3, toluene/THF/H_2O, reflux, overnight, 70%; (g) $Pd(PPh_3)_4$, K_2CO_3, toluene/THF/H_2O, reflux, overnight, 88%.

2.1.2. Physical Properties

The absorption and emission spectra of **7**, **10**, and **14** are shown in Fig. 2.17. An important observation is that the increased conjugation in **7** and **14**, compared to **10,** extends the absorption envelope further into the visible portion of the spectrum (Table 2.1). This is of significance because it implies that it is not necessary to synthesize longer oligomers (six or more thiophene units) to obtain materials with an absorption spectrum that is well-matched to incident solar radiation, *ca.* 40% of which is in the visible region. The emission spectra of **7** and **14** display a large Stokes shift indicative of a polar excited state, presumably due to the electron-withdrawing nature of the end-groups. These results indicate that the molecular recognition units are conjugated with the thiophene π-system.

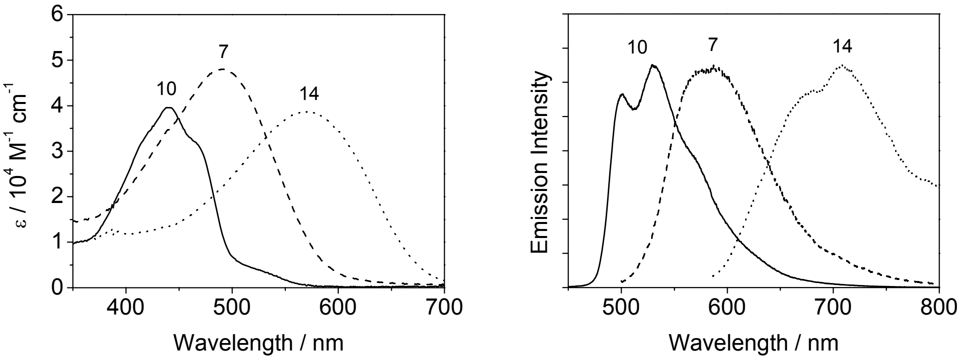

Figure 2.17. (a) Absorption (above) and normalized fluorescence (below) spectra of **10** (solid line), **7** (dash line), and **14** (dot line) in DMSO.

molecules	λ_{max} (nm)	ε_{max} ($M^{-1}cm^{-1}$)	λ_{em} (nm)
7	490	48000	587
10	438	39600	501, 529
14	573	38800	708

Table 2.1. Absorption and fluorescence spectroscopy data of molecule **7**, **10**, **14**. (solvent: DMSO)

The UV-Vis absorption and emission spectra of **17** are shown in Figure 2.18. Compared with thiophene pentamer **10** which has one central EDOT, (Table 2.2), the additional EDOT unit in the π-conjugated system extends λ_{max} and λ_{em} values by 40 nm and 30 nm respectively.[35] Also, the extinction coefficient (ε) of **17** at 479 nm is increased to 62000.

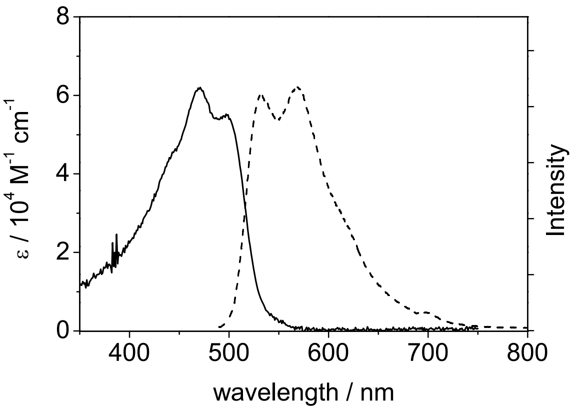

Figure 2.18. (a) Absorption (solid line) and fluorescence (dash line) spectra of **17** in DMSO.

λ_{max} (nm)	ε_{max} ($M^{-1}cm^{-1}$)
479	62000
499	55000

Table 2.2. Absorption and fluorescence spectroscopy data of molecule **17** (solvent: DMSO).

The synthesis and optical properties study of soluble sexithiophene which has no EDOT unit has been reported by Sotgiu et al.[37] Whereas the λ_{max} of sexithiophene **22** (Figure 2.19) is 390 nm in THF, the absorption of **17** at 480 nm is displaced by nearly 100 nm. This suggests that further modification of **17** with two molecular recognition end-units (melamine or barbituric acid) should lead it to absorb with a higher extinction coefficient beyond 650 nm, which would be in the centre of the solar spectrum.

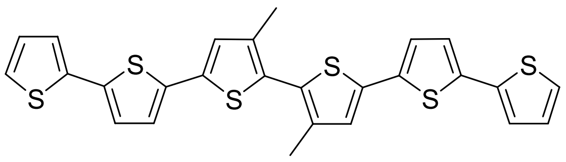

22

Figure 2.19. The structure of non-EDOT substituted sexithiophene **22** (λ_{max} = 390 nm, in THF).[37]

In the case of molecule **10**, the incorporation of a central EDOT unit increases the solubility and diminishes the oxidation potential with respect to the parent pentathiophene (E_{ox} = 0.31 V vs. – for **10**, respectively, and pentathiophene vs. ferrocene in CH_3CN, see Figure 2.20).[35, 38] The observation of two reversible one-electron oxidative peaks at 0.12 and 0.53 V (vs. Ferrocene in CH_3CN) in cyclic voltammograms of molecule **17** indicated the successive formation of the cation radical and dication.[35,38a,39]

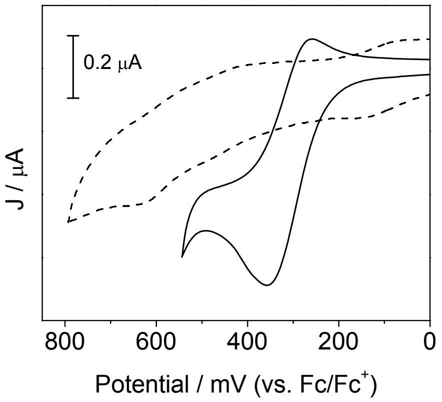

Figure. 2.20. Cyclic voltammetry diagram of **10** (solid line) and **17** (dash line) in CH_3CN containing 0.1 M Bu_4NPF_6 as electrolyte (set Fc/Fc$^+$ *vs.* Ag wire as zero, scan rate = 20 mVs^{-1}).

2.1.3. X-ray Crystal Structure of oligothiophene pentamer

Conjugation and hence electron-hole pair delocalization over adjacent heterocycles in oligo- and polythiophenes derivatives is highest when the structure adopts a planar geometry maximizing π-overlap. This is indeed the case in most oligothiophenes (with the exception of some 3,4-disubsitituted thiophene-containing derivatives), for which a large number of solid-state structures have been reported.[21] Substitution in the thiophene C-3 and C-4 position generally introduces sufficient steric repulsion to induce a deviation from planarity. Although only a few crystal structures of

EDOT-containing oligothiophenes have been reported, these do not indicate that the EDOT moiety introduces a substantial deviation from planarity. To investigate whether this is the case in **10**, its solid-state structure was determined by X-ray diffraction. Single crystals were grown from THF solution, crystallizing in a monoclinic *p21/n* unit cell.

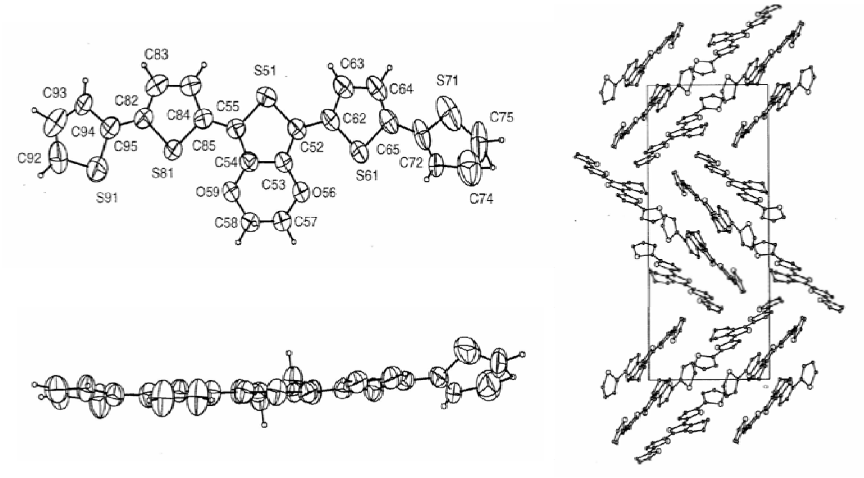

Figure 2.21. X-ray crystal structure of **10** and crystal packing.

The structure of **10**, shown in Figure 2.21, indicates that the planarity of the pentameric oligomer is retained even upon introduction of the functionalized central unit, although one of the terminal thiophenes shows a torsion angle of 24.7° in the S(61)-C(65)-C(72)-(S71) plane, presumably due to crystal packing forces. The extended crystal packing structure is a herringbone type as observed with related oligothiophene species.[21]

2.1.4. Thin films comprising photo-/electroactive oligomer and fullerene units

In the current study, the focus is directed at the combination of a melamine-appended oligothiophene **7** with the complementary barbiturate-appended fullerene **1**, and the development of the subsequent self-assembled optoelectronic devices based on the resulting assemblies. Different microscopic H-B structures may be anticipated using these molecular building blocks bearing complementary units, in line with findings on simpler binary melamine : barbiturate structures described previously, as shown schematically in Figure 2.22.[10c, 27] Although rosettes, crinkled tapes and linear tapes are possible, only the linear tape architecture can satisfy all the hydrogen-bonding sites present in the complementary components and thus their formation is expected to be thermodynamically favored.[10c,27]

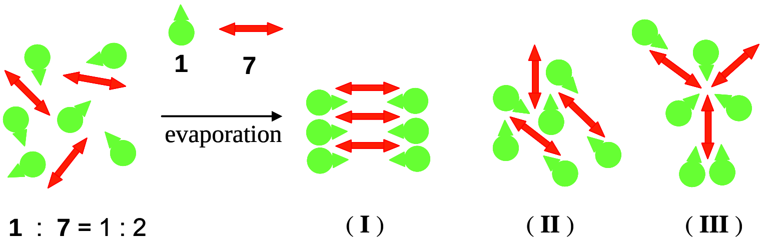

Figure 2.22. Possible microscopic hydrogen-bonding architectures formed with compounds **1** and **7**. Compared to the crinkled tape (Ⅱ) and rosette (Ⅲ), only the hydrogen-bonded tape structure (Ⅰ) satisfies all the hydrogen-bonding requirements of both components.

Blends of π-conjugated oligomers and fullerenes have the tendency to undergo phase separation, and high-speed spin-coating of these species onto the appropriate substrate from volatile solvents is often used to overcome this process. In the current study, drop-casting of thin films from solution (0.5 mM **7** in DMSO or DMSO / THF solutions) onto a solid substrate followed by slow evaporation of the solvent is anticipated to favor the formation of thermodynamically equilibrated non-covalent architectures. As a preliminary test to see if a more homogeneous film would result from this drop-casting technique, mixtures of the two species were deposited on microscope slides in order to visualize the residual fluorescence of the thiophene component. Bearing in mind that the oligomer fluorescence would be quenched in the presence of fullerene (either via energy or electron-transfer), an estimation of bulk homogeneity can be made by examining the intensity and distribution of the residual fluorescent areas. The fluorescence microcopy images of three different thin films are shown in Figure 2.23. In the first case (A), where no fullerene component is present, the intense fluorescence of oligomer **7** can be clearly seen. In the second case (B), **7** and C_{60} are co-deposited in a 1:2 stoichiometry from toluene/DMSO solution. Though a portion of the inherent oligomer fluorescence is quenched by the presence of C60, localized regions of fluorescence are visible, showing that the film exhibits considerable heterogeneity, presumably due to phase separation during the deposition process. In the third case (C), films of **7** and **1** (in a 1:2 stoichiometry) are deposited. The oligomer fluorescence is comprehensively quenched, indicating that the fullerene and oligomer components are more homogeneously dispersed than in (B). While these results by themselves do not provide direct evidence as to the formation of the H-B architectures proposed above, they do indicate that the compatibility between inherently incompatible compounds such as oligothiophenes and C60 can be significantly enhanced by the presence of complementary molecular recognition groups. In practical terms, this implies that the electron-rich oligomers are mostly located in the vicinity of a fullerene moiety, which can translate into enhanced charge separation efficiency.

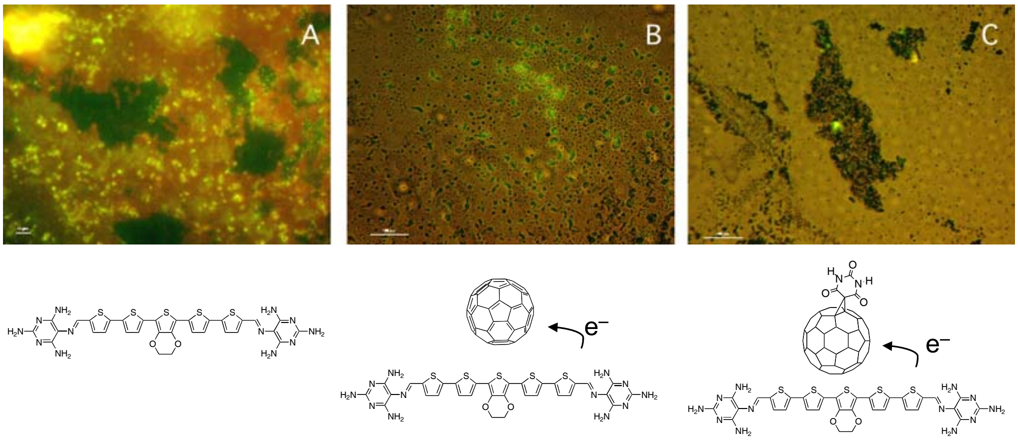

Figure 2.23. Fluorescence microscopy images of thin films of oligomer **7** (left); **7** : C_{60}; 1:2 eq. (center); and **7**: **1**; 1 : 2 eq. (right).

2.2. Oligo(*p*-phenylene vinylene)s

The recent progress in the development of organic light emitting diodes (*o*-LED),[40] nonlinear optics and photoconductive devices[41] has showed that oligo- and poly(*p*-phenylene vinylene)s represent a highly interesting and important class of materials. This type of material also serves as a very efficient chromophore in solar energy absorption process[42] for which they can be suitable candidates. The key step to synthesize oligo(*p*-phenylene vinylene)s is to apply the *Wittig-Honor* reaction to extend the length of the molecule. As shown in Scheme 2.3, hydroquinone is alkylated with 2-ethylhexyl bromide in DMF and then reacts with paraformaldehyde in 33 % HBr/AcOH solution to give the bis(bromomethyl) derivative **24,** followed by conversion into 2,5-bis(phosphonate) **25** *via* an Arbuzov reaction. Double Wittig-Honor olefination between 4-bromobenzaldehyde and the phosphonate **25** in KO*t*Bu/DMF at room temperature gives *E,E*-oligo(PPV)s **26**. The oligo(PPV)s bisbromide **26** transformed into bis-aldehyde **27** by treatment with *n*-BuLi and DMF in dry diethyl ether.[43] This α,ω-dialdehyde oligo(*p*-phenylene vinylene)s **27** can once more be considered to be a versatile starting point for the introduction of terminal molecular recognition motifs as described before in Section 2.1. The desired double Schiff base product **28** is obtained in 70% yield by simply refluxing with an excess of 2,4,5,6-tetraaminopyrimidine and K_2CO_3 in 2-propanol. By introducing two branched alkoxy side chain on the central styrylbenzene ring, this bispyrimidine-appended substituted oligomer **28** is soluble in common organic solvent such as THF, CH_3CN, and partially soluble in CH_2Cl_2.

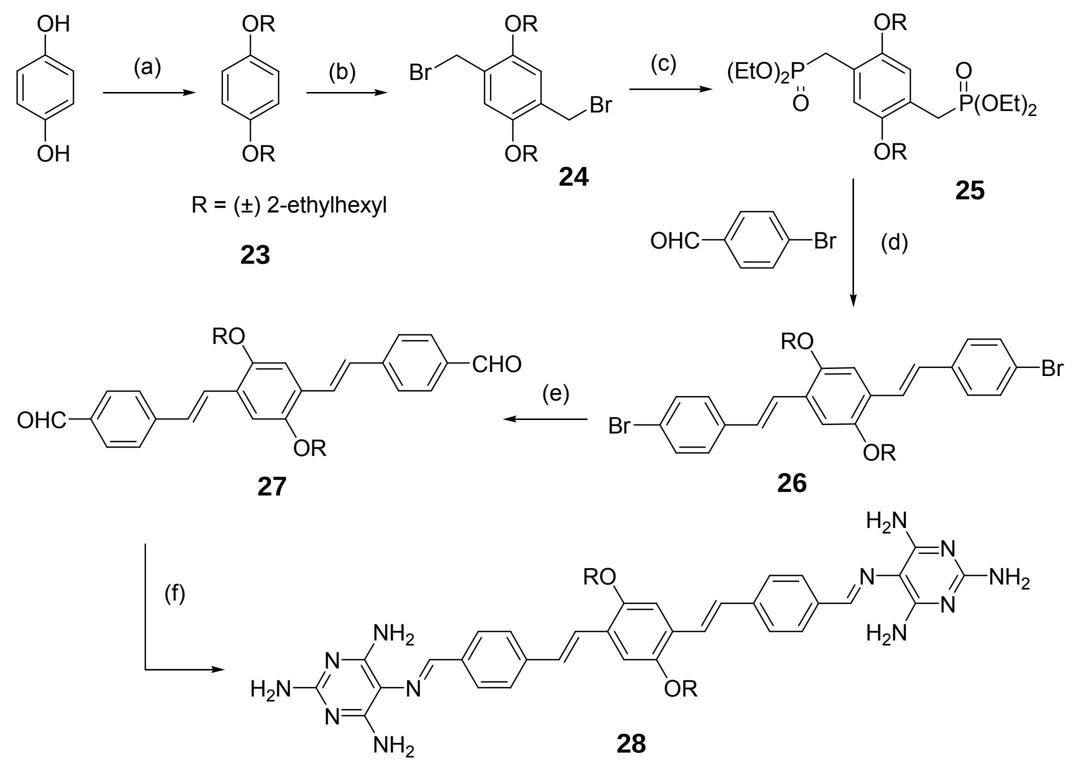

Scheme 2.3. Reagents and conditions: (a) (±) 2-ethylhexyl bromide, K_2CO_3, DMF, 80℃, 2 days, 62%; (b) paraformaldehyde, HBr (33% in AcOH), AcOH, 70℃, 3 hr, 83%; (c) triethyl phosphite, 150℃, 2 hr, 99%; (d) 4-bromobenzaldehyde, KO*t*Bu, DMF, rt, overnight, 77%; (e) n-BuLi, Et_2O, 0℃, then DMF, 2 hr, 93%; (f) 2,4,5,6-tetraaminopyrimidine sulfate, K_2CO_3, 2-propanol, reflux, 2 days, 70%.

The absorption and emission spectra of **28** is shown in Figure 2.24. It is known that poly(*p*-phenylene vinylene)s and oligo(*p*-phenylene vinylene)s are highly fluorescent and have very high molar extinction coefficient.[44] Compared with literature reports an non-substituted oligo(*p*-phenylene vinylene)s trimers (λ_{max} = 400 nm)[44] and α,ω-bispyrimidine oligothiophene **7**, the extinction coefficient of **28** increases to 62000 (Table 2.3). The emission spectra of compound **28** shows a 60 nm Stokes shift which is attributed to the presence of the two electron-withdrawing melamine units.

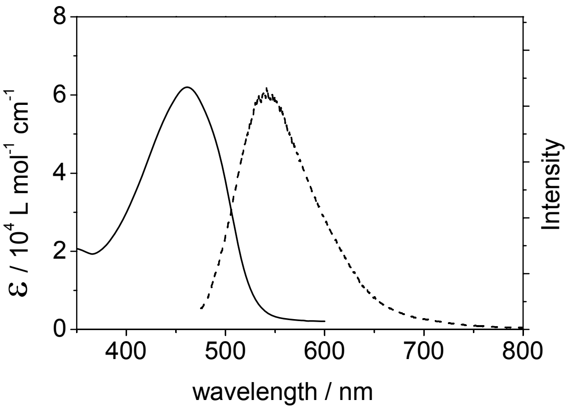

Figure 2.24. (a) Absorption (solid line) and fluorescence (dash line) spectra of **28** in DMSO.

λ_{max} (nm)	ε_{max} ($M^{-1}cm^{-1}$)	λ_{em} (nm)
461	62000	542

Table 2.3. Absorption and fluorescence spectroscopy data of molecule **28**. (solvent: DMSO)

To achieve the formation of self-assembled H-B supramolecular architectures, it is frequently necessary to dissolve the components in non-polar organic solvent such as CH_2Cl_2, $CHCl_3$ or *ortho*-dichlorobenzene. Therefore, the introduction of additional solublizing alkoxy side chains onto the oligo(PPV)s can be necessary. The synthesis of all-alkoxy chain-substituted oligo(PPV)s is shown in Scheme 2.4.

The one-step bromination of compound **29** introduces two bromo atoms both on the methylene and on the phenyl position.[44] Similarly to the reaction sequence outlined in Scheme 2.3, the Wittig-Honor reaction precursor **31** obtained was used directly in the olefin formation. The core styrylbenzene unit is converted *via* the oxidation of intermediate **32** to the 2,5-bisalkoxy terephthalaldehyde **33** (using PCC).[45] The bis-bromide **34** is then converted into bis-aldehyde **35** by treatment with *n*-BuLi and DMF in dry diethyl ether. The $CHCl_3$ soluble barbituric acid-appended oligomer **36** was synthesized by a Knoevenagel condensation in $CHCl_3$/EtOH mixed solvent.

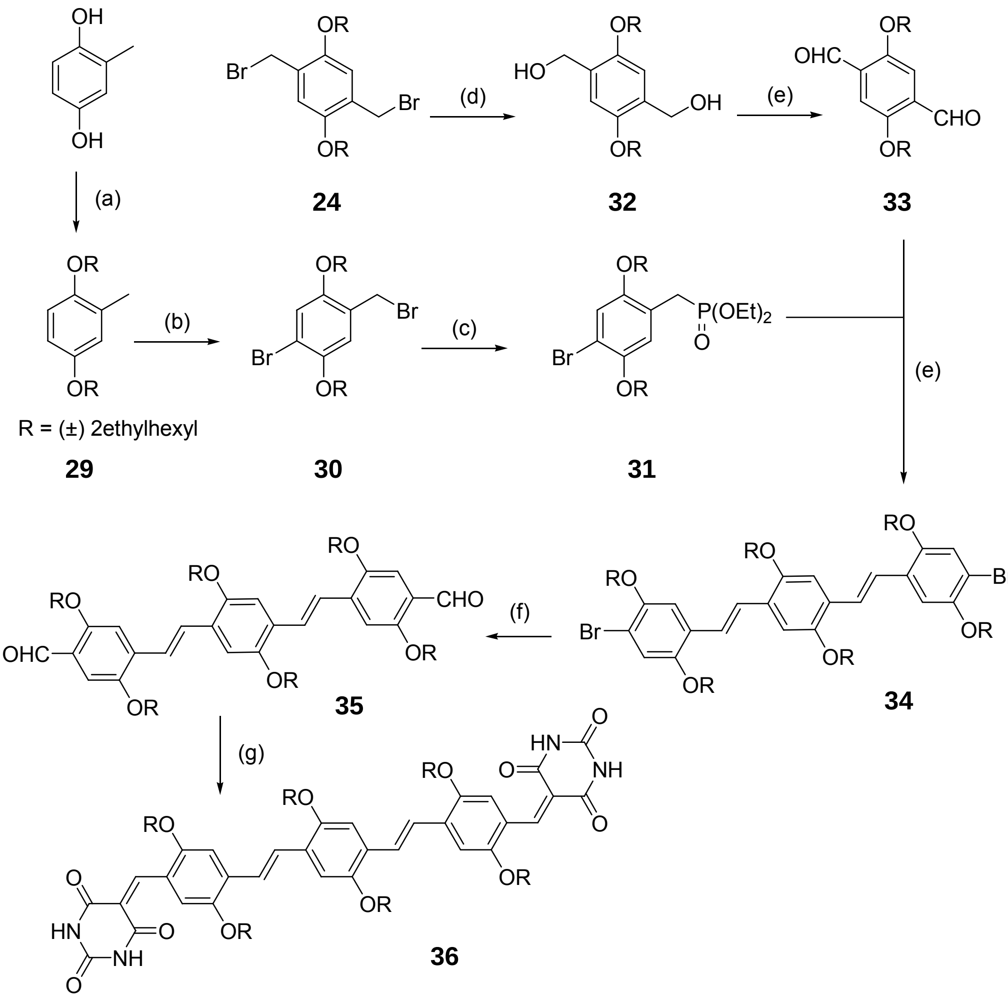

Scheme 2.4. Reagents and conditions: (a) (±) 2-ethylhexyl bromide, K_2CO_3, DMF, 80℃, 2 days, 46%; (b) Br_2, CCl_4, reflux and hν, 3 hr, 61%; (c) triethyl phosphite, 150℃, 2 hr, 99%; (d) $CaCO_3$, 1,4-dioxane/H_2O, reflux, 2 days, 96%; (e) PCC, CH_2Cl_2, rt, 2 hr, 85%; (e) KO*t*Bu, DMF, 0℃, then rt, 2 days, 62%; (f) n-BuLi, Et_2O, 0℃, then DMF, 2 hr, 19%; (g) barbituric acid, $CHCl_3$/EtOH, reflux, overnight, 25%.

2.3. Thioacetate terminated molecules

2.3.1. Synthesis

The alkylthioacetate appended barbituric acid or cyanurate derivatives were prepared by adapting the methodologies developped for the synthesis of α,ω-substituted oligothiophene.[46] As shown in Scheme 2.5, 4-hydroxybenzaldehyde was alkylated with the appropriate α,ω-dibromoalkane[47] followed by condensation with potassium thioacetate,[48] giving an intermediate which could be subsequently reacted with either barbituric acid or tetraaminopyrimidine using Knoevenagel and Schiff-base reactions. For the barbituric acid substituted molecules, the reaction proceeded in EtOH with a small amount of water which helps to dissolve barbituric acid in EtOH. Barbituric acid plays dual rule as the acidic auto-catalyst in the reaction, and due to the low solubility of the final product in H_2O/EtOH mixed-solvent, quantitative conversion in high purity is easily obtained by simply washing the precipitate with H_2O and EtOH. In order to compare the hydrogen-bond induced effect on SAMs, *N*-methyl barbituric acid-substituted **41**, *and* **42** and non-polar alkyl end-group thioacetate **47** were also synthesized. The *sec*-butyl tail group was chosen to mimic the cross section of barbituric acid substitute on molecule **39,** with the same number of methylene group between the phenyl moiety and the thioacetate head group (Figure 2.25). Again, using the same synthetic strategy described above, hydroquinone was first alkylated with an excess of 1-bromo-2-methylpropane, and then reacted with 1,5-dibromopentane, before converting it to the thioacetate end-product. The synthesis of similar barbiturate species were previously reported by Ringsdorf *et al.*, albeit in lower yields.[49]

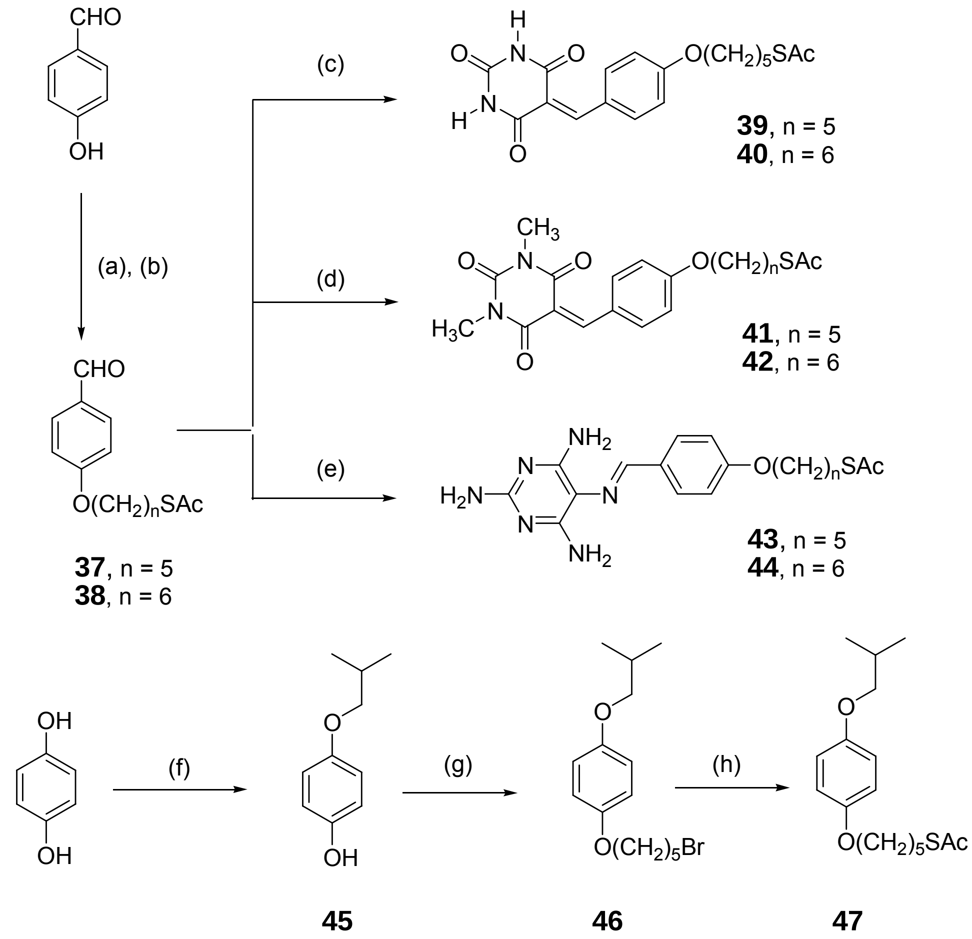

Scheme 2.5. Reagents and conditions: (a) Br$(CH_2)_n$Br, K_2CO_3, acetone, reflux, overnight (n = 5, 58%; n = 6, 68%); (b) potassium thioacetate, acetone, rt, overnight, (n = 5, 99%; n = 6, 91%); (c) barbituric acid, H_2O, EtOH, reflux, 2hr, (n = 5, 92%; n = 6, 85%); (d) N,N-dimethyl barbituric, benzene, TsOH (cat.), reflux, 3 hr, (n = 5, 76%; n = 6, 71%); (e) 2,4,5,6-tetraaminopyrimidine sulfate, Et_3N, 2-propanol, reflux, 2 days, (n = 5, 90%; n = 6, 27%); (f) 1-bromo-2-methylpropane, K_2CO_3, DMF, 100℃, overnight; (g) 1,5-dibromopentane, K_2CO_3, DMF, 100℃, overnight; (h) potassium thioacetate, acetone, rt, overnight, 65%.

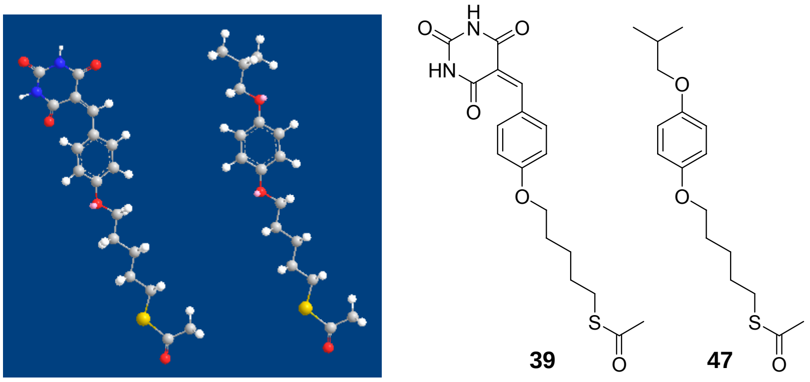

Figure 2.25.. MM2 calculation (left) and schematic illustration (right) of molecule **39**, **47**.

2.3.2. Self-assembled monolayer formation on gold substrates

Hydrogen-bonding SAMs were obtained by dipping the gold substrates into a THF/EtOH solution of the appropriate thioacetate **39**– **44** or **47** overnight. The surface coverage was subsequently evaluated by electrochemical and surface ellipsometry measurements. The determination of the surface coverage can be obtained by electrochemistry, while the thickness of the monolayer can be determined by ellipsometry, and the surface coverage estimated by rastering the surface with the incident laser beam.

The surface coverage of the self-assembled monolayer can be readily evaluated by electrochemistry when the chemisorbed molecules serve as a barrier to block a redox process involving a species in solution.[50] In the case of the reduction of Fe^{3+} to Fe^{2+} (as its potassium hexacyanate salt), the redox process can be employed to check for defects in the SAM. For the surface coated with **39**, a highly uniform close-packed monolayer layer is likely formed because, as shown in Figure 2.24, essentially no Fe^{III} reduction can be measured upon modification of the gold surface with the barbiturate-appended alkane-thioacetate (compared with the electrochemical response for bare gold). The situation is somewhat different when the experiment is repeated with the corresponding melamine-appended alkane-thioacetate (Figure 2.26, left). A much poorer blocking effect is observed with **43** suggesting a less ordered SAM. This result was rationalized by taking into account the experimentally determined “odd-even” effect reported for simple alkanethiol SAM where the number of repeat units (odd/or even) dictate whether the surface coverage is better or worse.[17a-c,51] The experiment is thus repeated with molecule **44**, which is identical to **43** except for the incorporation of an additional methylene repeat unit in the alkyl chain. This “odd-even” rule appears to be effective even with these more elaborate H-B SAMs, as this simple structural modification resulted in a much better blocking of the surface.

This result is consistent with the formation of a better monolayer, shown in Figure 2.26 (right). A similar behavior was observed upon investigation of C-6 alkyl chain molecule **40** and the *N*-methylated derivatives of **41** and **42**, for which compact SAMs took several days to form, see Figure 2.27. Compared to **39**, the non-polar molecule **47** forms a highly uniform close packed monolayer (Figure 2.28).

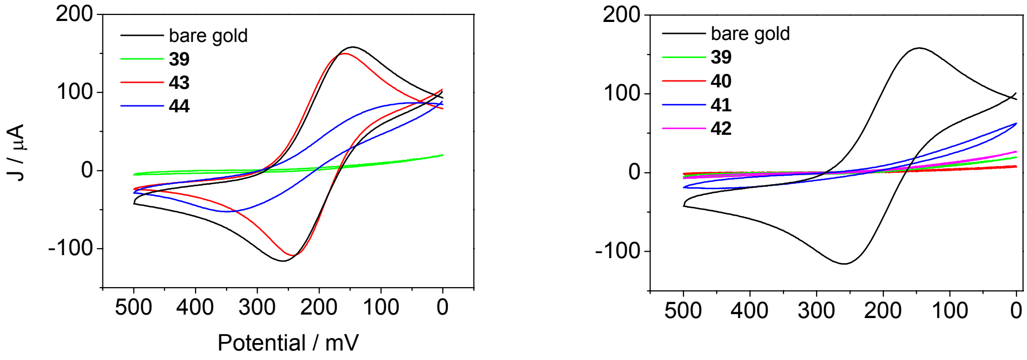

Figure 2.26. Cyclic voltammograms of the reduction of aqueous $K_3[Fe(CN)_6]$ using gold electrodes whose surfaces were modified with **39** – **44**. Bare gold (black line) was used as control experiment.

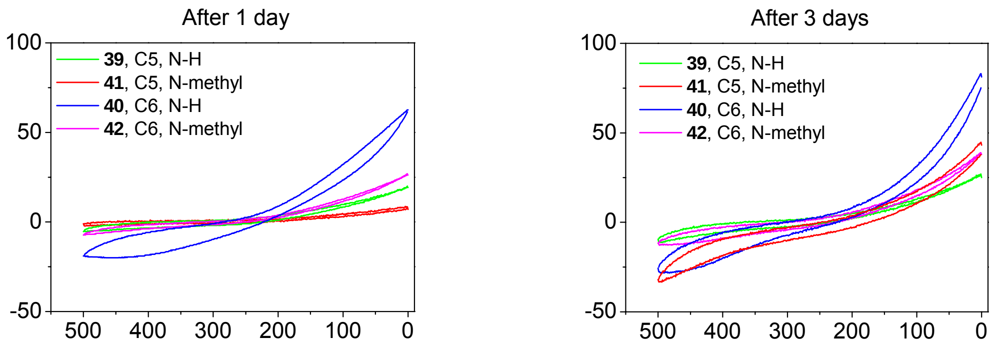

Figure 2.27. Cyclic voltammograms of the reduction of aqueous $K_3[Fe(CN)_6]$ using gold electrodes whose surfaces were modified with **39** – **43** with different immersion time. For 1 day (left), for 3 days (right).

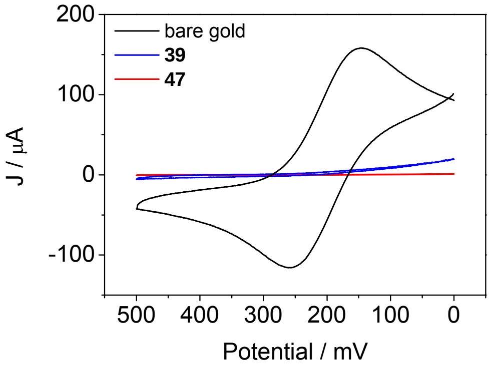

Figure 2.28. Cyclic voltammograms of the reduction of aqueous $K_3[Fe(CN)_6]$ using gold electrodes whose surfaces were modified with **39** or **47**.

Ellipsometry measurements[50] of the gold substrates modified with **39** and **44** are shown in Figure 2.29, which correspond to the closest packed SAMs as estimated by electrochemistry. Rastering the surface gives information on the coverage, and a homogeneous layer in terms of height is obtained as shown in Figure 2.29(A). The height profile of the self-assembled monolayer shown in Figure 2.29(B) can be used to estimate the geometry adopted by the molecules, as represented in Figure 2.29(C) for both **39** and **44**. The measured height corresponds well to the dimensions obtained using molecular modeling and considering an angle of 30° between the S-C bond and the surface normal.[17,51] In the case of **39** the measured height is 1.50 nm while the calculated value is 1.42 nm. For **44** the measured height is 1.83 nm with a calculated value of 1.90 nm.

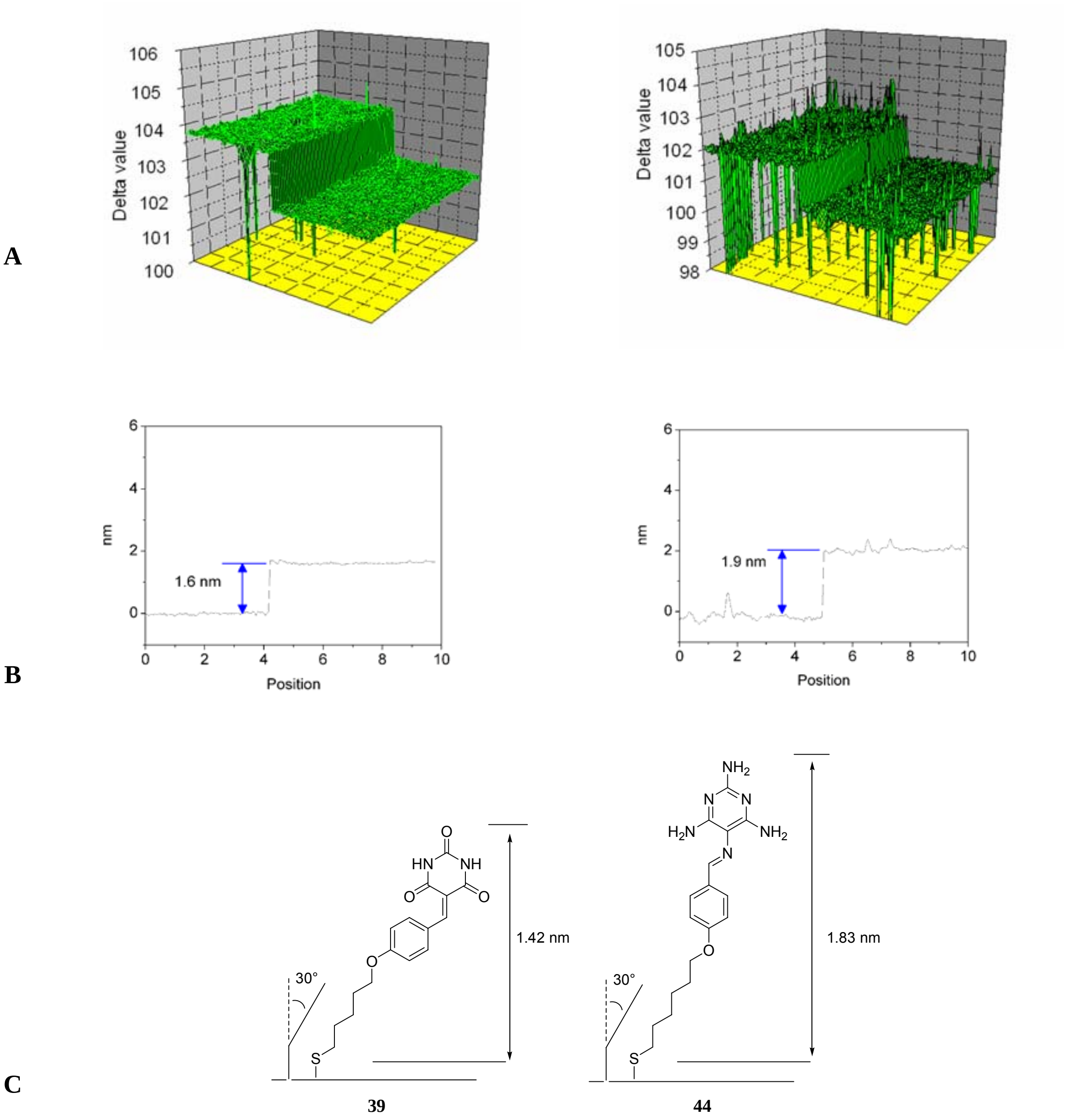

Figure 2.29. Characterization of SAMs obtained for **39** (left) and **44** (right) modified gold surfaces using ellipsometry: A) Topology of surface; B) height profile and C) calculated height assuming close-packing of the molecules.

2.3.3. Layer-by-layer self-assembly on gold substrates

Based on the previous studies, the thioacetate molecule **39** appended with a barbituric acid head group forms a highly uniform close packed monolayer. These could form the basis for the hierarchical construction of multi-layer devices, and directly dipping the SAM **39** modified gold substrate into a solution of melamine-appended oligo(p-phenyl vinylene)s **28** did lead to the assembly of a second layer, as shown in Figure 2.30. Rasterization of the modified surface gives information on the coverage, and the measured height (3.5 nm) is close to the calculated value (4.0 nm), where the orientation of the molecule in the model is a an upper limit estimate.[17a-c] It is reasoned that the driving force of the hydrogen-bonded assembly is much weaker than Au-S bonds, hence the second layer may form less uniformly by comparing to the fist layer. Any defect (loose packing) region in the bottom layer will be transmitted in the upper layer and diminish its packing quality. Perhaps for this reason, deposition of a third assembled layer through the complementary hydrogen-bonds proceeded unsuccessful.

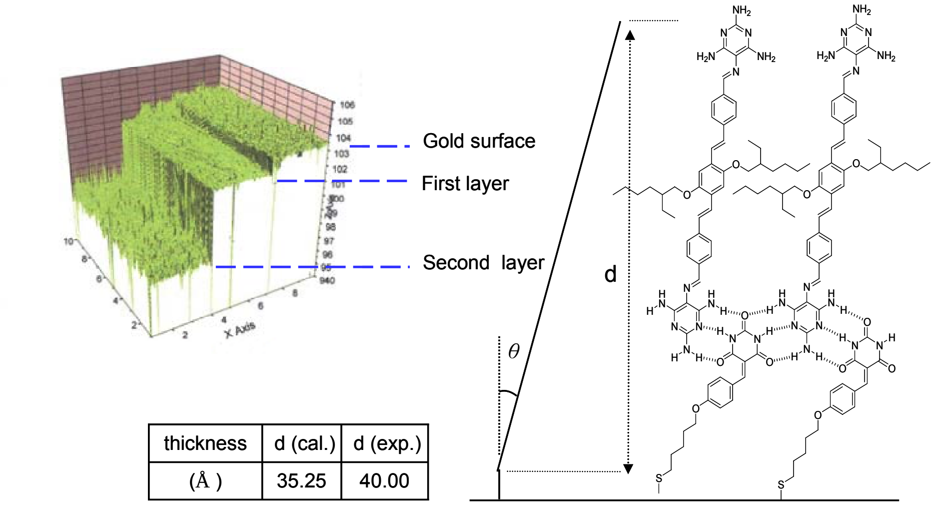

thickness	d (cal.)	d (exp.)
(Å)	35.25	40.00

Figure 2.30. Characterization of double self-assembled layers within barbituric acid derivative **39** (first layer) and melamine derivative **28** (second layer) modified gold surface using ellipsometry: (Left) Topology of surface; (Right) calculated height assuming close-packing of the molecules.

2.4. References

1. M. W. Hosseini, *Acc. Chem. Res.* **2005**, *38*, 313-323.
2. (a) J.-M. Lehn, *Supramolecular Chemistry*, VCH, Weinheim, **1995**. (b) J.-M. Lehn: *Supramolecular Chemistry - Scope and Perspectives Molecules, Supermolecules, and Molecular Devices* (Nobel lecture), *Angew. Chem. Int. Ed. Engl.* **1988**, *27*, 89-112.; (c) J.-M. Lehn, *Angew. Chem. Int. Ed. Eng.* **1990**, *29*, 1304-1319.; (d) P. J. Stang, B. Olenyuk, *Acc. Chem. Res.* **1997,** *30*, 502-518.
3. M. Barboiu, G. Vaughan, R. Graff, J.-M. Lehn, *J. Am. Chem. Soc.* **2003**, *125*, 10257-10265.
4. I.-W. Hwang, T. Kamada, T. K. Ahn, D. M. Ko, T. Nakamura, A. Tsuda, A. Osuka, D. Kim, *J. Am. Chem. Soc.* **2004**, *126*, 16187-16198.
5. M. Yoshizawa, Y. Takeyama, T. Kusukawa, M. Fujita, *Angew. Chem. Int. Ed.* **2002**, *41*, 1347-1349.
6. (a) D. M. Bassani, V. Darcos, S. Mahony, J.-P. Desvergne, *J. Am. Chem. Soc.* **2000**, *122*, 8795-8796.; (b) N. D. McClenaghan, C. Absalon, D. M. Bassani, *J. Am. Chem. Soc.* **2003**, *125*, 13004-13005.
7. A. Del Guerzo, A. G. L. Olive, J. Reichwagen, H. Hopf, J.-P. Desvergne, *J. Am. Chem. Soc.* **2005**, *127*, 17984-17985.
8. W. Jin, T. Fukushima, A. Kosaka, M. Niki, N. Ishii, T. Aida, *J. Am. Chem. Soc.* **2005**, *127*, 8284-8285.
9. (a) G. M. Whitesides, J. P. Mathias, C. T. Seto, *Science*, **1991**, *254*, 1312.; (b) Jr. J. Rebek, *Angew. Chem. Int. Ed. Engl.* **1990**, *29*, 245-255.; (c) S.-K. Chang, A. D. Hamilton, *J. Am. Chem. Soc.* **1988**, *110*, 1318-1319.
10. (a) S. Yagai, M. Higashi, T. Karatsu, A. Kitamura, *Chem. Mater.* **2005,** *17,* 4392-4398.; (b) M. Arduini, M. Crego-Calama, P. Timmerman, D. N. Reinhoudt, *J. Org. Chem.* **2003**, *68*, 1097-1106.; (c) G. M. Whitesides, E. E.Simanek, J. P. Mathias, C.T. Seto, D. N. Chin, M. Mannen, D. M. Gordon, *Acc. Chem. Res.* **1995**, *28*, 37-44.; (d) J. P. Mathias, C. T. Seto, E. E. Simanek, G. M. Whitesides, *J. Am. Chem. Soc.* **1994**, *116*, 1275-1236.; (e) J. A. Zerkowski, G. M. Whitesides, *J. Am. Chem. Soc.* **1994**, *116*, 4298-4304.
11. Y. Wang, B, Wei, Q, J. Wang, *Crystallor. Spectrosc. Res.* **1990**, *20*, 79.
12. (a) J.-M. Lehn, M. Mascal, A. DeCian, J. Fischer, *J. Chem. Soc., Chem. Commun.* **1990**, 479-480.; (b) C. T. Seto, G. M. Whitesides, *J. Am. Chem. Soc.* **1993**, *115*, 905-916.
13. J. C. MacDonald, G. M. Whitesides, *Chem. Rev.* **1994**, *94*, 2383-2420.
14. K. Ariga, T. Kunitake, *Acc. Chem. Res.* **1998**, *31*, 371-378.
15. F. Rakotondradany, A. Palmer, V Toader, B. Chen, M. A. Whitehead, H. F.

Sleiman *Chem. Commun.* **2005**, 5441-5443.; (b) F. Cardullo, M. Crego Calama, B. H. M. Snellink-Ruël, J.-L. Weidmann, A. Bielejewska, P. Timmerman, D. N. Reinhoudt, R. Fokkens, N. M. M. Nibbering, *Chem. Commun.*, **2000**, 367-368.

16. (a) M. S. Johal, Y. W. Cao, X. D. Chai, L. B. Smilowitz, J. M. Robinson, T. J. Li, D. McBranch, D.-Q. Li, *Chem. Mater.* **1999,** *11,* 1962-1965.; (b) D.-W. Kim, S.-G. Lim, C.-H. Jun, *Organic Lett.* **2006**, *8*, 2937-2940.
17. (a) J. C. Love, L. A. Estroff, J. K. Kriebel, R. G. Nuzzo, G. M. Whitesides, *Chem. Rev.* **2005,** *105*, 1103-1169.; (b) F. Schreiber, *Progress in surface Science*, **2000**, *65*, 151-256. (c) A. Ulman, *Chem. Rev.* **1996**, *96*, 1533-1554. (d) A. Ulman, *An Introduction to Ultrathin Organic Films: From Langmuir-Blodgeet to Self-Assembly*, Academic Press, Boston, **1991**; (e) C. D. Bain, E. B. Troughton, Y. Tao, J. Evall, G. M. Whitesides and R. G. Nuzzo, *J. Am. Chem. Soc.*, **1989**, *111*, 321-335.
18. (a) K. Motesharei, D. C. Myles, *J. Am.Chem. Soc.* **1994**, *116*, 7413-7414.; (b) K. Motesharei, D. C. Myles, *J. Am. Chem. Soc.* **1998**, *120*, 7328-7336.
19. P. Zhu, H. Kang, A. Facchetti, G. Evmenenko, P. Dutta, T. J. Marks, *J. Am. Chem. Soc***.** **2003**, *125*, 11496-11497.
20. (a) J.-L. Brédas, D. Beljonne, V. Coropceanu, J. Cornil, *Chem. Rev.* **2004**, *104*, 4971-5003.; (b) M. A. Fox, *Acc. Chem. Res.* **1999**, *32*, 201-207.
21. (a) B. Servet, G. Horowitz, S. Ries, O. Lagorse, P. Alnot, A. Yassar, F. Deloffre, P. Srivastava, R. Hajlaoui, P. Lang, F. Garnier, *Chem. Mater.* **1994**, *6*, 1809-1815.; (b) G. Horowitz, F. Garnier, A. Yassar, R. Hajlaoui, F. Kouki, *Adv. Mater.* **1996**, *8*, 52-54.; (c) F. Garnier, *Philos. Trans. R. Soc. London, Ser. A: Math. Phys. Eng. Sci.* **1997**, *355*, 815-827.
22. L. Sánchez, N. Martín, D. M. Guldi, *Angew. Chem., Int. Ed.* **2005**, *44*, 5374-5382.
23. P. J. F. De Rege, S. A. Williams, M. J. Therien, *Science*, **1995**, *269*, 1409-1413.
24. M. Guttierrez-Nava, H. Nierengarten, P. Masson, A. Van Dorsselaer, J.-F. Nierengarten, *Tetrahedron Lett.* **2003**, *44*, 3043-3046.
25. E. H. A. Beckers, A. P. H. J. Schenning, P. A. Van Hal, A. El-Ghayoury, L. Sanchez, J. C. Hummelen, E. W. Meijer, R. A. Janssen, *J. Chem. Commun.* **2002**, 2888-2889.
26. N. D. McClenaghan, D. M. Bassani, *Int. J. Photoenergy* **2004**, *6*, 185-192.
27. (a) N. Martin*, Chem. Commun.*, **2006**, 2093–2104.; (b) E. E. Simanek, X. Li, I. S. Choi, G. M. Whitesides, In *Comprehensive Supramolecular Chemistry*; J.-M. Lehn, Ed.; Pergamon, New York, **1996**, *Vol.9*, Chapter 17.
28. N. D. McClenaghan, Z. Grote, K. Darriet, M. Zimine, R. M. Williams, L. De Cola, D. M. Bassani, *Org. Lett.* **2005**, *7*, 807-810.
29. (a) E. H. A. Beckers, A. P. H. J. Schenning, P. A. Van Hal, A. El-Ghayoury, L.

Sanchez, J. C. Hummelen, E. W. Meijer, R. A. Janssen, *J. Chem. Commun.* **2002**, 2888-2889.; (b) A. P. G. Robinson, R. E. Palmer, T. Tada, T. Kanayama, J. A. Preece, D. Philp, U. Jonas, F. Diederich, *Chem. Phys. Lett.* **1998**, *289*, 586-590.; (c) I. Lamparth, G. Schick, A. Hirsch, *Lieb. Annal.* **1997**, 253-258.

30. C.-H. Huang, N. D. McClenaghan, A. Kuhn, J. W. Hofstraat, D. M. Bassani, *Org. Lett.* **2005**, *7*, 3409-3412.
31. C. Bingel, *Chem. Ber.* **1993**, *126*, 1957-1959.
32. G. A. Sotzing, J. R. Reynolds, P. J. Steel, *Chem. Mater.* **1996**, *8*, 882-889.
33. M. Turbiez, P. Frére, J. Roncali, *J. Org. Chem.*, **2003**, *68*, 5357-5360.
34. (a) J. Kalinowski, W. Stampor, P. Di Marco, F. Garnier, *Chem. Phys.* **1998**, *237*, 233. (b) R. N. Marks, M. Muccini, E. Lunedi, R. H. Michel, M. Murgia, R. Zamboni, C. Taliani, G. Horowitz, F. Garnier, M. Hopmeier, M. Oestreich, R. F. Mahrt, *Chem. Phys*. **1998**, *227*, 49.
35. M.Turbiez, P. Frere, P. Blanchard, J. Roncali, *Tetrahedron Lett*. **2000**, *41*, 5521-5525.
36. Y. Wei, Y. Yang, J-M. Yeh, *Chem. Mater.* **1996**, *8*, 2659-2666.
37. G. Sotgiu, M. Zambianchi, G. Barbarella, C. Botta, *Tetrahedron*, **2002**, *58*, 2245-2251.
38. (a) J. J. Apperloo, L. B. Groenendaal, H. Verheyen, M. Jayakannan, R. A. J. Janssen, A. Dkhissi, D. Beljonne, R. Lazzaroni, J.-L. Brédas, *Chem. Eur. J.* **2002**, *8*, 2384. (b) L. B. Groenendaal, F. Jonas, D. Freitag, H. Pielartzik, J. R. Reynolds, *Adv. Mater*. **2000,** *12,* 481.; (c) A. Facchetti, M. H. Yoon, C. L. Stern, G. R. Hutchison, M. A. Ratner, T. J. Marks, *J. Am. Chem. Soc*. **2004**, *126*, 13480-13501.
39. S. Akoudad, J. Roncali, *Synth. Met.,* **1998**, *93*, 111-114.
40. (a) J. L. Segura, N. Martin, *J. Mater. Chem.* **2000**, *10*, 2403-2435. (b) R. E. Martin, F. Diederich, *Angew. Chem. Int. Ed.* **1999**, *38*, 1350-1377. (c) U. Scherf, *Top. Curr. Chem.* **1999**, *201*, 163-222. (d) K. Müllen, G. Wegner, *Electronic Materials: The Oligomer Approach*, Wiley VCH, Weinheim, **1998**. (e) A. Kraft, A. C. Grimsdale, A. B. Holmes, *Angew. Chem. Int. Ed.* **1998**, *37*, 403-428. (f) J. M. Tour, *Chem. Rev.* **1996**, *96*, 537-553. (g) D. Braun, A. J. Heeger, *Appl. Phys. Lett.* **1991**, *58*, 1982-1984. (h) J. H. Burroughes, D. D. C. Bradley, A. R. Brown, R. N. Marks, K. Mackay, R. H. Friend, P. L. Burns, A. B. Holmes, *Nature,* **1990**, *347*, 5392541.
41. (a) A. Mathy, K. Ueberhofen, R. Schenk, H. Gregorius, R. Garay, K. Müllen, C. Bubeck, *Phys. Rev. B.* **1996**, *53*, 4367-4376. (b) H. Meier, H. Kretzschmann, M. Lang, W. Fraß, C. Albrecht, K. März, *J. Prakt. Chem.* **1994**, *336*, 297-302.
42. (a) E. Peeters, P. A. van Hal, J. Knol, C. J. Brabec, N. S. Sariciftci, J. C. Hummelen, R. A. J. Janssen, *J. Phys. Chem. B* **2000**, *104,* 10174-10190. (b) H. Detert, D. Schollmeyer, E. Sugiono, *Eur. J. Org. Chem.* **2001**, 2927-2938. (c) U.

Stalmach, H. Kolshorn, I. Brehm, H. Meier. *Liebigs Ann.* **1996**, 1449-1446.

43. (a) H. Detert, D. Schollmeyer, E. Sugiono, *Eur. J. Org. Chem.* **2001**, 2927-2938. (b) U. Stalmach, H. Kolshorn, I. Brehm, H. Meier. *Liebigs Ann.* **1996**, 1449-1446.
44. H. Meier, D. Ickenroth, *Eur. J. Org. Chem.* **2002**, 1745-1749.
45. M. E. Thibault, T. L. L. Closson, S. C. Manning, P. W. Dibble, *J. Org. Chem.* **2003**, *68*, 8373-8378.
46. R. Baron, C.-H. Huang, D. M. Bassani, A. Onopriyenko, M. Zayats, I. Willner, *Angew. Chem., Int. Ed.* **2005**, *44*, 4010-4015.
47. P. K. Sudeep, B. I. Ipe, K. G. Thomas, M. V. Gerore, S. Barazzouk, S. Hotchandani, P. V. Kama, *Nano Lett.* **2002**, *2*, 29-35.
48. K. C. Nicolaou, S. Y. Cho, R. Hughes, N. Winssinger, C. Smethurst, H. Labischinski, R. Endermann, *Chem. Eur. J.* **2001**, *7*, 3798-3823.
49. M. Steinbeck, H. Ringsdorf, *Chem. Commun.* **1996**, 1193-1194.
50. M. D. Porter, T. B. Bright, D. L. Allara, C. E. D. Chidsey, *J. Am. Chem. Soc.* **1987**, *109*, 3559-3568.
51. (a) H.-T. Rong, S. Frey, Y.-J. Yang, M. Zharnikov, M. Buck, M. Wühn, C. Wöll, G. Helmchen, *Langmuir*, **2001**, *17*, 1582-1593.; (b) P. Cyganik, M. Buck, M. *J. Am. Chem. Soc.* **2004**, *126*, 5960-5961. (c) A. Shaporenko, M. Brunnbauer, A. Terfort, L. S. O. Johansson, M. Grunze, M. Zharnikov, *Langmuir* **2000**, *21*, 4370-4375

Chapter 3

Photoelectrochemical Solar Cells

3.1. Introduction

Photoinduced electron transfer in donor-acceptor molecular systems has received considerable attention for applications such as optoelectronics, photonics, sensors, and other nanoscale molecular devices.[1] In this regard, self-assembled monolayers and multilayer thin films with chemical or electronic potential gradients have proven to be promising in mimicking the natural photosynthetic apparatus and fabricating efficient photovoltaic cells.[2] In general, artificial photoelectrochemical solar cells are based on hybrid structures of organic/inorganic semiconductors, where this working material is in contact with electrolyte and electron carrier (as redox couple) in the liquid phase. Upon exposure of the photoactive materials to light, the photogenerated charges (holes and electrons) separate and migrate to opposite electrodes due to a built-in or externally applied electric field. The capture of the electron (or hole) by the electron carrier at the material-liquid interface joined with the process of the opposite charge moving to the working electrode completes an electric circuit. The electron carrier releases the captured charge to the counter electrode which results in charge balance of the redox species. Several interesting all-organic systems have been recently reported in the context of photovoltaic devices, including examples based on photoactive SAMs[3] and chromophore-appended nanotubes,[4] as well as fullerene-oligomer dyads/triads.[5] For example, coupled with porphyrins and/or ferrocenes as electron donors, [60]fullerene-containing systems such as dyad and triad have recently been demonstrated as very prominent photovoltaic devices in artificial photoelectrochemical cells.[6] Two of these photoactive SAMs devices are shown in Figure 3.1. Highly efficient photoinduced energy and electron transfer were observed in donor-acceptor molecular systems, and the photodynamic studies on porphyrin–fullerene-linked systems revealed that fullerenes accelerate photoinduced electron transfer and charge-shift, slowing down charge recombination.[7] In such systems, a rapid and stable cathodic photocurrent response was produced under the irradiation over several on/off cycles.

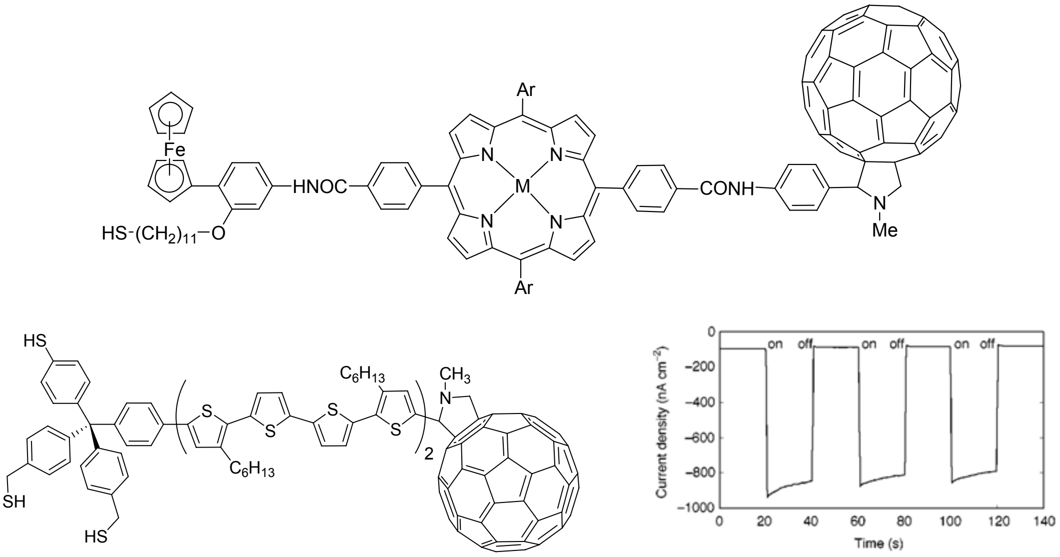

Figure 3.1. (Top): Ferrocene-porphyrin-fullerene-linked system for deposition on a gold surface; (Below, left): oligothiophene-fullerene-linked SAMs system bearing a tripod thiol anchor. (Below, right): and its photocurrent response with incident irradiation (400 nm) at -100 mV of bias vs. Ag/AgCl.[7]

The preparation of the covalently-linked photoactive materials described above requires lengthy and costly multi-step syntheses necessitating extensive purification techniques, which impede further development towards large-scale applications. As shown in Figure 3.2, Cho *et al.* reported a self-assembled architecture using metal-ligand coordination to connect the electron donor-acceptor system, producing a highly ordered fullerene-osmium-porphyrin cluster complex dyad SAM on ITO surface in the presence of DABCO used to bind the two porphyrin moieties. High photocurrent generation was achieved upon illumination (6.0 μA cm^{-2}).[8]

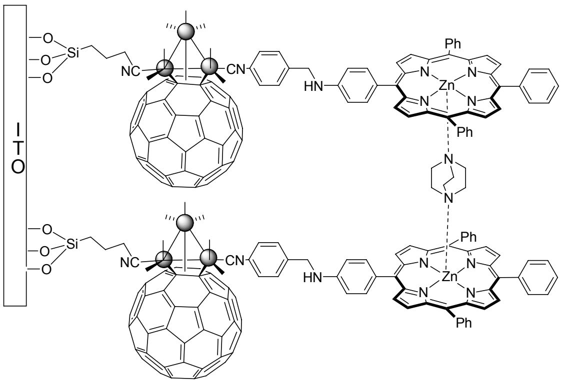

(ZnP)-C_{60}/ITO

Figure 3.2. Photovoltaic cell base on a fullerene metal cluster-porphyrin dyad SAMs on ITO electrode.[8]

A limitation in the performance of photoactive SAM-based systems is that the current density generated from such cells is limited by the number of photoactive molecules per unit area. To obtain higher photocurrents, one of the direct strategies is to construct multilayer thin films on the electrode in order to include more material in the device. A multilayer photovoltaic device system was recently reported by Zhuang *et al.* where the supramolecular self-assembly between a perylene bisimide bearing diaminopyridine-substituted isophthalamide groups (PP) and a fullerene containing barbituric acid derivative (C60bar) through a complementary six-point hydrogen-bonding interaction was used (Figure. 3.3).[9] A low cathodic (0.15 μA cm^{-2}) photocurrent response of the PP/C60bar film deposited onto an ITO electrode was produced under the irradiation. Both perylene and fullerene derivatives had high aggregation tendency because of the strong intermolecular π–π stacking, which led to the formation of spherical particle aggregates of the hydrogen-bonded perylene/fullerene supramolecular structure on electrode surface.

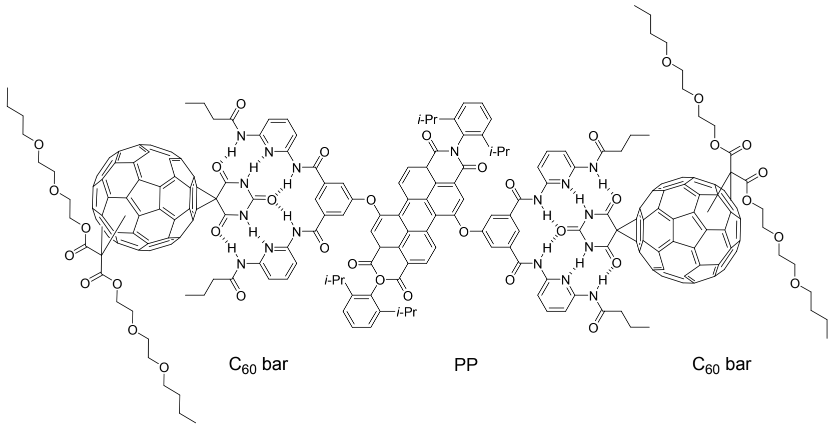

Figure 3.3. Hydrogen-bonded self-assembly of perlyene and C60 derivatives.[9]

Furthermore, different supramolecular hydrogen-bonded nanostructures consisting of fullerene have been prepared, and their application for photocurrent generation has been reported (Figure 3.4).[10]

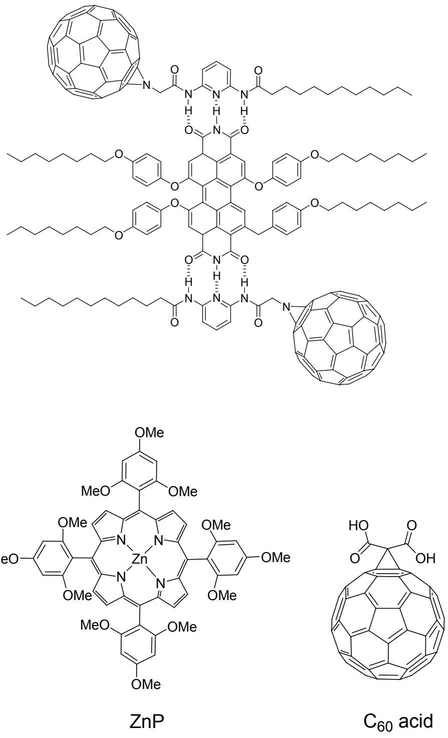

Figure 3.4. Examples of self-assembled hydrogen-bonded nanostructures applied to the photoelectrochemical solar cells study: (Top) perylene-fullerene derivatives assembly[10a] (Below): porphyrin-fullerene assembly.[10c]

In addition to the use of artificial binding design above, complementary biorecognition complexes such as biotinvidin, antigen–antibody, or DNA have also been used to assemble layered structures of nanoparticals on surfaces.[11] Long *et al.* reported the construction and properties of self-assembled monolayers of the chromophore fluorescein (Fl) which was attached through a 20 base-pair duplex DNA linker to a gold microelectrode (Figure 3.5).[12] A fluorescein (Fl)-labeled DNA monolayer on Au was formed such that under applied potential of –750 mV and incident irradiation, a photocurrent (0.2 μA cm^{-2}) was generated that ultimately reduced $NAD(P)^+$ to biologically active NAD(P)H, which was proposed to replicate the two electron transfer process in photosystem I (PSI).

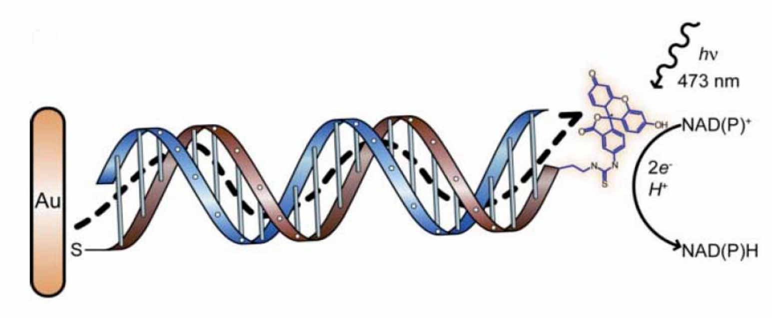

Figure 3.5. A DNA monolayer that contains an electrochemically reduced Fl radical anion that is irradiated by hν at 473 nm, which further photo reduces $NAD(P)^+$ to NAD(P)H.[12]

Although multilayer thin film photovoltaic devices present the advantage of producing higher photocurrent, the morphology of the film greatly affects the overall photoenergy conversion efficiency. This is illustrated in a recent report[13] on hydrogen-bonded layered assembly possessing an alternating 3-D construction built using selective DNA nucleotides able to precisely control the formation process in the layer-by-layer supramolecular architecture (Figure 3.6). This nearly ideal bottom-up CdS nanoparticles assembly opens-up new perspectives for future molecular-level photovoltaic device design. Such nanostructures exhibit high stability in aqueous media, where the photocurrents generated by the systems are higher, revealing that the hydrogen-bonded nucleotide arrays may provide effective bridges for transporting electrons to the electrode.

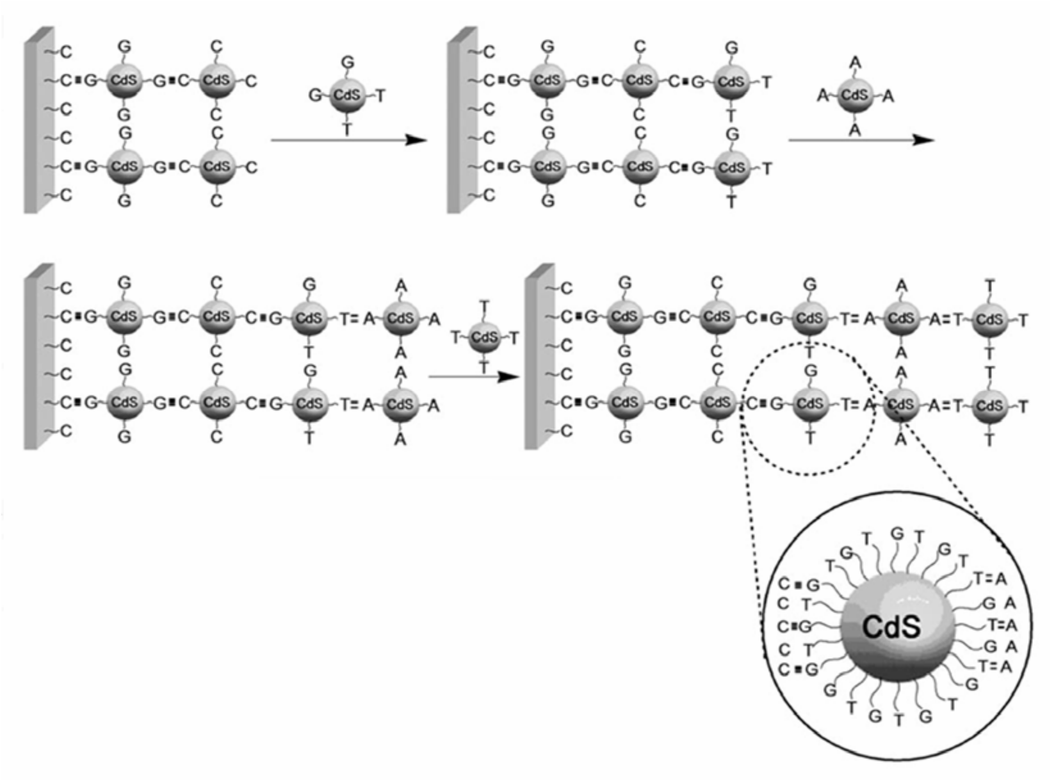

Figure 3.6. Layered hydrogen-bonded nucleotide-functionalized CdS nanoparticals for photo-electrochemical applications.[13]

3.2. Photoelectrochemical studies of thin films on bare gold electrode

The photovoltaic response of conjugated oligothiophene and oligo(*p*-phenylene vinylene)s materials when used in conjunction with a barbiturate-substituted fullerene derivative was investigated to assess their usefulness in the construction of photovoltaic devices. Typical device set-up is as follows: Solutions of **1** and **7** (ratio 2:1) were prepared in polar anhydrous DMSO (not conducive with the formation of hydrogen-bonded structures). Drop-casting and slow evaporation of the solvent on a gold slide resulted in the formation of a thin film whose response could be measured in a standard three electrode photoelectrochemical cell, using methyl viologen dichloride hydrate in deionized water as an electron carrier, sodium sulfate as the supporting electrolyte and a platinum wire as the counter electrode. Irradiation was performed using a high-pressure mercury lamp equipped with a band-pass filter and fiber-optic light guide (400-500 nm; intensity = 150 mW.cm^{-2}).[14]

At first, oligothiophene **7** was tested alone (device A) to verify that there is a photovoltaic response with films of this molecule. A typical *I/V* graph of photocurrent generated *vs.* applied potential is shown in Figure 3.7 (left) for device A. The thickness of the film was estimated at *ca.* 200 nm using AFM (see, Figure 3.7 right). From the *I/V* curve, and using Eqs. 1 and 2, the open-circuit voltage conversion efficiency, $\Phi(V_{\mathrm{oc}})$, and short-circuit quantum conversion efficiency, $\Phi(I_{\mathrm{sc}})$, of the photovoltaic device can be estimated. Respectively, these values express the fraction of light energy that is converted into voltage, and the fraction of electrons generated for every photon of light that is absorbed.[15]

$$\Phi(V_{\mathrm{oc}}) = V_{\mathrm{oc}} \,/\, E_{oo} \qquad (1)$$

$$\Phi(I_{\mathrm{sc}}) = (\mathrm{d}n_{\mathrm{e}}/\mathrm{d}t) \,/\, (\mathrm{d}n_{\mathrm{h\nu}}/\mathrm{d}t) \qquad (2)$$

where n_e and $n_{h\nu}$ are the number of charges generated and number of photons absorbed, respectively, and E_{oo} is the energy of the $S_1 \leftarrow S_0$ transition in eV. The incident light intensity was determined to be 150 mW.cm^{-2}, which corresponds to an average photon flux of 5.6 x 10^{-8} Einstein (at 450 nm).

Considering the device comprising an oligomer film without fullerene, it is estimated that ca. 2.7% of incident light is absorbed (based on the measured thickness of the film and the extinction coefficient of **7** at 490 nm, ε = 48000 M^{-1}cm^{-1}). From Eqs. 1 and 2 above and values of V_{oc} = 0.39 V and I_{sc} = 6.8 μA, one can obtain $\Phi(V_{oc})$ = 0.14, and $\Phi(I_{sc})$ = 0.05. These values are comparable to other photovoltaic devices based on similar technology (although experimental error, associated mainly with the determination of film thickness, must be taken into consideration).

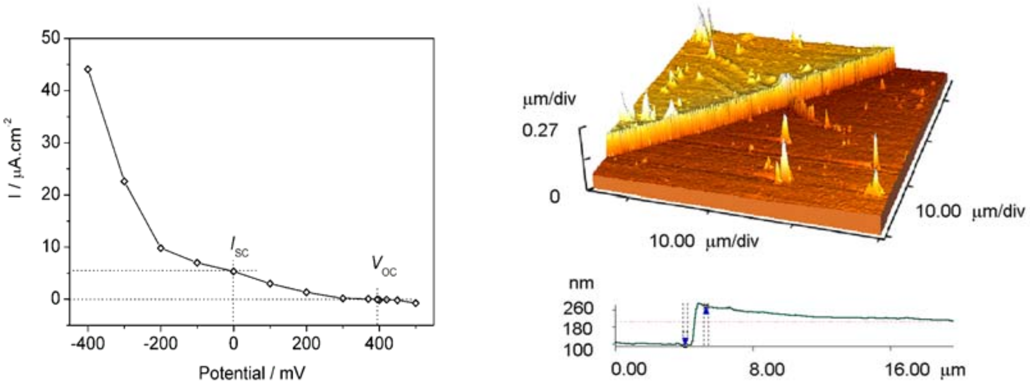

Figure 3.7. I/V-curve obtained from a drop-cast film of **7** on Au (left), and AFM image of the film showing its thickness (right).

Identical devices were then prepared using **7** (1 eq.) in the presence of either 2 eq. of pristine C_{60} (device B), or 2 eq. of **1** (device C) as showed in Figure 3.8. It should be noted that **1** is only sparingly soluble in DMSO. However, compound **1** was completely solubilized in the presence of **7**. This behavior is typical of compounds possessing complementary molecular recognition sites, and is taken as an indication of site-specific interactions at the molecular level.

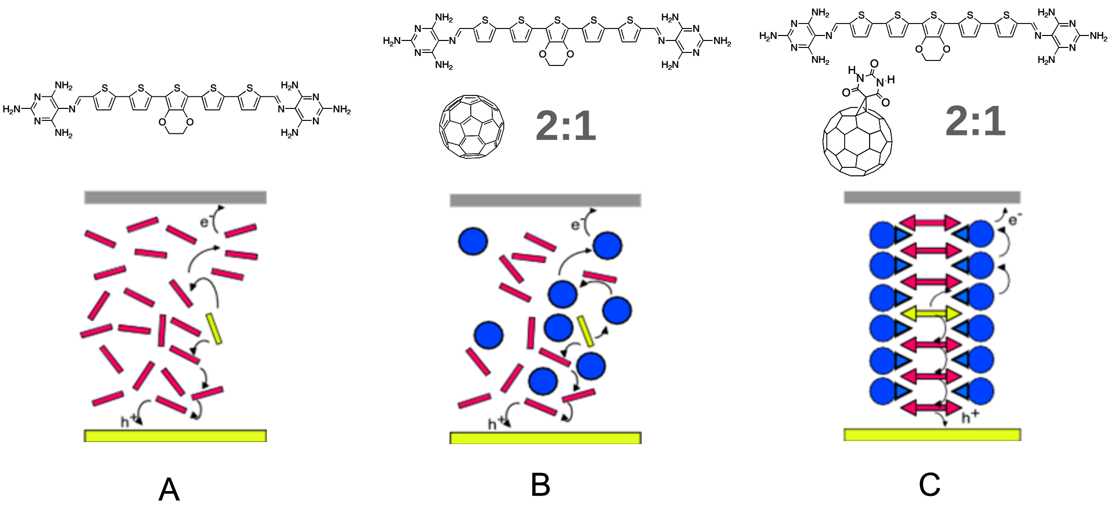

Figure 3.8. Schematic illustration of three different photovoltaic devices

The response of the photovoltaic devices A, B, and C in the presence and absence of light at an applied potential of – 100 mV is shown in Fig.3.9. As noted by others,[16] a gain in performance (ca. two-fold) is obtained by the incorporation of C_{60} in conjugated polymer blends. More importantly, a five-fold enhancement in photocurrent under identical experimental conditions is obtained from the use of the modified C_{60} (device C). In line with the idea of higher organization and better compatibility of the two different electron-donor and acceptor materials giving the highest photocurrent, the best performance was measured for a mixture of **1** and **7**, which was anticipated to be the most organized thin film comprising the hydrogen-bonding fullerene and the complementary π-conjugated oligomer. This response was 2.5 times higher than that obtained on combining **7** with unsubstituted C60, while the lowest conversion was obtained for the film of oligomer **7** alone with a value which was half that obtained with **7** : pristine C60. This improvement is attributed, at least in part, to better miscibility compared to pristine C_{60} which forms partially phase-separated domains in the film of device B, of **1** with the conjugated oligomer. This in turn allows a more even incorporation of C_{60} derivative in the device, leading to a greater degree of charge separation (also see Figure 2.16).

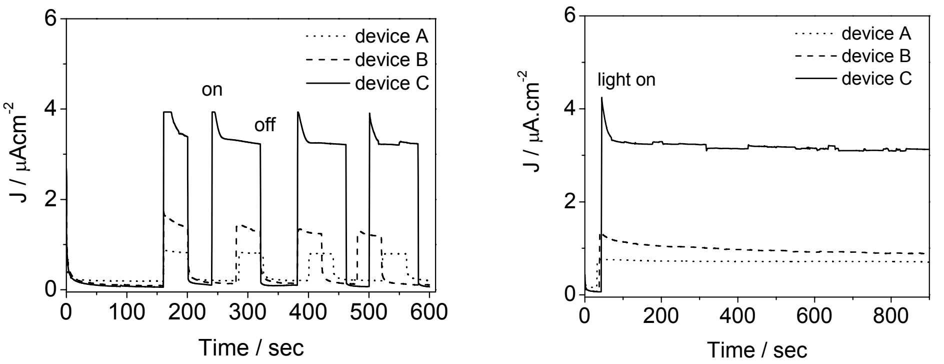

Figure 3.9. (Left) Illumination-dependence of the photovoltaic response of devices A (solid line), B (dashed line), and C (dotted line) at an applied potential of -100 mV. (Right) Variations in current density as a function of time under continuous irradiation.

Based on the calculated efficiency of device A, one can estimate the efficiency of devices incorporating the modified C_{60} derivative **1** to be as high as 25%. This value compares favorably with recent photovoltaic devices based on the layer-by-layer construction of conjugated polymers and C_{60} and with IPCE values of 15%.[17] In all cases it can be assumed that absorption of light is affected predominantly by the oligomer, as fullerene derivatives possesses low molar absorptivities above 400 nm. Therefore, despite uncertainties in the absolute values for the efficiency of these simple devices, these results show that the films comprising two complementary hydrogen-bonding electroactive units are more performant. However, attempts to increase the absorbance of the film by increasing its thickness resulted in a drop of photocurrent. This is consistent with a low-charge carrier mobility in the material, in agreement with previous measurements of charge transport based on Field-Effect Transistor devices.[18]

An important factor that became immediately apparent during this initial testing phase of the devices is their inherent stability towards air and moisture. Indeed, the photovoltaic cell set-up uses an aerated aqueous solution of methylviologen as the electron transport agent. The response of **7** (device A) is stable over time, whereas device B (**7** + pristine C_{60}) exhibits a slow (*ca.* 10% loss) of efficiency over a period of 1 hour (Figure 3.3, right). During this same period, no measurable decrease in efficiency was detected for the device prepared with **1** + **7**.

Figure 3.10 shows the photovoltaic response of devices incorporating **1** and **7** in different composition ratios (4:1, 2:1, 1:1, or 0:1 ratio, respectively). The performance of the device which is composed of fullerene **1** and oligothiophene **7** in 2:1 ratio revealed the highest photocurrent. This is in agreement with the previous discussion (Chapter 2.1.4) at the formation of supramolecular assemblies in which all the H-B sites present in the complementary components anticipated.

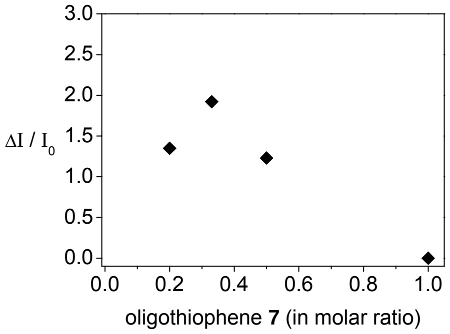

Figure 3.10. The enhanced photocurrent versed molar ratio of oligothiophene **7**.

The observed improvement in photovoltaic response is attributed to the presence of complementary hydrogen-bonding between the active components. At the very least, this is expected to provide increased compatibility between otherwise poorly-miscible materials. Additionally, the hydrogen-bonding pattern employed is conducive to the formation of extended organized domains, which are expected to be beneficial to charge separation and transport.

3.3. Photoelectrochemical studies of thin films on SAMs modified gold electrodes

The success of the photovoltaic experiments in section 3.2 is attributed to the self-assembled supramolecular architecture which considerably improves the efficiency of charge generation and separation between the electron donor (oligothiophene) and electron acceptor (fullerene). Base on these preliminary results we set out to improve the performance of the photovoltaic cells. While there is no evidence that the self-assembled supramolecular architectures of molecules **1** and **7** form an extended network through-out the whole layer, such a highly order network would be highly beneficial. To improve the degree of alignment and to obtain photoactive fullerene-containing architectures directed by a hierarchical combination of supramolecular self-assembly processes, gold-thiol interactions can be employed in addition to hydrogen-bonding where the assembly array can conduct from a fixed starting point and is parallel to the electrode surface (Figure 3.11. right).

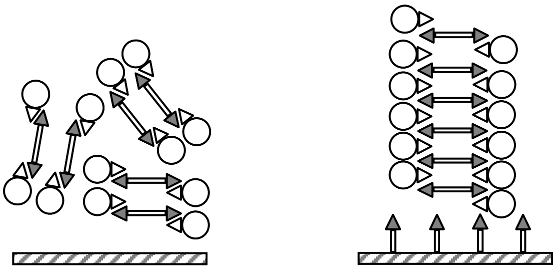

Figure 3.11. Schematic illustration of possible self-assembled array of **1** and **7** on bare gold (left), and a proposed ideal alignment on SAMs modified gold (right).

The study of well-defined self-assembled monolayer formed from different polar end-group thioacetate molecules has been discussed in Section 2.3. A series of photoelectronic devices similar to those reported in Section 3.2 were prepared by depositing a DMSO solution of molecule **1** and **7** (1:2 ratio) on gold electrodes modified with SAMs prepared from compounds **39**, **42**, **44**, or **47**. (See Figure 3.12) Comparison of the response obtained from electrodes modified with **39** vs. **44** (devices E and G, respectively) provides an indication as to the effect of the hydrogen-bonding endgroup, whereas the use of **42** serves as a control in which hydrogen-bonding is blocked.[19] SAMs made using **47** possess a hydrophobic character which excludes any hydrogen-bonding effect and serve only as a protecting layer to prevent phonon quenching from the gold surface.

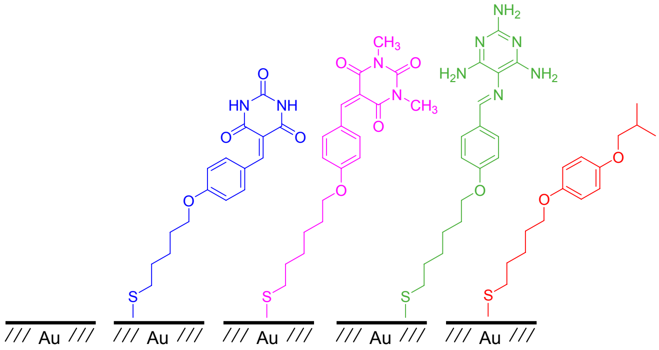

molecule		**39**	42	**44**	47
device	D	E	F	G	H

Figure 3.12. Schematic illustration of SAMs modified gold electrodes with molecules **39**, **42**, **44**, or **47** for preparation of photovoltaic devices E, F, G, or H, respectively. Device D is the film deposited on bare gold.

The photocurrent response for each of the five different devices is shown in Figure 3.13 (left), where device D is the film deposited on the bare gold as a control experiment; device E is the thin film deposited on the surface decorated with barbiturate **39**; device F is the film deposited on the surface decorated with the *N*-methyl barbitrate **42**; device G is the film deposited on the surface decorated with melamine **44**; and device H is the film deposited on the surface with thiol **47**. All photocurrent measurements are performed with an identical experimental set-up as described in Section 3.2.

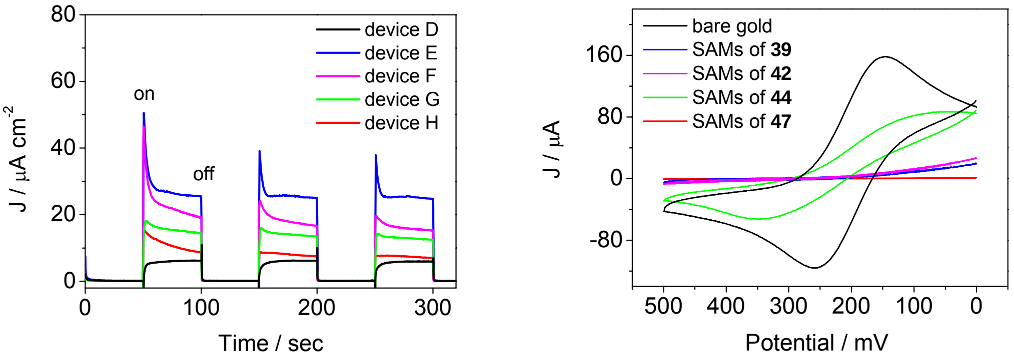

Figure 3.13. Left: Photocurrent generated with thin films of **7**:**1**; 1:2 eq. on: bare gold (device D) and on SAMs modified gold (device E, F, G, and H). Right: Cyclic voltammograms of the reduction of aqueous $K_3[Fe(CN)_6]$ using bare gold and gold electrodes whose surfaces were modified with **39**, **42**, **44**, or **47**.

It was immediately clear that device D is the least performant device when compared to the devices incorporating SAM-decorated surfaces, all of which gave a higher photocurrent. The basic multi-step electron transfer mechanism of these SAMs modified devices can be considered as showed in Figure 3.14. After the photogenerated exciton separated by highly electron negative affinity of fullerene, the electron transferred along with others fullerene to the material layer and solution interface where the electron was carried away by MV^{+2} or oxygen.[6] At the other side of the charge transport pathway, the hole is transferred along the oligothiophene array, and then reaches the material layer and SAMs interface where this positive charge is conducted through SAM to the anode via a tunneling mechanism.[20] The improvement of the photovoltaic response when using the SAM-modified surfaces may in part originate from one or more of the following reasons: (1) Variations in the surface properties as the increased hydrophobicity of the SAM-covered surface results in lower contact angles when exposed to organic solvents which intern modifies the resulting film morphology. (2) Sergeant-soldier principle,[21] where the recognition motifs on the SAMs induce ordered assembly of molecules possessing complementary binding units. This then induces further self-assembly within the device. (3) Reduction of the phonon quenching of the excited states generated in close proximity of the gold surface,[22] and (4) Variation in the gold workfunction due to the formation of the Au-S bonds.

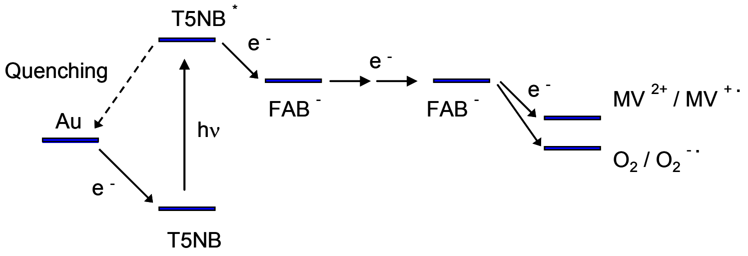

Figure 3.14. Schematic illustration of energy diagram in photo-induced multi-step electron transfer mechanism on SAMs modified gold electrode.[6d]

Additionally, it is possible that the presence of the barbituric acid-appended SAM may induce the preferential adsorption of the complementary melamine-containing oligothiophene unit **7**. Due to the electrical bias applied during the photovoltaic measurements, it is expected that this construction should be more efficient as the presence of the thiophene proximal to the gold electrode would be beneficial to the energy transport of holes towards the cathode. Device H is a direct experiment to clarify the influence of distance from gold surface by the alkyl chain due to the phonon quenching, and the result clearly shows that extra photocurrent was gained.[23]

The behavior of the most performed device (E) shown in Figure 3.13 is intriguing, displaying a sharp spike in the photogenerated current upon each illumination cycle. This reproducible behavior was attributed to compression of the diffusion layer due to depletion of the MV^{2+} in the vicinity of the electrode. To confirm this, the photovoltaic response of device D and E were monitored upon mechanical stirring of the solution. The results are presented in Figure 3.15 (left), in which it is quite clear that the photovoltaic response of E increases substantially upon stirring, in a way that is proportional to the rate of stirring. Therefore, in the case of device E the observed performance is limited by the rate of diffusion of the electron-carrying species in solution rather than the charge-carrier mobility in the material. This is not the case for the other devices, for which the effect of stirring the solution is much lower or negligible, as in the case of device D. Device E also displayed exceptional stability, no deterioration in its response being observed after two week storage under ambient conditions.(see, Figure 3.15 right, green line)

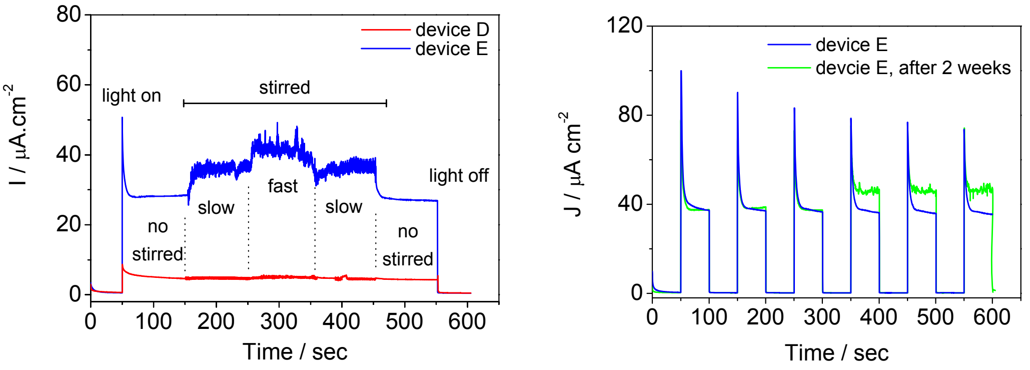

Figure 3.15. Left: Effect of stirring on the photocurrent of devices D (red) and E (blue); with stirring off, slow stirring and fast stirring regions. Right: The comparison of photocurrent generated from device E (blue, no stirring during 600 sec illumination) with its repeated measurement after two weeks storage. (green, upon stirring of the solution after first 350 sec)

The maximum inherent photocurrent attainable by device E could not be measured due to the diffusion-controlled limitation of the electron carrier in solution. These experiments allow some insight on the electron transfer in devices D and E. As schematically illustrated in Figure 3.16, devices D and E were both loaded with the same amount of photoactive material, and it can be assumed that both devices absorb the same amount of light and have similar charge generation efficiency. In the absence of stirring, the diffusion rate (denoted as k_{diff}) of MV^{+2} and the rate of electron transfer (denoted as k_{et}) from C_{60}^{-} to methylene viologen (MV^{+2}) are constant. We can consider a variable parameter representing the rate of charge transport (denoted as k_1 and k_2 for device D, E respectively) in the organic material. Because in device E, the photovoltaic response increases proportionally to the rate of stirring, it can be reasoned that the electron transport rate within the organic layer (k_2) is faster than the diffusion rate of MV^{+2} in solution (k_{diff}). In contrast, no effect of stirring is observed at the photocurrent generation in device D, indicating that the charge transport rate (k_1) is slower than k_{diff}. The higher value of transport rate in E ($k_2 > k_1$) results a 6-fold current enhancement compared to device D revealing that the SAM can dramatically improve the degree of charge transport in the device. The C-5 alkyl chain of the SAM also inhibits phonon quenching of the chromophor by gold surface, but contribution is expected to be minor, and is evaluated at *ca.* 40% of enhancement.

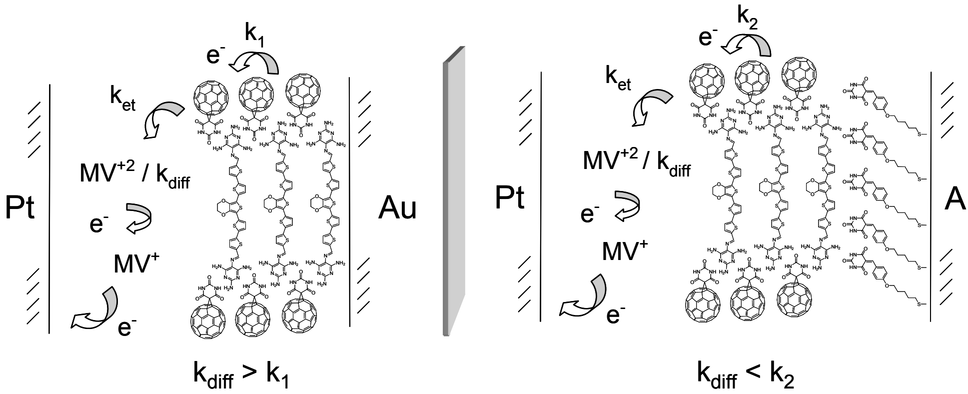

Figure 3.16. Schematic illustration of electron-transfer mechanism at device D (on bare gold, left), and at device E (on SAMs of **39** modified gold, right).

3.4. Conclusion

The introduction of hydrogen-bonding molecular recognition motifs in direct conjugation to an oligothiophene when used in conjunction with a barbiturate-substituted fullerene derivative was investigated to assess their usefulness in the construction of photovoltaic devices. A better degree of charge separation was expected to be a beneficial factor in light-electricity conversion process which has been observed in comparison with device A and B (see, Figure 3.17 I and II).

The formation of SAMs appended with suitable recognition motifs is shown to be advantageous in the construction of supramolecular all-organic photovoltaic devices. Based on the formation of hydrogen-bonded networks, the molecular constituents in these devices are programmed to self-assemble into molecular-level heterojunctions. A *ca.* 6-fold photocurrent enhancement was obtained, indicating that an important increase in electron transport efficiency and/or charge collection can be achieved simply by improving molecular interactions at the electrode interface. Although direct probing of the degree of order instilled by the presence of complementary hydrogen-bonding donor-acceptor sites is difficult (Figure 3.16 III, IV, and V), considerable differences in efficiency and behavior are noted.

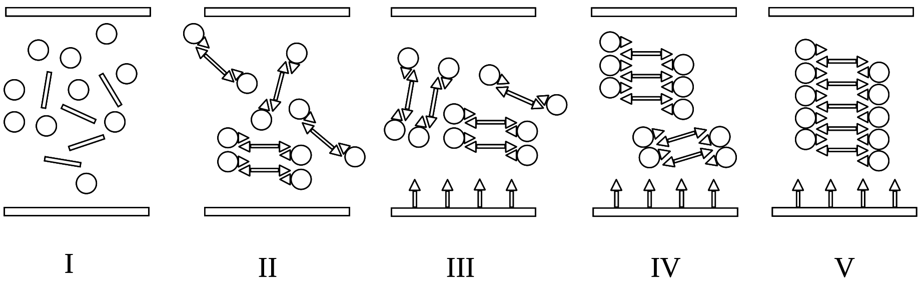

Figure 3.17. Schematic illustration of self-assembly on bare gold : in bulk composition (I); with recognition motifs (II); and on SAMs modified gold: with different degree of order (III, IV, and V).

References

1. (a) M. R. Wasielewski, *Chem. Re*v. **1992**, *92*, 435-461. (b) D. Gust, T. A. Moore, A. L. Moore, *Acc. Chem. Res.* **2001**, *34*, 40-48.
2. (a) B. O'Regan, M. Gra¨tzel, M. *Nature* **1991**, *353*, 737-740. (b) C. J. Kleverlaan, M. T. Indelli, C. A. Bignozzi, L. Pavanin, F. Scandola, G. M. Hasselman, G. J. Meyer, *J. Am. Chem. Soc*. **2000**, *125*, 2840-2849. (c) H. Yamada, H. Imahori, Y. Nishimura, I. Yamazaki, T. K. Ahn, S. K. Kim, D. Kim, S. Fukuzumi, *J. Am. Chem. Soc.* **2003**, *125*, 9129-9139. (d) H. Imahori, M. Kimura, K. Hosomizu, T. Sato, T. K. Ahn, S. K. Kim, D. Kim, Y. Nishimura, I. Yamazaki, Y. Araki, O. Ito, S. Fukuzumi, *Chem.-Eur. J.* **2004**, *10*, 5111-5122. (e) D. M. Guldi, I. Zilbermann, G. Anderson, A. Li, D. Balbinot, N. Jux, M. Hatzimarinaki, A. Hirsch, M. Prato, *Chem. Commun*. **2004**, 726-727.
3. (a) Y.-J. Cho, T. K. Ahn, H. Song, K. S. Kim, C. Y. Lee, W. S. Se, K. Lee, K. Kwangyeol, K. Seong, D. Kim, J. T. Park, *J. Am. Chem. Soc*. **2005**, *127*, 2380-2381.; (b) K.-S. Kim, M. S. Kang, H. Ma, A. K.-Y. Jen, *Chem. Mater.* **2004**, *16*, 5058-5062.
4. D. M. Guldi, G. M. A. Rahman, M. Prato, N. Jux, S. Qin, W. Ford, *Angew. Chem., Int. Ed*. **2005**, *44*, 2015-2018
5. (a) D. M. Guldi, C. Luo, A. Swartz, R. Gómez, J. L. Segura, N. Martìn, C. Brabec, N. S. Sariciftci, *J. Org. Chem*. **2002**, *67*, 1141-1152.; (b) N. Negishi, K. Takimiya, T. Otsubo, Y. Harima, Y. Aso, *Chem. Lett.* **2004**, *33*, 654-655.
6. (a) C. Luo, D. M. Guldi, M. Maggini, E. Menna, S. Mondini, N. A. Kotov, M. Prato, *Angew. Chem., Int. Ed.* **2000**, *39*, 3905-3909. (b) J.-F. Eckert, J.-F.; Nicoud, J.-F.; Nierengarten, S.-G. Liu, L. Echegoyen, F. Barigelletti, N. Armaroli, L. Ouali, V. Krasnikov, G. Hadziioannou, *J. Am. Chem. Soc.* **2000**, *122*, 7467-7479. (c) A. Ikeda, T. Hatano, S. Shinkai, T. Akiyama, S. Yamada, *J. Am. Chem. Soc.* **2001**, *123*, 4855-4856. (d) H. Imahori, Y. Mori, Y. Matano, *J. Photochem. Photobiol. C,* **2003**, *4*, 51-83.
7. (a) H. Imahori, H. Yamada, Y. Nishimura, I. Yamazaki, Y. Sakata, *J. Phys. Chem. B,* **2000**, *104*, 2099-2108. (b) D. Hirayama, K. Takimiya, Y. Aso, T. Otsubo, T. Hasobe, H. Yamada, H. Imahori, S. Fukuzumi, Y. Sakata, *J. Am. Soc. Chem.* **2002**, *124*, 532-533.
8. Y.-J. Cho, T. K. Ahn, H. Song, K. S. Kim, C. Y. Lee, W. S. Se, K. Lee, K. Kwangyeol, K. Seong, D. Kim, J. T. Park, *J. Am. Chem. Soc*. **2005**, *127*, 2380-2381.
9. J. Zhuang, W. Zhou, X. Li, Y. Li, N. Wang, X. He, H. Liu, Y. Li, Li Jiang, C. Huang, S. Cui, S. Wang, D. Zhu, *Tetrahedron*, **2005**, *61*, 8686–8693.

10. (a) Y. Liu, S. Xiao, H. Li, Y. Li, H. Liu, F. Lu, J. Zhuang, D. Zhu, *J. Phys. Chem. B* **2004,** *108,* 6256-6260. (b) H. Imahori, J.-C. Liu, K. Hosomizu, T. Sato, Y. Mori, H. Hotta, Y. Matano, Y. Araki, O. Ito, N. Maruyamae, S. Fujita; *Chem. Commun.*, **2004**, 2066-2067. (c) H. Imahori, J.-C. Liu, H. Hotta, A. Kira, T. Umeyama, Y. Matano, G. Li, S. Ye, M. Isosomppi, N. V. Tkachenko, H. Lemmetyinen *J. Phys. Chem. B* **2005**, *109,* 18465-18474.
11. (a) C. M. Niemeyer, B. Ceyhan, P. Hazarika, *Angew. Chem. Int. Ed.* **2003**, *42*, 5766–5770. (b) F.Patolsky , K.T. Ranjit, A. Lichtenstein, I. Willner, *Chem. Commun.* **2000**, 1025–1026. (c) S. Cobbe, S. Connolly, D. Ryan, L. Nagle, R. Eritja, D. Fitzmaurice, *J. Phys. Chem. B* **2003**, *107*, 470–477; (d) S. Mann, W. Shenton, M. Li, S. Connolly, D.Fitzmaurice, *Adv. Mater.* **2000**, *12*, 147–150.
12. Y.-T. Long, T. C. Sutherland, H.-B. Kraatz, J. S. Lee, *Chem. Commun.,* **2004**, 2032-2033.
13. J.-P. Xu, Y. Weizmann, N. Krikhely, R. Baron, I. Willner, *Small*, **2006**, *2*, 1178-1182.
14. Compare with:- Hirayama, D.; Takimiya, K.; Aso, Y.; Otsubo, T.; Hasobe, T.; Yamada, H.; Imahori, H.; Fukuzumi, S.; Sakata, Y. *J. Am. Chem. Soc*. **2002**, *124*, 532-533.; Imahori, H.; Liu, J.-C.; Hosomizu, K.; Sato, T.; Mori, Y.; Hotta, H.; Matano, Y.; Araki, Y.; Ito, O.; Maruyama, N.; Fujita, S. *Chem. Commun*. **2004**, 2066-2067.
15. (a) M. Lahav, V. Heleg-Shabtai, J. Wasserman, E. Katz, I. Willner, H. Dürr, Y.-Z. Hu, S. H. Bossmann, *J. Am. Chem. Soc.* **2000**, *122*, 11480-11487. (b) H. Imahori, H. Norieda, H. Yamada, Y. Nishimura, I. Yamazaki, Y. Sakata, S. Fukuzumi, *J. Am. Chem. Soc.* **2001**, *123*, 100-110.
16. N. S. Sariciftci, L. Smilowitz, A. J. Heeger, F.Wudl, *Science* **1992**, *258*, 1474-1476.
17. Brabec, C. J.; Padinger, F.; Hummelen, J. C.; Janssen, R. A. J.; Sariciftci, N. S. *Synth. Met*. **1999,** *102*, 861-864.
18. (a) Hong, X. M.; Katz, H. E.; Lovinger, A. J.; Wang, B.-C.; Raghavachari, K. *Chem. Mater.* **2001**, *13*, 4686. (b) Facchetti, A.; Mushrush, M.; Yoon, M.-H.; Hutchison, G. R.; Ratner, M. A.; Marks, T. J. *J. Am. Chem. Soc.* **2004**, *126*, 13859.
19. D. M. Bassani, V. Darcos, S. Mahony, J.-P. Desvergne, *J. Am. Chem. Soc.* **2000**, *122*, 8795-8796.
20. (a) S. Maisch, F. Buckel, F. Effenberger, *J. Am. Chem. Soc.* **2005**, *127*, 17315-17322. (b) Engelkes, V. B.; Beebe, J. M.; Frisbie, C. D. *J. Am. Chem. Soc.* **2004**, *126*, 14287-14296. (c) Wang, W.; Lee, T.; Reed, M. A. *Phys. Rev. B: Condens. Matter* **2003**, *68*, 035416/1. (d) Wold, D. J.; Haag, R.; Rampi, M. A.;

Frisbie, C. D. *J. Phys. Chem. B* **2002**, *106*, 2813-2816. (e) J. C. Love, L. A. Estroff, J. K. Kriebel, R. G. Nuzzo, G. M. Whitesides, *Chem. Rev*. **2005,** *105*, 1103-1169.

21. M. De Napoli, S. Nardis, R. Paolesse, M. G. H. Vicente, R. Lauceri, R. Purrello, *J. Am. Chem. Soc.* **2004**, *126*, 5934-5935.
22. (a) Ekgasit, S.; Yu, F.; Knoll, W. *Langmuir* **2005**, *21*, 4077-4082. (b) H. Imahori, H. Norieda, Y. Nishimura, I. Yamazaki, K. Higuchi, N. Kato, T. Motohiro, H. Yamada, K. Tamaki, M. Arimura, Y. Sakata, *J. Phys. Chem. B* **2000**, *104,* 1253-1256.
23. H. Imahori, H. Norieda, Y. Nishimura, I. Yamazaki, K. Higuchi, N. Kato, T. Motohiro, H. Yamada, K. Tamaki, M. Arimura, Y. Sakata, *J. Phys. Chem. B* **2000**, *104,* 1253-1256

Chapter 4

Solid-State Photovoltaic Devices

4.1. Introduction

In our previous study, photovoltaic devices built using SAM modified electrodes exhibited improved properties, attributed to more efficient charge separation and charge transport process. The photocurrent value of the most performant devices is proportional to the diffusion rate of methylene viologen in the electrochemical cell, indicating that conventional electrochemical cells research has a appear limit in which the photocurrent cannot be higher than the diffusion rate of the electron carrier in solution. In order to go beyond this limitation, as well as for practical reason of device sturdiness and reliability, the fabrication of solid-state devices based on supramolecular material is an appealing alternative.

The basic working principle of solid-state photovoltaic devices can be summarized as follows: (1) absorption of a photon by the material leading to the formation of a photoexcited charge transfer state, (exciton formation). (2) Exciton diffusion to a region where dissociation occurs (charge separation). (3) The separated charges migrate to the electrode where they are collected by the difference in the work function of the two electrodes.[1]

As the exciton binding energy in organic semiconductors is relatively large (0.1–1eV) compared to silicon,[2] the built-in electric fields (on the order of 10^6–10^7 V/m) are usually not high enough to dissociate the excitons directly. Therefore, a process has to be introduced assists the separation of the bound electron-hole pairs.[1a]

Two basic device architectures have proven their effectiveness in separating the bound electron-hole pairs: bilayer heterojunction and bulk heterojunction. The main differences of these two structures are the exciton dissociation process that occurs at different locations in the material layer and the charge transporting pathway. In a bilayer device, an electron donor and an electron acceptor material are layered with a planar interface, where the excitons are dissociated (Figure 4.1, left).[3] The charges are extracted by the difference of energy level between the HOMO of donor and the LUMO of acceptor. One advantage in bilayer devices is the monomolecular charge transport. After the excitons are dissociated at the materials interface, the electrons travel within the *n*-type acceptor, and the holes travel within the *p*-type donor material. Hence, holes and electrons are effectively separated from each other, and thus charge recombination is greatly reduced. A typical bilayer device using copper phthalocyanine and [60]fullerene was reported with a 3.6 % power conversion efficiency.[4] The main drawback of bilayer device is the finite surface area of interface which is not enough for complete light absorption and exciton dissociation, thus limiting the photocurrent and overall efficiency of the solar cell.

In the bulk heterojunction type device, the donor and acceptor components are mixed, resulting in a three-dimensional dispersion which greatly increases the surface area of donor-acceptor interface which promotes charge separation (Figure 4.1, right). However, the charge transporting process becomes more complicated as both holes and electrons have to travel through a tortuous pathway in a massive material layer. Even so, the most efficient devices are constructed based on fullerene derivative/polymer blended materials.[5]

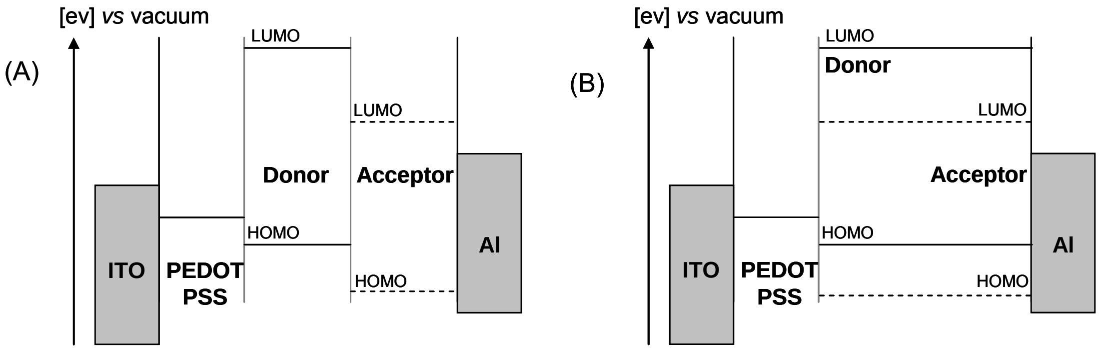

Figure 4.1. Schematic representation of (A) a bilayer heterojunction devices, (B) a bulk heterojunction device in energetic diagrams. ITO and Al as anode and cathode electrodes, respectively.[1b]

Recent researches focused on "nanomorphology" control demonstrate the influence of phase separation in bulk materials, and much better performance can be achieved by implementing a post-fabrication treatment.[6] The efficiency enhancement originates from microcrystalline C_{60} domains formed during curing at elevated tempertures.[7] This is quite relevant as it points out that even with 100 % exciton generation and charge separation at the donor-acceptor heterojunction, charge transport and collection become the efficiency-limiting processes in overall conversion efficiency.

Small molecules constituting an intramolecular electron donor-acceptor system have been fabricated on solid state device in ITO/PEDOT/molecules/metal sandwich-type structure.[8] The deposition of photoactive molecules by spin-coating process forms a homogenuous layer but lacks the intermolecular alignment and it is widely felt that this is part responsible for a lower I_{SC} value. For example, photovoltaic devices built using the dumbbell-shaped fullerene-oligothiophene-fullerene **16T-2C$_{60}$** (Figure 4.2, left) show a remarkable V_{OC} (580 mV) but a low (376 nA cm^{-2}) photocurrent.[9] Also, a V_{OC} of 650 mV and I_{SC} of 235 μA cm^{-2} were measured in a covalent-bonded fullerene-oligo(2,5-dialkyloxy-1,4-phenylene vinylene)s system (Figure 4.2, right).[10]

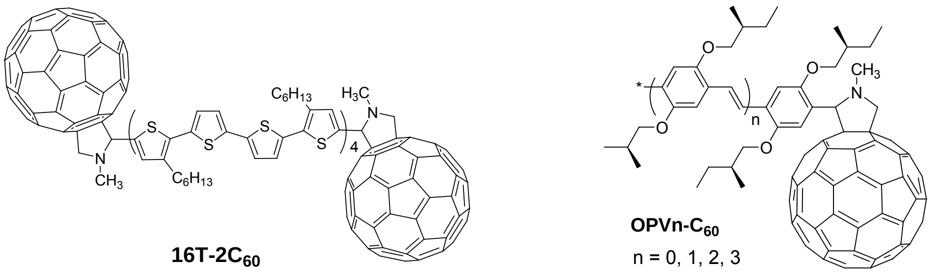

Figure 4.2. Structural representation of Dumbbells-shape fullerene-oligothiophene molecule (left),[9] and fullerene-oligo(2,5-dialkyloxy-1,4-phenylene vinylene)s (right).[10]

Some of the hydrogen-bonded supramolecular architectures which have been applied to photovoltaic devices in an electro-donor/acceptor type structure are shown in Figure 4.3.[11] Of these, only few examples have been reported where they are applied to construction of solid-state devices.[12] Meijer and co-workers[13] reported a hydrogen-bonded oligo(*p*-phenylene vinylene)s folded polymer blended with PCBM solid-state device, where the photoactive material layer was spun from a toluene solution (Figure 4.4). The random-coil OPVs assembles into a quadruple hydrogen-bonded system,[14] which then folds on to itself in non-polar solutions. Under white-light illumination, a short circuit current of 0.64 mA/cm^2 and an open circuit voltage of 790 mV was measured in these devices. Although lower than MDMO-PPV/PCBM blended devices, this performance is most promising.

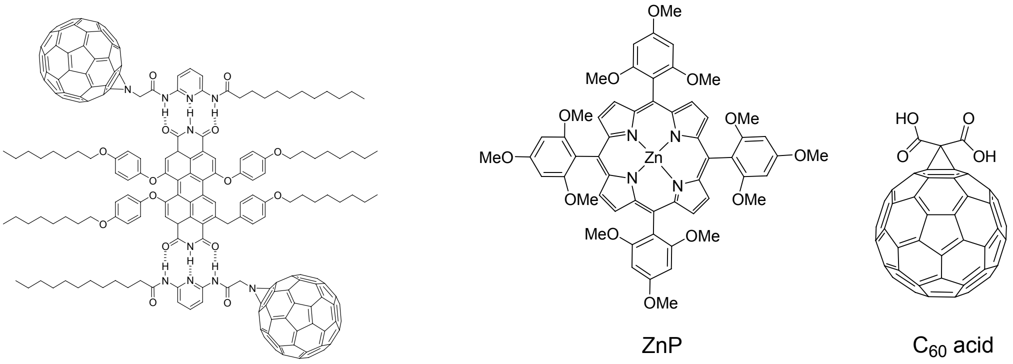

Figure 4.3. Structural representation of hydrogen-bonded supramolecular assembly in photoelectrochemical studies: perylene-fullerene derivatives assembly (left),[11a] and porphyrin-fullerene assembly (right).[11c]

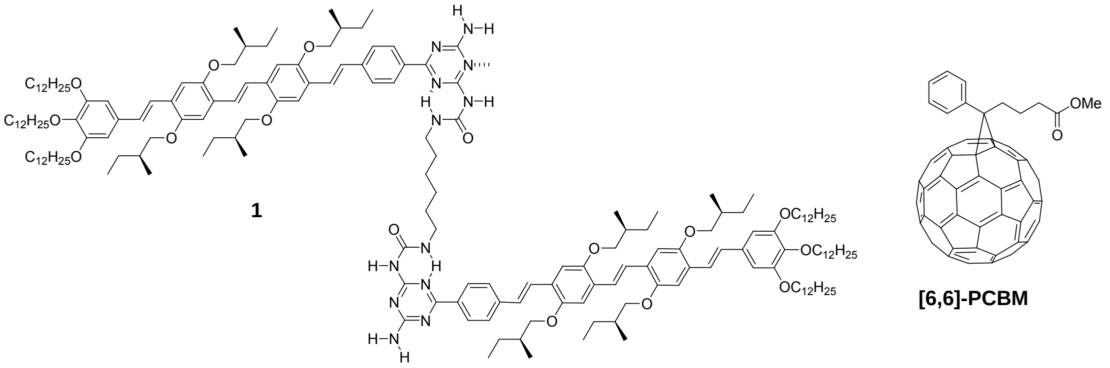

1

[6,6]-PCBM

Figure 4.4. Construction of solid state devices by folding hydrogen-bonded oligo(p-phenylene vinylene)s polymer blended with PCBM.[13]

Another example based on the direct assembly of oligo(*p*-phenylene vinylene)s (donor) and bay-substituted perylene bisimides (acceptor) using hydrogen-binding was reported by Wuerthner *et al.* in 2004 (Figure 4.5).[15] This donor-acceptor-donor dye solar cell exhibited a photovoltaic behavior with a V_{OC} of 740 mV and a I_{SC} of 2.6 μA cm^{-2}. The poor behavior in I_{SC} is attributed by the authors to the co-aggregated dyes which tend to organize themselves laterally on the surface, which is not favorable for charge transport to the metal electrodes.

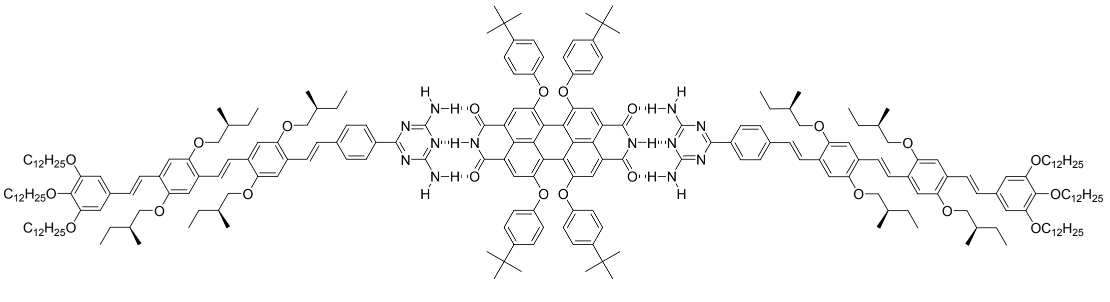

1b-2-1b

Figure 4.5. Structural representation of hydrogen-bonded donor-acceptor-donor dye.[15]

4.2. Solid-state photovoltaic devices fabrication

4.2.1. Devices built on SAM-modified ITO and gold substrates

Incorporating self-assembled monolayers possessing hydrogen–bonding recognition moieties may indeed promote the formation of three-dimensional supramolecular architectures of higher complexity. The results discussed in Chapter 3 led us to investigate the utility of SAMs on gold or on ITO/glass substrates. Typically, forming SAM molecules from strong covalent binds on ITO surfaces through siloxane or carboxylic acid functional groups, whereas the assembly of SAMs on gold surfaces requires the presence of thiol endgroups.[16] Scheme 4.1 shows the synthesis of two different molecules that were used in the SAM formation studies. Both target molecules were synthesized by reacting 4-hydroxybenzaldehyde with either ethyl 5-bromovalerate or 4-bromo-1-pentene to give molecules **48** and **51**, respectively. Ester **48** was hydrolyzed to carboxylic acid **49**,[17] and then was substituted with barbituric acid moiety via Knoevenagel condensation reaction at the carbaldehyde functionality in 70% yield to give **40** (three steps). The siloxane **54** was similarly obtained in three steps. After Knoevenagel condensation reaction, the benzylic position C=C bond of molecule **52** was reduced by $NaBH_4$, and then the terminal C=C bond was converted to the desired product **54** *via* a hydrosilylation reaction using H_2PtCl_6 as catalyst.[18]

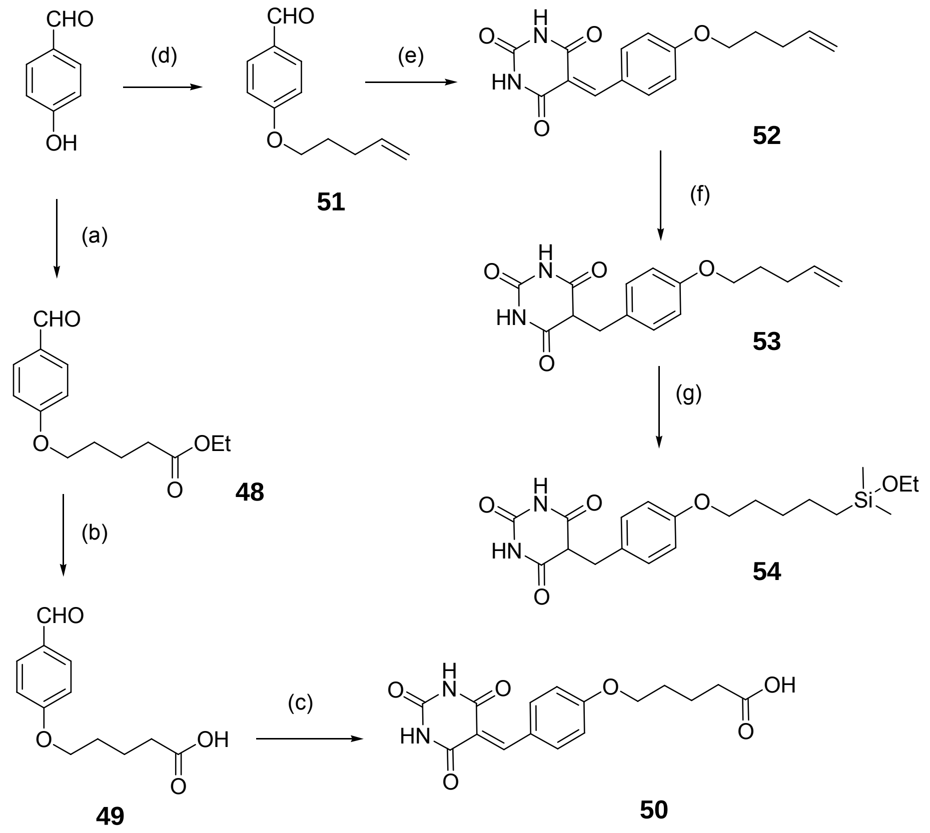

Scheme 4.1. Reagents and conditions: (a) ethyl 5-bromovalerate, K_2CO_3, DMF, 105 ℃, overnight; (b) LiOH, H_2O/THF, room temperature, 2 hr; (c) barbituric acid, H_2O/EtOH, reflux, 2 hr, 70% (three steps). (d) 4-penten-1-ol, SOCl2, reflux, 2 hr; then K_2CO_3, DMF, 80 ℃, 2 days, 88%; (e) barbituric acid, H_2O/EtOH, reflux, 3 hr, 78%; (f) $NaBH_4$, 2-propanol, 0 ℃, 5 hr, 86%; (g) H_2PtCl_6, $Me_2SiH(OEt)$, THF, room temperature, then reflux, 1 hr, 46%.

4.2.1.1. Electrochemical study of SAMs on ITO, Au/ITO, and Au/glass subtrates

The properties of the SAM were interpreted using cyclic voltammetry (Figure 4.6). Thus, SAMs of **54** blocked the redox behavior of the ITO electrode similarly to thioacetate molecule **39** deposited on gold electrode surface. A much poorer blocking effect was observed with carboxylic acid **50** suggesting a less close-packed SAM layer formation. Due to the difficulties in obtained reproducible close-packed SAMs directly on ITO, this approach was abandoned.

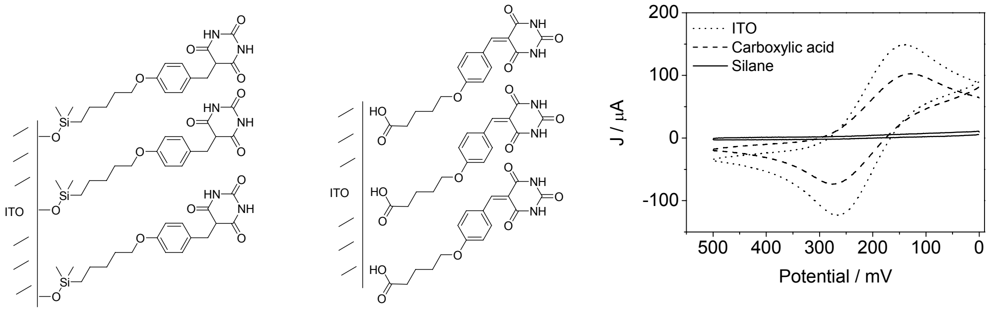

Figure 4.6. (Left) Schematic representation of SAMs for molecules **50** and **54**. (Right) Cyclic voltammograms of the reduction of aqueous $K_3[Fe(CN)_6]$ using bare ITO (dot line) and ITO electrodes whose surfaces were modified with **50** (dash line), or **54** (solid line).

In addition to forming SAMs directly onto ITO, deposition of a very thin gold layer on glass or on ITO substrates also allows us to assemble thioacetate **39**. To this end, three different thickness of gold layers (16, 24, or 46 nm) were deposited onto glass substrates or onto ITO surface. The transparency of the gold layer was examined using UV-Visible spectroscopy, and their results are shown in Figure 4.7. As expected, the thicker gold layer gave lowest transmittance (down to 20% on glass, 10% on ITO). The formation of SAM layer with molecule **39** was identical to that described in Chapter 2.3. Figure 4.8 shows the results of SAMs in cyclic voltammograms. The behaviors of all six electrodes are in good agreement with previous studies on normal gold layer slides where the SAM layer pack uniformly.

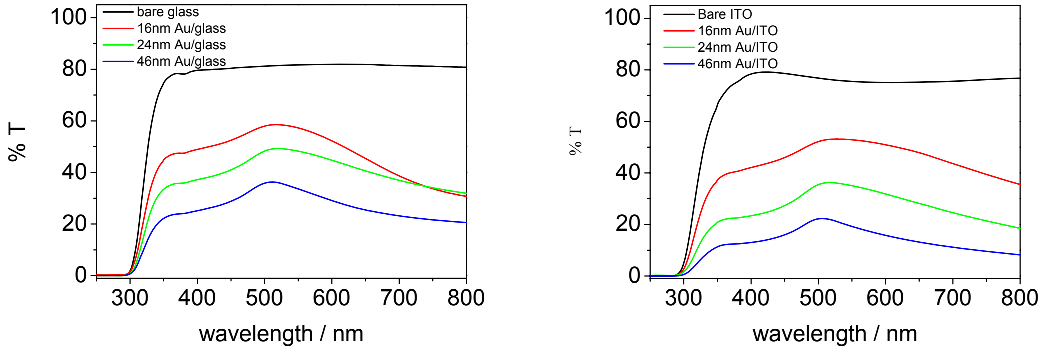

Figure 4.7 UV spectras of gold layers deposited on glass (left), or on ITO substrates (right).

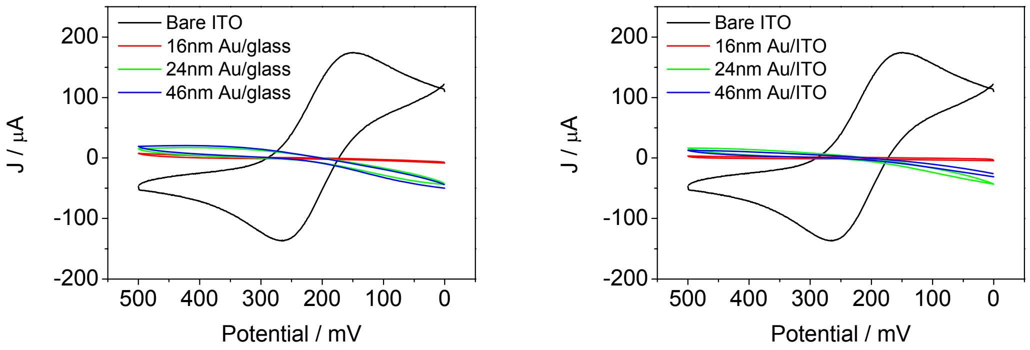

Figure 4.8. Cyclic voltammograms of the reduction of aqueous $K_3[Fe(CN)_6]$ using Au/glass electrodes (left) and Au/ITO electrodes (right) modified with SAMs of molecule **39**.

A typical procedure for the preparation of solid-state devices on SAM modified electrodes was as follows: A DMSO solution of fullerene **1** and oligothiophene **7** (2×10^{-4} M, in 2 : 1 ratio) was drop-cast onto the SAM modified electrode, followed by slow evaporation of the solvent under vacuum, resulting in the formation of a thin film. The fabrication of the anode electrode was performed in an high vacuum (HV) chamber to thermally deposit a 1.2 nm of LiF buffer layer followed by a 100 nm thick Al layer. The photocurrent characterization was carried out under irradiation with a 470 nm LED light source. The first results were disappointing as all devices showed a similar short-circuit behavior. It is know that even the close packing self-assembled monolayers cannot prevent the penetration of metal vapor to the anodic electrode.[19] The reason behind this short-circuit behavior was quite clear after the surface profile was examined. The supramolecular assembled materials obviously did not cover the entire surface of the electrode. Instead, the molecules exhibited rod-like aggregation, thus leaving pinholes that allow the Al layer to touch the anode.

4.2.2. Photoactive materials blended with poly(9-vinylcarbazole) matrix

Another approach was followed to deposit a thicker and more homogeneous photoactive layer by dispensing the self-assembled domains in a conductive polymer. Inside each microdomain, hydrogen-bonded self-assembly spatially aligns the electron-donor and acceptor, possibly forming a ribbon-type structure locally (see, Figure 4.9).

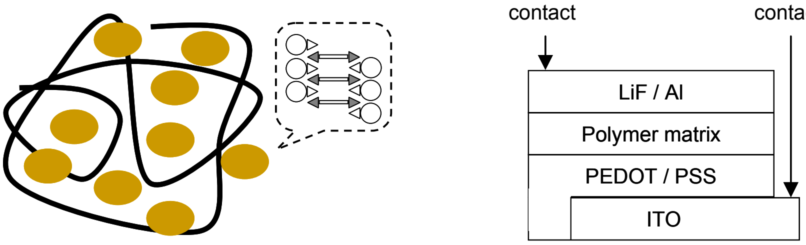

Figure 4.9. Schematic representation of supramolecular assembly microdomains blended in polymer (left), and device structure (right).

A hole transporting polymer: poly(9-vinylcarbazole), PVK, was chosen as a supporting matrix, in light of its availability and its solubility in different organic solvent (Table 4.1). PVK in chloroform and in *ortho*-dichlorobenzene solution were chosen to prepare various mixture of photoactive materials (see Table 4.2) in order to determine the best composition.

solvent	$CHCl_3$	THF	Xylene	Toluene	*o*-DCB
PVK Solubility	60 mg/mL	60 mg/mL	non soluble	40 mg/mL	40 mg/mL

Table 4.1. The solubility of PVK polymer in different organic solvents.

Device	**A**	**B**	**C**
DMSO/$CHCl_3$ (V/V)	5 %	10 %	20 %
Device	**D**	**E**	**F**
DMSO/*o*-DCB (V/V)	5 %	10 %	20 %

Table 4.2. Various concentrations of photoactive materials in chloroform and *ortho*-dichlorobenzene. PVK solution concentration: 60 mg/mL in chloroform, and 40 mg/mL in *o*-DCB. Fullerene **1** and oligothiophene **7** (2:1 ratio) solution concentration: 5 mg/mL in DMSO.

The fabrication of devices was conducted as follows: partially etched ITO slides were cleaned and then a layer of PEDOT/PSS was deposited by spin-coating. The layer of photoactive material blended in PVK was then deposited by spin-coating on top of the PEDOT/PSS buffer layer. A layer of LiF (1.2 nm), followed by an Al layer (116 nm), were then deposited under HV. The surface profiles of the devices are shown in Figure 4.10, and it is clear that all the devices possessed a thick and continuous layer. Devices prepared from chloroform (devices A, B, and C) gave a relatively smooth surface compared devices D and F, prepared from *o*-DCB solution, which showed a very rough surface due to aggregation (up to micrometer scale in device F, prepared from 20% DMSO/*o*-DCB solution).

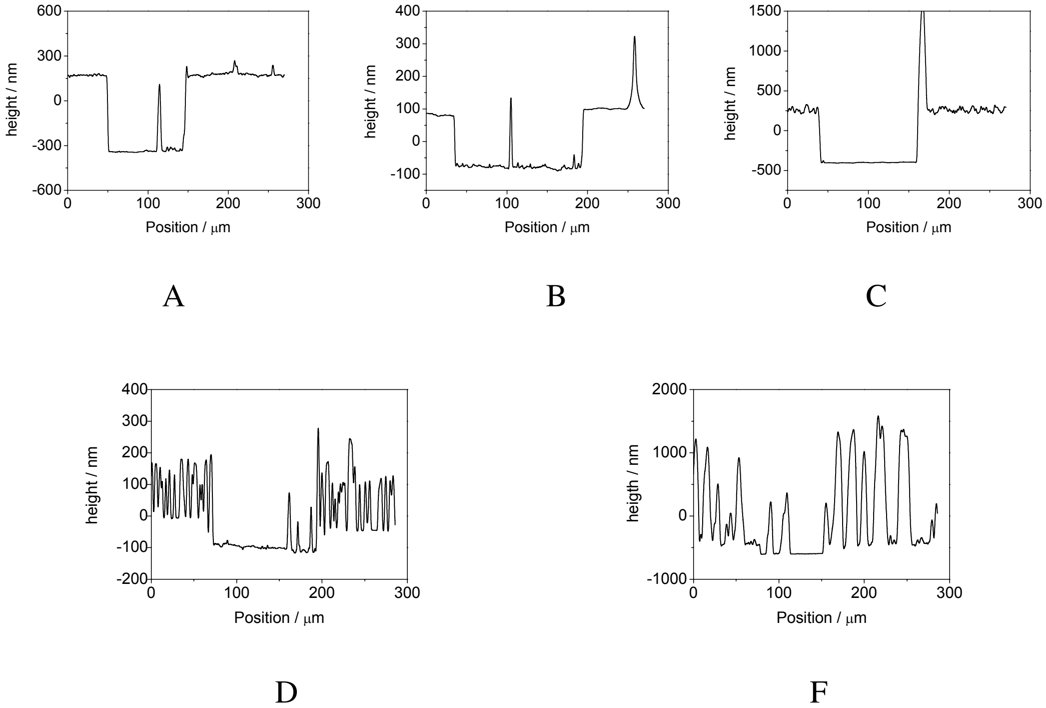

Figure 4.10. Surface profiles of devices A, B, C, D and F.

All the devices tested gave similar behavior in *I*/*V* curves characterization (Figure 4.11). For example, device D showed a typical photodiode behavior at a bias voltage between-3 V and +3 V. The photocurrent is generated under irradiation, and no open-circuit voltage (V_{OC}) shift is observed. This result can be attributed the fact that PVK is a good hole transporting material which favors the transport of positive charges (holes) through the blend polymer to the cathode. However, this material has slow electron mobility, which slows the transport of electrons generated from the microdomains to the anode. Because open circuit voltage of a polymer blended donor-acceptor bulk-heterojunction is related directly to the energy difference between the HOMO level of the donor and the LUMO level of the acceptor components,[20] it is possible that in these systems the open-circuit voltage of the device under irradiation is not high enough to drive the charge through the PVK layer. Hence, the charges are extracted to the opposite electrodes only at high bias voltage.

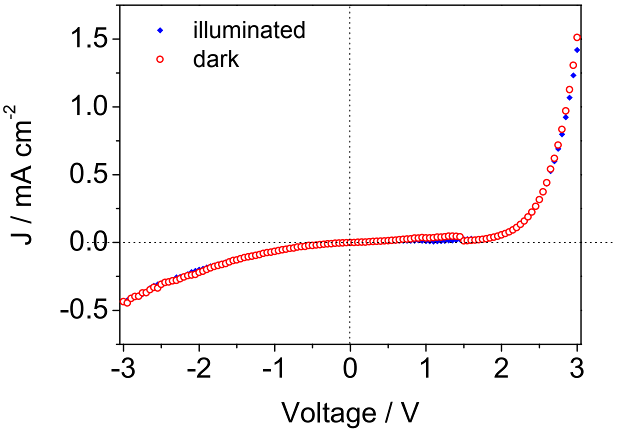

Figure 4.11. *I*/V curve of device D in dark, (open squares) and under illuminated (solid squares).

4.3. Organic multilayered devices

The results obtained in the previous studies are promising in that a functional device could be obtained. A logical sequence is to place the hole-conducting polymer only on the cathode. This approach has the added benefit of protecting the PEDOT/PSS layer against dissolution during the deposition of the active layer. Indeed, it was obvious that the PEDOT/PSS buffer does not resist dissolution by to the DMSO solution during the drop-casting and solvent evaporation processes. In collaboration with Prof. N. S. Sariciftci and Prof. G. Dennler (LIOS, Linz, Austria), we explored further possibilities in device fabrication introducing the use of a polymer material. In order to keep the basic organic solar cell structure as a bulk heterojunction model, we attempted to incorporate a thin semi-conductive polymer layer to seclude the PEDOT layer from the DMSO solution during drop-casting. The structure of devices is shown in Figure 4.12, two hydrophobic semi-conductive polymers: poly(3-hexylthiophene (P3HT), and poly([2-methyloxy-5(3,7-dimethyloctyloxy)]-1,4-phenylene vinylene)s (MDMO-PPV) were chosen as the buffer layer.

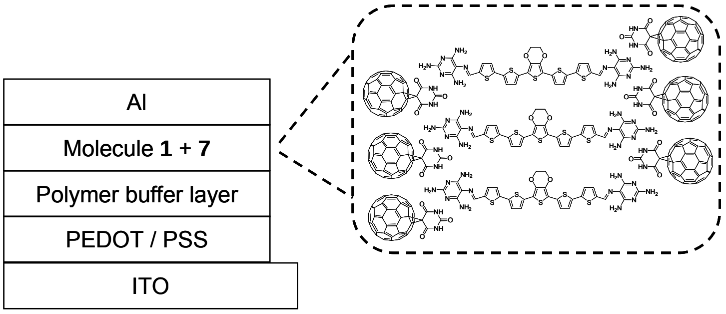

Figure 4.12. Schematic representation of the device structure with polymer buffer layer.

Polymer solution (mg/mL in chlorobenzene)	MDMO-PPV 0.07 %	MDMO-PPV 0.7 %	P3HT 0.1 %	P3HT 1.0 %
Device	**A**	**B**	**C**	**D**

Table.4.3.

The devices Al/(molecule **1** + **7**)/polymer/PEDOT/ITO were fabricated as follows: Partially etched ITO slides were cleaned and then the PEDOT/PSS layer was deposited by spin-coating. A second layer of semi-conductive polymer (MDMO-PPV or P3HT) at two different concentrations (see Table 4.3), was deposited by spin-coating on top of the PEDOT/PSS layer. After drying, a DMSO solution of fullerene **1** and oligothiophene **7** (2×10^{-4} M, in 2 : 1 ratio) was drop-cast onto the devices. Slow evaporation of the solvent resulted in the formation of a thin film. The deposition of the anode Al layer (100 nm) was accomplished as usual. The characterization of the devices was carried out in the dark and under illumination using a solar simulator AM 1.5 (power intensity: 100 mW/cm^2) directly in the glove box. The *I*/*V* curves of devices are shown in Figure 4.13 (in semi logarithmic plot, left; and in linear plot, right). All *I*/*V* curves are completely reversible, and devices A and D showed a diode behavior with a rectification ratio between -2 and +2 V of approximately 10-100.

Device	**A**	**B**	**C**	**D**
Polymer solution (mg/mL in chlorobenzene)	MDMO-PPV 0.07 %	MDMO-PPV 0.7 %	P3HT 0.1 %	P3HT 1.0 %
Polymer layer Thickness	10 nm	65 nm	5 nm	35 nm
I_{SC} / μA cm^{-2}	184	82	55	406
V_{OC} / mV	400	350	150	300
Fill factor / FF	0.36	0.26	0.23	0.38
Fullerene-oligothiophene layer thickness	70 nm	135 nm	165 nm	105 nm

Table 4.4. I_{SC}, V_{OC}, fill factor and layer thickness of device **A**-**D**.

In the case of devices fabricated with MDMO-PPV, device A with a polymer layer deposited from 0.07% solution gave a short-circuit current (I_{SC}) of 184 μA cm^{-2} and an open-circuit voltage (V_{OC}) of 400 mV. Device B, with a thicker polymer layer, showed a lower short-circuit current of 82 μA cm^{-2} and an open-circuit voltage of 350 mV. For the P3HT based devices, a short-circuit current of 55 μA cm^{-2} and an open-circuit voltage of 150 mV were observed for device C. A significantly higher short-circuit current of 406 μA cm^{-2} and an open-circuit voltage of 300 mV were observed for device D (Table 4.4). These results can be reasoned that in the devices, the I_{SC} value is governed by the hole mobility of polymer. The hole mobility in regio-regular P3HT (up to 0.1 cm^2 V^{-1}s^{-1}) is much higher than in MDMO-PPV,[21] and can differ by 3 orders of magnitude. This discrepancy originates from the strong dependence of the hole mobility on the charge carrier density in disordered semi-conducting polymers.[22] Hence, the devices have better hole mobility on thinner MDMO-PPV, and shows a higher short-circuit current compared to the device on thicker MDMO-PPV layer. In contrast, the P3HT devices have better hole mobility and can benefit from the thicker layer, thus showing a higher I_{SC} compared to the device on thinner P3HT layer.

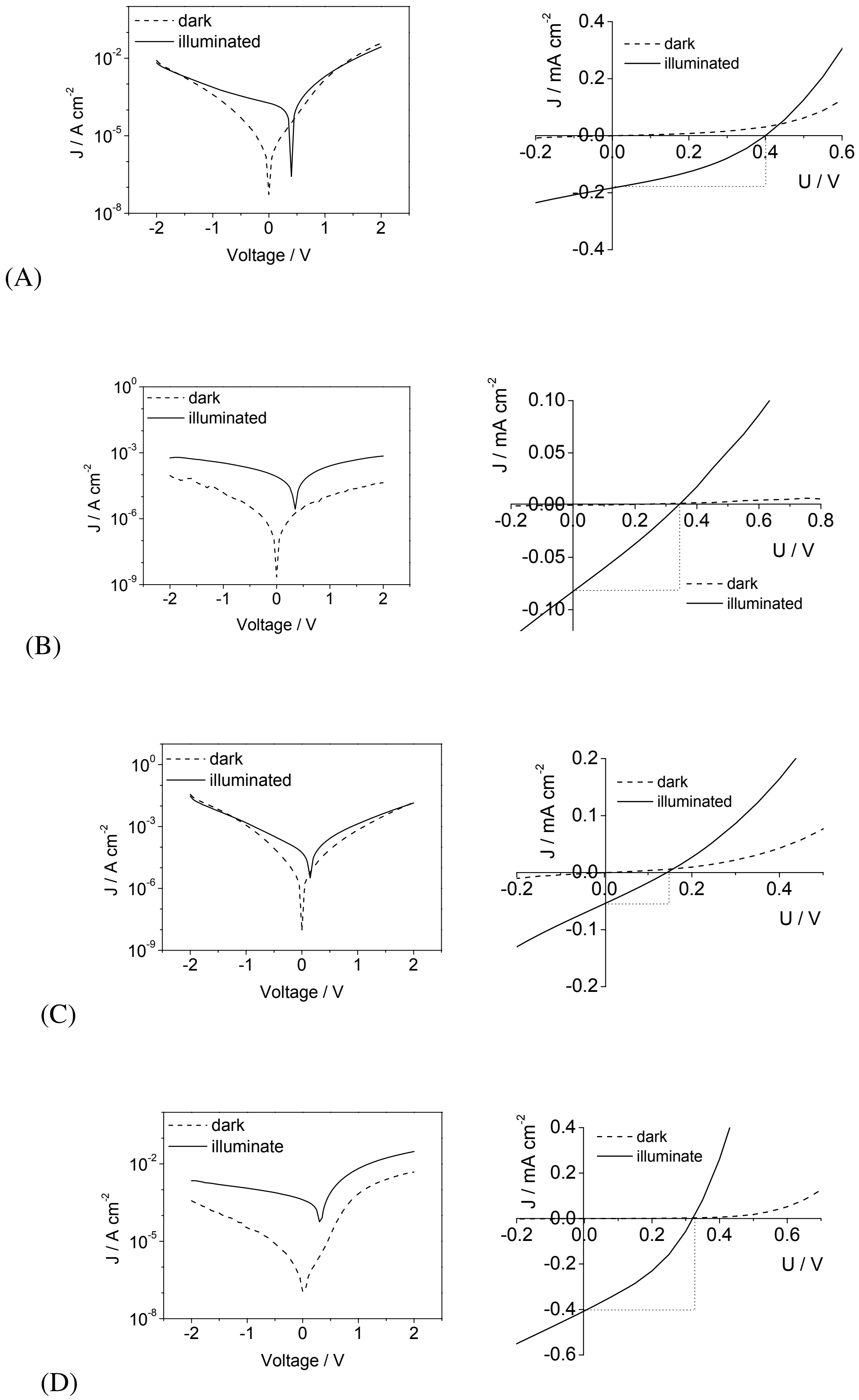

Figure 4.13. I/V curve of device A, B, C, and D; in semi logarithmic plot (left) and in linear plot (right).

The V_{OC} behavior in these multi-layer devices is more complicated to explain. The polymer layer in contact with the supramolecular component can be considered as a bilayer heterojunction structure. Within the active layer, there is another supramolecular fullerene-oligothiophene assembled heterojunction. In order to understand the influence of the polymer on the device properties, four model devices (denoted as A', B', C' and D') without the supramolecular fullerene-oligothiophene materials were prepared and studied (Table 4.5). In Figure 4.14, the *I*/*V* curve of these model devices are presented, and show very little or no V_{OC} shift between dark and illumination cycles. This result is consistant with previous experiences that without the presence of electron-acceptor material, the very thin MDMO-PPV or P3HT single layer devices do not function well.

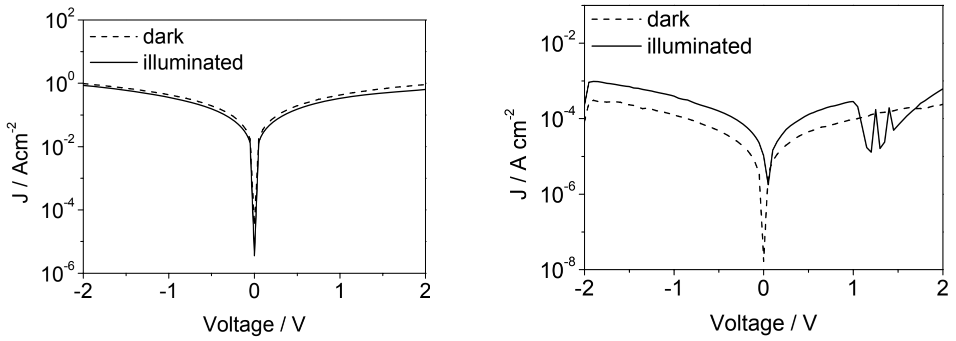

Device A'   Device B'

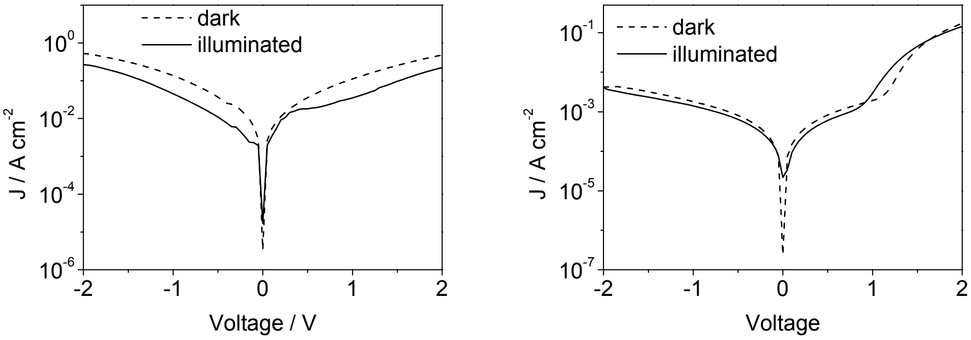

Device C'   Device D'

Figure 4.14. I/V curve of model devices d A', B', C' and D' without the inclusion of compound **1** and **7**.

Polymer solution (mg/mL in chlorobenzene)	MDMO-PPV 0.07 %	MDMO-PPV 0.7 %	P3HT 0.1 %	P3HT 1.0 %
Device	**A'**	**B'**	**C'**	**D'**

Table.4.5. The fabrication of model devices with different polymer buffer layer (structure: Al/polymer/PEDOT/ITO).

The multilayer structure in the above devices leads to a complicated situation in turns of interpreting the *I*/*V* curve behavior. In fact, there are several factors which have to be considered in detail. For example, the very thin polymer layer (in device C, down to 5 nm) is not sure to withstand contact with DMSO. Both MDMO-PPV and P3HT are well-know photoactive materials, and have excellent properties when used in all-organic solid-state devices. Partial dissolution of the polymer film by the DMSO could lead to a small amount of fullerene **1** diffusing into the polymer layer, thus forming another electron-donor/acceptor bulk heterojunction layer, and a new interface between the polymer layer and hydrogen-bonded assembly. Of course, this thin polymer-fullerene bulk heterojunction could provide an efficient charge separation process and thus contribute to the observed I_{SC} and V_{OC} shift. In addition, MDMO-PPV and P3HT have very high absorption coefficients[23] (1.3×10^5 $M^{-1}cm^{-1}$ of MDMO-PPV and 9.0×10^4 $M^{-1}cm^{-1}$ of P3HT at $\lambda = 450$ nm) and may absorb up to 40 % of incident light (based on a ~35 nm thick of polymer layer). The absorption spectra of these two polymers overlap with that of oligothiophene **7** in the region at 400-600 nm, thus it is difficult to exclude their contribution based on incident photon to converted electron efficiency (IPCE) calculation, see Figure 4.15.

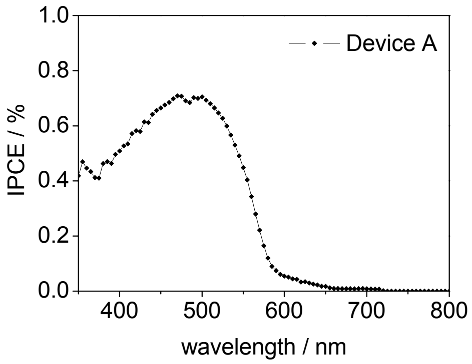

Figure 4.15. Spectrally resolved photocurrent, converted to incident photon to converted electron efficiency (IPCE) of device A.

The morphology of the fullerene-oligothiophene assembled layer remains an important issue. In Figure 4.16, the AFM images of devices A (left) and B (right) show the irregular, gorge-like domains that indicate serious aggregation of the materials on the surface. This result was confirmed by examining the surface profiles of all devices shown in Figure 4.17. Subtracting the thickness of polymer/PEDOT layer, the thickness of the continuous fullerene-oligothiophene layer was obtained (see Table 4.4). Compared to the relatively thin but continuous layer, the major part of the photoactive material **1** and **7** is aggregated. It is not clear weather this saw-toothed structure contributes to the performance of the device.

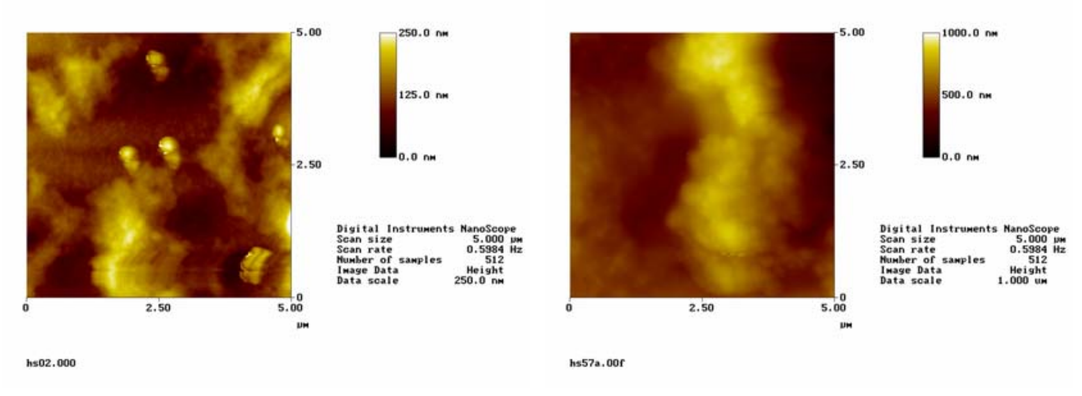

Device A Device B

Figure 4.16. AFM images of layer of **1** and **7** surface in device A (left) and in device B (right); scan area: 5 µm x 5 µm.

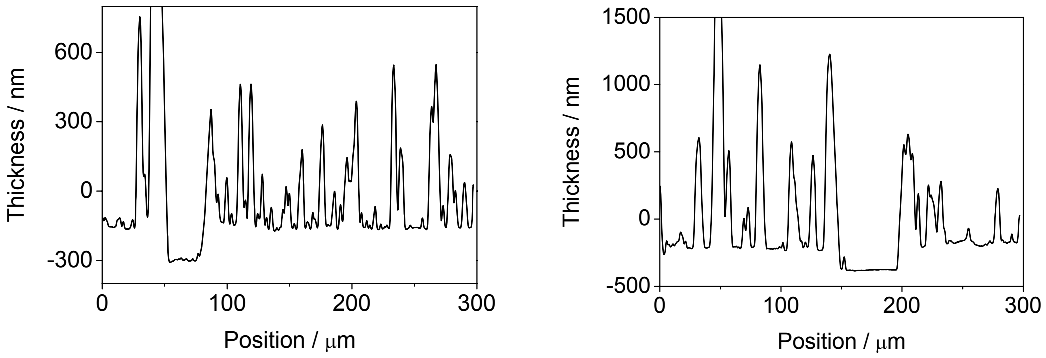

Device A

Device B

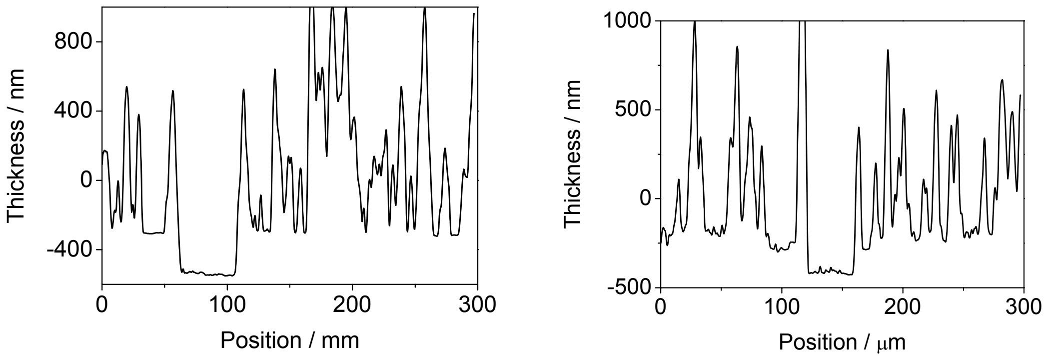

Device C

Device D

Figure 4.17. Surface profiles of device A, B, C, and D on the active layer surface.

The best way to clarify the contribution of the MDMO-PPV and P3HT layer in the I_{SC} and V_{OC} shift is to keep the same multilayer structure but without adding the oligothiophene chromophor **7** in the devices (see Figure 4.18). An Alkyl chain-bridged bispyrimidine molecule **56** was chosen and synthesized (see Scheme 4.2), *via* the intermediate bis-aldehyde **55**, which was obtained by reacting 1,5-dibromopentane with an excess of 4-hydroxybenzaldehyde (60 % yield) and then converted to bispyrimidine **56** by double imine bond formation (96 % yield).

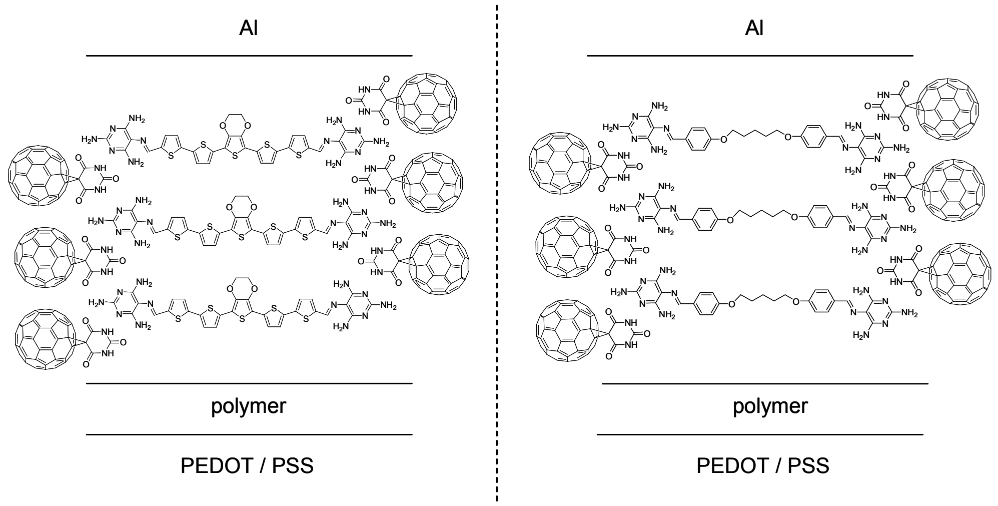

Device E Device F

Figure 4.18. Schematic representation of device structure: with fullerene **1** and oligothiophene **7** (left), and with fullerene **1** and alkyl chain-bridged bis-pyrimidine **56** as a control experiment (right).

In the hydrogen-bonded self-assembled structure replacing oligothiophene **7** by bispyrimidine **56** is expected to keep a similar supramolecular architecture, but should not absorb light. Devices E and F were prepared using same fabrication procedure as previously described. The structure of the devices and the *I/V* curve characterization are shown in Table 4.6 and in Figure 4.19, respectively. Device E has a much higher V_{OC} shift (550 mV) than Device F does (160 mV), and indicating that the contribution in V_{OC} in this multilayer type structure originates from the fullerene-oligothiophene **7** heterojunction. Comparison with the results in model device B', which was only fabricated with polymer layer (see Table 4.5 and Figure 4.14), the slight V_{OC} shift in Device F is possibly resulting from a small amount of fullerene which diffused into the MDMO-PPV as we assumed before. To our surprise, the I_{SC} values obtained are not reproducible possible due to differences in the device preparation. The I_{SC} of control experiment E is one sixth lower than in device B , and is marginally different from device F. Preparation of devices A~D and model device A'~D' were done at the LIOS laboratory (Linz, Austria), whereas devices E and F were prepared at the PIOM laboratory (Bordeaux, France). Some experimental parameters and conditions differ, such as different PEDOT/PSS solutions, variation in the thickness of PEDOT/PSS layer.

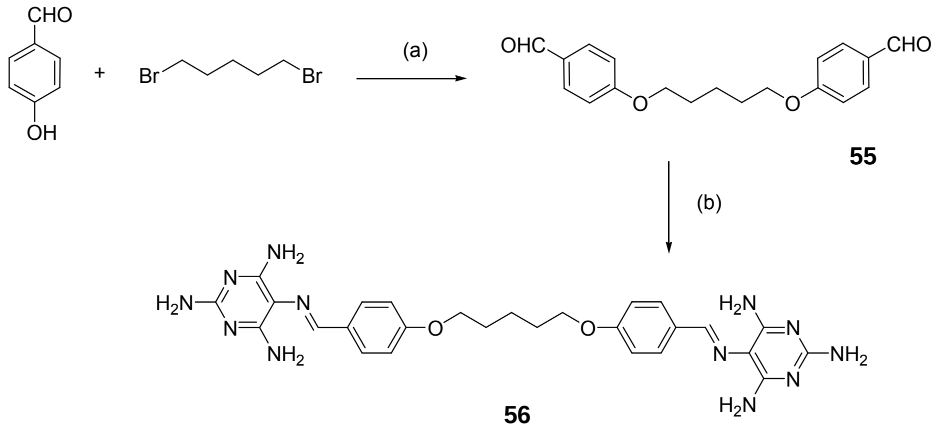

Scheme 4.2. Reagents and conditions: (a) K_2CO_3, DMF, 100 ℃, 2 days (60%); (b) 2,4,5,6-tetraaminopyrimidine sulfate, $(i\text{-Pr})_2NEt$, K_2CO_3, *i*-PrOH/THF, reflux, overnight, (96%).

Device	**E**	**F**
Polymer (from 0.7 % mg/mL chlorobenzene solution)	MDMO-PPV	MDMO-PPV
Assembled materials	**1** and **7**	**1** and **56**
I_{SC} / μA cm^{-2}	13.6	10.8
V_{OC} / mV	550	160

Table. 4.6. The fabrication of devices E and F with MDMO-PPV polymer layer (device structure: Al/polymer/assembled materials/PEDOT/ITO).

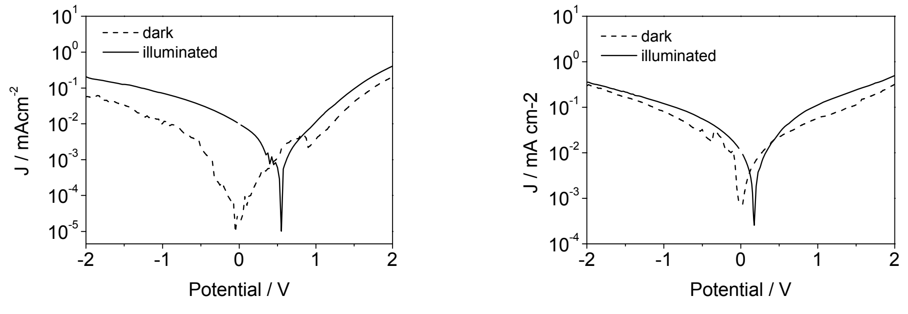

Device E

Device F

Figure 4.19. I/V curve of device E (left) and F (right) in semi logarithmic plot.

4.4. Conclusion

In conclusion, we have constructed all-organic solid-state devices based on the incorporation of hydrogen-bonded supramolecular assemblies of **1** and **7**. Several methodologies and fabrication processes have been expected, such as preparing SAMs on ITO or on thin Au layers, spin-coating photoactive materials blended with PVK polymer, and also with semi-conductive polymer (MDMO-PPV and P3HT) as a protective buffer layer. Prototype devices were built using a polymer buffer layer to seclude PEDOT/PSS from a DMSO solution of photoactive materials. The preliminary results showed a 0.4 mA/cm^2 photocurrent in I_{SC} and a moderate V_{OC} value (300 mV) using a 35 nm P3HT buffer layer. The solubility of oligothiophene-fullerene in non-polar organic solvent restricts the flexibility of material layer fabrication. Directly spin-coating materials led to a very thin layer on surface, and drop-casting method gave poor homogeneity of the active layer that caused large uncertainties.

To overcome these difficulties, several improvements can be adapted. By modifying the oligothiophene or other chromophores with branched alkyl chain, one can dramatically improve the solubility (up to 10~100 mg/mL) in organic solvents such as chloroform and chlorobenzene. In this way, it will be possible to fabricate the devices by spin-coating, or by drop-casting directly on top of the PEDOT/PSS layer, omitting the MDMO-PPV or P3HT buffer layer. Combined with thermal-annealing processes, this may be able to reduce the propensity towards aggregation of the material, leading to better morphologies. In the photoelectrochemical studies, the hydrogen-bonded material **1** and **7** demonstrated its potential to successfully achieve charge separation and charge transport at the molecular-level. It is therefore expected it will exhibit this in solid-state solar cells, provided the current device fabrication in used.

4.5. References

1. (a) H. Hoppe, N. S. Sariciftci, *J. Mater. Res.*, **2004**, *19*, 1924-1945.; (b) G. Dennler, N.S. Sariciftci, *Proceedings of the IEEE*, **2005**, *93*, 1429-1439. (c) C. J. Brabec, N. S. Sariciftci, J. C. Hummelen *Adv. Funct. Mater.* **2001**, *11*, 15-26.; (d) C. J. Brabec，A. Cravino，D. Meissner，N. S. Sariciftci，T. Fromherz，M. T. Rispens，L. Sanchez，J. C. Hummelen, *Adv. Funct. Mater.* **2001**, *11*, 374-380.
2. (a) *Primary Photoexcitations in Conjugated Polymers: Molecular Exciton versus Semiconductor Band Model*; edited by N.S. Sariciftci, **1997**, World Scientific, Singapore. (b) B.A. Gregg and M.C. Hanna, *J. Appl. Phys.* **2003**, *93*, 3605-3614.
3. L. A. A. Pettersson, L. S. Roman, O. Ingana¨s, *J. Appl. Phys.* **1999**, *86*, 487-496.
4. (a) P. Peumanns, S. R. Forrest, *Appl. Phys. Lett.* **2001**, *79*, 126-128.; (b) R. Koeppe, N.S. Sariciftci, P. Troshin, R. Lyubovskaya, *Applied Physics Letters*, **2005**, *87(1)*, 244102.; (c) Al-Ibrahim, M.; Ambacher, O.; Sensfuss, S.; Gobsch, G. *Appl. Phys. Lett.* **2005**, *86*, 201120/1-201120/3.
5. (a) W. Ma, C. Yang, X. Gong, K. Lee, A. J. Heeger, *Adv. Funct. Mater.,* **2005**, *15*, 1617-1622. (b) G. Li, V. Shrotriya, J. Huang, Y. Tao, T. Moriarty, K. Emery, Y. Yang, *Nat. Mater.*, **2005**, *4*, 864.
6. F. Padinger, R. S. Rittberger, N. S. Sariciftci, *Adv. Funct. Mater.* **2003**, *13*, 1-4.
7. (a) H. Hoppe N. S. Sariciftci, *J. Mater. Chem.*, **2006**, *16*, 45-61. (b) H. Hoppe, T. Glatzel, M. Niggemann, W. Schwinger, F. Schaeffler, A. Hinsch, M. Ch. Lux-Steiner, N. S. Sariciftci, *Thin Solid Films* **2006**, *511-512*, 587-592.
8. C. M. Atienza, G. Fernàndez, L. Sànchez, N. Martin, I. Sà Dantas, M. M. Wienk, R. A. J. Janssen, G. M. A. Rahmanc, D. M. Guldi, *Chem. Commun.,* **2006**, 514-516.
9. N. Negishi, K. Takimiya, T. Otsubo, Y. Harima, Y. Aso, *Chemistry Letters* **2004**, *33*, 654-655.
10. E. Peeters, P. A. van Hal, J. Knol, C. J. Brabec, N. S. Sariciftci, J. C. Hummelen, R. A. J. Janssen, *J. Phys. Chem. B* **2000,** *104,* 10174-10190.
11. (a) Y. Liu, S. Xiao, H. Li, Y. Li, H. Liu, F. Lu, J. Zhuang, and D. Zhu, *J. Phys. Chem. B* **2004,** *108,* 6256-6260. (b) H. Imahori, J.-C. Liu, K. Hosomizu, T. Sato, Y. Mori, H. Hotta, Y. Matano, Y. Araki, O. Ito, N. Maruyamae, S. Fujita; *Chem. Commun.*, **2004**, 2066-2067. (c) H. Imahori, J.-C. Liu, H. Hotta, A. Kira, T. Umeyama, Y. Matano, G. Li, S. Ye, M. Isosomppi, N. V. Tkachenko, H. Lemmetyinen *J. Phys. Chem. B* **2005**, *109,* 18465-18474.
12. N. Martin, *Chem. Commun.*, **2006**, 2093-2104.

13. P. Jonkheijm, J. K. J. van Duren, M, Kemerink, R, A. J. Janssen, A. P. H. J. Schenning, E. W. Meijer, *Macromolecules* **2006**, *39*, 784-788.
14. R. P. Sijbesma, E. W. Meijer, *Chem. Commun.*, **2003**, 5-16.
15. F. Wuerthner, Z. Chen, F. J. M. Hoeben, P. Osswald, C.-C. You, P. Jonkheijm, J. v. Herrikhuyzen, A. P. H. J. Schenning, P. P. A. M. van der Schoot, E. W. Meijer, E. H. A. Beckers, S. C. J. Meskers, R. A. J. Janssen, *J. Am. Chem. So*c. **2004**, *126*, 10611-10618.
16. (a) A. Ulman, *Chem. Rev.* **1996**, *96*, 1533-1554. (b) Y. Barness, O. Gershevitz, M. Sekar, C. N. Sukenik *Langmuir* **2000**, *16*, 247-251.; (c) s. Onclin, B. J. Ravoo, D. N. Reinhoudt, *Angew. Chem. Int. Ed.* **2005**, *44*, 2-24.(d) Q. Huang, J. Li, G. A. Evmenenko, P. Dutta, T. J. Marks, *Chem. Mater.* **2006**, *18*, 2431-2442.
17. G. T. Bourne, W. D. F. Meutermans, M. L. Smythe, *Tetrahedron Lett.* **1999**, *40*, 7271-7274.
18. D. A. Annis, E. N. Jacobsen, *J. Am. Chem. Soc.* **1999**, *17*, 4147-4154.
19. S. Maisch, F. Buckel, F. Effenberger, *J. Am. Chem. Soc.* **2005**, *127*, 17315-17322.
20. C. J. Brabec, A. Cravino, D. Meissner, N. S. Sariciftci, T. Fromherz, M. T. Rispens, L. Sanchez, J. C. Hummelen, *Adv. Funct. Mater.* **2001**, *11*, 374-380.
21. (a) Bao, Z.; Dodabalapur, A.; Lovinger, A. *Appl. Phys. Lett.* **1996,** *69*, 4108.; (b) Sirringhaus, H.; Brown, P. J.; Friend, R. H.; Nielsen, M. M.; Bechgaard, K.; Langeveld-Voss, B. M. W.; Spiering, A. J. H.; Janssen, R. A. J.; Meijer, E. W. Herwig, P.; de Leeuw, D. M. *Nature* **1999**, *401*, 685.; (c) Sirringhaus, H.; Tessler, N.; Friend, R. H. *Science* **1998**, *280*, 1741.
22. (a) C. Tanase, E. J. Meijer, P.W.M. Blom, D.M. de Leeuw, Phys. Rev. Lett. 2003, 91, 216601.; (b) Geens, W.; Shaheen, S. E.; Brabec, C. J.; Poortmans, J.; Sariciftci, N. S. *In Electronic Properties of Novel Materials - Molecular Nanostructures*; Kuzmany, H., Fink, J., Mehring, M., Roth, S., Eds.; American Institute of Physics: New York, **2000**; Vol. *544*, pp 516-520.; (c) Pacios, R.; Bradley, D. D. C.; Nelson, J.; Brabec, C. J. *Synth. Met.* **2003**, *137*, 1469.
23. (a) H. Hoppe, N. S. Sariciftci, *J. Mater. Res.*, **2004**, *19*, 1924-1945.; (b) T. J. Savenije, J. E. Kroeze, M. M. Wienk, J. M. Kroon, J. M. Warman, *Phys. Rev. B* **2004**, *69*, 155205.

Chapter 5

Future Direction and Perspectives

5.1. Macroporous gold electrode

Previous fundamental electrochemical studies have been performed on classic flat gold electrode surfaces. However, for some applications such as biochemical studies, which have to work with microelectrodes (or ultra-microelectrodes), the measured current is often close to the detection limits due to the limited active surface area. A related problem is encountered in organic photovoltaic devices, where the absorption of the incident radiation is limited by the small active volume of the organic substrates. In both cases, porous electrodes might provide a solution to the problem because of their very large electroactive surface per projection area. Electrodeposition routes[1] provide a well organized, precisely controlled pore size distribution in metallic porous electrodes compared to those consisting of platinum black and carbon felt electrodes. Further applications of extended surface-modified macroporous electrodes include electrocatalytic enzymatic biosensors.[2] In general, these highly organized structures are obtained by using colloidal crystal films as templates forming an almost perfect arrangement.[3] After electrodeposition through the colloidal lattice, an appropriate solvent removes the template and the porous electrode is ready for use. Recently, a Langmuir-Blodgett (LB) technique was used to prepare colloidal crystals of up to 50 layers useful as templates for the synthesis of metallic macroporous gold electrodes.[4] This technique offers the advantage of perfectly controlling the ordering of the colloids in the surface normal direction without cracks in the template, which ensures a homogeneous electrodeposition of the metal through the structure (Figure 5.1). In Figure 5.2, a scanning electron microscopy image shows the well ordered 3-dimensional hexagonal close-packed structure, where the connections between the spherical voids can be seen. The pinholes connecting two pores allow light and electroactive species in solution to easily penetrate into the bottom layers.

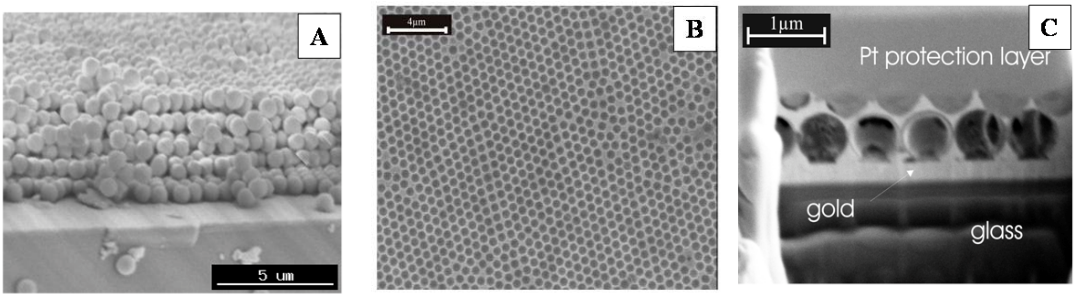

Figure 5.1. (a) Image obtained by scanning electron microscopy (SEM) of the section of a colloidal crystal made up of five layers; (b) Top view of macroporous gold, 1/2 layer of hollow spheres; (c) Cross section of macroporous gold, 11=2 layers of hollow spheres (Latex bead diameter = 680 nm).[4]

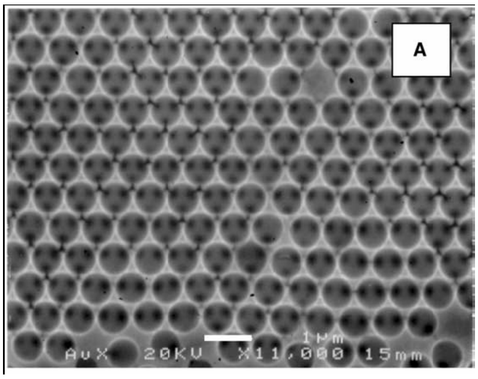

Figure 5.2. Scanning electron micrograph (top view) of a honeycomb-type structure of 3/2 layer macroporous gold film obtained by electrodeposition. White scale bar: 1 μm.[4]

The use of well-organized metallic porous electrodes strongly attracted our attention during the study of hydrogen-bonded multilayer photovoltaic devices. In order to generate higher photocurrent based on a limited photoenergy-conversion efficiency, current solar cells require large surface areas to absorb more light from the

Sun. Combining photovoltaic devices with porous electrodes provides a convenient means to produce more photocurrent in finite plane using available organic systems. A photoactive tetrakis(thioacetyl) porphyrin **57** was chosen to demonstrate this idea because of its ready availability and high extinction coefficient. The porphyrin SAM is expected to decorate the whole electroactive porous surface and, as a consequence, the photoinduced current thus generated by monolayer of porphyrin should be proportional to the total surface area of the macroporous electrode (Figure 5.3).

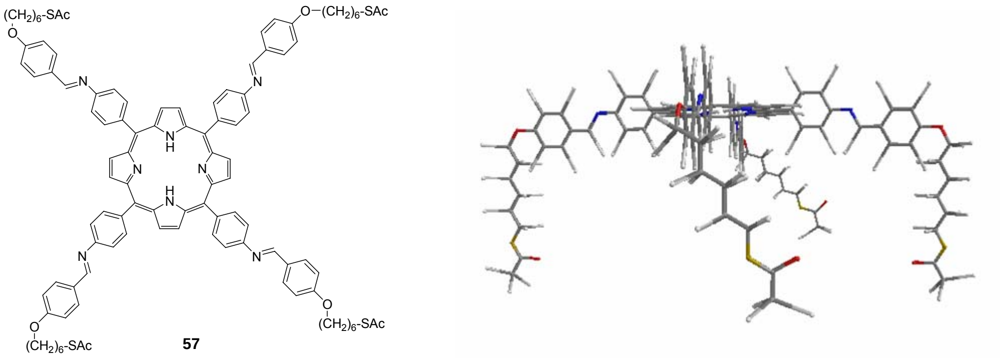

57

Figure 5.3. Structural model and energy-minimizing three-dimensional representation of $(SAc)_4$ porphyrin **57** in which the four thio-alkyl groups are in the same plane.

The synthesis of a structurally similar tetra-dentate porphyrin and the electrochemical study of the corresponding SAM on Ag(111) surface have been reported by Lambert *et al.*[5,6] The synthesis of tetra(thioacetyl) porphyrin **57** was carried out as shown in Scheme 5.1: Schiff base formation between tetrakis(4-aminophenyl)porphyrin[7] and 4-(6'-thioacetylhexyl)benzaldehyde **38** formed the desired porphyrin in one-step.

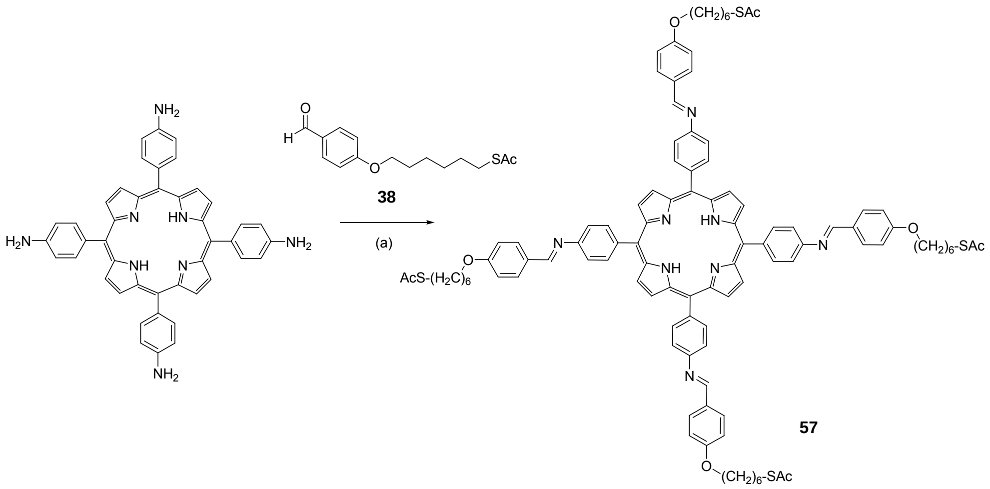

Scheme 5.1. Reagents and conditions: (a) TsOH (cat.), benzene, reflux, 3hr, (yield = 17%).

The metallic porous electrodes used in this project were prepared as described in reference 4. The diameter of the silica beads was 680 nm, and three macroporous electrodes with different numbers of layers (1, 2, or 3, corresponding to 1/2, 3/2, and 5/2 layers) were prepared in collaboration with Prof. A. Kuhn (ENSCPB) in Bordeaux. The total surface area of the porous electrodes was determined in 1 N sulfuric acid aqueous solution by cyclic voltammetry to check whether all pores are electrochemically active. As shown in Figure 5.4, the characteristic gold oxide reduction peak increased regularly from flat gold to 1/2, 3/2 and 5/2 porous gold layers. By measuring the number of charges transferred from the gold oxide stripping peak and by taking account of the specific charge density of metallic gold (386 $\mu C/cm^2$),[8] it is possible to estimate the total active surface area of each electrode (Table 5.1). All values fitted well to the theoretical calculation obtained in an approximation for a hexagonal close packed half sphere layer, and only the 1/2 electrode showed an excess value which is attributed to over deposition during the electrodeposition process.

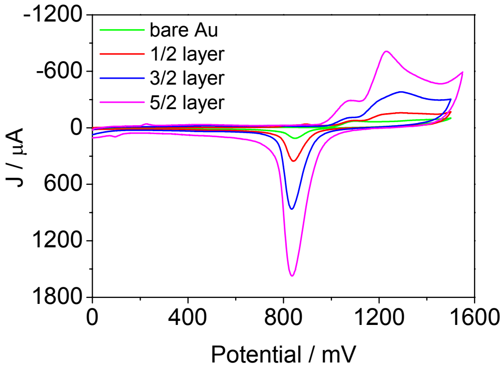

Figure 5.4. Cyclic voltammograms of (a) flat gold, (b) 1/2, (b) 3/2 and (c) 5/2 sphere layer gold electrodes in 1 N H_2SO_4 (scan rate = 100 mV/s).

	flat Au	1/2 layer	3/2 layer	5/2 layer
Geometric area	0.287 cm^2	0.293 cm^2	0.360 cm^2	0.403 cm^2
Measured charge	111.48 μC	326.47 μC	814.69 μC	1680 μC
Calculated area (386 $\mu C/cm^2$)	0.288 cm^2	0.846 cm^2	2.110 cm^2	4.352 cm^2
Ratio (*vs.* flat Au) (cal.)	0.99 (1.0)	2.82 (1.92)	5.86 (5.53)	10.81 (9.16)

Table 5.1. Experimental data of total surface area measurement calculated from the gold oxide reduction peak.

Porphyrin SAMs on flat gold substrates were obtained from deposition of a CH_2Cl_2 solution. The quality of SAMs could not be directly probed by cyclic voltammetry of the Fe^{3+}/Fe^{2+} peak because the porphyrin is also electroactive and overlaps with the ferric ion (Figure 5.5).

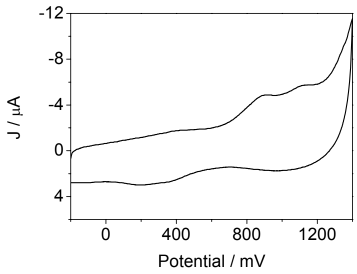

Figure 5.5. Cyclic voltammograms of tetra-dentated porphyrin **57** SAM on a flat gold electrode. Recorded in CH_2Cl_2 with 0.1 M tetrabutylammonium hexafluorophosphate ($TBAPF_6$) as the supporting electrolyte (scan rate: 50 $mV.s^{-1}$).

To investigate the influence of the porous electrode structure onto SAM formation, molecule **39** was used to modify three different layered electrodes (with 1/2, 3/2 or 5/2 porous layer, denoted as P12, P32, or P52 respectively). Additionally, SAM-modified flat gold electrode (denoted as P02) was also prepared as a reference. A waterproof mask was used to isolate the flat gold region from the electrolyte, so that only the porous area was direct contact with the solution. The surface coverage of SAMs were examined by cyclic voltammetry using $K_3[Fe(CN)_6]$ as electroactive species.[9] Both flat and 1/2 layer gold electrodes formed highly uniform close-packed monolayers after one day of immersion in an THF/EtOH solution of **39** (1.0×10^{-3} M). However, that is not the case for the 3/2 and 5/2 layer electrodes. These two porous electrodes needed longer immersion time (totally 3 days) to stabilize (Figure 5.6).

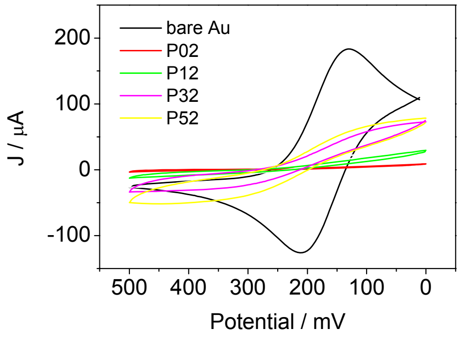

Figure 5.6. Cyclic voltammograms of the reduction of aqueous $K_3[Fe(CN)_6]$ using flat gold electrode, (device P02); and 1/2, 3/2 and 5/2 porous electrodes (devices P12, P32, and P52, respectively). All electrodes were modified with thiolate molecule **39**. Bare gold (black line) was used as control experiment.

In the meantime, another parallel experiment was processed to study the reductive desorption of self-assembled monolayers in order to regenerate the Au(0) surface and able to reuse these well-organized porous electrodes. The potential at which desorption occurs was shown by Porter to be dependent on the chain length of SAMs molecule and the nature of the tail group, as well as on pH.[10] The modified electrodes were biased at -1.0 V (vs. Ag/AgCl) for 5 min in phosphate-buffered saline (PBS, pH = 7.4) solution, resulting in the desorption of the SAMs. Although working at further negative potential (between -1.1 V and -1.5 V) can speed up this desorption process, the formation of hydrogen bubbles, produced by the electrolysis of water at the bottom layers, might destroy the very fine porous structure of the electrodes. The results of the desorption were evidenced by observing the regenerated redox signal of Fe^{3+}/Fe^{2+} (see, Figure 5.7) and comparing the regenerated electrode surface area with that previously obtained.

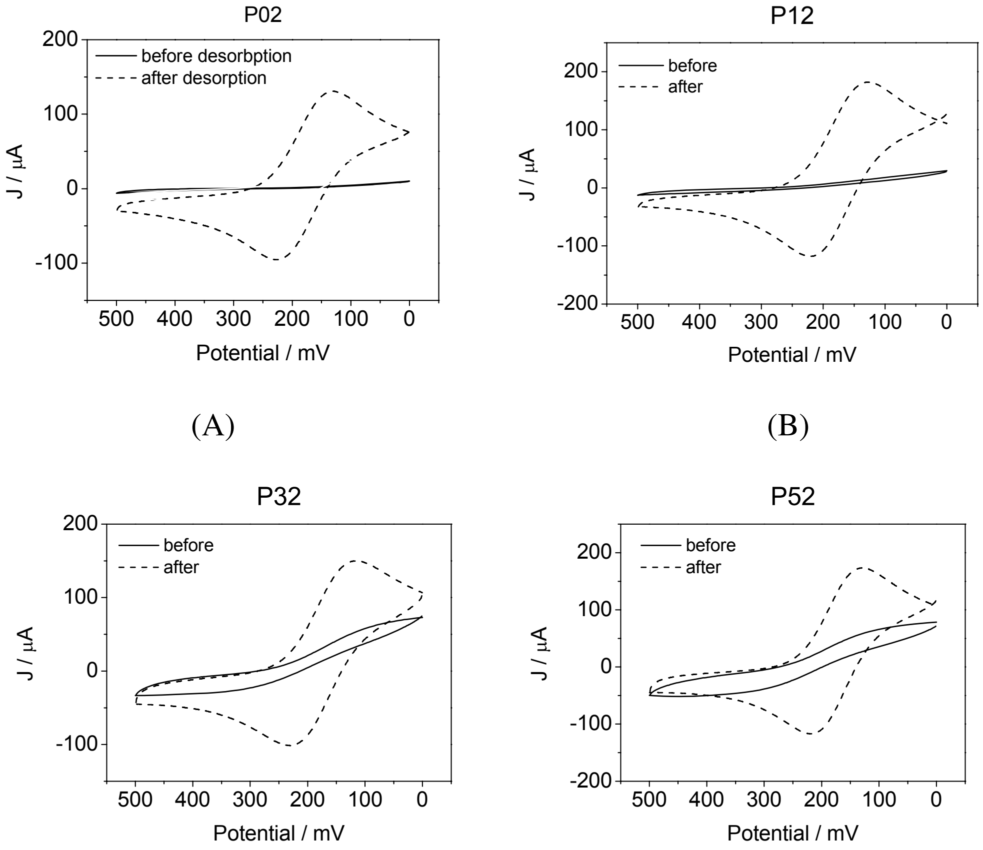

(A)

(B)

(C)

(D)

Figure 5.7. Cyclic voltammograms of the reduction of aqueous $K_3[Fe(CN)_6]$ *vs*. flat gold electrode, (device P02) and 1/2, 3/2 and 5/2 layer porous electrodes (devices P12, P32, and P52, respectively) after removing the SAM.

The SAM decorated porous electrodes were obtained by immersing the electrodes in a chloroform solution of porphyrin **57**. Photo-induced current measurements with porphyrin SAMs on multilayer porous electrodes are shown in Figure 5.8 (A, B, and C). In agreement with previous electrochemical investigations, the SAM assembly of **57** on multilayer porous electrodes needed much longer time for the photocurrent to reach equilibrium, as confirmed by monitoring the photocurrent of the layered devices as a function of immersion time. Both the flat surface device and 1/2 layer porous electrode device showed a steady photocurrent value after two days immersion. The remaining two porous electrode (P32 and P52) devices suggested a slower assembly process (up to 25 days), which was much longer than we anticipated.

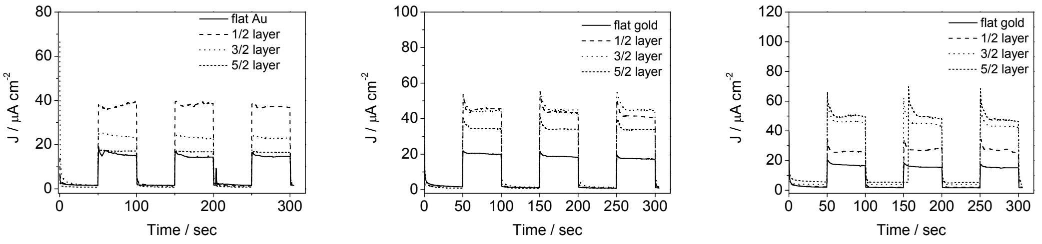

A B C

Figure 5.8. Photocurrent generated from flat gold electrode and porous electrodes upon irradiation as a function of immersion time: (A) Immersed time: 2 days, (B) immersed time: 5 days, (c) immersed time: 25 days.

To explain the difference in behavior between 3/2 and 5/2 layered devices, it is necessary to consider the penetration of incident light in multilayer pores, as shown in Figure 5.9. Additionally, when incident light passes through a micro-channel, which is approximately 100 nm in diameter, diffraction occurs. Right now, we are not able to measure the actual light intensity of each porous layer, but we expect the photocurrent enhancement should reach a maximum level after certain number of layers.

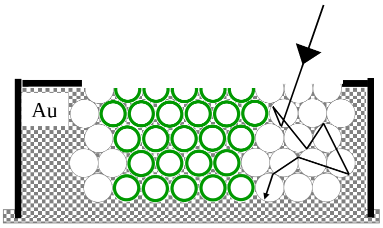

Figure 5.9. Schematic illustration of possible pathway of incident light in multilayer porous electrode.

If the porphyrin adsorbs onto the surface through all four thiolate-groups bonding to the gold, this would lead the porphyrin ring to lie perpendicularly to surface normal. To confirm this, we investigated the ability of the porphyrin SAM to bind [60]fullerene by π-π interactions (see, Figure 5.10, left).[11] The present of a secondary electro-acceptor layer on top of the porphyrin SAM layer should improve the photo-electron conversion process and give higher photoinduced current (Figure 5.10, left). A modified flat gold electrode was chosen to demonstrate this concept, and results are shown in Figure 5.10 (right).

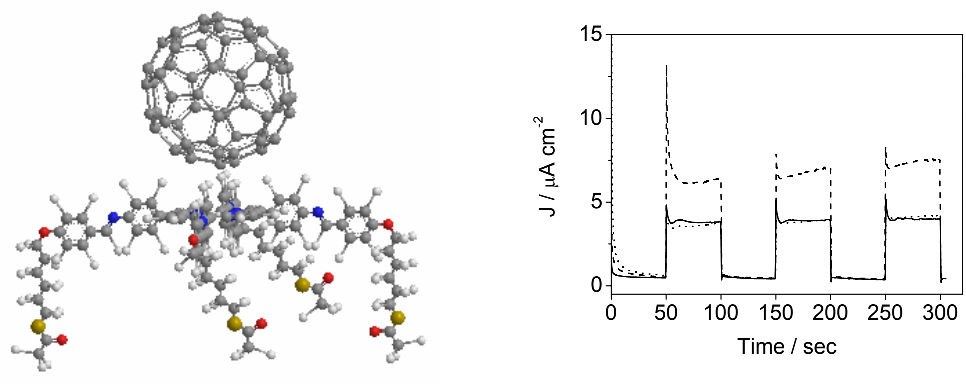

Figure 5.10. (Left) 3-dimesional representation of $(SAc)_4$Porphyrin **57** assembled with [60]fullerene. (Right) photocurrent generated from flat modified gold electrodes of porphyrin SAM only (solid line), porphyrin SAM + C_{60} with rinsing treatment (dot line), and porphyrin SAM + C_{60} without rinsing treatment (dash line).

Porphyrin SAMs electrode was immersed in a fullerene solution (0.2 mg/mL in toluene) overnight and showed a *ca.* 50% enhancement of the photocurrent. Another sample, which was prepared in same procedure and rinsing with chloroform to remove any physic-absorbed of C_{60} revealed no enhancement compared to original porphyrin SAM (solid line), These results can be interpreted by considering that the chloroform rinsing post-treatment washed off the assembled fullerenes due to the low binding constant between metal-free porphyrin and fullerene (5.2×10^3 M^{-1})[11]. Although without rinsing, it is possible that a multiple-layered fullerene on top of porphyrin SAMs is formed (Figure 5.11, left), the small extinction coefficient of fullerene at the incidental wavelength absorption (400~500 nm) suggests that the contribution of photocurrent generated from fullerene can be ignored (Figure 5.11, right). Metalloporphyrin, for example: Zn(II)-Porphyrin or Co(II)-Porphyrin, should give a much stronger binding affinity with [60]fullerene, where the bonded fullerene should be able to withstand rinsing.

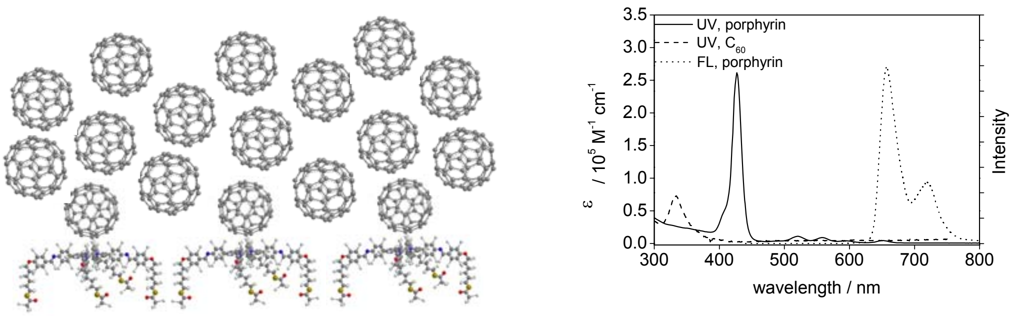

Figure 5.11 (Left) Schematic representation of $(SAc)_4$Porphyrin **54** assembled with heavy layered fullerene. (Right) Electronic spectrum (solid line) and fluorescence spectrum (dot line) of $(SAc)_4$Porphyrin **57**, solvent: $CHCl_3$; and electronic spectrum of C_{60} (dash line), solvent: toluene.

The application of porous electrodes towards hydrogen-bonded fullerene **1** and oligothiophene **7** was also investigated, and the structure of photovoltaic devices was schematically illustrated in Figure 5.12. First, the porous gold was modified with

SAMs of molecule **39,** and then decorated with photoactive material **1** and **7** (in 2:1 ratio), which can assemble onto the SAMs. Three different layered photovoltaic devices (with 1/2, 5/2 or 9/2 porous layer) were prepared (denoted as P12, P52, or P92, respectively). An additional photovoltaic device built on SAM-modified flat gold electrode was also prepared as the control experiment (denoted as P02). Waterproof masks were used to isolate the flat gold region from the electrolyte, so that only the porous area was in contact with the methylviologen and supporting electrolyte in solution.

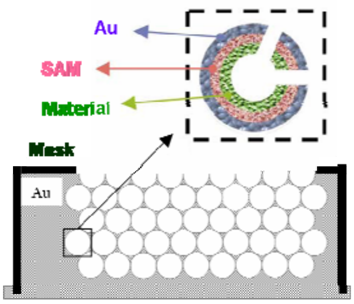

Figure 5.12. Schematic drawing of the structure of a 5/2 sphere layer photovoltaic device.

The preliminary results of the photo-irradiation response of devices built on SAMs-modified porous electrodes are shown in Figure 5.13. Compared to device P02, the photocurrent generated from device P12 shows an almost 2-fold enhancement. This value is very close to the proportion of the surface area (see Table 5.1 of the two devices) However, this is not the case for devices P52 and P92, which are expected to have much higher photocurrent than device P21.

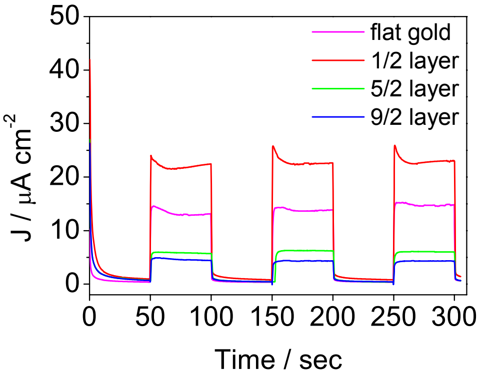

Figure 5.13. Photocurrent generated from flat gold electrode and porous electrodes upon irradiation during 3 on/off cycles.

Possible explanations for these unexpected results must take into consideration that during the slow evaporation process, the photoactive material assembles either uniformly over the SAM, forming an inner circle-type layer, or could fill up the entire pore. The later situation would block the incident light and the electron carrier (MV^{+2}) going into the deeper porous layers. Furthermore, the organic material may remain on the top due to the small connecting channels between two pores being obstructed (estimated diameter = 100 nm, see Figure 5.14). These possibilities are not mutually exclusive, and in all of the cases the non-even distribution of material should cause a lower photocurrent.

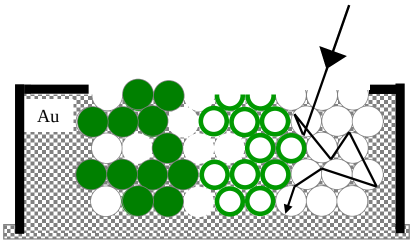

Figure 5.14. Schematic illustration of photoactive material distributed unevenly in a multilayer porous electrode.

In conclusion, multilayer porous electrodes exhibit a great potential in photovoltaic device application based on these preliminary studies. Definitely, lots of effort has to be done in the future in order to understand the scope and the limitation of photovoltaic devices built on porous electrodes.

In the porphyrin self-assembled monolayer study, many questions remain. For example, thus far the decreased photocurrent of 1/2 layer device after 25 days immersion time as shown in Figure 5.8.C is not understood. The structure of porphyrin self-assembled monolayer is another possible factor that causes the variations in photocurrent, where the geometry of the porphyrin ring could be either parallel to the surface due to four S-Au bonds or perpendicular to the surface by only one /or two arms. Further experiments in electrochemistry aimed at measuring the quantity of porphyrin molecules on surface are needed. These values will provide a density of SAM molecules per surface area unit, which is an important parameter to understand the relationship between photocurrent response, and the number of porphyrin molecules.

References

1. (a) J.E.G.J. Wijnhoven, S.J.M. Zevenhuizen, M.A. Hendriks, D. Vanmaekelbergh, J.J. Kelly, W.L. Vos, *Adv. Mater.* **2000**, *12*, 888-890. (b) P. Bartlett, P. Birkin, M. Ghanem, *Chem. Commun.* , **2000**, 1671-1672.
2. (a) S. Ben-Ali, D.A. Cook, S.A.G. Evans, A. Thienpont, P.N. Bartlett, A. Kuhn, *Electrochem. Commun.* **2003**, *5*, 747-751. (b) S. Ben-Ali , D. A. Cook, P. N. Bartlett, A. Kuhn, *Journal of Electroanalytical Chemistry*, **2005**, *579*, 181–187.
3. (a) S. Wong, V. Kitaev, G.A. Ozin, *J. Am. Chem. Soc.* **2003**, *125*, 15589-15598. (b) Y. Xia, Y. Yin, Y. Lu, J. McLellan, *Adv. Funct. Mater.* **2003**, *13*, 907-918.
4. R. Szamocki, S. Reculusa, S. Ravaine, P. N. Bartlett, A. Kuhn, R. Hempelmann, *Angew. Chem. Int. Ed.* **2006**, *45*, 1317-1321.
5. Gryko, D. T.; Clausen, C.; Lindsey, J. S. *J. Org. Chem.* **1999**, *64*, 8635-8647.
6. O. P. H. Vaughan, M. Turner, F. J. Williams, A. Hille, J. K. M. Sanders, R. M. Lambert, *J. Am. Chem. Soc.* **2006**, *128*, 9578-9579.
7. A. Bettelheim, B. A. White, S. A. Raybuck, R. W. Murray, *Inorg. Chem.* **1987**, *26*, 1009-1017.
8. R. Woods, in: A.J. Bard (Ed.), *Electroanalytical Chemistry: A Series of Advances*, vol. 9, Marcel Dekker, New York, **1980**.
9. M. D. Porter, T. B. Bright, D. L. Allara, C. E.D. Chidsey, *J. Am. Chem. Soc.* **1987**, *109*, 3559-3568.
10. (a) C. A. Widrig, C. Chung, M. D. Porter, *J. Electroanal. Chem.* **1991**, *310*, 335-359. (b) D. F. Yang, C. P. Wilde, M. Morin, *Langmuir* **1997**, *13*, 243-249. (c) S. S. Wong, M. D. Porter, *J. Electroanal. Chem.* **2000**, *485*, 135-143.; (d) P. Mali, N. Bhattacharjee, P. C. Searson, *Nano Lett.* **2006**, *6*, 1250-1253.
11. (a) P. D. W. Boyd, C. A. Reed, *Acc. Chem. Res.* **2005**, *38*, 235-242. (b) T. Hasobe, H. Imahori, P. V. Kamat, T. K. Ahn, S. K. Kim, D. Kim, A. Fuji, *J. Am. Chem. Soc.* **2005**, *127*, 1216-1228. (c) M. Shirakawa, N. Fujita, H. Shimakoshi, Y. Hisaeda S. Shinkai, *Tetrahedron* **2006**, *62*, 2016–2024.

5.2. Hydrogen-bonded CdS nanoparticle assemblies on electrodes for photoelectrochemical applications

To extent the application of self-assembly into the wider field of materials for solar energy conversion, we worked with Prof. I. Willner at Hebrew University of Jerusalem, Israel to combine supramolecular chemistry with semiconductor nanoparticles (NPs) systems.[1] Recent efforts in organized functional semiconductor nanoparticles for photoelectrochemical applications have shown significant potential because of their unique physical properties.[2] Different strategies have been used to deposit layered semiconductor nanoparticles on surfaces, such as electrostatic interactions,[5] covalent bonds,[6] and carboxylic acid-pyridine cross-linkers.[7] Our approach involved the study of cadmium sulfide and gold nanoparticle self-assembly on gold surfaces through complementary barbiturate-triaminodiazine hydrogen-bonded interactions and their application for photocurrent generation.

Two complementary CdS nanoparticles were assembled onto gold electrodes as depicted in Figure 5.15. CdS nanoparticles (4~5 nm diameter)[8] were modified by either molecule **39** or molecule **44**. Then, molecule **44** or **39** which have complementary recognition sites, were assembled directly on the gold surface. The characterizations of the loading of the different components on the surfaces was followed by microgravimetric quartz-crystal microbalance (QCM). From the frequency change (Δf = - 420 Hz in air), it was possible to estimate the surface coverage of the CdS nanoparticles to be 3.1×10^{12} particles/cm^2. In the first assembly configuration (Figure 5.15, A), the CdS nanoparticles assembled to the electrode were also evidenced by observing using FT-IR measurements the slightly shift of the N-H band stretch from $\bar{\nu} = 3250$ cm^{-1} to $\bar{\nu} = 3255$ cm^{-1}, and of the three vibration pertaining to the carbonyl group (at $\bar{\nu}$ = 1747, 1717, and 1687 cm^{-1}) which were shifted and reduced to two bands (at $\bar{\nu}$ = 1702 and 1698 cm^{-1}). These data are consistent with the formation of hydrogen bonds between CdS nanoparticles and the gold surface.[9] In addition, the absorption spectrum of the modified surface bearing the CdS nanoparticles shows the characteristic phonon band of the nanoparticles (see, Figure 2.15 below right).

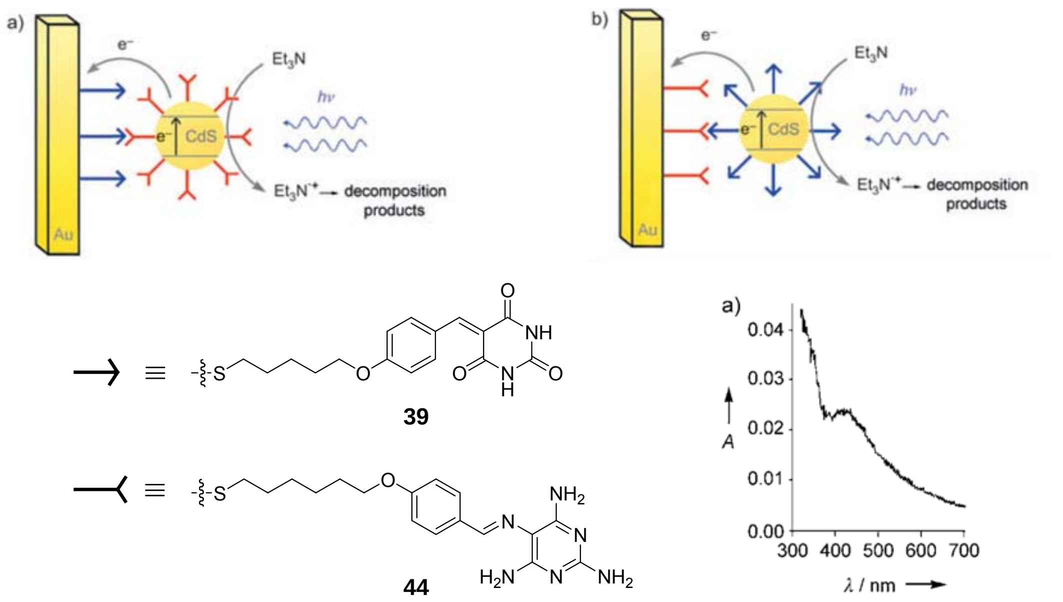

Figure 5.15. Schematic presentation of hydrogen-bonded CdS nanoparticles assemblies in which (A) **39** was bound to the gold electrode and **44** was bound to the CdS nanoparticles; and (B) **44** was bound to the electrode and **39** was associated with the CdS nanoparticles. (Below right) Absorbance spectrum of the CdS nanoparticle layer on a gold-coated glass support prepared according to (A).

It has been shown that by employing a layered gold nanoparticle/CdS nanoparticle hybrid system, it is possible to enhance photocurrent generation.[10] Thus, a further extension of these hydrogen-bonded architectures consisted in building a metal/semiconductor nanoparticles bi-layer assembly on gold electrodes as shown in Figure 5.16. First, citrate-stabilized gold nanoparticles[11] (12 ± 1 nm) were linked by a thiolated monolayer on gold-coated (~ 50 nm thickness) glass slides. In a second step, a monolayer of **44** was assembled on the gold nanoparticles. These were then placed in contact with a solution of CdS nanoparticles functionalized with **39,** which became linked through hydrogen bonds to the gold nanoparticles. The bi-layer nanoparticles assembly that decorated on propandithiol SAMs modified gold surface were characterized by both of QCM analyses and the absorption spectroscopy. QCM analyses showed that the surface coverage of the gold nanoparticles and the CdS nanoparticles corresponded to 7.0×10^{10} and 2.6×10^{12} particles/cm^2, respectively.

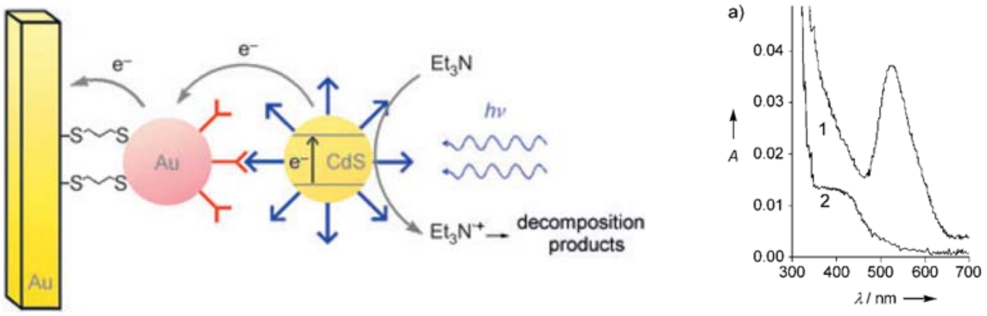

Figure 5.16. (Left) Schematic representation of the layered hydrogen-bonded gold nanoparticle/CdS nanoparticle assembly associated with a gold electrode in which the gold nanoparticles are functionalized with **44** and the CdS nanoparticles are modified with complementary **39**. (Right) Absorbance spectra on a gold-coated glass support of the gold nanoparticle layer (curve **1**) and on the gold nanoparticle/CdS nanoparticle assembly (curve **2**).

Photocurrent generation experiments were recorded in anhydrous THF using triethylamine (Et_3N) as a sacrificial electron donor and tetra-*n*-butylammonium hexafluorophosphate (TBPF) as the supporting electrolyte. The *I/V* graph of photocurrent generated *vs.* applied potential is shown in Figure 5.17 (left), which is useful in defining the mechanism of photocurrent generation. Upon photoexcitation of the CdS nanoparticles, an exciton is generated in the CdS nanoparticles. Charge separation, followed by transfer of the conduction-band electrons to the electrode and oxidation of the electron donor (Et_3N) completes the electrochemical cycle. By biasing the electrode potential at -0.5 V, it is possible to block the transfer of the conduction-band electrons to the electrode, thus prohibiting the generation of photocurrent. The photocurrent spectrums *vs.* irradiated wavelength of two systems (with /without gold nanoparticles assemblies) are shown in Figure 5.17 (center and right). It is clear that the bi-layer system (Figure 5.16, left) gave an approximately 2.6-fold enhancement relative to the system that lacked the gold nanoparticles (Figure 5.15, A). This enhanced photocurrent in the gold nanoparticle/CdS nanoparticle composite system was attributed to more efficient charge separation between the gold nanoparticles and CdS nanoparticles. The transfer of the conduction-band electrons to the gold nanoparticles spatially separates the electron-hole pair, thus leading to slower charge recombination.

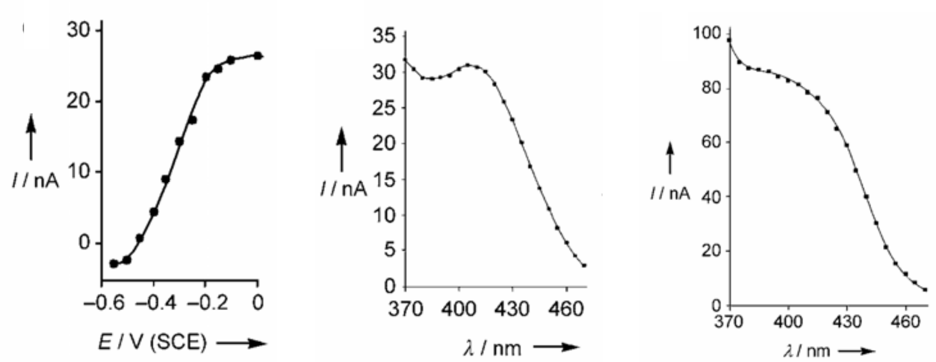

Figure 5.17. (Left) photocurrent recorded as a function of the applied potential at λ=410 nm (SCE=standard calomel electrode). (Center) photocurrent action spectrum corresponding to the CdS nanoparticle assembly shown in Figure 5.15 (A). (Right) Photocurrent action spectrum corresponding to the gold nanoparticle/CdS nanoparticle assembly shown in Figure 5.16 left.

In conclusion, the present study has employed complementary hydrogen bonds to fabricate metal and semiconductor nanoparticle arrays on surfaces and has demonstrated the functional use of the resulting nanostructures for the generation of photocurrents. This study highlighted fundamental effects of hydrogen-bonded complexes on charge transport at semiconductor nanoparticle/electrode interfaces, and additionally indicated some alternative routes in the future to build three-dimensional self-assembled architectures with other hybrid nano-sized particles in higher complexity (Figure 5.18).

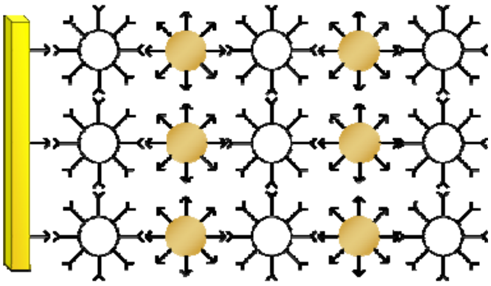

Figure 5.18. Schematic representation of the multilayer hydrogen-bonded hybrid nanoparticles architecture.

References

1. R. Baron, C.-H. Huang, D. M. Bassani,A. Onopriyenko, M. Zayats, I. Willner, *Angew. Chem. Int. Ed.* **2005**, *44*, 4010-4015.
2. (a) A. N. Shipway, E. Katz, I. Willner, *ChemPhysChem* **2000**, *1*, 18-52.; (b) A. N. Shipway, I. Willner, *Chem. Commun.* **2001**, 2035-2045.; (c) E. Katz, I. Willner, *Angew. Chem. Int. Ed.* **2004**, *43*, 6042-6108.
3. (a) C. Nasr, S. Hotchandani, W. Y. Kim, R. S. Schmehl, P. V. Kamat, *J. Phys. Chem. B* **1997**, *101*, 7480-7487.; (b) V. Pardo-Yissar, E. Katz, J. Wasserman, I. Willner, *J. Am. Chem. Soc.* **2003**, *125*, 622 -623.; (c) D. Dong, D. Zheng, F.-Q. Wang, X.-Q. Yang, N. Wang, Y.-G. Li, L.-H. Guo, J. Cheng, *Anal. Chem.* **2004**, *76*, 499 -501.
4. (a) N.-G. Park, M. G. Kang, K. M. Kim, K. S. Ryu, S. H. Chang, D.-K. Kim, J. van de Lagemaat, K. D. Benkstein, A. J. Frank, **Langmuir 2004**, *20*, 4246-4253.; (b) A. Zaban, S. G. Chen, S. Chappel, B. A. Gregg, *Chem. Commun.* **2000**, 2231-2232.
5. (a) N. A. Kotov, I. Dekany, J. H. Fendler, *J. Phys. Chem.* **1995**, *99*, 13065-13069. (b) K. Ariga, Y. Lvov, M. Onda, I. Ichinose, T. Kunitake, *Chem. Lett.* **1997**, 125-126. (c) Z. Tang, Y.Wang, N. A. Kotov, *Langmuir* **2002**, *18*, 7035-7040.
6. (a) V. L. Colvin, A. N. Goldstein, A. P. Alivisatos, *J. Am. Chem.Soc.* **1992**, *114*, 5221-5230. (b) S. Westenhoff, N. A. Kotov, *J. Am. Chem. Soc.* **2002**, *124*, 2448-2449.
7. E. Hao, T. Lian, *Chem. Mater.* **2000**, *12*, 3392-3396.
8. M. Miyake, H. Matsumoto, M. Nishizawa, T. Sakata, H. Mori, S. Kuwabata, H. Yoneyama, *Langmuir* **1997**, *13*, 742-746.
9. W.-S. Yang, S.-G. Chen, X.-D. Chai, Y.-W. Cao, R. Lu, W.-P. Chai, Y.-J. Jiang, T.-J. Li, J.-M. Lehn, *Synth. Met.* **1995**, *71*, 2107-2108
10. (a) L. Sheeney-Haj-Ichia, S. Pogorelova, Y. Gofer, I. Willner, *Adv. Funct. Mater.*

2004, *14*, 416-424.; (b) L. Sheeney-Haj-Ichia, B. Basnar, I. Willner, *Angew. Chem. Int. Ed.* **2005**, *44*, 78-83.

11. (a) K. C. Grabar, R. G. Freeman, M. B. Hommer, M. J. Natan, *Anal. Chem.* **1995**, *67*, 735-743.; (b) P. D. W. Boyd, C. A. Reed, *Acc. Chem. Res.* **2005**, *38*, 235-242.

5.3. Double-decker supramolecular cage

As amply demonstrated in the previous studies, the presence of molecular recognition motifs in oligothiophene **7** and oligo(*p*-phenylene vinylene)s **36** are well-suited for the assembly of supramolecular H-B architectures. Whereas the formation of infinite networks is promising for photovoltaic applications, finite, well-defined architectures provide useful information and excess to physical constants. Through-space orbital overlaps is an important factor determining charge-carrier mobility in organic devices. To investigate the through-space interaction between adjacent OPV's, the assembly of stacked molecules **36** was studies. This assembly was designed based on the fused Hamilton receptor[1], capable of binding two or more barbitrate guests in a linear arrangement.

Ideally, the barbituric acid-appended oligo(*p*-phenylene vinylene)s: OPV **36** and Hamilton-type bis-receptor should assemble in a 2:2 ratio; and OPV **36** should assemble with the tris-receptor in a 3:2 ratio (Figure 5.18). In these complexes, the steric hindrance between alkyloxy substitutes of neighbouring OPV molecules leads the *p*-phenylene vinylene moiety to slightly twist with respect to the surface normal. Although this multi-component self-assembled process is not favored entropycally, but taking account of the enthalpy gained by multiple hydrogen bonds formation: 24 H-bonds in **BisHR2-OPV2** and 36 H-bonds in **TrisHR2-OPV3**, the formation of supramolecular double- or triple-decker cage is expected.

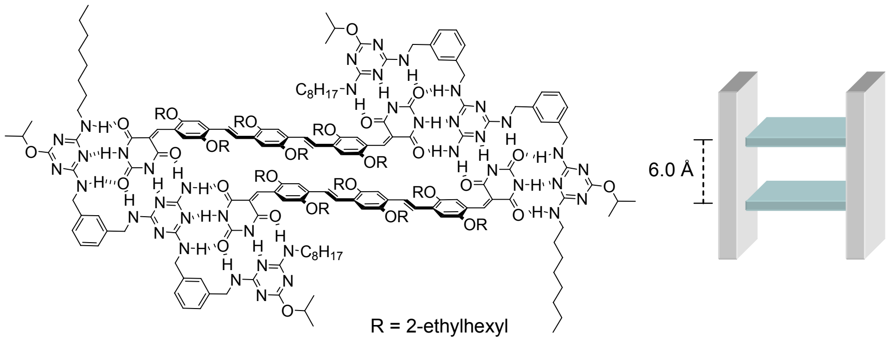

BisHR$_2$-OPV$_2$ complex

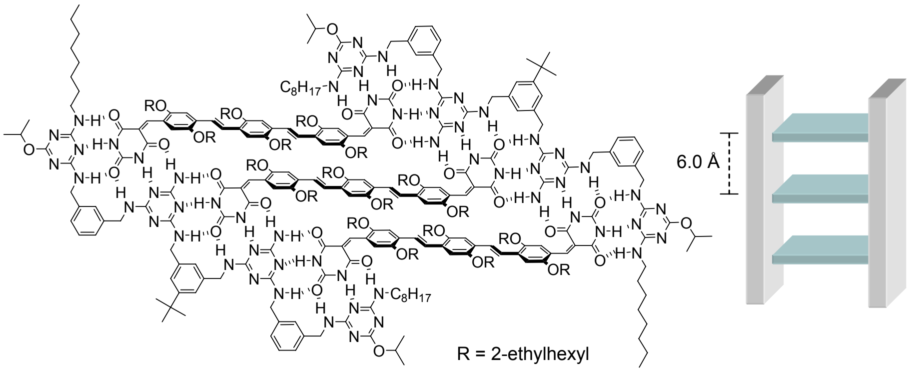

Tris-HR$_2$-OPV$_3$ complex

Figure 5.18. Schematic representation of **BisHR$_2$-OPV$_2$** (top) and **TrisHR$_2$-OPV$_3$** (below) supramolecular complexes.

Figure 5.19 shows the expected molecular structures of barbituric acid-appended oligo(*p*-phenylene vinylene)s: OPV **36**, bis-receptor and tris-receptor[2] (denoted as **Bis-HR** and **Tris-HR**, respectively). The synthesis of OPV **36** has been described in Chapter 2. The six alkyloxy branched side chains of OPV **36** and the solublizing groups (*iso*-propoxy and n-octyl groups) of the receptors greatly increase their solubility in the non-polar organic solvents, which is the prerequisite for H-B formation.

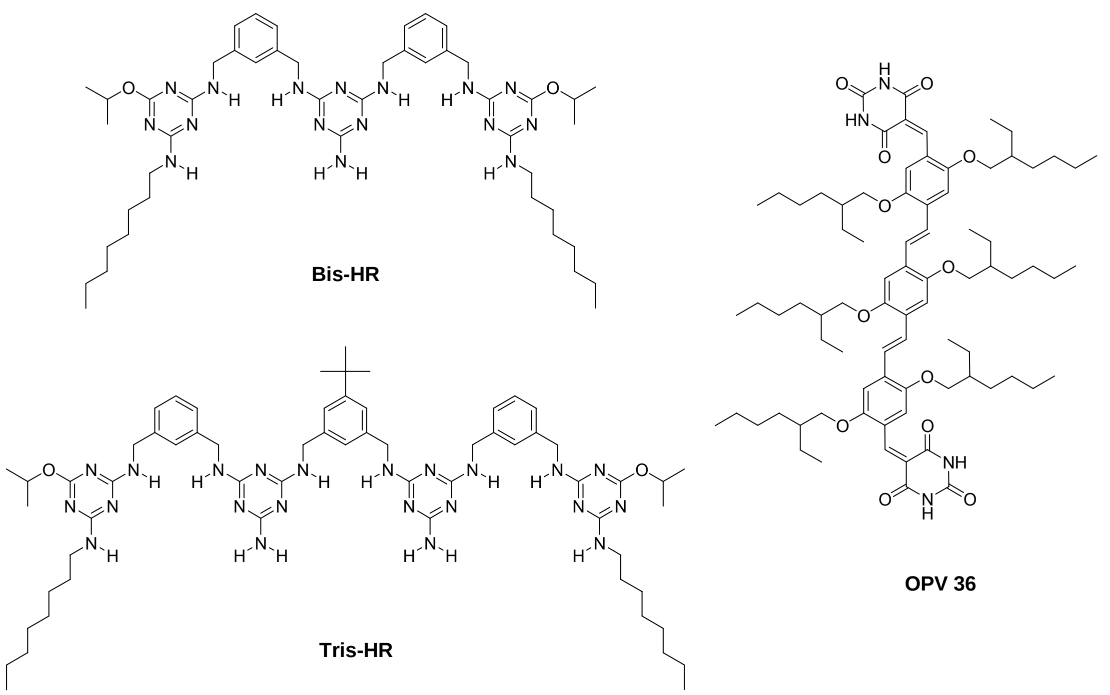

Bis-HR

Tris-HR

OPV 36

Figure 5.19 Molecular structures of barbituric acid derivative OPV **36**, and receptors: **Bis-HR** and **Tris-HR**.

NMR measurements

NMR spectroscopy was used to investigate the formation of H-B supramolecular cages. In Figure 5.20, an equimolar mixture of OPV **36** and **Bis-HR** in $CDCl_3$ exhibits a well-resolved spectrum with the H-B imide resonating proton at δ 13.95 ppm, accompanied by good agreement of the signal intensities, supporting the formation of the hydrogen-bonded complex **BisHR$_2$-OPV$_2$** (Figure 5.20 C). The broadened proton (H_a), aromatic proton (H_b) and proton (H_c) peaks of OPV **36** are attributed to the fact that the OPV moiety is no longer able to rotate freely.

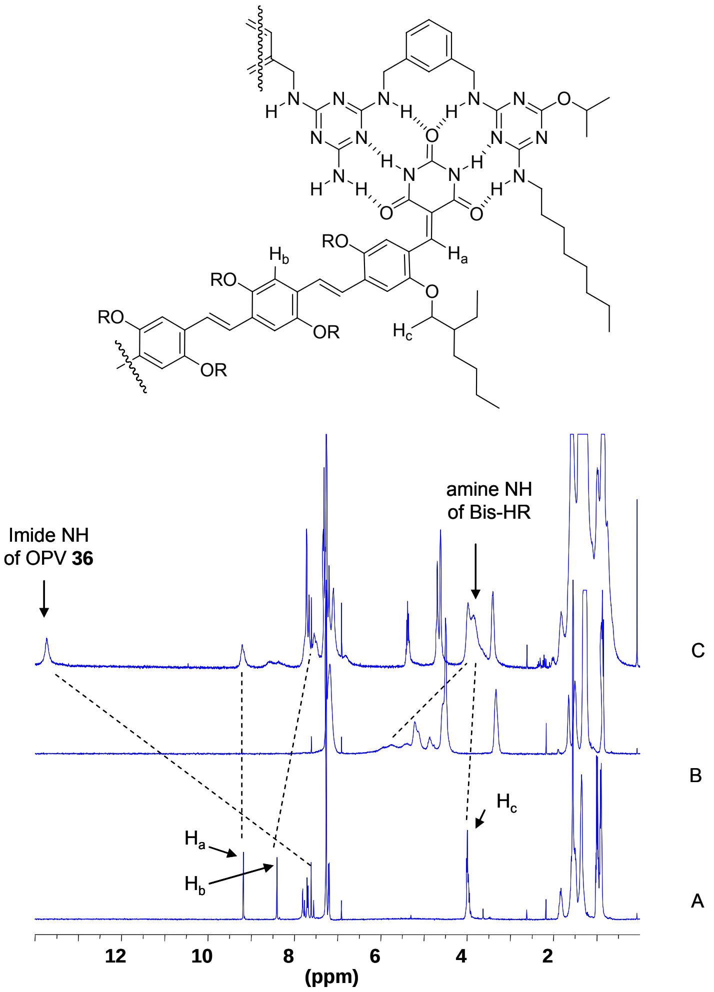

Figure 5.20 ^1H NMR (300MHz, in $CDCl_3$) spectrums of OPV **36** (A), bis-receptor **Bis-HR** (B), and supramolecular complex **BisHR$_2$-OPV$_2$** (C).

The complexation of OPV **36** and **Tris-HR** receptor is more complicated as revealed in Figure 5.21 (B). Upon mixing stoichiometric amounts of OPV **36** and receptor **Tris-HR**, the formation of complex is anticipated by the appearing hydrogen-bonded signal at 14.0 ppm. The multiple H-bond peaks indicate more than one configuration or that isomers exist in the complex **TrisHR$_2$-OPV$_3$**, which can be rationalized by considering that assembling the second OPV **36** in the middle receptor site is less favorable than at the external position due to the steric repulsion of the neighbouring OPV molecule.

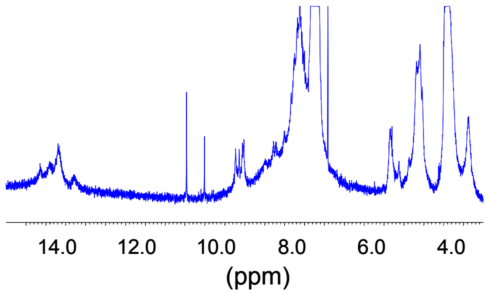

Figure 5.21. ^{1}H NMR (300MHz, in $CDCl_3$) spectrum of complex **TrisHR$_2$-OPV$_3$**.

In the variable-temperature ^{1}H NMR experiment of complex **BisHR$_2$-OPV$_2$** (between -35℃ and 115℃, in 1,1,2,2-tetrachloroethane-d_2 solvent), the rupture of hydrogen bonds occurs at *ca.* 45℃ (Figure 5.22), as suggested by the disapperence of imide proton at 13.9 ppm. Above 65℃, the ^{1}H NMR spectrum shows a significant sharpening of the peaks indicating the formation of free OPV **36** and receptor **Bis-HR**. At low temperatures (< 15℃), the slow exchange process leads to the appearance of asymmetric signals of H_a protons (at 9.0 ppm) and broadening peak of the hydrogen-bonded imide proton.

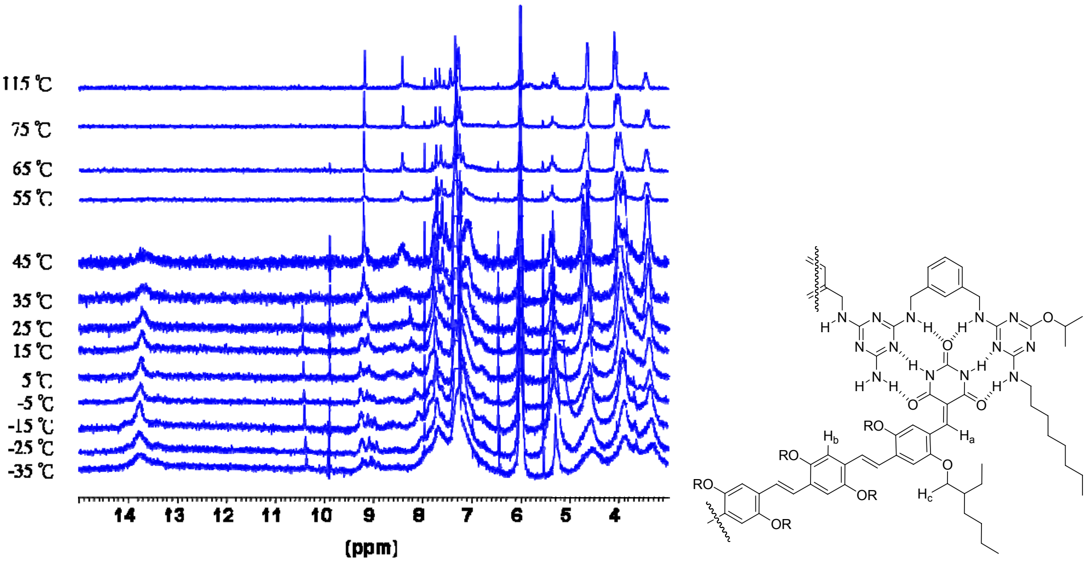

Figure 5.22. Variable-temperature experiment ^{1}H NMR spectra (200 MHz, in 1,1,2,2-tetrachloroethane deuterium solvent) of complex BisHR$_2$-OPV$_2$.

A titration experiment was performed by adding a **Bis-HR** solution to OPV **36** and monitoring the assembly using ^{1}H NMR spectroscopy (200MHz, 1.9 mM in $CDCl_3$).

The H-bond signal appearing at the equimolar ratio possibly indicates a slow exchange mechanism (Figure 5.23). Upon adding six equivalent of **Bis-HR**, a new H-bond signal at 13.5 ppm appeared, accompanied by the sharpening of proton H$_a$, which also indicates the rupture of **BisHR$_2$-OPV$_2$**. Upon addition of an excess of the receptor, OPV **36** binds with **Bis-HR** in 1:2 ratio, thus the asymmetric imide proton is restared.

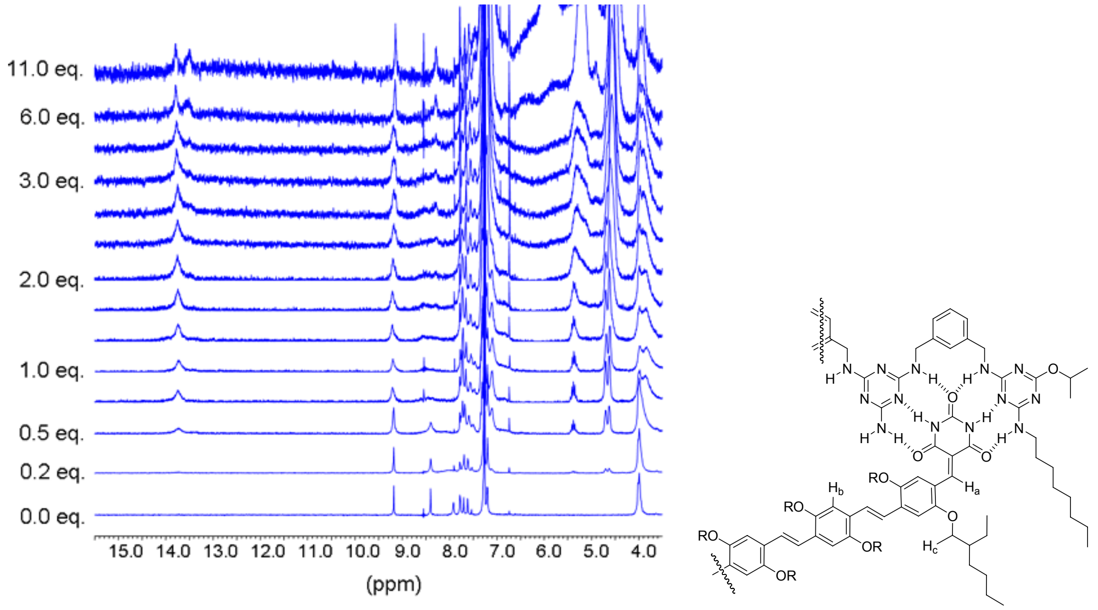

Figure 5.23. ^{1}H NMR spectra (200 MHz in CDCl$_3$) of complex **BisHR$_2$-OPV$_2$**: addition of receptor **Bis-HR** to OPV **36** (1.9 mM).

Electrochemical Study

The electrochemical study of two complexes (**BisHR$_2$-OPV$_2$** and **TrisHR$_2$-OPV$_3$**) by cyclic voltammetry shows very interesting responses (Figure 5.24 and 5.25). Whereas free OPV **36** shows a reversible one-electron oxidative peak at 0.575 V (*vs.* ferrocene in CH$_2$Cl$_2$) and the bis- or tris-receptor itself has no electrochemical responses at the forward direction up to 1.0 V. **BisHR$_2$-OPV$_2$** complex reveals a one-electron oxidative peak at 0.64 V. Two reversible one-electron oxidative peaks at 0.635 V and 0.745 V are observed for the **TrisHR$_2$-OPV$_3$** complex, indicating the formation of the dication. A 60 mV shift of the first oxidative peak (at 0.64 V and

0.635 V for **BisHR$_2$-OPV$_2$** and **TrisHR$_2$-OPV$_3$**, respectively) from OPV **36** is attributed to either the multiple hydrogen bonds formed in the complex, or π-π interactions between two neighbouring OPV molecules, thus changing the HOMO energy level of OPV moiety. The absence of an oxidative peak for the other OPV molecule is probably due to a very high oxidative potential due the presence of the nearly radical cation. The observed second oxidative peak (at 0.745 V, Figure 5.25) of **TrisHR$_2$-OPV$_3$** complex is corresponding to the third OPV molecule. Thus in the presence of first radical cation, it results a 0.11V shift at the forward direction.

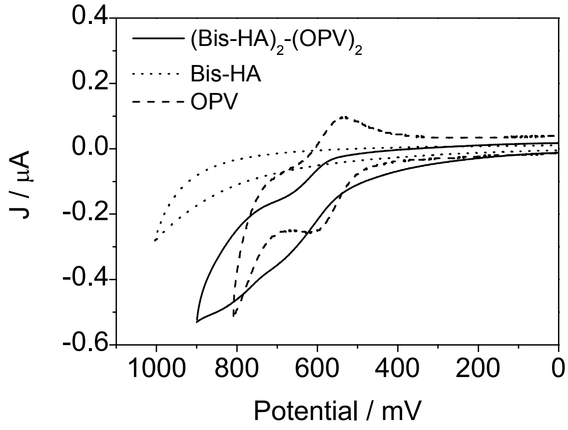

Figure. 5.32. Cyclic voltammetry diagram of OPV **36** (dash line), bis-receptor (dot line) and the complex **BisHR$_2$-OPV$_2$** (solid line) in CH_2Cl_2 containing 0.1 M Bu_4NPF_6 as electrolyte (set Fc/Fc$^+$ *vs.* Ag wire as zero, scan rate = 50 mVs^{-1}).

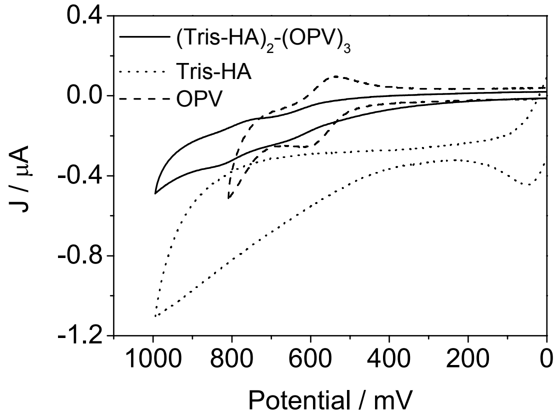

Figure. 5.33. Cyclic voltammetry diagram of OPV **36** (dash line), tris-receptor (dot line) and the complex **TrisHR$_2$-OPV$_3$** (solid line) in CH_2Cl_2 containing 0.1 M Bu_4NPF_6 as electrolyte (set Fc/Fc$^+$ *vs.* Ag wire as zero, scan rate = 50 mVs^{-1}).

UV-visible spectroscopy study

The study of supramolecular assembly **BisHR$_2$-OPV$_2$** by UV-Vis spectroscopy reveals more information of complex stability and possible π-π interactions. Figure 5.26 shows the absorption spectra of free OPV **36** and **BisHR$_2$-OPV$_2$** complex at different concentrations (10^{-4} and 10^{-5} M, in $CHCl_3$). The identical extinction coefficient (ε = 78500 at 570nm) of OPV **36** at different concentrations excludes the possible intermolecular π-π interaction of the free molecules. Also, almost identical absorption behavior are observed for the complex **BisHR$_2$-OPV$_2$** (Figure 5.26, A and B) indicating a strong complexation tendency in the assembly. Notably, a lower extinction coefficient in the absorption spectra of **BisHR$_2$-OPV$_2$** (between 600 and 700 nm) is accompanied by a slight shift of the absorption envelope to longer wavelength. These are characteristic of the formation of H-aggregates.

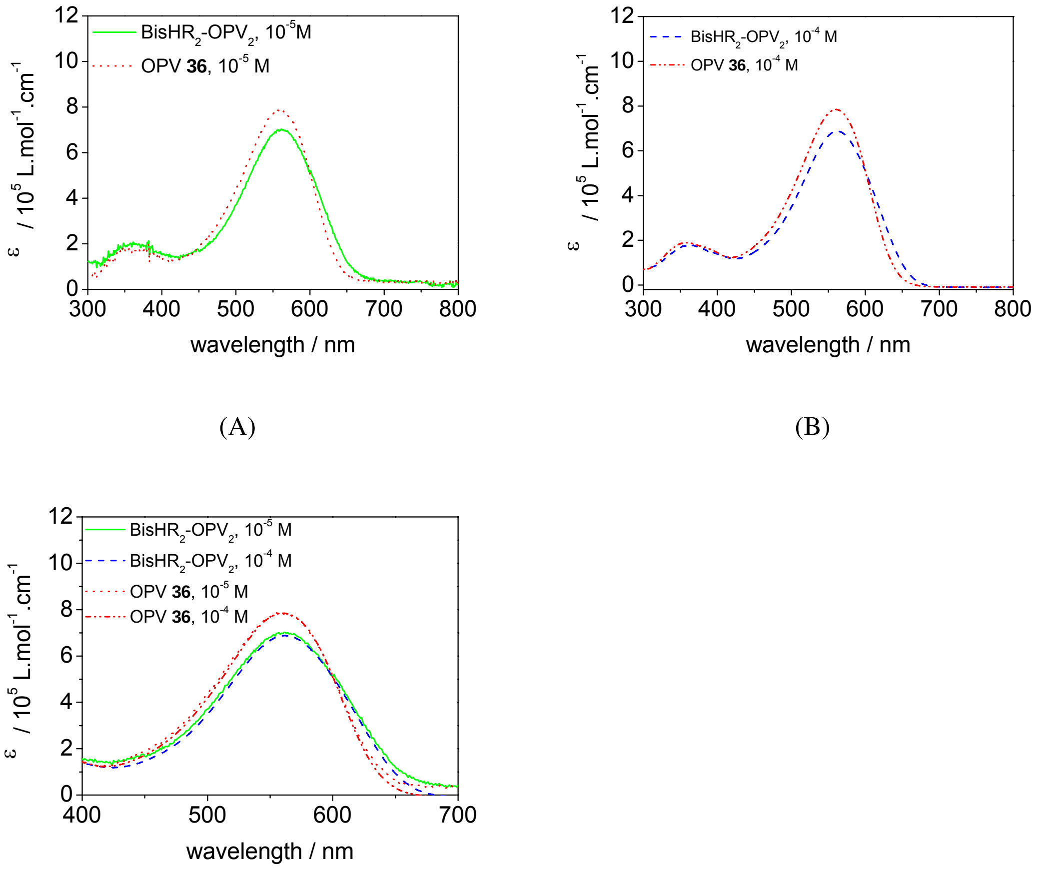

(A)

(B)

(C)

Figure 5.34. Absorption spectra of: (A) in 10^{-5} M, OPV **36** (dot line) and complex **BisHR$_2$-OPV$_2$** (solid line); (B) in 10^{-4} M, OPV **36** (dash-dot-dot line) and complex **BisHR$_2$-OPV$_2$** (dash line); (C) overlapped spectrums of (A) and (B); solvent: $CHCl_3$.

Up to present, and with the preliminary results described above, it is possible to conclude that the hydrogen-bonded supramolecular complexes do assemble in non-polar solvents ($CHCl_3$ or 1,2-tetrachloroethane). The investigation by NMR reveals that the multiple hydrogen bonds form between the barbituric moieties and receptors, and the titration experiment suggests a possibly slow exchange process. The observations in the electrochemical and the photophysical measurements indicate the HOMO energy level of the assembled OPV moieties different from the HOMO of freestanding molecule due to the formation of H-aggregate structures. A control experiment in which OPV **36** assembles with mono-receptor is required to clarify the absence of the hydrogen-bonding influencing the HOMO and LUMO of POV **36**. Ultimately, a crystalline structure will be the direct evidence for the formation of these H-B supramolecular architectures.

References:

1. (a) S.-K. Chang, A. D. Halmiton, *J. Am. Soc. Chem.* **1988**, *110*, 1318-1319.; (b) P. Tecilla, R. P. Dixon, G. Slobodkin, D. S. Alavi, D. H. Waldeck, A. D. Hamilton, *J. Am. Chem. Soc.* **1990**, *112*, 9408-9410. (c) P. Tecilla, A. D. Halmiton, *J. Chem. Soc. Chem. Commun.* **1990**, 1232-1234. (d) S.-K. Chang, D. van Engen, E. Fan, A. D. Halmiton, *J. Am. Soc. Chem.* **1991**, *113*, 7640-7645.; (e) S. J. Geib, C. Vicent, E. Fan, A. D. Hamilton, *Angew. Chem., Int. Ed. Engl.* **1993**, *32*, 119-121.
2. Dr. D. M. Bassani, University Bordeaux 1, CNRS 5802, France, Unpublished results.

Chapter 6

Summary and Conclusion

Solar cells capable of efficient light-to-electrical energy conversion will represent an important component of future renewable energy sources. In this context, fullerene-based photovoltaic devices are promising candidates for the development of high performance all-organic devices. The aim of this doctoral research is to focus on the implementation of supramolecular self-assembly of photo-and electro-active components programmed to self-organize into molecular hetero-junctions to efficiently construct complex fullerene-containing supramolecular architectures suitable for solar energy conversion. In this approach, hydrogen-bonded melamine-cyanuric acid assemblies were chosen because of their unique property of forming linear, tape-like structure able to induce phase separation of the components at the molecular-level during the self-assembly process. In these architectures, charge separation and migration are expected to be more efficient than in conventional blended materials, potentially leading to improved devices performance.

The first part of this study focused on the design and the synthesis of new photoactive materials capable of undergoing self-assembly. From the synthetic point of view, the introduction of hydrogen-bonding molecular recognition motifs in direct conjugation to oligothiophene or oligo(*p*-phenylene vinylene)s units *via* a Schiff base reaction or Knoevenagel condensation provides a straightforward route from the corresponding dialdehyde intermediates. This strategy is applicable and of interest for the preparation of ordered supramolecular assemblies. In addition, the synthesis of EDOT-containing oligothiophene derivatives and their substitution with melamine and barbitrate moieties was also achieved successfully. The development of straightforward, high-yielding synthetic procedures that do not require column purification by chromatography is amenable to scale-up.

The assembly of fullerene **1** and oligothiophene **7** *via* hydrogen bonding was examined by fluorescence microscopy to visualize the residual fluorescence in drop-cast thin films. In the presence of **1**, the oligomer fluorescence is comprehensively quenched, indicating that the fullerene and oligothiophene components are more homogeneously dispersed compared to other films where **7** is blended with pristine C_{60}. The latter presents considerable heterogeneity, presumably due to phase separation during the deposition process. In practical terms, this result reveals that the compatibility between inherently incompatible compounds such as oligothiophenes and C_{60} can be significantly enhanced by the presence of complementary molecular recognition groups.

To test the photovoltaic capability of hydrogen-bonded self-assembly, prototype devices incorporating with the recognition motifs-bearing photoactive materials were built on bare gold electrode and were studied in photoelectrochemical cells. The investigation of photovoltaic response reveals very promising, showing 2.5-fold, and 5-fold enhancement in photocurrent compared to the pristine C_{60}-blended oligothiophene and to the oligothiophene alone, respectively. These findings clearly indicate that a substantial increase in photovoltaic efficiency results from the use of fullerene **1** capable of undergoing self-assembly with the oligothiophene **7**. Thus the hydrogen-bonding pattern employed is conducive to the formation more performant devices.

Device fabrication on self-assembled monolayer, bearing H-B sites brings another unexpected breakthrough. A further 6-fold enhancement of photocurrent is observed in the corresponding self-assembly devices based on modified gold electrodes where the SAMs molecules have barbitrate end groups. In these devices, it is found that the performance is limited by the diffusion rate of the electron-carrying species (methyl viologen) in solution rather than by the charge carrier mobility in the assembly. By systematically examining the behavior of devices on different SAM modified surfaces, we conclude that the improvement of the photovoltaic response when using the SAM modified surfaces originates from two effects. (1) Based on the formation of hydrogen-bonded networks, the superposition of two levels of self-assembly facilitates the generation of binary supramolecular architectures. Hence, a promotional alignment occurred in the self-assembly accelerating the charge transport. (2) The introduction of the alkyl chain inhibits the phonon quenching of the excited states when generated in close proximity to the gold surface.

Solid-state devices were fabricated in order to demonstrate the capability of hydrogen-bonded supramolecular chemistry towards to all-organic solar cells, but suffered from the poor processability of the molecules. The preliminary devices constructed using in a lamellar structure with a thin polymer layer (MDMO-PPV or P3HT) to isolate PEDOT/PSS from the self-assembled materials were more promising. Although this prototype only shows moderate photocurrent (I_{SC} 0.18 mA/cm^2) and V_{OC} shift (0.4 V), it is plausible to expect better performance relying on further understanding in nanomorphology of supramolecular self-assembly and on the investigation of more processible materials which can directly deposit on top of PEDOT/PSS without other assistant layers

In conclusion, starting from molecular engineering to material synthesis and device fabrication, the results from this research reveal the potential of supramolecular chemistry towards future applications in photonic devices. Although substantial progress has been made in this project, huge space for future discovery still remains.

Future challenges are to better understand the nanomorphology of the supramolecular organization to design materials which are more solution processible, and to develop solid-state device fabrication procedure compatible with self-assembly processes. From a fundamental perspective, direct evidence for the self-assembled structure in the solid state would be very interesting. The supramolecular self-assembly of EDOT-containing oligothiophene and [60]fullerene derivatives presented here is the preliminary demonstration towards to this photovoltaic devices. The concept of hydrogen-binding self-assembly can be extended to other potentially photoactive species: for example, chromophores with large absorption bands matched to the solar spectrum such as zinc phthalocyanines, oligo(*p*-phenylene vinylene)s, or poly(9,9'-dioctylfluoreneco-benzothiadiazole) F8TB analogues; even other electron acceptors such as perylene bisimide derivatives, [n]fullerenes (n ≧ 70), or single-walled carbon nanotubes (SWCNs). Compared to silicon-based and dye-sensitized solar cells, the power conversion efficiency of all-organic devices (up to 5 %) is still quite low. This field developed tremendously since 1992, and it is an exciting and fast-pored area for scientists. Solar energy is inexhaustible, and this clean and regenerative energy source will be the ultimate solution for the future development of human society.

Chapter 7

Experimental Section

7.1 General

^{1}H NMR and ^{13}C NMR spectra were recorded at room temperature on a Bruker DPS-200 FT, AC-250 FT or DPX-300 FT spectrometer using the residual solvent proton peaks as internal references unless otherwise indicated. Chemical shifts are given in ppm (δ) with respect to tetramethylsilane. Abbreviations used are s = singlet, d = doublet, t = triplet, q = quartet, and br = broad. Mass spectra were recorded on a VG Autospec-Q by EI (70 eV); m/z (%). High resolution mass spectra were recorded on a FTICR mass spectrometer Bruker 4.7T BioApex II. The elemental analysis was carried out by the Service Centrale d'Analyse at Vernaison (CNRS-France). Merck silica gel 60 (70-230 mesh) was used for flash chromatography. Electronic absorption spectra were obtained using a Hitachi U-3300 spectrophotometer. Fluorescence spectra were recorded on a Hitachi F-4500 fluorescence spectrophotometer. Fluorescence microscopy images were taken on a Nikon Eclipse E600 FN instrument equipped with a 365 nm excitation filter.

7.2 Materials

All commercially available starting materials from Aldrich, Lancaster, Avocado, and anhydrous solvent: absolute ethanol, chlorobenzene, 1,2-dichlorobenzene, DMSO and DMF (Fluka) were used as received. Dichloromethane, chloroform and acetonitrile were distilled over calcium hydride (CaH_2). Tetrahydrofuran (THF) , toluene, and diethyl ether were distilled over sodium / benzophenone immediately before use. All reactions were carried out under a nitrogen atmosphere. The polycrystalline gold electrodes [nickel (80 Å), chromium (20 Å) and gold (3900 Å) on 1.0 mm glass] were purchased from ACM France.

Gold substrates cleaning, self-assembled mono- and multilayer preparation and photoelectrochemical devices preparation

The gold electrodes were cut into slides (ca. 2.5 cm x 1.0 cm) and were cleaned by immersion in “piranha” solution (H_2SO_4 / 30% H_2O_2, 7:3 (v/v); *Caution: “Piranha” solution is an extremely dangerous oxidizing agent and should be handled with care using appropriate shielding*) for 30 min, and were then rinsed with deionized water and absolute ethanol, and dried with a stream of argon.

For SAM-based gold substrates, the clean gold slides were immersed in anhydrous THF : ethanol (1:5) mixed-solutions of alkylthioacetate terminated **39**, **40**, **41**, **42**, **43**, **44**, or **47** (1.0 mM) overnight. To remove any solution-deposited material, the slides were then rinsed with ca. 5 mL of anhydrous ethanol, followed by immersing in an ethanol solution for 5 min, and then dried with a stream of argon. The self-assembled multilayer modified gold substrate was prepared by immersing of molecule **39** SAM patterned gold substrate into a 1,2-dichlorobenzene solution saturated with molecule **28** overnight, and then immersing into a clean CH_2Cl_2 solution for 5 seconds, thendried with a stream of nitrogen.

The porphyrin decorated gold substrates, including porous Au electrodes, were prepared in the same condition as the preparation of the monolayer except for immersing the electrodes in a chloroform solution of the thioacetate porphyrin. The modified electrodes were immersed in a clean chloroform solution, and then in a THF solution to diffuse out any physico-adsorbed porphyrin in the bottom porous layers. Fullerene-assembled porphyrin monolayer was prepared by immersing the corresponding monolayer-modified gold electrode in a fullerene-containing toluene solution (0.2 mg/mL) overnight, and then was flushed with nitrogen.

For all electrochemical photovoltaic devices described in chapter 3, deposition was carried out by drop-casting 20 μL of 2×10^{-5} M DMSO solutions of oligothiophene **7** with 2.0 eq. of fullerene **1** in the presence of a self-adhesive plastic mask. The slow evaporation of the solvent under reduced pressure left a thin film of material on a well-defined area (0.254 cm^2) of the gold electrode. The modified slide was then dried with a stream of argon and before use in photoelectrochemical measurements.

7.3 Solid-state device fabrication

ITO/glass substrate was etched by immersing into a HNO_3 : HCl (1:3 ratio) mixed solution at room temperature for 20 min and monitored by the ohmmeter, followed by rinsing with deionized water and absolute ethanol. Partial etched ITO/glass substrates were cleaned in ultrasonic baths of acetone and 2-propanol for 20 min. The organic films were prepared under ambient conditions or in an Argon glove box. Poly(3,4-ethylenedioxythiophene) doped with polystyrene sulfuric acid (PEDOT:PSS, HC Stark) from an aqueous solution with a concentration of 0.5% (wt.) was stirred for 30 min and filtered through a 0.45 μm membrane just prior to casting. The PEDOT:PSS solution was spun onto ITO-glass substrates and then was dried under vacuum for 40 min. All polymer solutions were prepared by dissolving MDMO-PPV or P3HT in chlorobenzene (HPLC grade, Aldrich) with the respective concentration (mg/mL). The solutions were stirred overnight under ambient temperatures without any sonication or filtering. The polymer (MDMO-PPV or P3HT) films were prepared by spin coating from chlorobenzene solutions of the materials onto (PEDOT:PSS)/ITO-glass substrates and then dried under vacuum for 40 min. The spin casting procedure included 40 s of 1500 rpm followed by 20 s of 2000 rpm. The deposition of the photoactive material was carried out by drop-casting 100 μL of **7** and **1** (1:2 molar ratio, 2.0 x10^{-4} M) DMSO solution. The slow evaporation of the solvent under reduced pressure left a thin film of material on the polymer/PEDOT:PSS/ITO/glass substrate. Deposition of the top electrode was proceeded by thermal evaporating of Al at 10^{-6} mbar through a shadow mask to define a device area of 10 mm^2. All electrodes were non-transparent with a thickness of ~ 110 nm. The thickness was controlled by an oscillating quartz monitor. After evaporation of the metal, electrode devices were characterized in a dry-box under an argon atmosphere. The *J*/*V* characteristics of the devices were recorded in the dark and under illumination using a source-meter (Keithley 2400) while illuminating the devices through the ITO/PEDOT side with 100 mW/cm^2 white light from a solar simulator (AM 1.5).

7.4 Experimental Conditions

Electrochemistry measurement

All electrochemical studies were performed on a BAS100B Electrochemical Analyzer. (Bioanalytical Systems, Inc.) Cyclic voltammograms of molecules **10** in solution phase were recorded in CH_3CN with 0.1 M tetrabutylammonium hexafluorophosphate ($TBAPF_6$) as the supporting electrolyte. The working electrode was a graphite disc, the counter electrode was a platinum wire, and an Ag wire in 0.1 M $TBAPF_6$ acetonitrile solution was used as the reference electrode. The reported oxidation potential was obtained with a scan speed of 20 mV.s^{-1}. The cyclic voltammograms of SAM's layer slides were recorded in 1 mM $K_3[Fe(CN)_6]$ aqueous solution with 0.1 M KNO_3 as the supporting electrolyte. The working electrode was a modified gold slide, the counter electrode was a platinum wire (o.5 mm diameter), and an Ag/AgCl (saturated KCl) reference electrode was used. The Fe^{3+}/Fe^{2+} redox potential was obtained with a scan speed of 50 $mV.s^{-1}$.

For 1/2, 3/2, and 5/2 layer macroporous gold substrates, the total surface area measurement and calculation were performed in a 0.5 M H_2SO_4 aqueous solution according to the literature.[1] Electrochemical desorption experiments were carried out in a PBS solution (pH = 7.4). The modified electrodes were biased at -1.0 V (vs. Ag/AgCl) for 5 min resulting in desorption of the SAM.

Photoelectrochemical measurement

The photoinduced current was measured in a three-electrode arrangement, a modified gold working electrode, a platinum wire counter electrode (the distance between the two electrodes is 0.5 cm), and a Ag/AgCl (saturated KCl) reference electrode in a UV cell (10 mL) under ambient atmosphere. The cell was illuminated with the band-pass filter (EL-1, filter assy. 400-500nm, Engineered Fiber Optic System, Canada) using a 50 W miniature Arc lamp (EXFO, E-3000 UV/Visible spot curing system) with a EXFO liquid light guide output (1.0 m) on the modified slide (the distance between light output and the working electrode is 2.0 cm). The device in a three-electrode system are denoted as Au/(device X)/MV^{2+}/Pt at applied potential: -100 mV *vs.* Ag/AgCl. The electrolyte solution: 0.1 M sodium sulfate aqueous solution containing 5 x 10^{-3} M methyl viologen dichloride (MV^{2+}) as electron carrier. The light intensity was monitored by an EXFO UV/Visible R5000 Radiometer, and the incident light intensity was determined to be 150 $mW.cm^{-2}$.

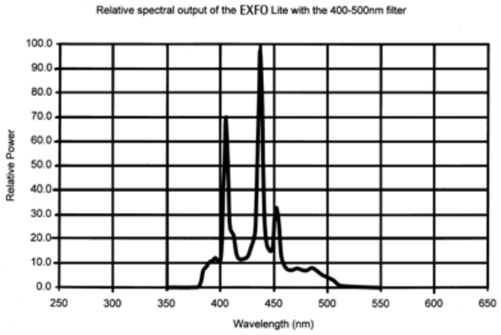

Figure 7.1. Relative spectral output of the EXFO Lite with the 400-500 nm filter (source: http://www.exfo.com/support/techdocs.asp).

Ellipsometry measurement

The ellipsometer (Ielli2000, Nanofilm Technologie GmbH, Germany) equipped with a frequency doubled Nd-Yag laser ($\lambda = 532$ nm, Pmax = 50 mW), was used for the thickness measurements, and the obtained data were analyzed with the furnished software. The incident angle was set to 65°. A refractive index of 1.50 was assumed for all films in the calculation of the thickness.

7.5 Synthesis

2,5-Bis[(2''',4''',6'''-triaminopyrimidinyl-5'''-yl)-5''-enaminyl-5',2''-bithienyl-2'-yl]-3,4-ethylenedioxythiophene.[2] **(7)**

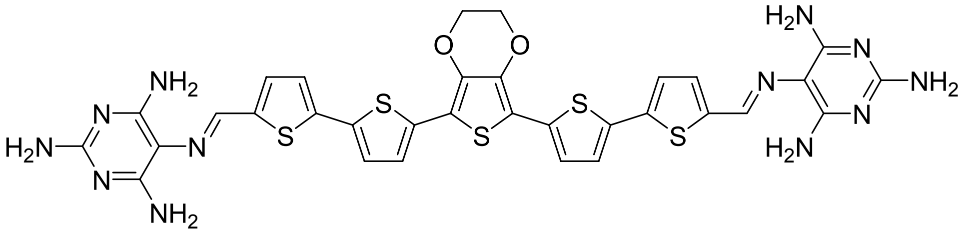

A solution of the 2,5-Bis(5''-formyl-5',2''-bithienyl-2'-yl)-3,4-ethylenedioxythiophene **13** (0.18 g 0.34 mmol) and 2,4,5,6-tetraaminopyrimidine sulfate (1.2 g, 4.88 mmol) in ethanol:DMSO (40 mL, 3:1, v/v) was added (*i*-Pr)$_2$NEt (4.0 mL) in one portion, and then the reaction mixture was stirred at reflux under $N_{2\,(g)}$ for 3 days. After cooled to room temperature, the resulting black solution was poured into water (300 mL). The precipitate was collected and washed with water, ethanol and diethyl ether. The solid was dried under vacuum and used without further purification (0.16g, yield = 61%). ^{1}H NMR (200MHz, d_6-DMSO) δ 8.62 (s, 2H, CH=N), 7.20-7.40 (m, 8H, ArH), 5.93 (s, 8H, NH$_2$), 5.68 (s, 4H, NH$_2$), 4.50 (s, 4H, OCH$_2$). FAB-MS *m/z* (M+H$^+$, 771.9). HRMS (M$^+$, 771.0994, Calcd 771.0984).

2,5-Bis(5',2''-bithienyl-2'-yl)-3,4-ethylenedioxythiophene.[2] (10)

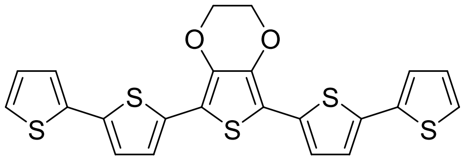

To Tetrakis(triphenyl phosphine) palladium(0) (1.74 g, 1.50 mmol), potassium carbonate (16.58 g, 120.16 mmol), and 2,5-dibromo-3,4-ethylenedioxythiophene **11** (4.50 g, 15.02 mmol) in toluene:water (40 mL, 3:1, v/v), was added a solution of the 2-bithienyl boronate ester **12** (10.15 g, 34.54 mmol) in THF (30 mL), in one portion. The reaction mixture was degassed by bubbling $N_{2\,(g)}$ through the solution for 20 min., which was then stirred under reflux for a further 20 h. After cooling to room temperature, the dark black solution was filtered through a short celite column, which was washed with THF (300 mL). The filtrate was dried over $MgSO_4$ and concentrated under reduced pressure to give a black solid, to which was then added EtOH (70 mL). The precipitated was isolated by filtration, washed with EtOH (10 mL), and dried under vacuum to give a brown solid (6.60 g, yield = 90%). ^{1}H NMR (300 MHz, $CDCl_3$) δ 7.19 (dd, 2H, *J* = 5.2; 1.1 Hz, ArH), 7.16 (dd, 2H, *J* = 3.8; 1.1Hz, ArH), 7.09 (m, 4H, ArH), 7.0 (dd, 2H, *J* = 5.2, 3.8 Hz, ArH), 4.41 (s, 4H, OCH_2); ^{13}C NMR (75 MHz, $CDCl_3$) δ 137.7, 137.4, 135.8, 133.3, 127.9, 124.2, 123.9, 123.5, 123.4, 109.6, 65.0. ESI-MS *m/z* (M^+, 470.1). HRMS (M^+, 469.9589, Calcd 469.9597). Anal. Calcd for $C_{22}H_{14}O_2S_5$: C 56.14, H 3.00, S 34.06. Found: C 56.43, H 2.22, S 32.05.

2,5-Dibromo-3,4-ethylenedioxythiophene.[3] (11)

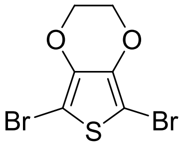

N-Bromosuccinimide (11.22 g, 63.0 mmol) was added to a solution of 3,4-ethylenedioxythiophene (4.26 g, 30.0 mmol) in THF:AcOH (120 mL, 1:1 v/v), and the reaction mixture was stirred at room temperature for 2 h. The resulting black solution was poured into water (700 mL). The precipitate was collected, washed with water (200 mL) and dried under vacuum to give a grey solid (8.32 g, yield = 92%). ^{1}H NMR (200 MHz, $CDCl_3$) δ 4.25 (s, 4H, OCH_2)

2-(2'-dithienyl)-4,4,5,5-tetramethyl-1,3,2-dioxaborolane.[4] (12)

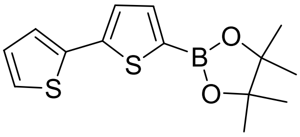

To 2,2'-Bithiophene (6.78 g, 40.0 mmol) in THF (50 mL) under $N_{2\,(g)}$ at –80°C was added *n*-butyl lithium (2.5 M, 16.8 mL, 42.0 mmol) over 10 min., and then the solution was stirred at –50°C for another 30 min. After cooling to -80°C, the suspension was added to a solution of the boronate ester (10.7 mL, 80.0 mmol) in THF (10 mL) over 5 min. The resulting solution was stirred at room temperature overnight. The reaction mixture was poured into $NH_4Cl_{\,(aq)}$ (1.0 M, 400 mL) and extracted with diethyl ether (2 x 200 mL). The organic layers were combined and washed with water (200 mL) followed by saturated $NaCl_{\,(aq)}$ (150 mL). The ethereal solution was then dried over $MgSO_4$, and concentrated to give a blue liquid (11.65 g). The crude blue liquid was used in the cross-coupling reaction without further purification. ^{1}H NMR (200 MHz, $CDCl_3$) δ 7.51 (d, 1H, *J* = 3.5 Hz, ArH), 7.21-7.23 (m, 3H, ArH), 6.98-7.02 (m, 1H, ArH), 1.33 (s, 12H, CH_3).

2,5-Bis(5''-formyl-5',2''-bithienyl-2'-yl)-3,4-ethylenedioxythiophene.[2] **(13)**

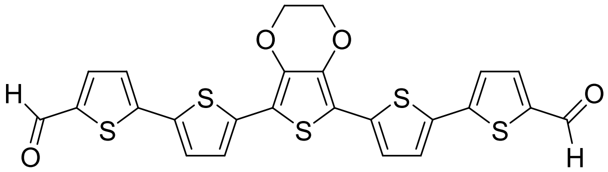

A solution of 2,5-Bis(5',2''-bithienyl-2'-yl)-3,4-ethylenedioxythiophene **10** (0.5 g, 1.1 mmol) in 1,2-dichloroethane (30 mL) and DMF (4.0 mL) was cooled to 0°C, and $POCl_3$ (3.0 mL) was added drop wise over 5 min. The reaction mixture was gradually warmed to room temperature over 4 h, and was then stirred at reflux overnight. After cooling to room temperature, an aqueous solution of sodium acetate (20 mL, 1.0 M) was added, and stirring was continued for 3 h. The resulting black solution was poured into water (400 mL). The black precipitate was collected and washed sequentially with water, THF, acetone, dichloromethane, and diethyl ether and then dried under vacuum (0.46g, yield = 82%). ^{1}H NMR (200MHz, d_6-DMSO) δ 9.87 (s, 2H, CHO), 7.98 (d, 2H, *J* = 3.7 Hz, ArH), 7.56 (m, 4H, ArH), 7.28 (d, 2H, *J* = 3.8 Hz, ArH), 4.52 (s, 4H, OCH_2). ^{13}C NMR (50 MHz, *d6*-DMSO, 50 °C) δ 183.8, 145.4, 141.4, 139.2, 139.1, 135.2, 133.9, 127.6, 125.2, 124.7, 65.6. FAB-MS *m/z* (M^+, 526)

2,5-Bis[(2''',4''',6'''-trioxopyrimidinyl-5'''-methylylidene)-5''-enaminyl-5',2''-bithienyl-2'-yl]-3,4-ethylenedioxythiophene.[2] (14)

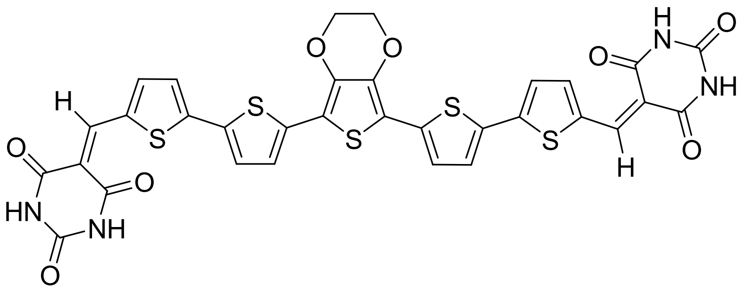

A solution of the 2,5-Bis(5''-formyl-5',2''-bithienyl-2'-yl)-3,4-ethylenedioxythiophene **13** (0.41 g 0.78 mmol) and barbituric acid (0.99 g, 7.78 mmol) in pyridine:ethanol (35 mL, 6:1, v/v) was added piperidine (1.0 mL) drop wise over 1 min, and then the reaction mixture was stirred at 80 ^{0}C under $N_{2\ (g)}$ for 3 h. After cooling to room temperature, the resulting deep-purple mixture was poured into water (400 mL). The precipitate was collected and washed with water, ethanol and diethyl ether. The solid was dried under vacuum overnight (0.52g, yield = 99 %). ^{1}H NMR (300MHz, d_6-DMSO) δ 11.22 (s, 4H, NH), 8.46 (s, 2H, CH=C), 8.13 (d, 2H, J = 4.5 Hz, ArH), 7.68 (d, 2H, J = 3.8 Hz), 7.64 (d, 2H, J = 4.1 Hz, ArH), 7.33 (d, 2H, J = 4.1 Hz, ArH), 4.56 (s, 4H, OCH_2). ^{13}C NMR (50 MHz, *d6*-DMSO, 50 °C) δ 163.5, 163.4, 150.9, 150.3, 147.4, 145.3, 139.2, 135.8, 135.1, 134.4, 127.9, 125.0, 124.8, 110.3, 65.6. Anal. Cacd for $C_{32}H_{18}N_4O_8S_5$: C 51.46, H 2.43, N 7.50. Found: C 51.23, H 3.11, N 7.41.

2,5'-Bis-(3,4-ethylenedioxy)thiophene.[5] (15)

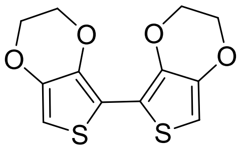

To 3,4-Ethylenedioxythiophene (5.44 g, 38.27 mmol) in dry THF (60 mL) under $N_{2\,(g)}$ at -80°C was added *n*-butyl lithium (2.5 M in hexane, 17.0 mL, 42.10 mmol) over 10 min. The solution was then warmed to -20°C and stirred for another 1h. At -20°C, $CuBr_2$ (9.50 g, 42.10 mmol) was added in one portion, and the resulting dark-blue mixture was stirred at room temperature overnight. The reaction mixture was filtered through a short celite column, which was then washed with diethyl ether (140 mL). The filtrate was washed with water (200 mL), and then brine (200 mL) and dried over $MgSO_4$. Removal of the solvent gave a brown solid, which was dissolved in dichloromethane (10 mL) and was added pentane (60 mL). The precipitate was collected and dried under vacuum (3.40 g, yield = 62%). ^1H NMR (200 MHz, $CDCl_3$) δ 6.25 (2H, ArH), 4.26-4.33 (m, 4H, CH_2), 4.18-4.24 (m, 4H, CH_2).

5,5'-dibromo-2,2'-bis-3,4-ethylenedioxythiophene.[6] (16)

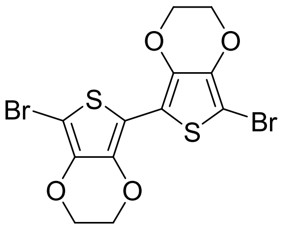

2,2'-Bis(3,4-ethylenedioxythiophene) (0.5 g, 1.77 mmol) in dry dichloromethane (60 mL) at 0℃ was added N-bromosuccinimide (0.67 g, 3.75 mmol), and then was stirred at 0 ℃ for 2h. The blue color mixture was added to 400 mL of dichloromethane and washed with 10% ammonium solution (150mL x 2), water (100mL, x 2), and with brine (150 mL). The pale-brown color solution was dried over $MgSO_{4(g)}$, and the solvent was removed under reduced pressure to give a light-yellow color solid. (0.675g, yield = 94%) ^1H NMR (200 MHz, $CDCl_3$) δ 4.31 (s, 8H, OCH_2).

5,5'-Bis(5'',2'''-bithienyl-2''-yl)-2,2'-bi-3,4-ethylenedioxythiophene. (17)

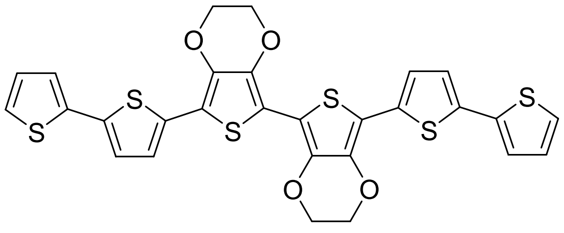

To a solution of tetrakis(triphenyl phosphine) palladium(0) (0.187 g, 0.16 mmol), 2,5'-dibromo-5-2'-bi-3,4-ethylenedioxythienyl **16** (0.658 g, 1.62 mmol), and potassium carbonate (1.79 g, 13.02 mmol) in toluene:water (13 mL, 1:0.3, v/v), was added a solution of the 2-bithienyl boronate ester **12** (1.97 g, 6.53 mmol) in THF (10 mL), in one portion. The reaction mixture was degassed by bubbling $N_{2\,(g)}$ through the solution for 20 min., which was then stirred under reflux for a further 48 h. After cooling to room temperature, the dark black solution was filtered through a short celite column, which was washed with THF (200 mL). The filtrate was dried over $MgSO_4$ and concentrated under reduced pressure to give a black solid, which was then added EtOH (60 mL); isolated by filtration, washed with EtOH (10 mL), and dried under vacuum to give a brown solid (0.59 g, yield = 61%). ^{1}H NMR (200 MHz, $CDCl_3$) δ 7.24-7.15 (m, 4H, ArH), 7.13 (d, 2H, *J* = 4.0 Hz, ArH), 7.09 (d, 2H, *J* = 4.0 Hz, ArH), 7.02 (dd, 2H, *J* = 5.1, 3.8 Hz, ArH), 4.43 (s, 8H, OCH_2); ^{13}C NMR (75 MHz, $CDCl_3$) δ 137.7, 137.4, 135.6, 133.9, 128.0, 124.7, 124.6, 124.4, 124.2, 124.0, 123.4, 123.2, 110.5, 107.9, 65.1.; FAB-MS *m/z* (M^+, 610). HRMS (M^+, 609.6617, Calcd 609.9529).

2-{2'-[5',2''-bis-(3',4'-ethylenedioxythienyl)]}-4,4,5,5-tetramethyl-1,3,2-dioxaborolane.[4] (18)

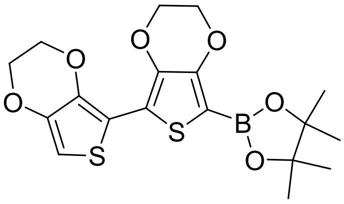

To bis-EDOT **15** (2.01 g, 12 mmol) in THF (30 mL) under $N_{2\,(g)}$ at –80°C was added *n*-butyl lithium (2.5 M in hexane, 16.8 mL, 42.0 mmol) over 10 min. The solution was stirred at –60°C for another 30 min. before cooling to -80°C, at which point it was added to the boronate ester (1.92 mL, 14.3 mmol) in THF (10 mL) over 5 min. The reaction mixture was slowly warmed to room temperature and stirred overnight. The reaction mixture was then poured into $NH_4Cl_{(aq)}$ (1.0 M, 200 mL), and extracted with diethyl ether (2 x 200 mL). The organic layers were combined and washed with water (150 mL), and then saturated NaCl $_{(aq)}$ (150 mL). After drying over $MgSO_4$, the solvent was removed to give a brown solid (2.54 g). The crude product (containing 28% BiEDOT) was used without further purification. ^{1}H NMR (200 MHz, $CDCl_3$) δ 6.29 (1H, ArH), 4.28-4.33 (m, 4H, CH_2), 4.18-4.24 (m, 4H, CH_2), 1.32 (s, 12H, CH_3); FAB-MS *m/z* (M^+, 408). HRMS (M^+, 408.0536, Calcd 408.0873).

5,5'-diiodo-dithienyl.[7] (19)

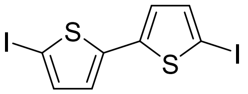

To dithienyl (1.46g, 8.78 mmol) in benzene (20 mL) at 0℃ was added mercuric oxide (3.84g, 17.90 mmol), and iodine (5.03g, 19.9 mmol) in 5 portions over 5 min. The reaction mixture was warmed up to room temperature slowly, and was stirred overnight. The resulting mixture was added to chloroform (200 mL) with vigorous stirring, and then was filtered through a short Celite® column, eluted with another 30 mL chloroform. The filtrate was washed with saturated NaI aqueous solution (150 mL), and then with saturated $Na_2S_2O_3$ solution. The organic layer was separated, dried with $MgSO_{4\,(s)}$, and then concentrated in vaccum. The residue was recrystallized from CHC13/ EtOH mixed-solvent (5/95) to give a white solid. (2.82g. yield = 77%) ^{1}H NMR (300 MHz, $CDCl_3$) δ 7.14 (d, 2H, *J* = 3.8 Hz, ArH), 6.78 (d, 2H, *J* = 3.8Hz, ArH). ^{13}C NMR (75 MHz, $CDCl_3$) δ 142.1, 137.7, 125.5, 72.5.

5,5'-Bis(5'',2'''-bi-(3,4-ethylenedioxy)thienyl-2''-yl)-2,2'-bithiophene. (20)

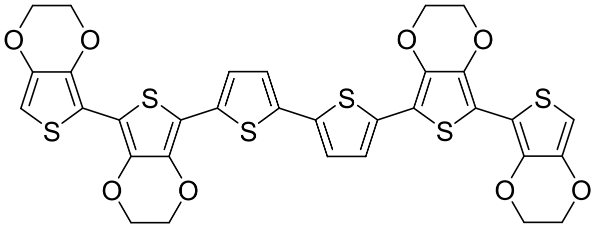

To a solution of tetrakis(triphenyl phosphine) palladium(0) (0.13 g, 0.11 mmol), potassium carbonate (1.23 g, 8.96 mmol), and 5,5'-diiodo-2,2'-bithienyl **19** (0.47 g, 1.12 mmol) in toluene:water (18 mL, 5:1, v/v), was added a solution of the 2-(5,5'-(3,4-ethylenedioxy)bithienyl boronate ester **18** (1.15 g, 2.81 mmol) in THF (15 mL), in one portion. The reaction mixture was degassed by bubbling $N_{2\,(g)}$ through the solution for 20 min., which was then stirred under reflux overnight. After cooling to room temperature, the dark black solution was filtered through a short celite column, which was washed with THF (100 mL). The filtrate was dried over $MgSO_4$ and concentrated under reduced pressure to give a black solid, which was then added EtOH (30 mL); isolated by filtration, washed with EtOH (10 mL), dried under vacuum to give a brown solid. The crude solid was purified by column chromatography, eluted with pentane/THF to give a dark brown solid (0.57 g, yield = 70%). ^{1}H NMR (200 MHz, $CDCl_3$) δ 7.27 (d, 2H, *J* = 3.8 Hz, ArH), 7.15 (d, 2H, *J* = 3.8 Hz, ArH), 6.62 (s, 2H, ArH), 4.45-4.32 (m, 16H, OCH_2).; ESI-MS *m/z* (M^+, 725). HRMS (M^+, 725.2997, Calcd 725.9639).

2,5-Bis(5',2''-bithienyl-2'-yl)-thiophene.[8] (21)

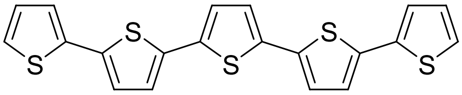

To a solution of tetrakis(triphenyl phosphine) palladium(0) (1.92 g, 1.67 mmol), potassium carbonate (18.5 g, 134.3 mmol e), and 2,5-dibromothiophene (4.18 g, 16.8 mmol) in toluene:water (40 mL, 3:1, v/v), was added a solution of the 2-bithienyl boronate ester **12** (10.80 g, 36.94 mmol) in THF (30 mL), in one portion. The reaction mixture was degassed by bubbling $N_{2\,(g)}$ through the solution for 20 min., which was then stirred under reflux for a further 20 h. After cooling to room temperature, the dark black suspension was filtered through a short celite column, which was washed with THF (300 mL). The filtrate was dried over $MgSO_4$ and concentrated under reduced pressure to give a black solid, which was then added EtOH (300 mL); isolated by filtration, washed with EtOH (30 mL), and diethyl ether (30 mL), and then dried under vacuum to give a orange color solid (5.7 g, yield = 83%). ^1H NMR (200 MHz, *d6*-DMSO/C_6F_6) δ 7.67-7.48 (m, 8H, ArH), 7.20 (dd, 2H, J = 4.0, 2.4 Hz, ArH), 7.11 (dd, 2H, J = 4.0, 2.4 Hz, ArH).

1,4-Bis(2'-ethylhexyloxy)benzene.[9, 10] (23)

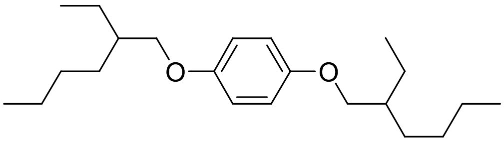

Hydroquinone (22.24 g, 200 mmol), and potassium carbonate (56.58 g, 410 mmol) in 120 mL DMF was added 2-ethylhexyl bromide (76.7 mL, 410 mmol) in one portion and the suspension was stirred at 80℃ for 2 days. After cooling to room temperature, the reaction was poured into water (800 mL), extracted with diethyl ether (300 mL) three times. The combined organic layer was washed with water (400 mL), and Saturated NaCl solution (400 mL), and then dried over $MgSO_4$ and concentrated under reduced pressure to give a brown crude liquid. The resulting liquid was purified by column chromatography (eluted with pure pentane, and pentane/dichloromethane = 4/1) to give a colorless liquid (41.0 g, 62 %). ^{1}H NMR (250 MHz, $CDCl_3$) δ 6.82 (4H, ArH), 3.78 (d, 4H, J = 5.8 Hz, OCH_2), 1.75-1.60 (m, 2H), 1.51-1.30 (m, 16H), 1.00-0.85 (m, 12H).

1,4-Bis(bromomethyl)-2,5-bis(2'-ethylhexyloxy)benzene.[11,12] (24)

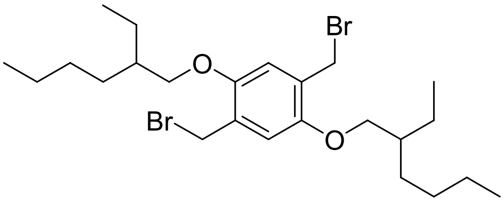

To 1,4-Bis(2'-ethylhexyloxy)benzene **23** (9.20 g, 27.74 mmol) and paraformaldehyde (1.83 g, 61.04 mmol) in acetic acid (60 mL) was added hydrobromic acid (33% in

AcOH, 15 mL) in one portion, and the solution was stirred at 70℃ for 3h. After cooling to room temperature, the resulting clear solution was poured into 500 mL water. The white solid was precipitated and was collected, washed with 50 mL water, dried under vacuum. (12.0 g, 83%) ^{1}H NMR (200 MHz, $CDCl_3$) δ 6.85 (s, 2H, ArH), 4.52 (s, 4H, CH_2-Br), 3.87 (d, 4H, *J* = 5.4 Hz, OCH_2), 1.80-1.68 (m, 2H), 1.60-1.30 (m, 16H), 1.00-0.82 (m, 12H). FAB-MS *m/z* (M^+, 520). HRMS (M^+, 520.8798, Calcd 520.1375).

Diethyl 4-[(Diethoxyphosphoryl)methyl]-2,5-bis(octyloxy)benzylphosphonate.[11,13] (25)

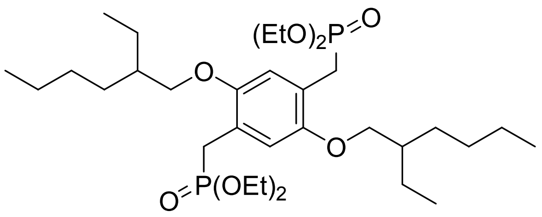

1,4-Bis(bromomethyl)-2,5-bis(2'-ethylhexyloxy)benzene **24** (1.66 g, 3.18 mmol), and triethyl phosphite (4.0 mL, 22.88 mmol) were stirred at 150℃ for 2 h. The excess triethyl phosphite was removed directly under reduced pressure at 90℃ to give a pale-yellow liquid (2.0g, yield = 99%). ^{1}H NMR (200 MHz, $CDCl_3$) δ 6.93 (s, 2H, ArH), 4.08-3.93 (m, 8H, OCH_2-CH_3), 3.80 (d, 4H, *J* = 5.4 Hz, OCH_2), 3.22 (d, 4H, *J* = 20.2 Hz, P-CH_2), 1.75-1.60 (m, 2H), 1.48-1.15 (m, 28H), 0.96-0.86 (m, 12H); ^{13}C NMR (50 MHz, $CDCl_3$) δ 150.4, 119.4, 114.7, 71.2, 61.8, 39.7, 30.6, 29.1, 27.5, 24.8, 23.9, 23.0, 16.3, 14.1, 11,1.

(E)-2,5-Bis-4'-bromostyryl-1,4-bis(2'-ethylhexyloxy)benzene.[9,14] (26)

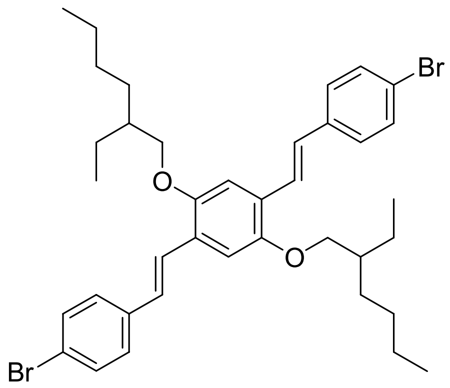

Potassium *tert*-butoxide (1.80g, 15.23 mmol) in 10 mL DMF at 0℃ was slowly added a solution of 4-bromobenzaldehyde (1.47 g, 7.88 mmol) and Diethyl 4-[(Diethoxyphosphoryl)methyl]-2,5-bis(octyloxy)benzylphosphonate **25** (2.33 g, 3.84 mmol) in 10 mL THF. The reaction mixture was stirred at room temperature overnight. The deep-yellow colored mixture was poured into 150 g ice and then 30 mL 6N HCl $_{(aq)}$ were added. The resulting solution was extracted with 150 mL diethyl ether, twice, and the combined organic phase were washed with water (150 mL), brine (100 mL), and dried over $MgSO_4$. After removing the solvent, the residue was purified by column chromatography (pentane/chloroform = 4/1, 3/1,and then 3/2) to give a fresh-yellow liquid. (2.07 g, 77%) ^{1}H NMR (200 MHz, $CDCl_3$) δ 7.50-7.35 (m, 10H, ArH), 7.12-7.03 (m, 4H, ArH and CH=C), 3.95 (d, 4H, *J* = 5.6 Hz, OCH_2), 1.86-1.75 (m, 2H), 1.60-1.30 (m, 16H), 1.02-0.88 (m, 12H); ^{13}C NMR (50 MHz, $CDCl_3$) δ 151.2, 136.9, 131.8, 127.9, 127.6, 126.7, 124.2, 121.1, 110.3, 71.8, 39.7, 30.9, 29.3, 24.2, 23.1, 14.1, 11.3.; FAB-MS *m/z* (M^+, 696). HRMS (M^+, 694.2018, Calcd 694.2020).

(*E*)-2,5-Bis-4'-formyl-1,4-bis(2'-ethylhexyloxy)benzene.[9,15] (27)

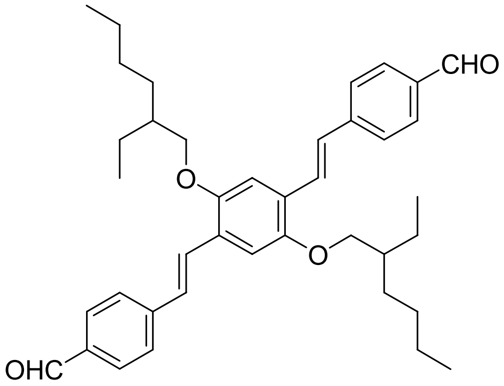

(*E*)-2,5-Bis-4'-bromostyryl-1,4-bis(2'-ethylhexyloxy)benzene **26** (1.53 g, 3.20 mmol) in 10 mL dry diethyl ether at 0℃ was added *n*-butyl lithium (2.87 mL, 6.60 mmol) drop wise over 5 min, and then was stirred at 0℃ for another 40 min. During this time, the reaction became a dark-orange color suspension. 0.5 mL dry DMF was added to the reaction mixture in one portion, and then was stirred at 0℃ for 1 h. After warming up to room temperature, 15 mL 6N $HCl_{(aq)}$ was added to the reaction mixture, and then was extracted with 150 mL diethyl ether twice, and the combined organic layer was washed with water (150 mL), and with brine (100 mL), dried over $MgSO_4$. After removing the solvent, the residue was purified by column chromatography (pentane/chloroform = 3/2, 1/4, and then pure chloroform) to give a fresh-yellow liquid. (1.22 g, 93%) ^1H NMR (200 MHz, CD_2Cl_2) δ 9.98 (s, 2H, CHO), 7.87 (d, 4H, *J* = 8.3 Hz, ArH), 7.69 (d, 4H, *J* = 8.3 Hz, ArH), 7.69 (d, 2H, *J* = 16.6 Hz, CH=C), 7.26 (d, 2H, *J* = 16.6 Hz, CH=C), 7.19 (s, 2H, ArH), 4.00 (d, 2H, *J* = 5.4 Hz, OCH_2) 1.92-1.76 (m, 2H), 1.62-1.30 (m, 16H), 1.05-0.87 (m, 12H); ^{13}C NMR (50 MHz, CD_2Cl_2) δ 192.0, 152.1, 144.5, 135.9, 130.7, 128.3, 127.4, 127.3, 110.9, 72.3, 40.3, 31.5, 29.8, 24.8, 23.7, 14.5, 11.7.; ESI-MS *m/z* (M^+, 594). HRMS (M^+, 594.3717, Calcd 594.3709).

2,5-Bis[(2'',4'',6''-triaminopyrimidinyl-5''-yl)-4'-enaminyl-styryl]-1,4-bis(2'-ethyl hexyloxy)benzene. (28)

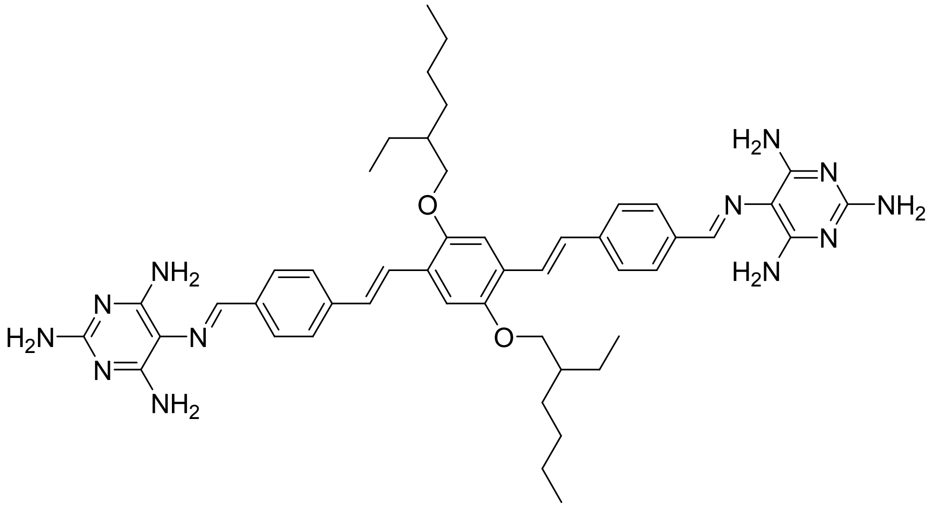

2,4,5,6-tetraaminopyrimidine sulfate (1.96 g, 8.0 mmol), potassium carbonate (1.5 g, 8.0 mmol), and *(E)*-2,5-Bis-4'-formyl-1,4-bis(2'-ethylhexyloxy)benzene **27** (0.6 g, 1.0 mmol) in 2-propanol (8.0 mL) were stirred under reflux for 2 days. After cooling to room temperature, water (150 mL) was added to the reaction. The brown suspension solution was filtered, washed with EtOH (5 mL), then dried under reduced pressure to give a deep-yellow solid (0.57 g, yield = 70 %). ^{1}H NMR (200 MHz, *d6*-DMSO, 125 ℃) δ 8.61 (s, 2H, CH=N), 7.62-7.30 (m, 10H, ArH and CH=C), 5.48 (s, 8H, NH_2), 5.09 (s, 4H, NH_2), 4.05 (d, 2H, *J* = 5.4 Hz, OCH_2) 1.86-1.80 (m, 2H), 1.60-1.35 (m, 16H), 1.05-0.87 (m, 12H); ^{13}C NMR (50 MHz, *d8*-THF) δ 161.9, 159.4, 152.5, 139.0, 128.5, 127.9, 127.3, 111.1, 72.4, 41.1, 32.1, 30.4, 24.3, 14.7, 11.8.

1,4-Bis(2'-ethylhexyloxy)-2-methylbenzene.[9,16] (29)

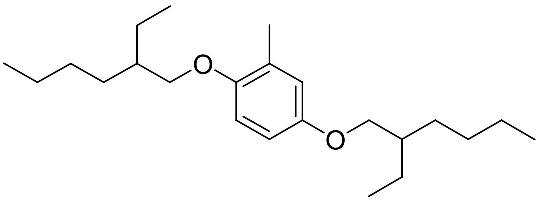

2-Methylhydroquenone (12.54 g, 100 mmol), and potassium carbonate (28.98 g, 210 mmol) in 60 mL DMF was added 2-ethylhexyl bromide (37.4 mL, 200 mmol) in one portion and was stirred at 80℃ for 2 days. After cooling to room temperature, the reaction was poured into water (600 mL), extracted with diethyl ether (300 mL x 2). The combined organic layer was washed with water (300 mL), and saturated NaCl solution (300 mL), and then dried over $MgSO_4$. After removing the solvent, the residue was purified by column chromatography (eluted with pure pentane) to give a colorless liquid. (16.19 g. yield = 46%) ^{1}H NMR (250 MHz, $CDCl_3$) δ 6.75-6.60 (m, 3H, ArH), 3.79-3.75 (m 4H, OCH_2), 2.20 (s, 3H, CH_3), 1.80-1.65 (m, 2H), 1.55-1.20 (m, 16H), 1.05-0.86 (m, 12H, CH_3).

2-Bromomethyl-5-bromo-1,4-bis(2'-ethylhexyloxy)benzene.[17,18] (30)

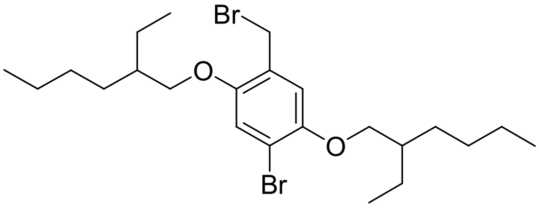

1,4-Bis(2'-ethylhexyloxy)-2-methylbenzene **29** (1.13 g, 3.23 mmol) was refluxed in 10 mL tetrachloromethane and irradiated with a medium pressure mercury vapor lamp

(400 W), and bromine (0.34 mL, 3.55 mmol) was added drop wise over 30 min. The solution was stirred at reflux until the bromine was consumed. After cooling to room temperature, the solution was washed with 30 mL of water, 30 mL of saturated NaHCO3 and again with 30 mL of water; dried over $MgSO_4$. After removing the solvent, the residue was purified by column chromatography (eluted with pentane/ chloroform, 92/8, and then 88/12) to give a pale-yellow liquid. (1.0g, yield = 61%)

^{1}H NMR (200 MHz, $CDCl_3$) δ 7.06 (s, 1H, ArH), 6.88 (s, 1H, ArH), 4.50 (s, 2H, Br-CH_2), 3.86-3.83 (m, 4H, OCH_2), 1.85-1.70 (m, 2H), 1.60-1.30 (m, 16H), 0.97-0.85 (m, 12H, CH_3); ^{13}C NMR (50 MHz, $CDCl_3$) δ 151.2, 149.5, 125.9, 117.0, 115.6, 113.2, 72.4, 71.1, 39.5, 30.6, 30.5, 29.0, 28.5, 24.0, 23.9, 23.0, 14.1, 11.2.

Diethyl [4-bromo-2,5-bis(2'-ethylhexyloxy)benzyl]phosphonate.[9,19] **(31)**

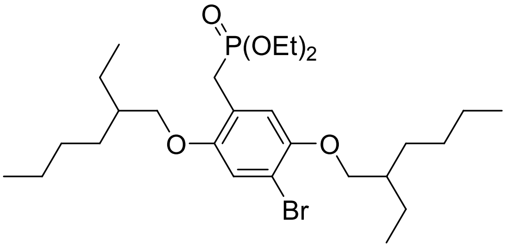

2-Bromomethyl-5-bromo-1,4-bis(2'-ethylhexyloxy)benzene **30** (1.00 g, 1.98 mmol), and triethyl phosphite (0.34 mL, 2.07 mmol) was stirred at 150℃ for 2 h. The excess triethyl phosphite was removed directly under reduced pressure at 150℃, and the liquid residue was used in the next step directly. ^{1}H NMR (200 MHz, $CDCl_3$) δ 7.03 (s, 1H, ArH), 6.97 (s, 1H, ArH), 4.05-3.94 (m, 4H, OCH_2-CH_3), 3.84 (d, 2H, J = 5.5 Hz, OCH_2), 3.78 (d, 2H, J = 5.5 Hz, OCH_2), 3.18 (d, 2H, J = 21.7 Hz, P-CH_2), 1.88-1.60 (m, 2H), 1.50-1.22 (m, 22H), 1.00-0.85 (m, 12H).

1,4-Bis(hydroxymethyl)-2,5-bis(2'-ethylhexyloxy)benzene.[20,21] (32)

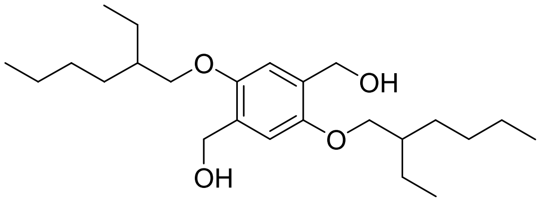

1,4-Bis(bromomethyl)-2,5-bis(2'-ethylhexyloxy)benzene **24** (10.10 g, 19.41 mmol) and calcium carbonate (4.27 g, 42.70 mmol) in 1,4-dioxane/H_2O (110 mL/60 mL) mixed-solvent were stirred at reflux for 2 days. After cooling to room temperature, the solvent was removed, and 300 mL water was added to the residue. The crude solution was acidified by adding dilute HCl $_{(aq)}$ solution until pH value < 3. The solution was extracted with diethyl ether (300 mL), twice, and the combined organic layer was washed with water (300 mL), and with brine (200 mL), dried over $MgSO_4$. The solvent was removed under reduced pressure to give a white solid. (7.36 g, yield = 96%) ^{1}H NMR (250 MHz, $CDCl_3$) δ 6.86 (s, 2H, ArH), 4.67 (d, 4H, J = 6.1 Hz, CH_2-OH), 3.88 (d, 4H, J = 5.2 Hz, OCH_2), 2.35 (t, 2H, J = 6.4 Hz, OH), 1.76-1.60 (m, 2H), 1.53-1.30 (m, 16H), 0.96-0.85 (m, 12H). ^{13}C NMR (50 MHz, $CDCl_3$) δ 150.7, 129.0, 112.0, 70.9, 62.1, 39.5, 30.7, 29.1, 24.1, 23.0, 14.0, 11.1.

2,5-Bis(2'-ethylhexyloxy)terephthaldehyde.[22] (33)

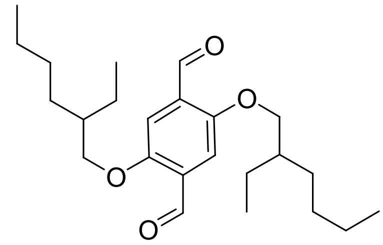

1,4-Bis(hydroxymethyl)-2,5-bis(2'-ethylhexyloxy)benzene **32** (7.36 g, 18.65 mmol), and pyridinium chlorochromate (12.30 g, 55.95 mmol) in 400 mL CH_2Cl_2 were stirred at room temperature for 2 h. The dark-brown color mixture was filtered through a short column (silica gel, 5 cm), eluted with 300 mL CH_2Cl_2. The solvent was removed to give a pale-yellow color liquid (6.20 g, 85%). ^{1}H NMR (200 MHz, $CDCl_3$) δ 10.52 (s, 2H, CHO), 7.44 (s, 2H, ArH), 3.98 (d, 4H, J = 5.6 Hz, OCH_2), 1.85-1.70 (m, 2H), 1.50-1.25 (m, 16H), 1.00-0.85 (m, 12H).

(*E,E*)-2,5-Bis-[4'-bromo-2',5'-bis-(2''-ethylhexyloxy)styryl]-1,4-bis(2'-ethylhexyloxy)benzene.[9,18] (34)

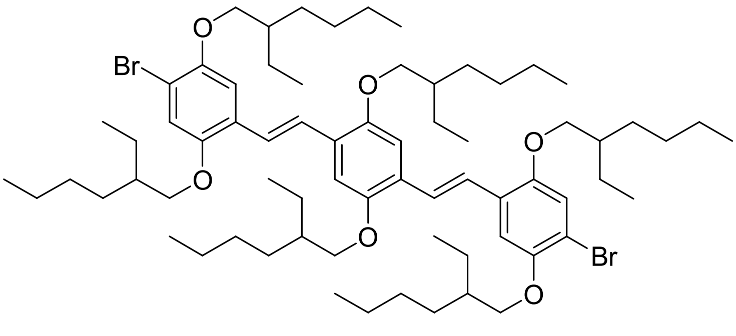

Potassium *tert*-butoxide (1.00g, 8.0 mmol) in 10 mL DMF at 0℃ was slowly added a solution of 2,5-Bis(2'-ethylhexyloxy)terephthaldehyde **33** (0.83 g, 2.12 mmol) and diethyl [4-bromo-2,5-bis(2'-ethylhexyloxy)benzyl]phosphonate **31** (2.45 g, 4.36 mmol) in 10 mL THF. The reaction mixture was stirred at room temperature for 2 days. The deep-yellow color mixture was poured into 200 g ice and then was added 30 mL 6N HCl $_{(aq)}$. The resulting solution was extracted with chloroform (200 mL x 2), and the combined organic layer was washed with water (200 mL), dried over $MgSO_4$. After removing the solvent, the residue was purified by column chromatography (pentane/chloroform = 4/1, 3/1,and then 3/2) to give a fresh-yellow liquid. (1.59 g, 62%) ^{1}H NMR (200 MHz, $CDCl_3$) δ 7.50-7.35 (m, 10H, ArH), 7.12-7.03 (m, 4H, ArH and CH=C), 3.95 (d, 4H, J = 5.6 Hz, OCH_2), 1.86-1.75 (m, 2H), 1.60-1.30 (m, 16H), 1.02-0.88 (m, 12H); ^{13}C NMR (50 MHz, $CDCl_3$) δ 151.0, 150.9, 150.0, 127.1, 123.1, 122.0, 117.6, 111.4, 110.2, 109.4, 72.2, 71.8, 71.4, 39.7, 39.6, 39.5, 30.8, 30.7, 30.5, 29.1, 29.0, 24.3, 24.2, 24.0, 23.1, 14.1, 11.3, 11.2.; FAB-MS *m/z* (M^+, 1208). HRMS (M^+, 1208.3726, Calcd 1208.6805).

(*E,E*)-2,5-Bis-[4'-formyl-2',5'-bis-(2''-ethylhexyloxy)styryl]-1,4-bis(2'-ethylhexyloxy)benzene.[9,23] (35)

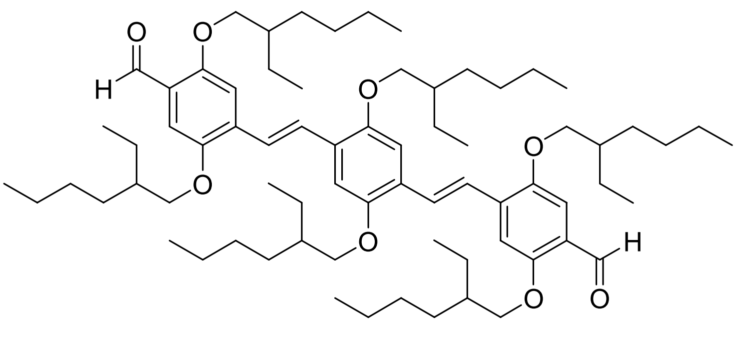

(*E,E*)-2,5-Bis-[4'-bromo-2',5'-bis-(2''-ethylhexyloxy)styryl]-1,4-bis(2'-ethylhexyloxy) benzene 34 (0.89 g, 0.74 mmol) in 10 mL dry diethyl ether at 0℃ was added *n*-butyl lithium (0.88 mL, 2.21 mmol) drop wise over 2 min, and then was stirred at 0℃ for another 40 min. During this time, the reaction became a dark-brown colored suspension. 0.2 mL dry DMF was added to the reaction mixture in one portion, and then was stirred at 0℃ for 1 h. After warming up to room temperature, 15 mL 6N $HCl_{(aq)}$ was added to the reaction mixture, and then was extracted with diethyl ether (100 mL x 2), and the combined organic layer was washed with water (100 mL), and with brine (100 mL), dried over $MgSO_4$. After removing the solvent, the residue was purified by column chromatography (pentane/chloroform = 4/1, 3/1, and then 1/1) to give a fresh-yellow liquid. (0.15 g, 19%) ^{1}H NMR (300 MHz, CD_2Cl_2) δ 10.4 (s, 2H, CHO), 7.66 (d, 2H, *J* = 15.0 Hz, CH=C), 7.53 (d, 2H, *J* = 15.0 Hz, CH=C), 7.30 (s, 2H, ArH), 7.27 (s, 2H, ArH), 7.20 (S, 2H, ArH), 4.00-3.88 (m, 12H, OCH_2) 1.92-1.70 (m, 6H), 1.60-1.20 (m, 48H), 1.05-0.80 (m, 24H); ^{13}C NMR (50 MHz, CD_2Cl_2) δ 196.9, 157.0, 152.0, 151.3, 127.9, 126.5, 124.8, 122.7, 110.4, 110.1, 72.1, 71.8, 40.4, 40.3, 40.2, 31.4, 31.2, 30.3, 29.7, 24.9, 24.6, 23.7, 23.6, 14.4, 14.4, 11.7, 11.5.; FAB-MS *m/z* (M^+, 1107). HRMS (M^+, 1106.7010, Calcd 1106.8154).

(*E,E*)-2,5-Bis-{4'-[(tetrahydro-2,4,6-trioxo-5(2H)-pyrimidinyliene)methyl]-2',5'-bis-(2''-ethylhexyloxy)styryl}-1,4-bis(2'-ethylhexyloxy)benzene. (36)

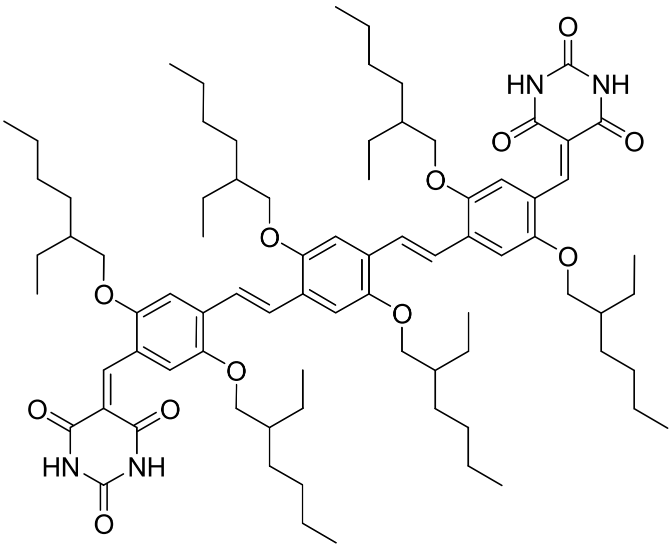

(*E,E*)-2,5-Bis-[4'-formyl-2',5'-bis-(2''-ethylhexyloxy)styryl]-1,4-bis(2'-ethylhexyloxy) benzene **35** (84 mg, 0.076 mmol) and barbituric acid (60 mg, 0.46 mmole) in chloroform/EtOH/H_2O (22 mL, 10/10/2, v/v) mixed-solvent were stirred under reflux overnight. After cooling to room temperature, the solvent was removed, and the residue was dissolved in $CHCl_3$ (50 mL), and was filtered. After removing the solvent, the purple color solid was dissolved in THF (10 mL), and then 100 mL pentane was added to the solution. The solid was precipitated out and was collected by centrifuge; dried under vacuum to give a purple solid (25 mg, yield = 25 %). ^1H NMR (300 MHz, DMSO) δ 11.30 (bs, 2H, NH), 11.19 (bs, 2H, NH), 8.70 (s, 2H C=CH), 8.25 (s, 2H, ArH), 7.67 (d, 2H, *J* = 15 Hz, C=CH), 7.56 (d, 2H, *J* = 15 Hz, C=CH), 7.26 (d, 4H, *J* = 6.0 Hz, ArH), 4.02 (d, 2H, *J* = 4.8 Hz, OCH_2), 3.98 (d, 2H, *J* = 4.8 Hz, OCH_2), 3.91 (d, 2H, *J* = 4.8 Hz, OCH_2), 1.90-1.65 (m, 6H), 1.50-1.25 (m, 48H), 1.0-0.7 (m, 24H).

4-(5-Bromopentyloxy)benzaldehyde.[24]

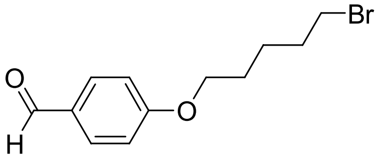

4-Hydroxybenzaldehyde (4.98 g, 40.0 mmol), and potassium carbonate (10.96 g, 80.0 mmol) in 25 mL DMF was added 1,5-dibromopentane (21.2 mL, 160.0 mmol) in one portion and was stirred at 80℃ overnight. After cooling to room temperature, the reaction was poured into water (300 mL), extracted with diethyl ether (200 mL x 2). The combined organic layer was washed with water (100 mL), and saturated NaCl solution (100 mL), and then dried over $MgSO_4$. After removing the solvent, the residue liquid was purified by column chromatography (pentane/ethyl acetate = 80/20) to give a colorless liquid (6.3 g, yield = 58 %). ^{1}H NMR (200 MHz, $CDCl_3$) δ 9.88 (s, 1H, CHO), 7.83 (d, 2H, J = 8.8 Hz, ArH), 6.98 (d, 2H, J = 8.7 Hz, ArH), 4.05 (t, 2H, J = 6.3 Hz, OCH_2), 3.44 (t, 2H, J = 6.7 Hz, Br-CH_2), 2.00-1.76 (m, 4H), 1.70-1.60 (m, 2H).

4-(6-Bromohexyloxy)benzaldehyde.[24]

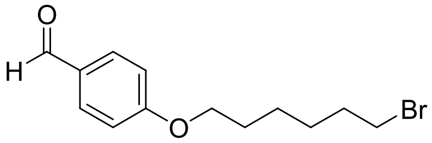

4-Hydroxybenzaldehyde (4.98 g, 40 mmol), and potassium carbonate (10.96 g, 80 mmol) in 50 mL DMF was added 1,6-dibromohexane (26.0 mL, 160.0 mmol) in one portion and was stirred at reflux for 40 h. After cooling to room temperature, the reaction was poured into water (100 mL), extracted with diethyl ether (200 mL x 2). The combined organic layer was washed with water (150 mL), and saturated NaCl solution (150 mL), and then dried over $MgSO_4$. After removing the solvent, the residue liquid was purified by column chromatography (pentane/ethyl acetate = 80/20) to give colorless liquid (7.78g, yield = 68%). ^1H NMR (200 MHz, $CDCl_3$) δ 9.85 (s, 1H, CHO), 7.79 (d, 2H, *J* = 8.8 Hz, ArH), 6.96 (d, 2H, *J* = 8.7 Hz, ArH), 4.01 (t, 2H, *J* = 6.3 Hz, OCH_2), 3.40 (t, 2H, *J* = 6.7 Hz, Br-CH_2), 2.00-1.65 (m, 4H), 1.60-1.42 (m, 4H). ^{13}C NMR (50 MHz, $CDCl_3$) δ 190.6, 164.0, 131.9, 129.7, 114.6, 68.0, 33.6, 32.5, 28.8, 27.7, 25.1.

5-(4'-Formylphenoxy)pentyl thioacetate.[25] (37)

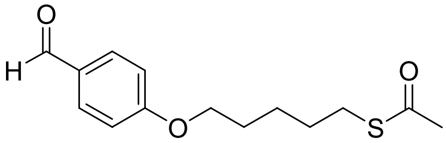

4-(5-Bromopentyloxy)benzaldehyde (1.00 g, 3.68 mmol) and potassium thioacetate (0.43 g, 3.68 mmol) in acetone (20 mL) were stirred at room temperature in the dark overnight. The resulting white precipitate was filtered off and the filtrate was concentrated under reduced pressure to give a white solid (0.97 g, yield = 99%). ^{1}H NMR (200 MHz, $CDCl_3$) δ 9.87 (s, 1H, CHO), 7.82 (d, 2H, *J* = 8.7 Hz, ArH), 6.98 (d, 2H, *J* = 8.7 Hz, ArH), 4.03 (t, 2H, *J* = 6.3 Hz, OCH_2), 2.90 (t, 2H, *J* = 7.0 Hz, S-CH_2), 2.33 (s, 3H, CH_3), 1.87-1.77 (m, 2H), 1.67-1.50 (m, 4H); ^{13}C NMR (50 MHz, $CDCl_3$) δ 195.2, 190.8, 164.1, 132.0, 129.8, 114.7, 104.5, 68.0, 30.6, 29.3, 28.9, 28.5, 25.2.

6-(4'-Formylphenoxy)hexyl thioacetate.[25] (38)

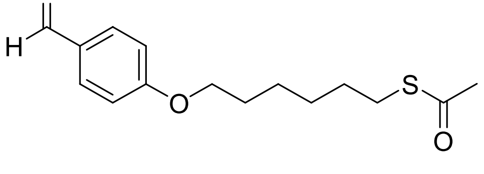

4-(6-Bromohexyloxy)-benzaldehyde (7.78 g, 27.28 mmol) and potassium thioacetate (3.18 g, 27.28 mmol) in acetone (20 mL) were stirred at room temperature in the dark overnight. The resulting white precipitate was filtered off and the filtrate was concentrated under reduced pressure to give a white solid (6.98 g, yield = 91%). ^{1}H

NMR (200 MHz, $CDCl_3$) δ 9.87 (s, 1H, CHO), 7.82 (d, 2H, *J* = 8.7 Hz, ArH), 6.98 (d, 2H, *J* = 8.7 Hz, ArH), 4.03 (t, 2H, *J* = 6.3 Hz, OCH_2), 2.87 (t, 2H, *J* = 7.1 Hz, S-CH_2), 2.32 (s, 3H, CH_3), 1.82-1.76 (m, 2H), 1.67-1.55 (m, 2H), 1.54-1.43 (m, 4H); ^{13}C NMR (50 MHz, $CDCl_3$) δ 195.5, 190.4, 163.9, 131.7, 129.5, 114.4, 104.5, 67.9, 30.3, 29.2, 28.7, 28.6, 28.1, 25.2.; FAB-MS *m/z* (M+H$^+$, 281). HRMS (M$^+$, 280.1018, Calcd 281.1167).

5-{4-[(tetrahydro-2,4,6-trioxo-5(2H)-pyrimidinyliene)methyl]phenoxy}pentyl thioacetate.[26] (39)

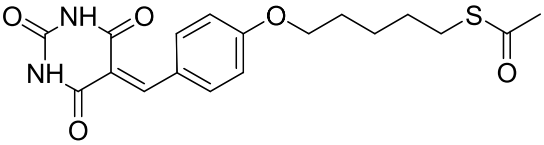

5-(4'-Formylphenoxy)pentyl thioacetate **37** (0.67 g, 2.52 mmol), and barbituric acid (0.33 g, 2.52 mmol) in ethanol : water (14 mL, 5 : 2; v/v), were stirred under reflux for 10 min, and then at room temperature overnight. The resulting yellow suspension was filtered, washed with EtOH (10 mL) and dried under reduced pressure to give a yellow solid (0.87 g, yield = 92 %). ^1H NMR (200 MHz, *d6*-DMSO) δ 11.29 (s, 1H, NH), 11.18 (s, 1H, NH), 8.36 (d, 2H, *J* = 9.0 Hz, ArH), 8.24 (s, 1H, CH=C), 7.05 (d, 2H, *J* = 9.0 Hz, ArH), 4.09 (t, 2H, *J* = 6.4 Hz, OCH_2), 2.86 (t, 2H, *J* = 6.9 Hz, S-CH_2), 2.31 (s, 3H, CH_3), 1.80-1.70 (m, 2H), 1.61-1.43 (m, 4H); ^{13}C NMR (50 MHz, *d6*-DMSO) δ 195.3, 163.9, 162.9, 162.2, 154.9, 150.2, 137.5, 125.0, 115.4, 114.3, 67.8, 30.6, 28.9, 28.2, 27.9, 24.6. APCI-MS m/z (%) 377 (M + 1, 100); 376 (M, 75).

HRMS 376.1088, M^+; Calcd. 376.1093. Anal. Calcd for $C_{18}H_{20}N_2O_5S$: C 57.43, H 5.36, N 7.44. Found: C 57.28, H 5.40, N 7.43.

6-{4-[(tetrahydro-2,4,6-trioxo-5(2H)-pyrimidinyliene)methyl]phenoxy}hexyl thioacetate.[26] (40)

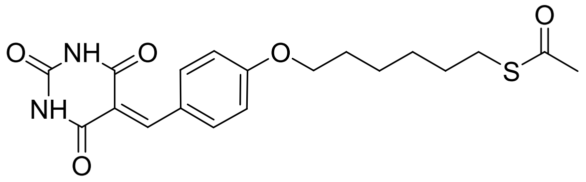

6-(4’-Formylphenoxy)hexyl thioacetate **38** (2.13 g, 7.47 mmol), and barbituric acid (0.97 g, 7.47 mmol) in ethanol : water (22 mL, 10 : 1; v/v), were stirred under reflux for 3 hr. After cooling to room temperature, the resulting yellow suspension was filtered, washed with EtOH (20 mL), chloroform (10 mL), and dried under reduced pressure to give a yellow solid (2.39 g, yield = 85 %). ^{1}H NMR (200 MHz, *d6*-DMSO) δ 11.30 (s, 1H, NH), 11.18 (s, 1H, NH), 8.36 (d, 2H, *J* = 9.0 Hz, ArH), 8.24 (s, 1H, CH=C), 7.05 (d, 2H, *J* = 9.0 Hz, ArH), 4.09 (t, 2H, *J* = 6.4 Hz, OCH_2), 2.83 (t, 2H, *J* = 6.9 Hz, $S\text{-}CH_2$), 2.31 (s, 3H, CH_3), 1.80-1.70 (m, 2H), 1.61-1.43 (m, 6H); ^{13}C NMR (50 MHz, *d6*-DMSO) δ 195.8, 164.4, 163.3, 162.6, 155.4, 150.6, 138.0, 125.4, 115.8, 114.7, 68.3, 29.5, 28.7, 28.6, 28.2, 25.3.; FAB-MS *m/z* (M^+, 391). HRMS (M^+, 391.1310, Calcd 391.1327).

5-{4-[(1,3-dimethyl-tetrahydro-2,4,6-trioxo-5(2H)-pyrimidinyliene)methyl] phenoxy}pentyl thioacetate.[26] (41)

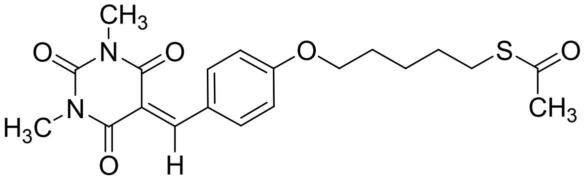

5-(4'-Formylphenoxy)pentyl thioacetate **37** (0.90 g, 3.38 mmol), and N,N'-dimethyl barbituric acid (0.54 g, 3.38 mmol) in benzene:EtOH (50 mL, 4:1, v/v) were stirred under reflux overnight using a Dean-Stark apparatus to remove water. After cooling to room temperature, the solvent was removed, and the residue was dissolved in $CHCl_3$ (100 mL), extracted with saturated aqueous $NaHCO_3$ solution (50 mL), dried over $MgSO_4$. After removing the solvent, the residue was dissolved in chloroform (5 mL) and then was slowly added pentane (150 mL). The yellow precipitate was formed and was collected, washed with 10 mL pentane, and then dried under reduced pressure to give a yellow solid (1.04 g, yield = 76 %). ^{1}H NMR (200 MHz, $CDCl_3$) δ 8.50 (s, 1H, CH=C), 8.31 (d, 2H, *J* = 8.9 Hz, ArH), 6.95 (d, 2H, *J* = 8.9 Hz, ArH), 4.05 (t, 2H, *J* = 6.4 Hz, OCH_2), 3.41 (s, 3H, N-CH_3), 3.39 (s, 3H, N-CH_3), 2.89 (t, 2H, *J* = 7.0 Hz, S-CH_2), 2.33 (s, 3H, CH_3), 1.87-1.77 (m, 2H), 1.67-1.50 (m, 4H); ^{13}C NMR (50 MHz,$CDCl_3$) δ 195.9, 163.8, 163.2, 161.0, 159.0, 151.4, 138.0, 125.3, 114.4, 114.1, 68.0, 30.6, 29.2, 29.0, 28.8, 28.5, 28.4, 25.1.; FAB-MS *m/z* (M^+, 405). HRMS (M^+, 405.1477, Calcd 405.1484).

6-{4-[(1,3-dimethyl-tetrahydro-2,4,6-trioxo-5(2H)-pyrimidinyliene)methyl] phenoxy}hexyl thioacetate.[26] (42)

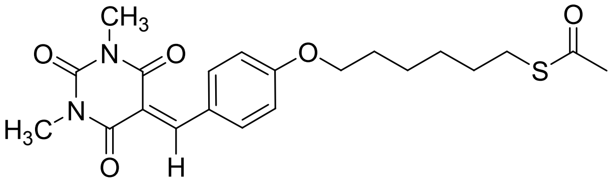

6-(4'-Formylphenoxy)hexyl thioacetate **38** (1.55 g, 5.54 mmol), and N,N'-dimethyl barbituric acid (0.88 g, 5.54 mmol) in benzene (100 mL) were stirred under reflux for 4 h using a Dean-Stark apparatus to remove water. After cooling to room temperature, the solvent was removed, and the residue was dissolved in $CHCl_3$ (100 mL), extracted with saturated aqueous $NaHCO_3$ solution (50 mL), dried over $MgSO_4$, and concentrated under reduced pressure to give a yellow solid (1.65 g, yield = 71 %). ^1H NMR (200 MHz, $CDCl_3$) δ 8.51 (s, 1H, CH=C), 8.32 (d, 2H, *J* = 9.0 Hz, ArH), 6.95 (d, 2H, *J* = 9.0 Hz, ArH), 4.06 (t, 2H, *J* = 6.4 Hz, OCH_2), 3.41 (s, 3H, N-CH_3), 3.39 (s, 3H, N-CH_3), 2.88 (t, 2H, *J* = 7.1 Hz, S-CH_2), 2.33 (s, 3H, CH_3), 1.87-1.77 (m, 2H), 1.65-1.42 (m, 6H); ^{13}C NMR (50 MHz,$CDCl_3$) δ 196.0, 164.0, 163.2, 161.0, 159.0, 151.4, 138.1, 125.3, 114.1, 114.0, 68.2, 30.6, 29.4, 29.0, 28.9, 28.8, 28.4, 28.3, 25.5.; FAB-MS *m/z* (M^+, 419). HRMS 419.1634, M^+; Calcd. 419.1640.

5-{4-[(2,4,6-triamino-N5-pyrimidinyliene)methyl]phenoxy}pentyl thioacetate.[26] (43)

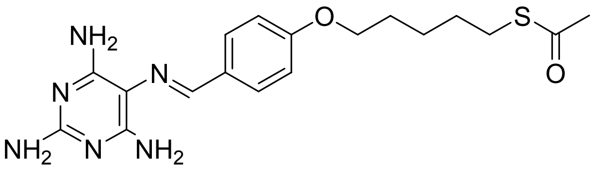

2,4,5,6-Tetraaminopyrimidine sulfate (3.21 g, 13.06 mmol), potassium carbonate (1.79 g, 13.06 mmol), and 5-(4'-formylphenoxy)pentyl thioacetate **37** (0.87 g, 3.27 mmol) in 2-propanol (15 mL) were stirred under reflux overnight. After cooling to room temperature, water (30 mL) was added to the reaction. The brown suspension solution was filtered, washed with water (10 mL), EtOH (10 mL), and diethyl ether (10 mL), then dried under reduced pressure to give a deep-yellow solid (1.31 g, yield = 90 %). ^{1}H NMR (200 MHz, *d6*-DMSO) δ 8.49 (s, 1H, N=CH), 7.79 (d, 2H, *J* = 8.6 Hz, ArH), 6.97 (d, 2H, *J* = 8.7 Hz, ArH), 5.95 (s, 4H, NH_2), 5.65 (s, 2H, NH_2), 4.00 (t, 2H, *J* = 6.3 Hz, OCH_2), 2.86 (t, 2H, *J* = 6.9 Hz, S-CH_2), 2.32 (s, 3H, CH_3), 1.80-1.67 (m, 2H), 1.65-1.43 (m, 4H); ^{13}C NMR (50 MHz, *d6*-DMSO) δ 195.4, 160.0, 159.2, 157.1, 152.9, 130.8, 129.0, 114.3, 102.0, 67.4, 30.6, 28.9, 28.3, 28.1, 24.7. ESI-MS m/z (M^+, 387.7). HRMS 388.1680, M^+; Calcd. 388.1681.

6-{4-[(2,4,6-triamino-N5-pyrimidinyliene)methyl]phenoxy}hexyl thioacetate.[26] (44)

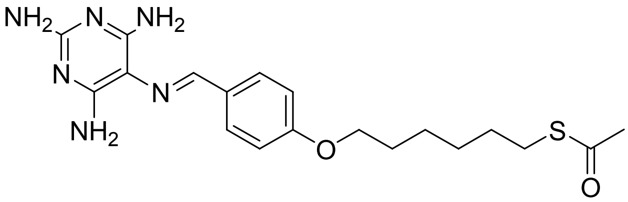

2,4,5,6-Tetraaminopyrimidine sulfate (8.51 g, 34.65 mmol), potassium carbonate (4.78 g, 34.65 mmol), and 6-(4'-formylphenoxy)hexyl thioacetate **38** (2.43 g, 8.66 mmol) in 2-propanol (25 mL) were stirred under reflux overnight. After cooling to room temperature, water (150 mL) was added to the reaction. The brown suspension solution was filtered, washed with water (100 mL), and CH_2Cl_2 (20 mL), then dried under reduced pressure to give a deep-yellow solid (0.92 g, yield = 27 %). ^{1}H NMR (200 MHz, *d6*-DMSO) δ 8.49 (s, 1H, N=CH), 7.78 (d, 2H, *J* = 8.6 Hz, ArH), 6.96 (d, 2H, *J* = 8.6 Hz, ArH), 5.90 (s, 4H, NH_2), 5.57 (s, 2H, NH_2), 4.00 (t, 2H, *J* = 6.4 Hz, OCH_2), 2.84 (t, 2H, *J* = 7.0 Hz, S-CH_2), 2.32 (s, 3H, CH_3), 1.80-1.60 (m, 2H), 1.60-1.30 (m, 6H); ^{13}C NMR (50 MHz, *d6*-DMSO) δ 195.3, 159.9, 159.8 157.4, 152.4, 130.9, 128.9, 114.3, 102.2, 67.4, 30.6, 29.1, 28.5, 28.3, 27.9, 25.0. APCI-MS m/z (%) 404 (M + 1, 100); 403 (M, 30). HRMS 403.1904, M^+; Calcd. 403.1916.

5-(4'-isobutoxyphenoxy)pentyl thioacetate.[25] (47)

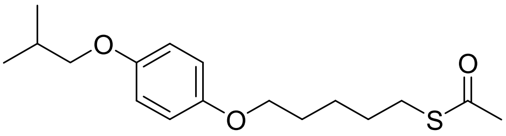

5-(4'-isobutoxyphenoxy)pentyl bromide **46** (27 mg, 0.085 mmol) and potassium thioacetate (20 mg, 0.175 mmol) in acetone (15 mL) were stirred at room temperature in the dark overnight. The resulting white precipitate was filtered off and the filtrate was concentrated under reduced pressure to give a white solid (17 mg, yield = 65%). ^{1}H NMR (200 MHz, $CDCl_3$) δ 6.81 (s, 4H, ArH), 3.89 (t, 2H, J = 6.3 Hz, OCH_2), 3.66 (d, 2H, J = 6.6 Hz, OCH_2), 2.89 (t, 2H, J = 7.0 Hz, S-CH_2), 2.33 (s, 3H, CH_3), 2.15-1.90 (m, 1H, CH), 1.80-1.45 (m, 6H), 1.00 (d, 6H, J = 6.7 Hz, CH_3); ^{13}C NMR (50 MHz, $CDCl_3$) δ 196.0, 153.4, 153.0, 115.4, 115.3, 75.1, 68.2, 30.6, 29.3,29.0, 28.9, 28.3, 25.3, 19.3. FAB-MS *m/z* (M^+, 310.1). HRMS (M^+, 310.1386, Calcd 310.1603).

Ethyl 5-(4'-formylphenoxy)pentanoate.[27] (48)

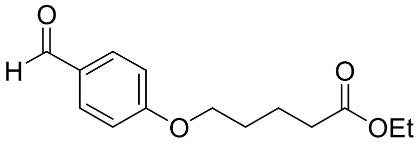

4-Hydroxybenzaldehyde (2.71 g, 21.75 mmol), and potassium carbonate (5.80 g, 42.0 mmol) in 20 mL DMF was added ethyl 5-bromovalerate (4.59 g , 21.75 mmol) in one portion and was stirred at 105℃ overnight. After cooling to room temperature, the reaction was poured into water (200 mL), extracted with diethyl ether (150 mL) twice. The combined organic layer was washed with water (150 mL), and saturated NaCl solution (100 mL), and then dried over $MgSO_4$. The solvent was removed under reduced pressure to give a pale-yellow solid. ^{1}H NMR (200 MHz, $CDCl_3$) δ 9.87 (s, 1H, CHO), 7.82 (d, 2H, $J = 8.7$ Hz, ArH), 6.98 (d, 2H, $J = 8.7$ Hz, ArH), 4.18-4.03 (m, 4H, OCH_2), 2.39 (t, 2H, $J = 6.9$ Hz, $CH_2(C{=}O)$), 1.90-1.80 (m, 4H), 1.22 (t, $J = 5.3$ Hz, 3H, CH_3). The ethyl ester **48** was used directly in the next step.

5-(4'-formylphenoxy)pentanoic acid.[28] (49)

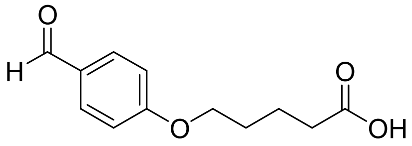

Ethyl 5-(4'-formylphenoxy)pentanoate **48** and lithium hydroxy monohydrate (1.39 g, 23.92 mmol) in H_2O/THF (50 mL/50 mL) were stirred at room temperature for 2 h. The organic solvent was removed and the residue was acidified by slowly adding conc. $HCl_{(aq)}$ until pH < 3. The yellow solid was precipitated and was collected, washed with 50 mL water, and then was dried under reduced pressure. ^{1}H NMR (200 MHz, *d6*-DMSO) δ 12.06 (bs, 1H, COOH), 9.86 (s, 1H, CHO), 7.85 (d, 2H, $J = 8.7$ Hz, ArH), 7.11 (d, 2H, $J = 8.7$ Hz, ArH), 4.09 (t, 2H, $J = 6.0$ Hz, OCH_2), 2.29 (t, 2H, $J = 7.0$ Hz, $CH_2(C{=}O)$), 1.80-1.60 (m, 4H); ^{13}C NMR (50 MHz, *d6*-DMSO) δ 191.7, 174.8, 164.0, 132.2, 129.9, 115.3, 68.1, 33.6, 28.3, 21.5.

5-{4-[(tetrahydro-2,4,6-trioxo-5(2H)-pyrimidinyliene)methyl]phenoxy}pentanoic acid.[29] (50)

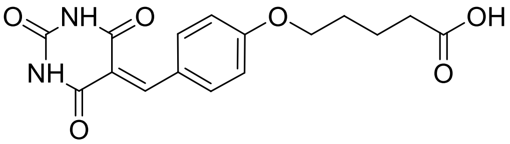

5-(4'-formylphenoxy)pentanoic acid **49** and barbituric acid (2.81 g, 21.75 mmol) in ethanol : water (42 mL, 20 : 1; v/v), were stirred under reflux for 2 hours. After cooling to room temperature, 20 mL water was added to the reaction to dissolve the excess barbituric acid. The resulting yellow suspension was filtered, washed with water (30 mL), chloroform (50 mL), and dried under reduced pressure to give a yellow solid (5.02 g, yield = 70 %, three steps). ^{1}H NMR (250 MHz, *d6*-DMSO) δ 12.06 (s, 1H, COOH), 11.30 (s, 1H, NH), 11.18 (s, 1H, NH), 8.36 (d, 2H, *J* = 9.0 Hz, ArH), 8.24 (s, 1H, CH=C), 7.05 (d, 2H, *J* = 9.0 Hz, ArH), 4.11 (t, 2H, *J* = 6.0 Hz, OCH_2), 2.29 (t, 2H, *J* = 7.0 Hz, $CH_2(C=O)$), 1.80-1.60 (m, 4H); ^{13}C NMR (50 MHz, *d6*-DMSO) δ 174.4, 164.0, 163.0, 162.2, 155.0, 150.2, 137.6, 125.1, 115.5, 114.4, 67.8, 33.2, 27.9, 21.1.; FAB-MS *m/z* ($M+H^+$, 333). HRMS (M^+, 333.1084, Calcd 333.1086).

4-(4'-pentenyloxy)benzaldehyde.[30] (51)

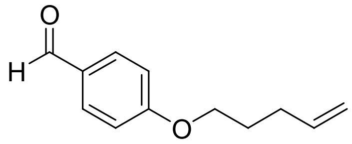

4-penten-1-ol (5.33 g, 61.26 mmol) and catalytic amount of DMF in 10 mL round bottle flask was added thionyl chloride (6.0 mL, 81.43 mmol) dropwise over 5min, and then was stirred at reflux for 2h. After cooling to room temperature, to the crude pale-brown liquid was added 10 mL DMF, and then added to a solution of 4-hydroxybenzaldehyde (7.60g, 61.0 mmol) and potassium carbonate (16.83 g, 122.0 mmol) in 20 mL DMF. The resulting mixture was stirred at 80℃ for 2 days. After cooling to room temperature, the reaction was poured into 300 mL water, extracted with 200 mL diethyl ether, twice. The combined organic layer was washed with water (200 mL), and with brine (200 mL), dried over $MgSO_4$. After removing the solvent, the residue was purified by column chromatography (pentane/dichloromethane = 6/4, 4/6, and then pure dichloromethane) to give a colorless liquid. (10.3 g, 88%) ^{1}H NMR (200 MHz, $CDCl_3$) δ 9.88 (s, 1H, CHO), 7.83 (d, 2H, *J* = 8.8 Hz, ArH), 6.98 (d, 2H, *J* = 8.7 Hz, ArH), 5.90-5.75 (m, 1H, CH=C), 5.10-4.95 (m, 2H, CH=C), 4.05 (t, 2H, *J* = 6.4 Hz, OCH_2), 2.25-2.10 (m, 2H), 1.90-1.78 (m, 2H) ; ^{13}C NMR (75 MHz, *d6*-DMSO) δ 190.8, 164.1, 137.4, 132.0, 129.8, 115.5, 114.7, 67.5, 30.0, 28.2.

4-[(4'-pentenyloxy)-benzylidene]-pyrimidine-2,4,6-trione (52)

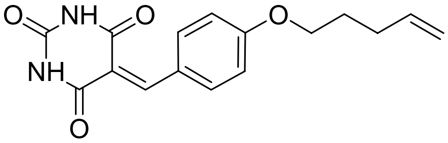

4-(4'-pentenyloxy)benzaldehyde **51** (1.77 g, 9.28 mmol) and barbituric acid (1.20 g, 9.27 mmol) in ethanol : water (20 mL, 40 : 1; v/v) were stirred under reflux for 3 hours. The resulting yellow suspension was filtered, washed with EtOH (10 mL) and dried under reduced pressure to give a yellow solid (2.17 g, yield = 78 %). ^{1}H NMR (250 MHz, *d6*-DMSO) δ 11.31 (s, 1H, NH), 11.19 (s, 1H, NH), 8.36 (d, 2H, *J* = 9.1 Hz, ArH), 8.24 (s, 1H, CH=C), 7.05 (d, 2H, *J* = 9.1 Hz, ArH), 5.93-5.77 (m, 1H, CH=C), 5.09-4.98 (m, 2H, CH=C), 4.11 (t, 2H, *J* = 6.4 Hz, OCH_2), 2.23-2.14 (m, 2H), 1.88-1.80 (m, 2H); ^{13}C NMR (62.5 MHz, *d6*-DMSO) δ 164.4, 163.3, 162.6, 155.3, 150.7, 138.3, 138.0, 125.5, 115.8, 114.8, 67.8, 30.0, 28.1.; FAB-MS *m/z* (M^+, 301). HRMS (M^+, 301.1186, Calcd 301.1188).

4-[(4'-pentenyloxy)benzyl]-pyrimidine-2,4,6-trione.[31] (53)

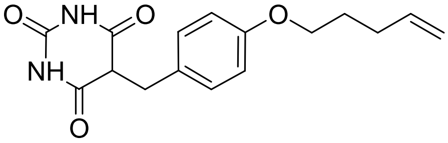

4-[(4'-pentenyloxy)-benzylidene]-pyrimidine-2,4,6-trione **52**, (4.20 g, 14.0 mmol) in 2-propranol (120 mL) at 0℃ was added sodium borohydride (2.16 g, 56.0 mmol), in 5 portions over 5 min, and then the mixture was stirred under $N_{2\,(g)}$ at 0℃ for 5 h. 1N

HCl aqueous solution was added slowly to the off-white colored suspension at 0℃ to quench the excess $NaBH_4$ until pH value was below 3. The solid was collected by filtration, washed with water (500 mL), and then dried under vacuum to give a white-off solid. (3.58 g, 86 %). ^{1}H NMR (300 MHz, *d6*-DMSO) δ 11.15 (s, 2H, NH), 6.97 (d, 2H, *J* = 7.9 Hz, ArH), 6.80 (d, 2H, *J* = 8.3 Hz, ArH), 5.92-5.78 (m, 1H, CH=C), 5.07-4.96 (m, 2H, CH=C), 3.90 (t, 2H, *J* = 6.2 Hz, OCH_2), 3.81 (bs, 1H, CH), 3.18 (bs, 2H, CH_2), 2.20-2.10 (m, 2H), 1.80-1.72 (m, 2H); ^{13}C NMR (50 MHz, *d6*-DMSO) δ 170.4, 157.8, 151.0, 138.4, 130.4, 129.2, 115.6, 114.6, 67.0, 49.9, 33.2, 30.0, 28.3.; FAB-MS *m/z* (M^+, 302). HRMS (M^+, 302.1265, Calcd 302.1267).

4-[(5'-(dimethylethyloxysilyl)-pentyloxy)benzyl]-pyrimidine-2,4,6-trione.[32] (54)

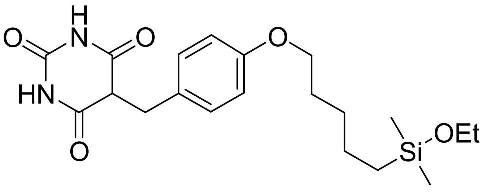

To a solution of 4-[(4'-pentenyloxy)benzyl]-pyrimidine-2,4,6-trione 53 (0.30g, 1.0 mmol) in 2.0 mL dry THF was added a 20 μL 2-propanol solution of $H_2Pt(IV)Cl_6$ (1.0 mg, 0.002 mmol), and then was added dimethylethoxysilane dropwise at room temperature. The reaction solution was stirred at 80℃ for 1h. After cooled to room temperature, the solvent was removed to give a off-white solid (0.42g, 99%). ^{1}H NMR (250 MHz, *d6*-DMSO) δ 11.16 (s, 2H, NH), 6.96 (d, 2H, *J* = 8.3 Hz, ArH), 6.79 (d, 2H, *J* = 8.3 Hz, ArH), 3.88 (t, 2H, *J* = 6.2 Hz, OCH_2), 3.81 (bs, 1H, CH), 3.66 (m, 2H, Si-OCH_2), 3.18 (bs, 2H, Ph-CH_2), 1.80-1.55 (m, 2H), 1.45-1.25 (m, 4H), 1.20-1.10 (m, 2H), 0.88 (t, 3H, *J* = 7.0 Hz, CH_3), 0.05 (s,6H, Si-CH_3).

1,5-Bis(4'-formylphenoxy)pentane.[33] **(55)**

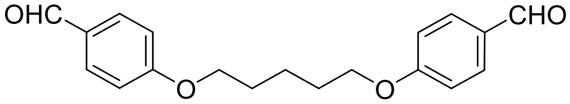

4-Hydroxybenzaldehyde (7.60 g, 61.0 mmol), and potassium carbonate (11.04 g, 80 mmol) in 30 mL DMF was added 1,5-dibromopentane (4.23 mL, 30 mmol) in one portion and was stirred at 100℃ for 2 days. After cooling to room temperature, the reaction was poured into water (400 mL), extracted with chloroform (200 mL) twice. The combined organic layer was washed with water (200 mL), and then dried over $MgSO_4$ and concentrated under reduced pressure. The residue was purified by column chromatography (pure chloroform) to give a 6.52 g white solid (60 %). ^{1}H NMR (200 MHz, $CDCl_3$) δ 9.87 (s, 2H, CHO), 7.82 (d, 4H, *J* = 8.7 Hz, ArH), 6.99 (d, 4H, *J* = 8.7 Hz, ArH), 4.08 (t, 4H, *J* = 6.2 Hz, OCH_2), 2.00-1.80 (m, 4H), 1.78-1.60 (m, 4H); ^{13}C NMR (50 MHz, $CDCl_3$) δ 190.8, 164.0, 132.0, 129.8, 114.7, 68.0, 28.8, 22.6

1,5-{4-[(2,4,6-triamino-N5-pyrimidinyliene)methyl]phenoxy}pentane.[34] **(56)**

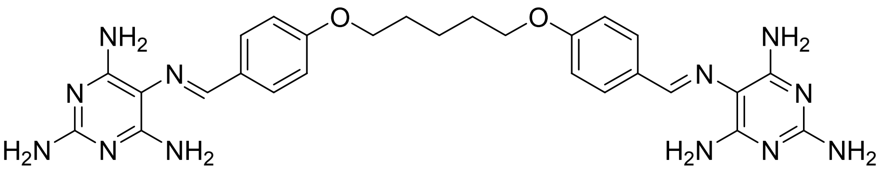

2,4,5,6-tetraaminopyrimidine sulfate (2.49 g, 10.23 mmol), potassium carbonate (0.3 g, 2.17 mmol), 1,5-di-(4'-formylphenoxy)pentane **55** (0.533 g, 1.7 mmol), and diisopropylethylamine (4.0 mL, 21.54 mmol) in 2-propanol/THF (30 mL / 2 mL) were stirred under reflux overnight. After cooling to room temperature, the pale-orange color suspension was poured into 200 mL water with vigorously stirring. The solid was collected, washed with water (100 mL), EtOH (10 mL), diethyl ether (20 mL), and $CHCl_3$ (50 mL), then dried under reduced pressure to give a orange color solid (0.89 g, yield = 96 %). ^{1}H NMR (250 MHz, *d6*-DMSO) δ 8.50 (s, 2H, N=CH), 7.79 (d, 4H, *J* = 8.6 Hz, ArH), 6.98 (d, 4H, *J* = 8.6 Hz, ArH), 5.88 (s, 8H, NH_2), 5.55 (s, 4H, NH_2), 4.05 (t, 4H, *J* = 6.4 Hz, OCH_2), 1.90-1.80 (m, 4H), 1.70-1.50 (m, 2H); ^{13}C NMR (50 MHz, *d6*-DMSO) δ 160.0, 159.7 157.6, 152.1, 131.0, 129.1, 114.6,102.8, 68.3, 28.6, 22.5.

5,10,15,20-Tetrakis(4'-{4''-[6'''-(acetylthio)hexyloxy]benzylideneamino}phenyl)-porphyrin. (57)

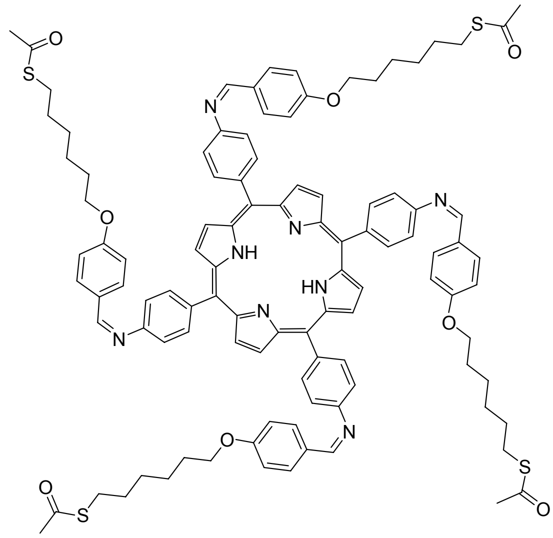

meso-Tetrakis(4'-aminophenyl)porphyrin (0.20 g, 0.29 mmol), TsOH (cat.), and 6-(4’-formylphenoxy)hexyl thioacetate **38** (1.50 g, 5.35 mmol) in benzene (50 mL) were stirred under reflux for 4 h using a Dean-Stark apparatus to remove. After cooling to room temperature, the solvent was removed, and the residue was dissolved in $CHCl_3$ (5.0 mL). 50 mL EtOH was added and the solid was precipitated and was collected by centrifuge and dried under vacuum to give a brown solid (0.183 g, yield = 36 %). ^{1}H NMR (250 MHz, $CDCl_3$) δ 8.94 (s, 8H, py-H), 8.76 (s, 4H, N=CH), 8.25 (d, 8H, *J* = 8.3 Hz, ArH), 8.01 (d, 8H, *J* = 8.6 Hz, ArH), 7.60 (d, 8H, *J* = 8.3 Hz, ArH), 7.06 (d, 8H, *J* = 8.6 Hz, ArH), 4.08 (t, 8H, *J* = 6.3 Hz, OCH_2), 2.92 (t, 8H, *J* = 7.2 Hz, S-CH_2), 2.35 (s, 12H, CH_3), 1.90-1.80 (m, 8H), 1.70-1.50 (m, 24H) -2.70 (s, 2H, py-NH); ^{13}C NMR (62.5 MHz,$CDCl_3$) δ 196.0, 162.0, 160.2, 151.8, 139.5, 135.4, 132.0, 130.7, 129.2, 119.9, 119.3, 114.8, 68.0, 30.7, 29.5, 29.0, 28.5, 25.6.; FAB-MS *m/z* (M^+, 1723). HRMS (M^+, 1723.2673, Calcd 1723.7050).

References:

1. R. Szamocki, S. Reculusa, S. Ravaine, P. N. Bartlett, A. Kuhn, R. Hempelmann, *Angew. Chem. Int. Ed.,* **2006**, *45*, 1317 –1321.
2. C.-H. Huang, N. D. McClenaghan, A. Kuhn, J. W. Hofstraat, D. M. Bassani, *Org. Lett.* **2005**, *7*, 3409-3412.
3. Y. Zhu, M. O. Wolf, *J. Am. Chem. Soc.* **2000**, *41*, 10121-10125.
4. A. K. Mohanakrishnan, A. Hucke, M. A. Lyon, M. V. Lakshmikantham, M. P. Cava, *Tetrahderon,* **1999**, *40*, 11745-11754.
5. A. Donat-Bouillud, I. Lévesque, Y. Tao, M. D'Iorio, S. Beaupré, P. Blondin, M. Ranger, J. Bouchard, M. Leclerc, *Chem. Mater.*, **2000**, 7, 1931-1936.
6. J. Cao, J. W. Kampf, M. D. Curtis, *Chem. Mater.***,** **2003**, *2*, 404-411.
7. L. L. Miller, Y. YU, *J. Org. Chem.* **1995**, *21*, 6813-6819.
8. Y. Wei, Y. Yang, J.-M. Yeh, *Chem. Mater.* **1996**, *8*, 2659-2666.
9. U. Stalmach, H. Kolshorn, I. Brehm, H. Meier, *Liebigs Ann.* **1996**, 1449-1456.
10. M. J. Piao, K. Chajara, S. J. Yoon, H. M. Kim, S.-J. Jeon, T.-H. Kim, K. Song, I. Asselberghs, A. Persoons, K. Clays, B. R. Cho, *J. Mater. Chem.*, **2006**, **16**, 2273-2281.
11. H. Detert; D. Schollmeyer; E. Sugiono.*Eur. J. Org. Chem.* **2001**, 2927-2938.
12. S. R. Amrutha, M. Jayakannan, *J. Phys. Chem. B*, **2006**, *110*, 4083 – 4091.
13. R. Koike, Y. Katayose, A. Ohta, J. Motoyoshiya, Y. Nishii, H. Aoyama, *Tetrahedron*, **2005**, *61*, 11020-11026.
14. C.-L. Lin, M.-Y. Yeh, C.-H. Chen, S. Sudhakar, S.-J. Luo, Y.-C. Hsu, C.-Y. Huang, K.-C. Ho, T.-Y. Luh, *Chem. Mater.* **2006**, *18*, 4157-4162.
15. H.-C. Lin, C.-M. Tsai, G.-H. Huang, J.-M. Lin, *J. Polymer Sci., Part A: Polymer Chemistry,* 2006, 44, 783-800.
16. B. D. Olsen, R. A. *Macromolecules*, **2005**, *38*, 10127-10137.
17. H. Meier, D. Ickenroth *Eur. J. Org.Chem***.** **2002**, *11*, 1745-1749.
18. A. M. Ramos, M. T. Rispens, Minze J. K. J. van Duren, J. C. Hummelen, A. A. J. Janssen, *J. Am. Chem. Soc.* **2001**, *123*, 6714-6715.
19. A. M. Ramos, M. T. Rispens, Minze J. K. J. van Duren, J. C. Hummelen, A. A. J. Janssen, *J. Am. Chem. Soc.* **2001**, *123*, 6714-6715.
20. M.E. Thibault, T.L. L. Closson, S.C. Manning, P.W. Dibble, *J. Org. Chem.* **2003**, *68*, 8373-8378.
21. E-J. Seo, J.-C. Bae, H.-K. Lee, J. Keun. *Eur. Polymer J.*, **2004**, *40*, 259-265.
22. R. Freudenmann, B. Behnisch, F. Lange, M. Hanack, *Synthetic Metals*, **2000**,

111-112, 441-443.

23. M. J. Gomez-Escalonilla, F. Langa, J.-M. Rueff, L. Oswald, J.-M. Nierengarten, *Tetrahedron Lett.* **2002**, *43*, 7507-7511.
24. Sudeep, P. K.; Ipe, B. I.; Thomas, K. G.; Gerore, M. V.; Barazzouk, S.; Hotchandani, S.; Kama, P. V. *Nano Lett*. **2002**, *2*, 29-35.
25. Nicolaou, K. C.; Cho, S. Y.; Hughes, R.; Winssinger, N.; Smethurst, C.; Labischinski, H.; Endermann, R. *Chem. Eur. J.* **2001**, *7*, 3798-3823.
26. C.-H. Huang, N. D. McClenaghan, A. Kuhn, G. Bravic, D. M. Bassani, *Tetrahedron*, **2006**, *62*, 2050-2059.
27. I. Furman, D. G. Whitten, T. L. Penner, A. Ulman, H. C. Geiger, H. *Langmuir*, **1994**, *10*, 837-843.
28. G. T. Bourne, W. D. F. Meutermans, M. L. Smythe, *Tetrahedron Lett.* **1999**, *40*, 7271-7274.
29. N. C. Kaarsholm, O. H. Birk Olsen, P. Madsen, S. Oestergaard, P. Jakobsen, T. Moeller Tagmose, *PCT Int. Appl*. **2006,** pp424, WO 2006082245, A1 20060810.
30. K. C. Nicolaou, T. Montagnon, P. S. Baran, Y.-L. Zhong, *J. Am. Chem. Soc.* **2002**, *124*, 2245-2258.
31. M. A. Kaldrikyan, N. A. Nersesyan, A. A. Aroyan, *Armyanskii Khimicheskii Zhurnal,* **1971**, *24*, 45-50.
32. D. A. Annis, E. N. Jacobsen, *J. Am. Chem. Soc.* **1999**, *17*, 4147-4154.
33. D. Ribera, A. Mantecon, A. Serra, *J. Polymer Sci., A: Polymer Chemistry*, **2002**, *40*, 4344-4356.
34. J. Davoll, A. M. Johnson, H. J. Davies, O. D. Bird, J. Clarke, E. F. Elslager, *J. Med. Chem.* **1972**, *15*, 812-826.

Appendix

X-ray Crystal Structure of oligothiophene 10

Crystallographic data (excluding structure factors) for the structures **10** with the *Cambridge Crystallographic Data Centre* as supplementary publication numbers CCDC 275009.

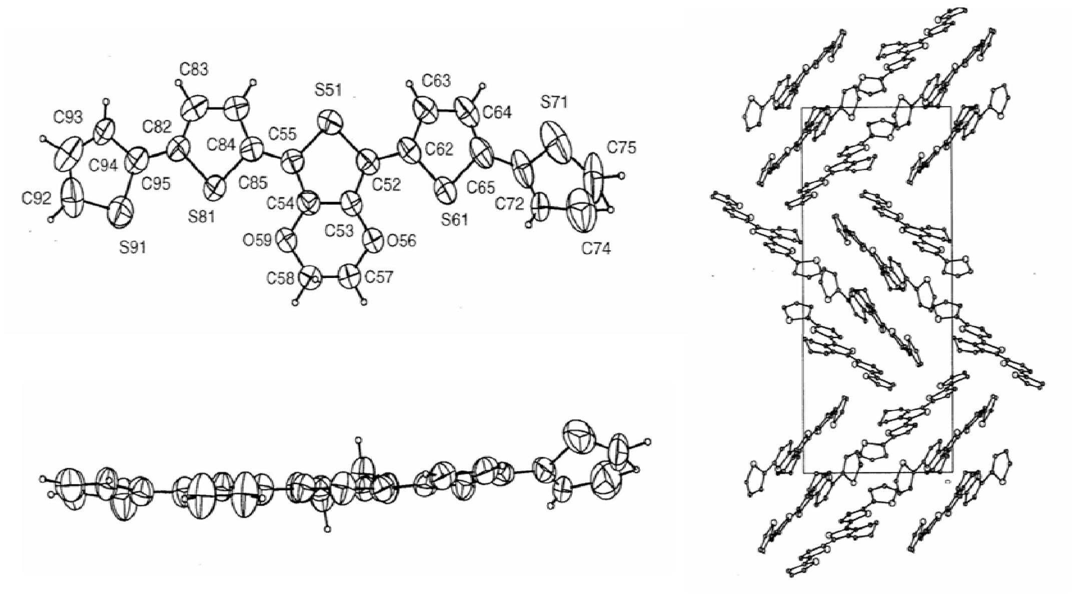

X-ray crystal structure of **10** and crystal packing.

Direct cell	a =	10.494	b =	13.314	c =	30.357
	alpha =	90.000	beta =	98.380	gamma =	90.000

Crystal family : monoclinic

Space group (centrosymmetric) : P 21/n

Symmetry-operations

1) x , y , z 2) -x+1/2, y+1/2, -z+1/2

3) -x , -y , -z 4) x+1/2, -y+1/2, z+1/2

Seminvariant condition : g g g

Space Group Number = 14

X-ray scattering factors

Unit cell contents and scattering factor constants

Atom	Symbol	Number in cell	Atomic number
Hydrogen	H	112	1
Carbon	C	176	6
Oxygen	O	66	8
Sulphur	S	40	16

f = sum (a(i) * exp(-b(i)*s2)) i=1,4 + c

	a(1)	b(1)	a(2)	b(2)	a(3)	b(3)	a(4)	b(4)	c
H	0.490	20.659	0.262	7.740	0.197	49.552	0.050	2.202	0.001
C	2.310	20.844	1.020	10.208	1.589	0.569	0.865	51.651	0.216
O	3.049	13.277	2.287	5.701	1.546	0.324	0.867	32.909	0.251
S	6.905	1.468	5.203	22.215	1.438	0.254	1.586	56.172	0.867

```
                 Number of atoms in asymmetric unit =     70.50

        Equivalent number of equal atoms in primitive cell =    165

                          Cell volume = 4196.11

                        Volume per atom =    14.88


7364          input reflections

719           Fo(s) negative set to 0.0

7364          independent input reflections

12  15  36    maximum   h, k, l   values

0.3542        maximum s**2 = (sin(theta)/lambda)**2

0.8401        Angstrom resolution

28287         maximum super-index ( must be less then 200000 )

45            reflections are not in input data


***    Final statistics section    ***


                 Distribution of <E**2> with sin(theta)/lambda

 sinth/lambda       0.0595    0.1190    0.1786    0.2381    0.2976

     <E**2>           0.0000    0.3904    1.0814    0.8040    1.1199

     number                0        39       259       518       867

 sinth/lambda       0.3571    0.4166    0.4761    0.5357    0.5952

     <E**2>           0.9007    1.1562    1.0313    0.9139    1.0108

     number             1332      1824      2456      3154      3936
```

Average values

Average	Numeric				Graphic
	all data	acentric	centric	hypercentric	a. c. h.
mod(E)	0.780	0.886	0.798	0.718	*
E**2	1.000	1.000	1.000	1.000	
E**3	1.638	1.329	1.596	1.916	*
E**4	3.206	2.000	3.000	4.500	*
E**5	7.185	3.323	6.383	12.260	*
E**6	17.926	6.000	15.000	37.500	*
mod(E**2-1)	0.981	0.736	0.968	1.145	*
(E**2-1)**2	2.206	1.000	2.000	3.500	*
(E**2-1)**3	10.308	2.000	8.000	26.000	*
(mod(E**2-1))**3	11.021	2.415	8.691	26.903	*

n(z) cumulative probability distribution

z	all data	acentric	centric	hypercentric	a. c. h.
0.1	0.258	0.095	0.248	0.368	*
0.2	0.348	0.181	0.345	0.463	*
0.3	0.416	0.259	0.416	0.526	*
0.4	0.474	0.330	0.473	0.574	*
0.5	0.526	0.393	0.520	0.612	*
0.6	0.569	0.451	0.561	0.643	*
0.7	0.605	0.503	0.597	0.670	*
0.8	0.635	0.551	0.629	0.694	*
0.9	0.661	0.593	0.657	0.715	*
1.0	0.687	0.632	0.683	0.733	*

1.2	0.731	0.699	0.727	0.765	*
1.4	0.772	0.753	0.763	0.791	*
1.6	0.800	0.798	0.794	0.813	*
1.8	0.826	0.835	0.820	0.832	*
2.0	0.848	0.865	0.843	0.848	*
2.2	0.871	0.889	0.862	0.863	*
2.4	0.885	0.909	0.879	0.875	*
2.6	0.897	0.926	0.893	0.886	*
2.8	0.908	0.939	0.906	0.896	*
3.0	0.918	0.950	0.917	0.905	*
3.2	0.927	0.959	0.926	0.913	*
3.4	0.935	0.967	0.935	0.920	*
3.6	0.941	0.973	0.942	0.926	*
3.8	0.949	0.978	0.949	0.932	*
4.0	0.954	0.982	0.954	0.938	*

Distribution of E - number of E's .gt. limit

E	0.6	0.7	0.8	0.9	1.0	1.1	1.2	1.3	1.4	1.5	
number	4031	3523	3067	2667	2301	1962	1640	1376	1150	922	
E	1.6	1.7	1.8	1.9	2.0	2.1	2.2	2.3	2.4	2.5	
number	772	638	526	433	345	289	236	197	155	128	

```
Number and percentage                        Number and percentage

      of   F's > param * sigma(F)                      of   F's > limit

      number     percentage   param                 number     percentage   limit

        5861         80%        0.50                   736          10%      25.77

        5590         76%        1.00                  1472          20%      15.68

        5590         76%        1.50                  2208          30%      11.09

        5472         74%        2.00                  2944          40%       8.12

        5281         72%        2.50                  3680          50%       6.24

        5058         69%        3.00                  4416          60%       4.69

        4853         66%        3.50                  5152          70%       3.61

        4614         63%        4.00                  5888          80%       2.45

        4506         61%        4.50                  6624          90%       0.00

        4349         59%        5.00                  7360         100%       0.00


     467   largest E-values to phase. (      10 printed )

  code   h    k    l      E       fo/sig.   Code    h    k    l     E         fo/sig.

    1    4    6    8     4.460     >6         2     1    6    9    3.747        >6

    3   10    2   -9     3.716     >6         4     4    8  -17    3.661        >6

    5    5    2   -8     3.604     >6         6     5    0   -1    3.501        >6

    7    9    8  -18     3.424     >6         8     7    1    2    3.409        >6

    9    8    2   13     3.376     >6        10     2   12  -22    3.294        >6
```

```
500    smallest E-values for psi0 and negative quartets (    10 printed )

   Code   h    k    l      E         fo/sig.   Code        h    k    l     E            fo/sig.

   7355   12   1    -12  0.000     0.00        7356        11   6    -9    0.000        0.00

   7357   11   7    -5   0.000     0.00        7358        12   2    -8    0.000        0.00

   7359   12   2    -7   0.000     0.00        7360        12   1    3     0.000        0.00

   7361   12   2    1    0.000      0.00       7362        12   2    3     0.000       0.00

   7363   12   3    -1   0.000     0.00        7364        12   3     1    0.000       0.00


Triplets statistic

                              distribution of g - number of g's .gt. limit

g     0.0     0.2     0.4     0.6     0.8     1.0     1.2     1.4     1.6     2.0     2.5     3.0

no.  5120  4905  4774   4374   3627   2927   2319   1767   1348    717     304

117


6445 strong triplets          found among 467 strongest reflections (E-min = 1.869)

                              strengthned by    70 free vectors using P-10 formula

8000 Psi-zero triplets        found among 467 strongest reflections

                              and the 500 weakest reflections

4918 negative quartets found among 8000 psi-zero relationships


Negative quartets statistic distribution of g - number of g's .gt. limit

g     0.0    0.2     0.4      0.6    0.8   1.0     1.2   1.4   1.6    2.0   2.5   3.0

no. 4000  3006   2034   1300   774   460   272   184   124   62    39   24
```

```
                                       number of relationships

                                          calculated      stored

positive estimated triplets               4680            4680

negative estimated triplets               440             440

enantiomorph sensitive triplets           -               -

psi-zero triplets                         8000            8000

negative estimated quartets               3210            3210

enantiomorph sensitive quartets           -               -


***      converge / diverge    section      ***


      Origin fixing reflexion(s)

           code     h     k     l       E            phase restriction    assigned phase

              2     1     6     9    3.75                 0,180               360

             52     5     1   -24    2.79                 0,180               360

            103     1     1    -9    2.57                 0,180               360

      Selected symbols

           code     h     k     l       E            phase restriction

             78     1     2   -10    2.67                 0,180

             64     1     3   -18    2.73                 0,180

              6     5     0    -1    3.50                 0,180

              1     4     6     8    4.46                 0,180

            297     4     4   -17    2.08                 0,180
```

```
***     tangent formula section      ***

                      the total number of permutations is      32

               the maximum number of sets stored will be      10

               the number of equivalent sets rejected is      12


               +++++++++++++    Figures    of    merit    ++++++++++++


                      mabs    alcomb pscomb R(x,y) cphase    cfom

               min    0.965    0.286    0.422    0.513    0.557    0.418

               max    1.342    0.862    0.675    0.721    1.000    0.914


   set    (trial)      mabs     alcomb pscomb R(x,y) cphase    cfom      nund

     1    (      28)    1.338    0.862    0.671    0.717    1.000    0.914      27

     2    (      18)    1.265    0.792    0.472    0.614    0.839    0.810      14

     3    (      22)    1.260    0.776    0.458    0.601    0.834    0.798      22

     4    (      24)    1.182    0.667    0.423    0.565    0.609    0.645      13

     5    (      16)    1.184    0.671    0.425    0.569    0.583    0.638      14

     6    (      30)    1.170    0.676    0.447    0.578    0.569    0.636      18

     7    (      17)    1.026    0.355    0.549    0.580    0.978    0.591      19

     8    (       9)    1.024    0.343    0.523    0.571    0.974    0.582      20

     9    (      21)    1.029    0.344    0.495    0.560    0.955    0.575      20

    10    (      27)    0.991    0.312    0.465    0.538    0.764    0.482       8


Final residual value =    17.97%
```

Serial	Atom		Height	x	y	z	Occ.	B[iso]	Frag
1)	S	1	1309	-1.025	0.595	0.386	1.000	4.70	1
2)	S	2	1098	-1.028	0.331	0.335	1.000	5.24	2
3)	S	3	1031	-0.389	0.330	0.488	1.000	5.01	1
4)	S	4	865	-0.809	0.070	0.392	1.000	5.95	2
5)	S	5	862	-1.450	0.345	0.297	1.000	5.40	2
6)	S	6	860	-0.611	0.532	0.392	1.000	5.35	1
7)	S	7	643	-1.312	0.699	0.369	1.000	7.99	1
8)	S	8	581	-0.048	0.167	0.473	1.000	9.02	1
9)	O	9	453	-0.657	0.367	0.494	1.000	4.34	1
10)	C	10	391	-0.783	0.478	0.439	1.000	7.45	1
11)	C	11	390	-0.666	0.427	0.458	1.000	7.03	1
12)	C	12	383	-0.560	0.453	0.434	1.000	7.38	1
13)	O	13	380	-1.663	0.601	0.240	1.000	4.27	2
14)	O	14	353	-0.895	0.464	0.455	1.000	4.52	1
15)	O	15	343	-1.085	0.053	0.362	1.000	6.25	2
16)	C	16	333	-1.194	0.299	0.323	1.000	8.82	2
17)	O	17	330	-0.577	-0.093	0.418	1.000	4.12	2
18)	O	18	326	-0.339	0.418	0.414	1.000	8.94	1
19)	O	19	312	-0.875	0.416	0.498	1.000	9.73	1
20)	O	20	295	-1.745	0.419	0.266	1.000	7.42	2
21)	O	21	292	-0.779	0.331	0.498	1.000	9.38	1
22)	C	22	283	-0.436	0.411	0.443	1.000	8.39	1
23)	O	23	283	-1.328	0.155	0.329	1.000	6.29	2
24)	O	24	280	-0.747	0.249	0.371	1.000	9.30	2

25)	C	25	276	-1.089	0.150	0.350	1.000	5.46	2
26)	C	26	268	-0.771	0.536	0.403	1.000	4.25	1
27)	C	27	267	-0.984	0.209	0.353	1.000	5.02	2
28)	C	28	264	-1.380	0.522	0.274	1.000	6.12	2
29)	C	29	256	-1.207	0.199	0.335	1.000	4.79	2
30)	C	30	251	-1.285	0.373	0.305	1.000	5.01	2
31)	C	31	247	-0.645	0.104	0.403	1.000	5.85	2
32)	C	32	242	-0.426	0.052	0.453	1.000	3.82	2
33)	C	33	240	-0.864	0.599	0.377	1.000	5.40	1
34)	C	34	237	-1.267	0.467	0.291	1.000	5.15	2
35)	C	35	225	-0.851	0.185	0.371	1.000	5.05	2
36)	C	36	225	-1.257	0.772	0.294	1.000	5.20	1
37)	C	37	225	-0.240	0.306	0.471	1.000	5.44	1
38)	C	38	221	-0.147	0.216	0.543	1.000	4.06	1
39)	C	39	220	-1.067	0.686	0.345	1.000	5.56	1
40)	C	40	219	-0.153	0.235	0.499	1.000	5.48	1
41)	C	41	214	-0.625	0.199	0.390	1.000	5.65	2
42)	C	42	214	-1.200	0.719	0.335	1.000	5.11	1
43)	C	43	212	-1.625	0.491	0.259	1.000	5.78	2
44)	C	44	209	-1.485	0.464	0.274	1.000	5.52	2
45)	C	45	197	-0.229	0.354	0.432	1.000	5.26	1
46)	C	46	195	-1.319	0.047	0.334	1.000	7.35	2
47)	C	47	190	-1.214	0.015	0.367	1.000	9.07	2
48)	C	48	188	-0.038	0.142	0.557	1.000	8.24	1
49)	C	49	170	-1.817	0.584	0.228	1.000	8.59	2
50)	C	50	164	-1.387	0.791	0.296	1.000	7.21	1

51)	C	51	159	0.011	0.118	0.523	1.000	8.68	1
52)	C	52	157	-0.552	0.031	0.423	1.000	5.91	2
53)	C	53	151	-0.849	0.665	0.342	1.000	7.06	1
54)	C	54	148	-0.964	0.713	0.327	1.000	7.97	1
55)	C	55	135	-0.441	-0.124	0.450	1.000	9.00	2
56)	C	56	134	-1.432	0.758	0.332	1.000	7.23	1
57)	C	57	133	-0.380	-0.051	0.464	1.000	8.94	2
58)	Q	58	128	-1.096	0.299	0.303	1.000		
59)	Q	59	118	-0.523	0.677	0.489	1.000		
60)	Q	60	117	-0.920	0.352	0.335	1.000		
61)	C	61	114	-1.852	0.496	0.237	1.000	10.33	2
62)	Q	62	113	-1.117	0.646	0.376	1.000		
63)	Q	63	110	-1.332	0.349	0.449	1.000		
64)	Q	64	109	-0.571	0.361	0.524	1.000		
65)	Q	65	108	-0.960	0.375	0.495	1.000		
66)	Q	66	103	-0.506	0.364	0.478	1.000		
67)	Q	67	103	-0.405	-0.091	0.463	1.000		
68)	Q	68	102	-1.713	0.637	0.203	1.000		
69)	Q	69	102	-0.716	0.657	0.484	1.000		
70)	Q	70	88	-0.920	0.203	0.465	1.000		
71)	C	71	87	-0.621	0.530	0.459	1.000	20.10	0
72)	Q	72	87	-1.531	0.382	0.265	1.000		
73)	Q	73	87	-0.689	0.705	0.479	1.000		
74)	Q	74	86	-0.476	0.249	0.476	1.000		
75)	Q	75	86	-0.907	0.044	0.407	1.000		
76)	Q	76	86	-0.495	0.504	0.387	1.000		

77)	Q 77	85	-1.015	0.259	0.277	1.000		
78)	Q 78	84	-0.644	0.461	0.409	1.000		
79)	Q 79	84	-1.273	0.087	0.325	1.000		
80)	Q 80	84	-0.880	0.530	0.432	1.000		
81)	C 81	84	-0.991	0.578	0.365	1.000	16.93	0
82)	Q 82	82	-0.460	-0.208	0.460	1.000		
83)	Q 83	82	-0.870	0.282	0.487	1.000		
84)	Q 84	81	-0.686	0.552	0.356	1.000		
85)	Q 85	81	-1.065	0.257	0.478	1.000		
86)	C 86	80	-0.117	0.351	0.414	1.000	16.49	1
87)	Q 87	80	-0.901	0.092	0.450	1.000		
88)	Q 88	80	-1.152	0.124	0.467	1.000		
89)	Q 89	79	-0.691	-0.051	0.467	1.000		
90)	Q 90	78	-1.080	0.524	0.375	1.000		
91)	Q 91	78	-1.275	0.283	0.238	1.000		
92)	Q 92	78	-1.072	0.528	0.270	1.000		
93)	Q 93	78	-0.408	0.753	0.363	1.000		
94)	Q 94	78	-0.836	0.646	0.497	1.000		
95)	Q 95	77	-1.523	0.270	0.275	1.000		
96)	Q 96	77	-0.622	0.560	0.355	1.000		
97)	Q 97	77	-0.715	0.225	0.498	1.000		
98)	Q 98	77	-1.420	0.330	0.372	1.000		
99)	Q 99	76	-1.307	0.274	0.229	1.000		
100)	Q 100	76	-0.887	0.820	0.324	1.000		
101)	Q 101	76	-0.844	0.351	0.323	1.000		
102)	Q 102	76	-1.383	0.514	0.342	1.000		

```
 103)    C 103    75    -1.455   0.736   0.268   1.000   16.47   1

 104)    C 104    75    -1.621   0.671   0.258   1.000   19.99   1

 105)    C 105    75    -1.270   0.669   0.261   1.000   20.11   1

 106)    Q 106    75    -1.836   0.743   0.233   1.000

 107)    Q 107    74    -0.785   0.260   0.443   1.000

The following atoms :

O20    O17

have been relabelled as :

S20    S17

The following atoms :

O19    O21    O24    O13    O18

have been relabelled as :

C19    C21    C24    C13    C18

The following Atom(s) has been deleted :

C(105 C(103 C(104 C(86)


+++++++++++++++++++++++++++++++++++++++++++++++++++++++++++++++++++

Least-Squares Routine                                   Release   97.01


+++++++++++++++++++++++++++++++++++++++++++++++++++++++++++++++++++

Used directives:

  Cutoff         3

  Damping      1.0

  Cycles         6

Structure factor least squares        (Vers. 2496)

Weighting scheme no.    6
```

```
Parameter(s) provided    1

        p(1)            p(2)            p(3)            p(4)

        1.00000

Cycle(s) requested       6


threshold=n*sig(fo)      3          4          5          6

no. reflections...      5095       4741       4374       4134

no(refl)/param....     21.14     19.67     18.15     17.15

 R(F)% ........... 28.933 28.285 27.507 27.048

wR(F**2)% ........ 26.863 26.624 26.260 26.037

goodnes of fit....    6.075    6.245    6.416    6.544

minimization function =                  179178.3125

Structure factor least squares calculation        1 ends

minimum (shift/e.s.d.) =      0.00

maximum (shift/e.s.d.) =    29.80

mean        (shift/e.s.d.) =      1.17

sum of the squares of the (shift/e.s.d.) =1913.20

average value of B(equiv) =          6.920

number of refined parameters        241


threshold=n*sig(fo)      3          4          5          6

no. reflections...      5095       4741       4374       4134

no(refl)/param....     21.14     19.67     18.15     17.15

 R(F)% ........... 20.016 19.416 18.766 18.309

wR(F**2)% ........ 18.718 18.487 18.202 17.998

goodnes of fit....    4.233    4.336    4.447    4.524
```

```
minimization function =                87023.6172
Structure factor least squares calculation      2 ends
minimum (shift/e.s.d.) =     0.00
maximum (shift/e.s.d.) =    22.40
mean        (shift/e.s.d.) =     0.93
sum of the squares of the (shift/e.s.d.) =1194.17

threshold=n*sig(fo)      3          4          5          6
no. reflections...      5095      4741      4374      4134
no(refl)/param....    21.14    19.67    18.15    17.15
  R(F)% ........... 17.559 16.991 16.392 15.995
wR(F**2)% ........ 16.373 16.145 15.883 15.699
goodnes of fit....    3.703    3.787    3.881    3.946
minimization function =                66604.4453
Structure factor least squares calculation      3 ends
minimum (shift/e.s.d.) =     0.00
maximum (shift/e.s.d.) =    10.75
mean        (shift/e.s.d.) =     0.65
sum of the squares of the (shift/e.s.d.) = 359.09

threshold=n*sig(fo)      3          4          5          6
no. reflections...      5095      4741      4374      4134
no(refl)/param....    21.14    19.67    18.15    17.15
  R(F)% ........... 17.123 16.551 15.957 15.577
wR(F**2)% ........ 15.671 15.431 15.164 14.982
goodnes of fit....    3.544    3.619    3.705    3.766
```

```
minimization function =                    61016.7188

Structure factor least squares calculation        4 ends

minimum (shift/e.s.d.) =      0.00

maximum (shift/e.s.d.) =      4.63

mean        (shift/e.s.d.) =      0.39

sum of the squares of the (shift/e.s.d.) = 100.42


threshold=n*sig(fo)      3           4           5           6

no. reflections...      5095      4741      4374      4134

no(refl)/param....    21.14    19.67    18.15    17.15

  R(F)% ........... 17.090 16.511 15.918 15.545

wR(F**2)% ........ 15.492 15.244 14.973 14.792

goodnes of fit....    3.503    3.576    3.658    3.718

minimization function =                    59630.1133

Structure factor least squares calculation        5 ends

minimum (shift/e.s.d.) =      0.00

maximum (shift/e.s.d.) =      1.63

mean        (shift/e.s.d.) =      0.18

sum of the squares of the (shift/e.s.d.) =    17.47


 ****************************************************

 *                          >>>>>>> ERROR <<<<<<<                        *

 *    Lsq module:    2 atoms have b(equiv) >      34.6 :      *

 *                               c(71)      c(81)                         *

 ****************************************************
```

```
threshold=n*sig(fo)      3           4           5           6

no. reflections...      5095      4741      4374      4134

no(refl)/param....    21.14    19.67    18.15    17.15

  R(F)% ........... 17.092 16.510 15.914 15.541

wR(F**2)% ........ 15.458 15.209 14.936 14.754

goodnes of fit....    3.496    3.567    3.649    3.708

minimization function =                    59375.4688

Structure factor least squares calculation        6 ends

minimum (shift/e.s.d.) =      0.00

maximum (shift/e.s.d.) =       1.11

mean        (shift/e.s.d.) =      0.10

sum of the squares of the (shift/e.s.d.) =      5.96


  **************************************************

  *                         >>>>>>> ERROR <<<<<<<                     *

  *   Lsq module:    2 atoms have b(equiv) >      34.6 :      *

  *                               c(71)      c(81)                          *

  **************************************************


threshold=n*sig(fo)      3           4           5           6

no. reflections...      5095      4741      4374      4134

no(refl)/param....    21.14    19.67    18.15    17.15

  R(F)% ........... 17.091 16.510 15.914 15.540

wR(F**2)% ........ 15.447 15.197 14.925 14.742

goodnes of fit....    3.493    3.564    3.646    3.706

minimization function =                    59285.0000
```

Structure factor least squares calculation 7 ends

```
TITLE

CELL        10.494    13.314    30.357    90.000    98.380    90.000

ATOM   S1      -1.025     0.595     0.386

ATOM   S2      -1.029     0.331     0.335

ATOM   S3      -0.389     0.330     0.488

ATOM   S4      -0.810     0.069     0.391

ATOM   S5      -1.451     0.345     0.297

ATOM   S6      -0.612     0.532     0.391

ATOM   S7      -1.312     0.700     0.369

ATOM   S8      -0.047     0.166     0.473

ATOM   O9       -0.657     0.367     0.493

ATOM   C10      -0.780     0.476     0.438

ATOM   C11      -0.665     0.430     0.457

ATOM   C12      -0.562     0.450     0.436

ATOM   C13      -1.664     0.602     0.240

ATOM   O14      -0.894     0.464     0.455

ATOM   O15      -1.087     0.053     0.361

ATOM   C16      -1.193     0.299     0.323

ATOM   S17     -0.576    -0.092     0.418

ATOM   C18      -0.341     0.415     0.415

ATOM   C19      -0.877     0.414     0.499

ATOM   S20     -1.743     0.420     0.264

ATOM   C21      -0.782     0.328     0.500

ATOM   C22      -0.435     0.407     0.443
```

ATOM	O23	-1.324	0.155	0.328
ATOM	C24	-0.745	0.249	0.371
ATOM	C25	-1.093	0.151	0.350
ATOM	C26	-0.771	0.535	0.403
ATOM	C27	-0.984	0.210	0.354
ATOM	C28	-1.381	0.519	0.274
ATOM	C29	-1.207	0.201	0.333
ATOM	C30	-1.285	0.371	0.306
ATOM	C31	-0.646	0.102	0.402
ATOM	C32	-0.426	0.053	0.453
ATOM	C33	-0.865	0.596	0.377
ATOM	C34	-1.263	0.469	0.291
ATOM	C35	-0.853	0.187	0.370
ATOM	C36	-1.255	0.771	0.294
ATOM	C37	-0.241	0.306	0.471
ATOM	C38	-0.146	0.215	0.543
ATOM	C39	-1.070	0.686	0.345
ATOM	C40	-0.155	0.237	0.499
ATOM	C41	-0.628	0.199	0.390
ATOM	C42	-1.200	0.718	0.334
ATOM	C43	-1.620	0.494	0.258
ATOM	C44	-1.488	0.462	0.275
ATOM	C45	-0.231	0.355	0.433
ATOM	C46	-1.315	0.050	0.334
ATOM	C47	-1.213	0.013	0.367
ATOM	C48	-0.040	0.142	0.557

```
ATOM     C49      -1.811      0.582      0.229
ATOM     C50      -1.386      0.789      0.297
ATOM     C51       0.014      0.118      0.523
ATOM     C52      -0.551      0.033      0.423
ATOM     C53      -0.847      0.663      0.343
ATOM     C54      -0.965      0.715      0.326
ATOM     C55      -0.437     -0.125      0.452
ATOM     C56      -1.433      0.758      0.334
ATOM     C57      -0.382     -0.041      0.464
ATOM     C58      -1.861      0.499      0.241
ATOM     C59      -0.539      0.610      0.475
ATOM     C60      -1.108      0.530      0.369
END
```

Introduction

Le problème actuel de la fourniture globale d'énergie et de sa consommation impacte profondément la vie quotidienne. Aujourd'hui, l'essentiel des ressources énergétiques exploitées sont des énergies stockées, principalement issues de combustibles tels que le charbon, le pétrole, le gaz naturel ou bien issues de l'énergie nucléaire. Cependant, une crise se dessine pour la population humaine et trouve son origine non seulement de la consommation effrénée de tous les combustibles fossiles mais également de la grave pollution environnementale qui en résulte comme le réchauffement global et la diminution de la couche d'ozone. Un problème urgent et mondial est de développer des sources d'énergie viables, renouvelables et respectueuses de l'environnement qui assureront un développement durable. La lumière du soleil fournit de loin la plus grande source d'énergie ($4{,}3*10^{20}$ J/heure). La production d'électricité grâce à la conversion d'énergie solaire en énergie électrique (conversion photovoltaïque) par des cellules solaires est la méthode la plus directe pour capturer et convertir l'énergie solaire sous une forme pratique.

Les dispositifs photovoltaïques à base de silicium ont joué un rôle majeur dans le développement de la conversion de la lumière en énergie électrique avec des efficacités qui, à l'échelle du laboratoire, approchent maintenant les 35%.[1] La durabilité et l'absence d'émission pendant le fonctionnement sont des caractéristiques très séduisantes qui sont pénalisées par leurs coûts élevés de fabrication et leur fragilité. Pour ces raisons ainsi que le souci de trouver des applications aux semi-conducteurs organiques, les systèmes hybrides organiques/inorganiques et les alternatives à base de polymères organiques ont été activement considérés au cours des dernières années comme des alternatives dont l'utilisation à grande échelle semble réaliste.[2] L'un des aspects les plus attractifs dans les cellules solaires en polymères tout organique est leur flexibilité qui permet de les fabriquer sur des supports plastiques. Au cours de la dernière décennie, les polymères conjugués ont bénéficié d'un intérêt croissant depuis les travaux de Heeger et al.[2a] et Sariciftci et al.[3] démontrant qu'une amélioration notable dans les propriétés photovoltaïques de ce type de matériaux pouvait être obtenue en mélangeant des [60]fullerènes à des polymères (Figure 1.1). Dans de tels dispositifs composites, il a été proposé que le fullerène se comportait comme un matériau transporteur d'électron qui augmente l'efficacité de la séparation et du transport de charges, et des ratios de rectification très élevés ont été observés dans des hétérojonctions PPV/C_{60} (PPV : poly(p-phénylène vinylène)).

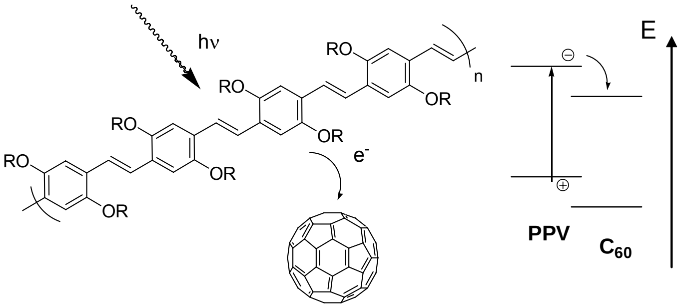

Figure 1.1. Schematic illustration of the photoinduced charge transfer (left) with a sketch of the energy level scheme (right). After excitation in the PPV polymer, the electron is transferred to the C_{60} due to its higher electron affinity.[2a]

En considérant le caractère inné de systèmes multi-couches auto-assemblées, dans lesquels il est possible d'anticiper la forte absorption de lumière comme un bon prérequis pour les systèmes photovoltaïques, l'association spontanée, dans des conditions d'équilibre, de molécules en agrégats stables ayant des compositions bien définies, conduit à un compromis entre la séparation de charges intra- et intermoléculaire et au transport de charges intermoléculaire dans le matériau organisé. Les interactions par liaisons hydrogène ont été exploitées avec succès par la Nature pour induire l'auto-assemblage de composants moléculaires en architectures possédant une complexité et une fonctionnalité très riche, étendues dans l'espace. Des systèmes efficaces à liaisons hydrogène nécessitent que la présence de sites de reconnaissance moléculaires dans des unités qui s'associent pour produire des architectures sophistiquées (Figure 1.2). Dans cette approche, le bénéfice immédiat obtenu à partir d'interactions par liaisons hydrogène est la capacité à aligner les composants donneur d'électron et accepteur d'électron, satisfaisant ainsi aux critères fondamentaux de fonctionnement des systèmes photovoltaïques : une distance faible entre la paire donneur-accepteur et le chemin le court pour le transport des charges aux électrodes

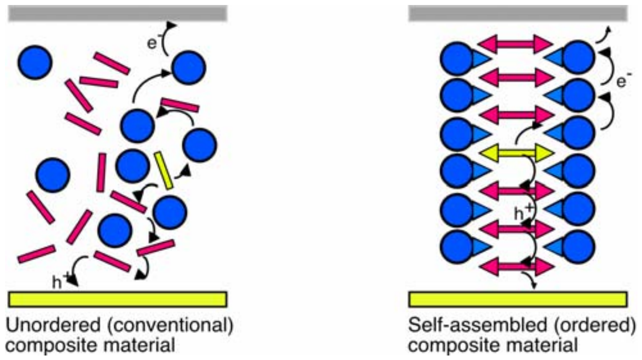

Figure 1.2. In a conventional composite material (left), charge separation from an excited donor (in yellow) results in an electron-hole pair that must then percolate through an ill-defined path to the corresponding electrodes. The same situation is much more efficient if the hole and electron transport materials are suitably ordered, for example thorough self-assembly (right).

L'objectif de ces travaux a été de tester et de vérifier la mise en œuvre de composants photo- et électro-actifs assemblés par interactions supramoléculaires, programmés pour s'auto-organiser en hétérojonctions moléculaires et construire efficacement des architectures supramoléculaires destinées à des applications photovoltaïques. Ce projet a eu pour but de concevoir et synthétiser de nouveaux matériaux hybrides auto-assemblés basés sur un couple donneur/accepteur (oligomère/fullerène) et de démontrer l'utilisation de ces nouveaux systèmes pour fabriquer de nouvelles cellules de conversion lumière-énergie électrique.

Références:

1. (a) S. J. Lade, A. Zahdi, *Microelectron. J.* **2005**, *35*, 401-410.; (b) W. Fuhs, "Silicon thin-film solar cells" In *Nanostructured and Advanced Materials*; A. Vaseashta, D. Dimova-Malinovska, J. M. Marshall, Ed.; Springer, the Netherlands, **2005**, pp:293-298.; (C) D. E. Caelson, *Sol. Energy Mater. Sol. Cells* **2003**, *78*, 627-645. (d) *PHOTON International,* Solar Verlag GmbH, **2003**, *9*, 17.
2. (a) N. S. Sariciftci, L. Smilowitz, A. J. Heeger, F. Wudl, *Science* **1992**, *258*, 1474-1476.; (b) C. J. Brabec, N. S. Sariciftci, J. C. Hummelen, *Adv. Funct. Mat.* **2001**, *11*, 15-26.; (c) C. J. Brabec, *Sol. Energy Mater. Sol. Cells,* **2004**, *83*, 273-292.
3. S. E. Shaheen, C. J. Brabec, T. Fromherz, F. Padinger, N. S. Sariciftci, E. Gloetzl, (**Patent** no. WO0184645, published 2001-11-08)

Conclusion

La première partie de ce travail a été focalisée sur la conception et la synthèse de nouveaux matériaux photoactifs capables de s'auto-assembler. L'introduction de motifs de reconnaissance moléculaire par liaisons hydrogène, tels que des mélamines ou des groupes barbiturates, directement conjugués avec les unités oligothiophène ou oligo(p-phénylène vinylène), a été réalisée avec succès.

Pour tester l'aptitude photovoltaïque des systèmes auto-assemblés par liaisons hydrogène, des prototypes sur électrode d'or sont préparés et étudiés dans des cellules photo-électrochimiques. L'étude de la réponse photovoltaïque se révèle très prometteuse, montrant une exaltation par un facteur 2,5 du photo-courant en comparaison au mélange C_{60}-olgothiophène. Ces découvertes indiquent clairement qu'une augmentation substantielle de l'efficacité photovoltaïque est le résultat de l'utilisation du fullerène **1**, lequel est capable de s'auto-assembler avec l'oligothiophène **7**.

La fabrication de dispositifs à partir de monocouches auto-assemblées, portant des sites susceptibles d'établir des liaisons hydrogène constitue une autre rupture technique. Une exaltation supplémentaire par un facteur 6 du photo-courant est observée dans ces dispositifs à auto-assemblage basés sur des électrodes d'or modifié et l'utilisation de molécules SAMs ayant des groupes terminaux barbiturates. Dans ces dispositifs, la performance est limitée par la vitesse de diffusion des espèces transportant les électrons (methylene viologen) en solution plutôt que par la mobilité des porteurs de charges dans l'assemblage supramoléculaire.

Des dispositifs à l'état solide ont été fabriqués dans le but de démontrer le potentiel de la chimie supramoléculaire reposant sur les interactions de type liaisons hydrogène à produire des cellules solaires tout organiques mais ces dispositifs souffrent de la faible processabilité des molécules. Bien que prototype n'est montré qu'un photo-courant modéré (I_{SC} 0.18 mA/cm^2) et un V_{OC} (0,4 V), de meilleures performances peuvent être attendues d'une meilleure compréhension de la nanomorphologie des auto-assemblages supramoléculaires.

En conclusion, partant de l'ingénierie de molécules jusqu'à la synthèse de matériaux et la fabrication de dispositifs photovoltaïques, les résultats de ces travaux révèlent le potentiel de la chimie supramoléculaire pour développer des nouvelles applications de systèmes photoniques. Le concept d'auto-assemblage basé sur des liaisons hydrogène peut être étendu à d'autres espèces photo-actives : par exemple, les chromophores présentant de larges bandes d'absorption recouvrant le spectre solaire tels que des phtalocyanines de zinc, des oligo(p-phénylène vinylènes) ou les analogues de poly(9,9'-dioctylfluoreneco-benzothiadiazole) F8TB. ; ou encore à d'autres accepteurs d'électrons tels que les dérivés bisimides de pérylène, les [n]fullerènes (n $\geqq$ 70) ou les nanotubes de carbone monoparoi.

Résumé

Ces travaux ont pour but la conception et la synthèse de composants moléculaires photo-et électro-actifs programmés l'auto-organiser en hétérojonctions supramoléculaires actives en conversion photovoltaïque. L'utilisation de fullerène (C_{60}) et d'oligothiophène portant des motifs de reconnaissances moléculaires par liaisons hydrogène permet la conception d'architectures supramoléculaires en ruban, optimisées pour la séparation et la transport de charges efficaces. L'étude de monocouches auto-assemblées portant des groupes de reconnaissance moléculaires permet de structurer la couche active et augmente la réponse photovoltaïque des dispositifs. La fabrication de cellules solaires organiques à l'état solide avec ces matériaux auto-assemblées a également été étudiée.

Mots clés:

auto-assemblage, liaisons hydrogène, énergie solaire, cellules solaires organiques, dispositifs photovoltaïques, reconnaissance moléculaire, fullerène, oligothiophene, monocouches auto-assemblées, électrodes d'or macroporeuses, nanoparticles semi-conductrices.

Abstract

The aim of this research is to focus on the implementation of supramolecular self-assembly of photo-and electro-active components programmed to self-organize into molecular hetero-junctions for efficient light-to-electrical energy conversion. The incorporation of fullerene and oligothiophene appended with complementary hydrogen-bonding molecular recognition motifs allows the design of supramolecular architectures engineered to achieve efficient charge separation and transport. In addition, the incorporation of self-assembled monolayers bearing hydrogen-bonding molecular recognition end-groups on electrode surface further enhances the photovoltaic response of the functional supramolecular devices. The fabrication of solid-state organic solar cells with the self-assembled photoactive materials also has been investigated.

Keywords

hydrogen-bonded self-assembly, solar energy, organic solar cells, photovoltaic devices, molecular recognition, fullerene, oligothiophene, self-assembled monolayers, macroporous gold electrodes, semiconductor nanoparticles.